L/E analysis of the atmospheric neutrino data from Super-Kamiokande

Masaki Ishitsuka

February 4, 2004

Abstract

Atmospheric neutrino data from Super-Kamiokande are presented. The Super-Kamiokande detector started the observation on April, 1996 and a 92 kiloton-yr (1489 live-day) exposure to atmospheric neutrino was achieved until July, 2001 during the SK-I running period. A precise study of neutrino oscillation is carried out using the large amount of atmospheric neutrino data. Measurement of the L/E dependence of flavor transition probability of muon neutrino is presented for the first time. Neutrino oscillation probability is predicted to be a sinusoidal function of L/E, where L is the neutrino flight length and E is the neutrino energy. The data are plotted on a L/E axis and are normalized by the Monte Carlo prediction without neutrino oscillations. A dip in the L/E distribution, which should correspond to the first maximum oscillation point, is observed in the muon neutrino data sample as expected by neutrino oscillation. The observed dip in the L/E distribution cannot be predicted by alternative models that could explain the zenith angle dependent deficit of muon neutrinos. These alternative models include neutrino decay or neutrino decoherence models. This is the first statistically significant evidence that the flavor transition probability of neutrinos obeys the sinusoidal function as predicted in neutrino oscillation.

Zenith angle distributions for the various data samples are used to estimate the neutrino oscillation parameter region assuming 2-flavor $\nu_\mu \leftrightarrow \nu_\tau$ oscillations. Various systematic effects in the detector, flux calculation and neutrino interactions are carefully taken into account to estimate the neutrino oscillation parameter region. The 90% confidence level allowed parameter region from this analysis is found to be $\sin^2 2\theta > 0.92$ and $1.5 \times 10^{-3} < \Delta m^2 < 3.4 \times 10^{-3}\mathrm{eV}^2$.

A fit to the L/E distribution of the observed data is carried out assuming 2-flavor $\nu_\mu \leftrightarrow \nu_\tau$ oscillations. Since neutrino oscillation probability is predicted to be as a function of L/E characterized by $\sin^2 2\theta$ and Δm^2, L/E is sensitive to estimate the oscillation parameters, especially the observed dip in the L/E distribution especially allows us to estimate the Δm^2 value accurately. The result of the analysis gives a constraint to neutrino oscillation parameters with $\sin^2 2\theta > 0.90$ and $1.9 \times 10^{-3} < \Delta m^2 < 3.1 \times 10^{-3}\mathrm{eV}^2$ at 90% confidence level. This result is consistent with that from the oscillation analysis based on zenith angle distributions.

Acknowledgments

I would like to express my great appreciation to my advisor, Prof. Takaaki Kajita. He introduced me to experimental physics, gave a chance to study the atmospheric neutrino and provided much advice and guidance. These were very valuable to me.

I would like to express my gratitude to Prof. Y.Suzuki, the spokesman of the Super-Kamiokande experiment, and Prof. Y.Totsuka for the leadership. They gave me advice and encouraged me in many cases.

I am grateful to all the members of the atmospheric neutrino analysis group, especially K.Kaneyuki, Y.Itow, A.Okada, K.Okumura, M.Miura, M.Shiozawa, Y.Obayashi, Y.Hayato, J.Kameda, C.Saji, S.Nakayama, T.Toshito, K.Kobayashi, K.Nitta, Y.Takenaga, H.Sobel, E.Kearns, C.K.Jung, D.Casper, J.Learned, C.McGrew, C.Yanagisawa, M.Messier, C.Walter, K.Scholberg, A.Kibayashi and T.Kato. Thanks to A.Habig for his useful advice especially in writing this thesis. Thanks to S.Moriyama. He was willing to give me his useful knowledge related to experimental physics since I entered graduate school. This thesis is greatly indebted to them.

I would like to extend my gratitude to the other ICRR staff, M.Nakahata, Y.Takeuchi, Y.Koshio, K.Ishihara, T.Namba and Y.Fukuda. They gave me many supports for my work.

I would like to thank all the people who supported and encouraged me during my time in graduate school.

Finally, I gratefully acknowledge the financial support by the Japan Society for the Promotion of Science.

Contents

Chapter 1

Introduction

1.1 Atmospheric Neutrino

When primary cosmic rays interact with air nuclei in the atmosphere of the Earth, secondary particles, mostly pions and some kaons, are produced in hadronic showers. Atmospheric neutrinos are produced from the decay of those secondary particles, mainly by the following decay chains of charged pions :

$$\begin{aligned} \pi^+ &\rightarrow \mu^+ + \nu_\mu \\ &\quad \hookrightarrow e^+ + \nu_e + \overline{\nu}_\mu \end{aligned} \tag{1.1}$$

$$\begin{aligned} \pi^- &\rightarrow \mu^- + \overline{\nu}_\mu \\ &\quad \hookrightarrow e^- + \overline{\nu}_e + \nu_\mu \end{aligned} \tag{1.2}$$

Two muon neutrinos and one electron neutrino are generated by the decay of a charged pion. Therefore, the flux ratio $(\nu_\mu + \overline{\nu}_\mu)/(\nu_e + \overline{\nu}_e)$ is expected to be two for relatively low energy neutrinos. For high energy neutrinos above a few GeV, this flavor ratio becomes greater than two because high energy muons reach the ground without decay and the number of electron neutrinos decreases. In Figure 1.1, the left-hand figure shows the flux ratio of $\nu_\mu + \overline{\nu}_\mu$ to $\nu_e + \overline{\nu}_e$ as a function of the neutrino energy, which is calculated by M. Honda *et al.* [1, 2].

Since the primary cosmic rays pour on the Earth isotropically and the Earth has a spherical form, the atmospheric neutrino flux is expected to be up-down symmetric. In Figure 1.1, two figures on the right show the neutrino flux as a function of the zenith angle of neutrino arrival direction where $\cos\Theta = -1$ ($\cos\Theta = +1$) indicates upward-going (downward-going) directions. The flux of low energy neutrinos is affected by the rigidity cutoff of the primary cosmic rays due to the geomagnetic field. Since the geomagnetic field above Super-Kamiokande is stronger than the average, the up-down symmetry is broken for low energy neutrinos. For energies above a few GeV, the geomagnetic effect is negligible. The flight length of atmospheric neutrinos ranges from $\sim 15\,\mathrm{km}$ to $\sim 13000\,\mathrm{km}$ depending on the zenith angle of the arrival direction.

The detailed explanation about the expectation of the atmospheric neutrino flux is described in Section 3.2.

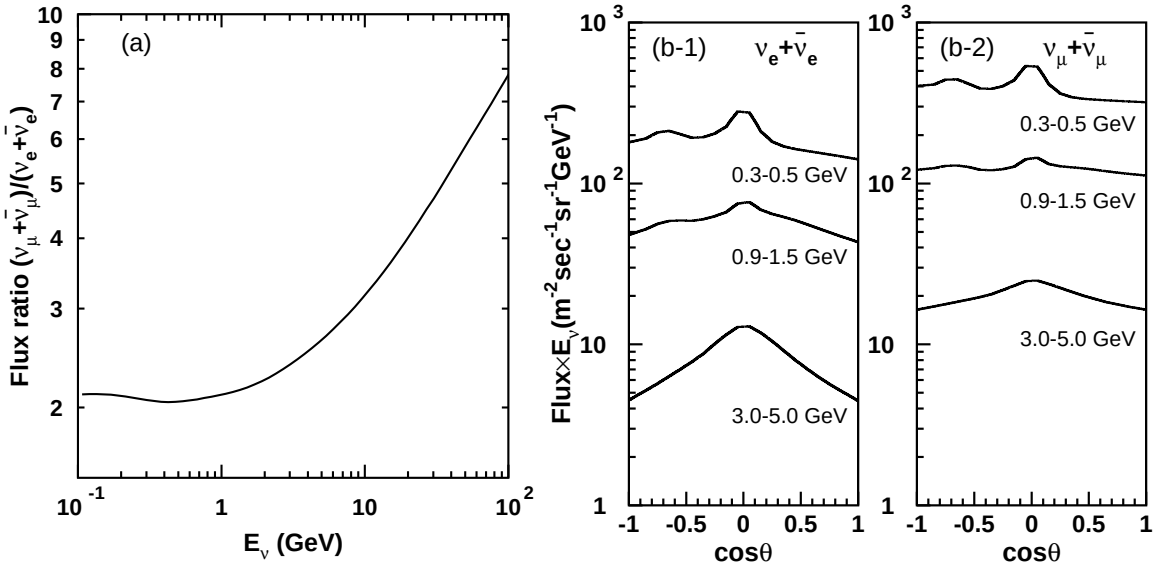

Figure 1.1: Flux ratio of $\nu_\mu+\overline{\nu}_\mu$ to $\nu_e+\overline{\nu}_e$ as function of the neutrino energy (a), and zenith angle dependence of atmospheric neutrino for $\nu_e+\overline{\nu}_e$ (b-1) and $\nu_\mu+\overline{\nu}_\mu$ (b-2). The flux is calculated by M. Honda *et al.* [1, 2].

1.2 Neutrino Oscillation

In the Standard Model of elementary particles, neutrinos are regarded as exactly massless particles [3, 4, 5]. However, there is no fundamental reason to forbid the finite mass of neutrinos. Neutrino oscillation is proposed by Maki, Nakagawa and Sakata in 1962 as a consequence of the finite mass of neutrinos [6]. If neutrinos have finite mass, and their flavor eigenstates are the superpositions of the mass eigenstates, flavor oscillations occur in neutrinos.

In case of two-flavor neutrino oscillation, two mass eigenstates $|\nu_i\rangle$ and $|\nu_j\rangle$ exist :

$$|\nu_i(t)\rangle = |\nu_i(0)\rangle \exp(-iE_i t) \tag{1.3}$$

$$E_i = \sqrt{p^2 + m_i^2} \simeq p + \frac{m_i^2}{2p} \tag{1.4}$$

and the flavor eigenstates can be expressed as their superpositions using the mixing angle θ by :

$$\begin{pmatrix} |\nu_\alpha\rangle \\ |\nu_\beta\rangle \end{pmatrix} = \begin{pmatrix} \cos\theta & \sin\theta \\ -\sin\theta & \cos\theta \end{pmatrix} \begin{pmatrix} |\nu_i\rangle \\ |\nu_j\rangle \end{pmatrix} \equiv U \begin{pmatrix} |\nu_i\rangle \\ |\nu_j\rangle \end{pmatrix} \tag{1.5}$$

where mass indices are shown by i and j, and flavor indices α and β are either two of e, μ or τ. The time evolution of flavor eigenstates is described as follows :

$$\begin{pmatrix} |\nu_\alpha(t)\rangle \\ |\nu_\beta(t)\rangle \end{pmatrix} = U \begin{pmatrix} \exp(-iE_i t) & 0 \\ 0 & \exp(-iE_j t) \end{pmatrix} U^{-1} \begin{pmatrix} |\nu_\alpha(0)\rangle \\ |\nu_\beta(0)\rangle \end{pmatrix} \tag{1.6}$$

Neutrinos produced via a weak interaction in ν_α at $t = 0$ is found in ν_α after time t with the

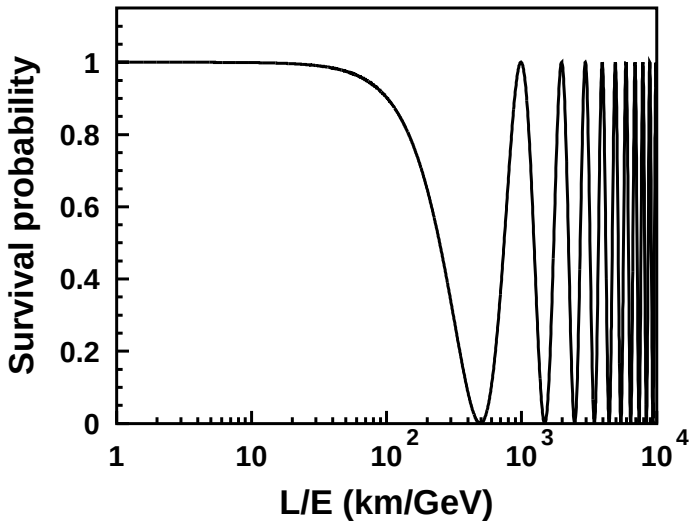

Figure 1.2: Survival probability of neutrinos predicted from neutrino oscillation.

probability expressed by :

$$P(\nu_\alpha \to \nu_\alpha : t) = |\langle \nu_\alpha | \nu_\alpha(t) \rangle|^2 = 1 - \sin^2 2\theta \sin^2 \left(\frac{(E_j - E_i)t}{2} \right) \tag{1.7}$$

Using Equation (1.4) and neutrino path length L_ν, the survival probability of ν_α is rewritten as follows :

$$P(\nu_\alpha \to \nu_\alpha) = 1 - \sin^2 2\theta \sin^2 \left(\frac{1.27 \Delta m^2(\mathrm{eV}^2) L_\nu(\mathrm{km})}{E_\nu(\mathrm{GeV})} \right) \tag{1.8}$$

where $\Delta m^2 \equiv m_j^2 - m_i^2$ is the mass-squared difference of neutrino mass eigenstates. Figure 1.2 shows the survival probability of neutrinos as a function of L_ν/E_ν predicted from Equation (1.8) with typical parameters. The survival probability of flavor eigenstates has an oscillation form. The amplitude is determined from the mixing angle θ, and the L/E dependence of the survival probability is characterized by the difference of mass square Δm^2.

1.3 Neutrino Oscillation Experiments

Evidence for oscillation of atmospheric neutrinos was resented from Super-Kamiokande experiment in 1998 [7]. The observed zenith angle dependent deposit of muon neutrinos could not be explained by the prediction of atmospheric neutrino flux within the systematic uncertainties and the statistic errors, but was consistent with two-flavor $\nu_\mu \leftrightarrow \nu_\tau$ oscillation. Neutrino oscillation has been studied by various other experiments before and after the evidence was reported. Some of the experiments related to the oscillation of atmospheric neutrinos are summarized in this section.

1.3.1 Kamiokande experiment

Kamiokande, the predecessor of Super-Kamiokande, was a water Cherenkov detector located at Kamioka Observatory in Gifu Prefecture, Japan [8, 9]. A cylindrical tank contained 3 kt pure

water. 948 20 inch photomultilier tubes (PMTs) were installed on the detector walls with 20 % photocathode coverage. In water Cherenkov detector, muons and electrons, which are produced from ν_e and ν_μ charged current interactions, can be distinguished by the shape of the ring image. Kamiokande reported lower value of the observed flavor ratio $(N_\mu/N_e)_{obs}$ than it was expected $(N_\mu/N_e)_{exp}$:

$$R(\mu/e) \equiv (N_\mu/N_e)_{obs}/(N_\mu/N_e)_{exp} = \begin{cases} 0.60\,^{+0.06}_{-0.05}\,(stat.) \pm 0.05\,(sys.) & \text{(Sub-GeV)} \\ \\ 0.57\,^{+0.08}_{-0.07}\,(stat.) \pm 0.07\,(sys.) & \text{(Multi-GeV)} \end{cases}$$

Furthermore, the zenith angle dependence of muon deficit in multi-GeV energy events was reported from Kamiokande. The results were explained by neutrino oscillation. Kamiokande started the observation at 1983 and ended at 1996, when Super-Kamiokande started the observation. Those reports from Kamiokande motivated the careful study of atmospheric neutrinos.

1.3.2 Soudan 2 experiment

Soudan 2 was a 963 tons iron tracking calorimeter located at a depth of 2070 m.w.e. (meters water equivalent) in the Soudan Underground Mine State Park in Minnesota. The detector started the data taking at 1989 and ceased the operation at 2001. The active elements were 1 m long, 1.5 cm diameter plastic drift tubes filled with an argon-CO_2 gas mixture. The tubes were encased in a honeycomb structure of 1.6 mm corrugated steel plates, and each operated as a time projection chamber. Electrons and muons were classified as "showers" and "tracks" by the form of the tracks. The data from the 5.90 kton-year exposure of Soudan 2 detector also gave s smaller flavor ratio than it was expected without neutrino oscillations :

$$R(\mu/e) = 0.69 \pm 0.10\,(stat.) \pm 0.06\,(sys.)$$

An unbinned maximum likelihood analysis of neutrino L/E distribution was carried out to the observed data using the Feldman-Cousins prescription. The observed data favored $\nu_\mu \leftrightarrow \nu_\tau$ oscillation. 90 % confidence level allowed region of neutrino oscillation parameters $(\sin^2 2\theta, \Delta m^2)$ obtained from Soudan 2 experiment is shown in Figure 1.3 by dotted line [10].

1.3.3 MACRO experiment

MACRO was a large multi-purpose detector composed of liquid scintillation counters for energy and timing measurements, limited streamer tubes for particle tracking and nuclear track detectors for rare particle searches. The detector operated from 1989 till the end of 2000 at the Gran Sasso Laboratory where the average rock overburden was 3700 m.w.e.. The energy spectrum and the angular distribution of upward-going muons were used to test atmospheric neutrino oscillation. The observed data was consistent with $\nu_\mu \leftrightarrow \nu_\tau$ oscillation. MACRO experiment gave a 90 % confidence level allowed parameter region as shown in Figure 1.3 by dashed line [11].

1.3.4 K2K experiment

K2K is a long baseline experiment using artificial neutrino beam produced by an accelerator. The aim of K2K experiment is to confirm the existence of atmospheric neutrino oscillation.

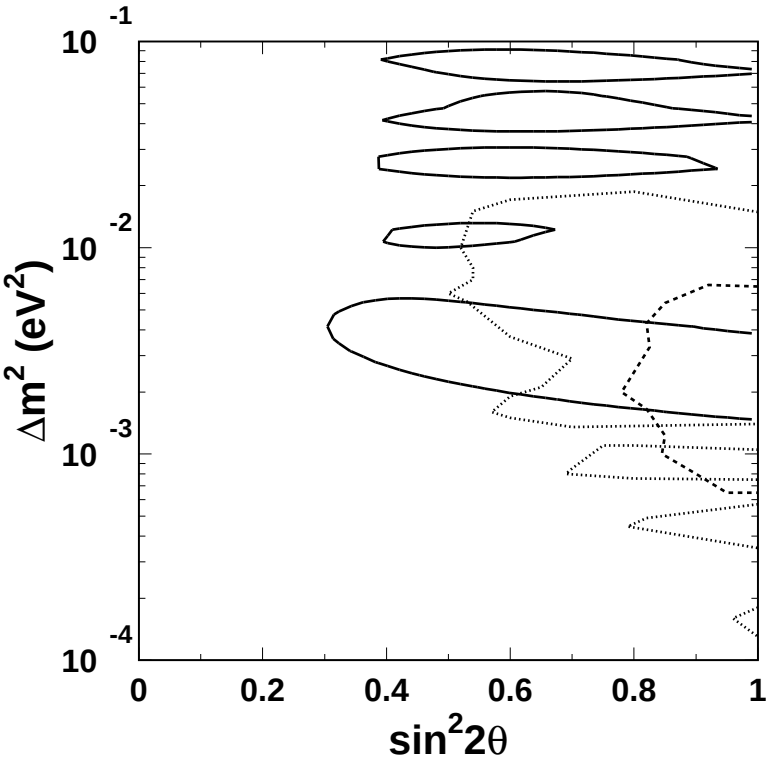

Figure 1.3: 90 % confidence level allowed regions for $\nu_\mu \leftrightarrow \nu_\tau$ oscillation. The horizontal axis shows $\sin^2 2\theta$, and the vertical axis shows Δm^2 in the plot. The results are taken from Soudan 2 [10] (dotted line), MACRO [11] (dashed line) and K2K experiment [12] (solid line).

Almost pure ν_μ beam is created by a 12 GeV proton synchrotron accelerator at KEK in Tsukuba city, Japan. The neutrinos are generated from the decay of charged pions, which are produced in collisions of accelerated protons and a target. The mean energy of beam neutrinos is 1.3 GeV. The neutrino beam passes through the Earth, and is observed by Super-Kamiokande detector at a distance of 250 km. The experiment started in June, 1999, and almost half of its allocated protons on target has been collected till July, 2001. The number of neutrino events observed in Super-Kamiokande is smaller than it was expected without neutrino oscillation by more than 2 standard deviations, while it is consistent with the prediction from atmospheric neutrino oscillation. The energy spectrum of the observed neutrino events is used for neutrino oscillation analysis. A 90 % confidence level allowed parameter region obtained from K2K experiment is shown in Figure 1.3 [12].

1.4 Motivation of This Thesis

Anomalous results in neutrino flavor ratio and a zenith angle dependent deficit of muon neutrinos are interpreted as the evidence for $\nu_\mu \leftrightarrow \nu_\tau$ oscillation, and which has been confirmed by several experiments as shown in the previous section. However, the sinusoidal function of the neutrino flavor transition probability which is predicted from neutrino oscillation as shown

in Figure 1.2 has not been observed yet. The measurement of the oscillation probability gives a direct evidence for neutrino oscillation. Furthermore, since neutrino decay [106] and neutrino decoherence [108], which also give possible solutions to the atmospheric neutrino data, predict different transition probabilities as a function of L/E, the measurement of the L/E distribution make it possible to distinguish neutrino oscillation from the other hypotheses.

A precise study of neutrino oscillation parameters is carried out using a large amount of atmospheric neutrino data from Super-Kamiokande. The result of the measurement of L/E distribution in Super-Kamiokande atmospheric neutrino data is presented for the first time. In the L/E analysis, the energy and the flight length of atmospheric neutrinos are carefully estimated for not only the fully contained sample but also the partially contained sample. High energy muon events, mostly categorized to partially contained events, have better angular resolution and therefore have high resolution of L. Since neutrino oscillation probability is predicted to be as a function of L/E characterized by $\sin^2 2\theta$ and Δm^2, L/E is the most sensitive way to estimate the oscillation parameters. Especially, measurement of a dip due to first maximum oscillation probability gives a strong constraint to the Δm^2.

Chapter 2

The Super-Kamiokande Detector

Super-Kamiokande is a cylindrical 50 kt water Cherenkov detector located at Kamioka Observatory in Gifu Prefecture, Japan. The geographic coordinates of the site are 36°25'N and 137°18'E, and the altitude above sea level is 370 m. The detector lies in a zinc mine under the peak of Mt.Ikenoyama, where the mean rock overburden is 1000 m (2700 m water equivalent). This overburden serves as a shield to cosmic ray background. The cosmic ray muon flux at the Super-Kamiokande site is reduced by 5 orders compared to that on the surface of the Earth.

The main scientific purposes of the Super-Kamiokande experiment are the searches for nucleon decays and the studies of various types of neutrinos: atmospheric neutrinos, solar neutrinos and the neutrinos from suparnovae and the other astrophysical sources. The Super-Kamiokande detector is also used as a target of the artificial neutrino beam in a long baseline neutrino oscillation experiment.

The Super-Kamiokande experiment started taking data in April, 1996 and continued the observation for five years within the running period referred to SK-I till the maintenance in July, 2001. During refilling water after maintenance, an accident occurred in November, 2001 in which more than a half of the PMTs were destroyed. The Super-Kamiokande detector was rebuilt after the accident and has resumed observation from October, 2002 which is referred to SK-II running period.

In this thesis the data observed in SK-I running period (1996-2001) is used. The configuration and operational characteristics of the detector in the SK-I period are described in this chapter.

2.1 Cherenkov Radiation

The Super-Kamiokande detector observes relativistic charged particles in water by detecting the emitted Cherenkov light. Cherenkov photons are radiated when the velocity of a charged particle exceeds the light velocity in the medium :

$$v \geq \frac{c}{n} \tag{2.1}$$

where v is the velocity of the particle, n is the refractive index of the medium and c is the light velocity in vacuum [13]. The momentum threshold of Cherenkov radiation is determined by the refractive index of the medium and the mass of the particle. In water, the refractive index is about 1.34, and the momentum thresholds for electrons, muons and pions are 0.57, 118 and 156 MeV/c, respectively.

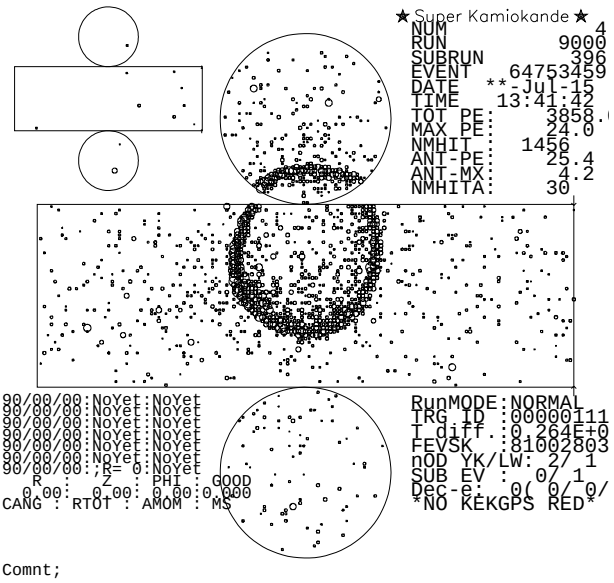

Figure 2.1: A typical observed neutrino event in Super-Kamiokande. The size of small circles in the unrolled cylinder represents the amount of Cherenkov photons detected in each photomultiplier tube. The Cherenkov ring image is clearly visible.

Cherenkov light is emitted on a cone with a characteristic half opening angle θ_C along the direction of the particle. The opening angle, called Cherenkov angle, is determined as follows :

$$\cos\theta_C = \frac{1}{n\beta} \tag{2.2}$$

where $\beta = v/c$. For the particle with $\beta \simeq 1$ in water, the Cherenkov angle is about 42°.

The number of photons emitted by Cherenkov radiation is given as a function of the wavelength λ as follows :

$$\frac{d^2N}{dxd\lambda} = \frac{2\pi\alpha}{\lambda^2}\left(1 - \frac{1}{n^2\beta^2}\right) \tag{2.3}$$

where x is the path length of the charged particle and α is the fine structure constant. About 340 photons/cm are emitted between the wavelength of 300 nm to 600 nm, which is the sensitive wavelength region of photomultiplier tubes (PMTs).

Particles emitting Cherenkov light project ring images on the wall inside the detector. Super-Kamiokande detects the Cherenkov photons by PMTs arranged on the wall and the Cherenkov rings can be recognized. Figure 2.1 shows a visual display of a typical neutrino event in the Super-Kamiokande detector.

2.2 Detector

2.2.1 Water tank

A schematic view of the detector is shown in Figure 2.2. The whole size of the water tank is 41.4 m in the hight and 39.3 m in the diameter, in which 50 kt highly pure water is filled.

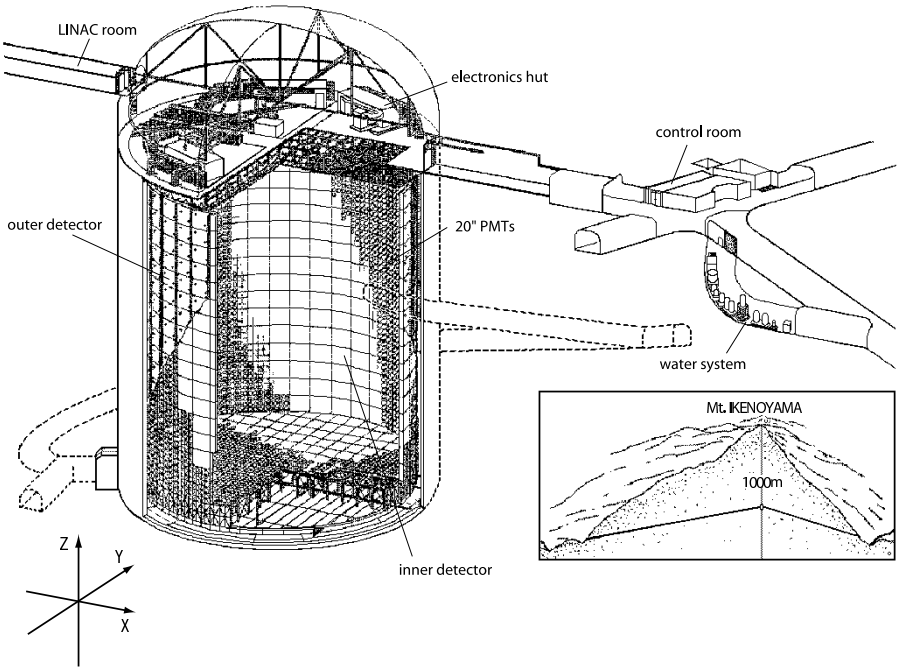

Figure 2.2: Super-Kamiokande detector and its location.

The water tank is optically separated into two concentric cylindrical regions by a PMT support structure and a pair of opaque sheets as shown in Figure 2.3.

The inner region, this part of the detector is referred to the inner detector (ID), contains 32 kt water with the size of 36.2 m in the hight and 33.8 m in the diameter. 11,146 inward-facing 20 inch PMTs are attached to the supporting frame uniformly at intervals of 70 cm. The photocathode coverage of the ID is about 40 %, and the rest of the surface is covered with black polyethylene terephthalate sheet, called "black sheet".

The outer region completely surrounds the ID with the thickness of 2.05 m on top and bottom and 2.2 m along the barrel wall. This region, called the outer detector (OD), is monitored by 1,885 outward-facing 8 inch PMTs attached to the outer side of the supporting frame. To increase the light collection, each PMT in the OD is equipped with a wavelength shifter plate, and the walls are covered with reflective material called "tyvek sheet". The OD is used to veto entering cosmic ray muons and to tag the outgoing charged particles. Furthermore, the 2 m thickness water layer itself serves as a shield to attenuate gamma ray and neutron fluxes from the rock.

The inner and outer volumes are separated by a 55 cm thick dead region. This region is not instrumented with any PMT. Stainless steel frames and signal and HV cables of the ID and OD PMTs are contained in this dead region.

2.2.2 Photomultiplier Tube

Inner detector photomultiplier tube

The photomultiplier tubes used in the ID, product name Hamamatsu R3600, have photocathode with a diameter of 50 cm (20 inch). 11,146 tubes are instrumented in the ID with 40 %

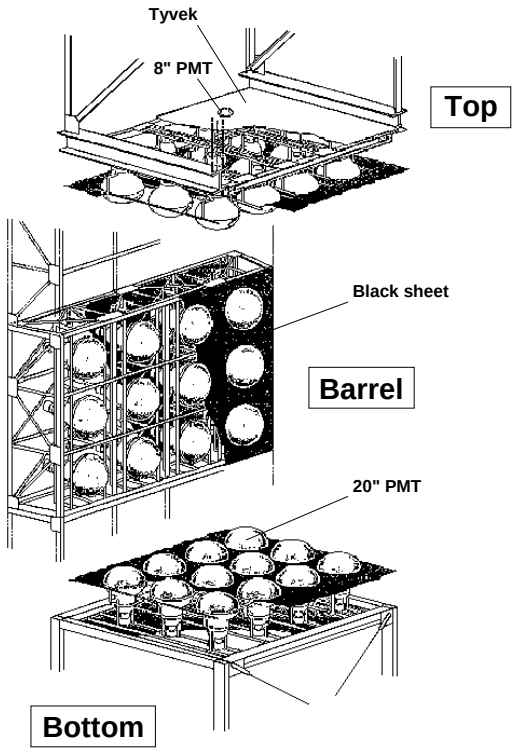

Figure 2.3: Supporting frame of PMTs.

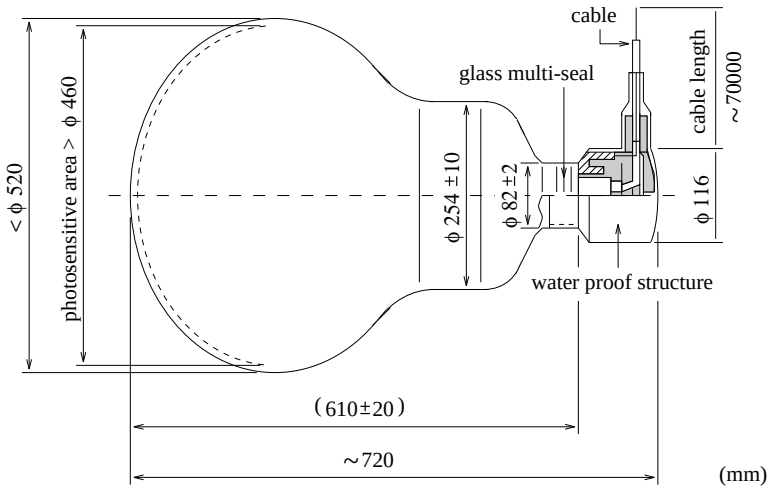

Figure 2.4: A schematic view of a 20 inch PMT.

photocathode coverage. This 20 inch PMT was originally developed by Hamamatsu Photonics K.K. in cooperation with the Kamiokande collaborators [14]. Later, the dynode structure and the bleeder circuit were modified for Super-Kamiokande to improve timing response and photon collection efficiency [15]. A schematic view of the PMT is shown in Figure 2.4 and the specifications are summarized in Table 2.1.

The photocathode of the PMT is coated by bialkali (Sb-K-Cs) owing to the high spectral sensitivity to Cherenkov light and the low thermionic emission. The quantum efficiency of the PMT is shown in Figure 2.5, in which the peak is 22 % at the wavelength of 390 nm. The dynode structure and the bleeder circuit are optimized to achieve high collection efficiency, which results in a fast timing response and good energy resolution. The averaged value of the collection efficiency at the first dynode is 70 %, which is uniform within a difference of ±7 % everywhere on photocathode. The gain of the PMT increases as V^x, where V is the voltage and x is typically 2.1, and 2000 V supplied voltage gives a typical gain of 10^7. Figure 2.6 shows the charge distribution for the single photoelectron signal in which a clear 1 p.e. peak can be seen. The transit time spread of single photoelectron signal is about 2.2 nsec.

The magnetic field over 100 mG affects photoelectron trajectories in the PMT and makes the timing resolution worse, while geomagnetic field at the detector site is about 450 mG. To compensate for the magnetic field, 26 sets of Helmholtz coils are installed around the tank. As a result of this, the magnetic field inside the detector is kept about 50 mG.

Outer detector photomultiplier tube

1885 8 inch PMTs, Hamamatsu R1408, are used in the OD. These PMTs were first adopted in the IMB experiment [16], and they are reused in the Super-Kamiokande detector after finish-

Shape	Hemispherical
Photocathode area	50 cm diameter
Window material	Pyrex glass ($4 \sim 5$ mm)
Photocathode material	Bialkali (Sb-K-Cs)
Quantum efficiency	22 % at $\lambda = 390$ nm
Dynodes	11 stage Venetian blind type
Gain	10^7 at ~ 2000 V
Dark current	200 nA at 10^7 gain
Dark pulse rate	3 kHz at 10^7 gain
Cathode non-uniformity	< 10 %
Anode non-uniformity	< 40 %
Transit time	90 nsec at 10^7 gain
Transit time spread	2.2 nsec ($1\,\sigma$) for 1 p.e. equivalent signals
Weight	13 kg
Pressure tolerance	6 kg/cm^2 water proof

Table 2.1: Specifications of 20 inch PMT.

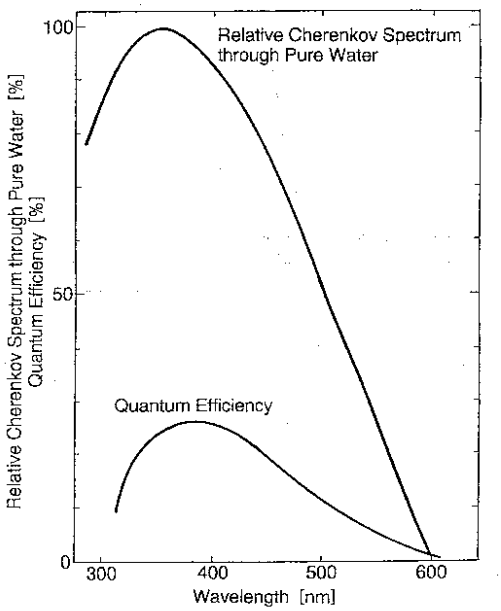

Figure 2.5: Quantum efficiency of 20 inch PMT as a function of wavelength together with the relative spectrum of Cherenkov light through pure water.

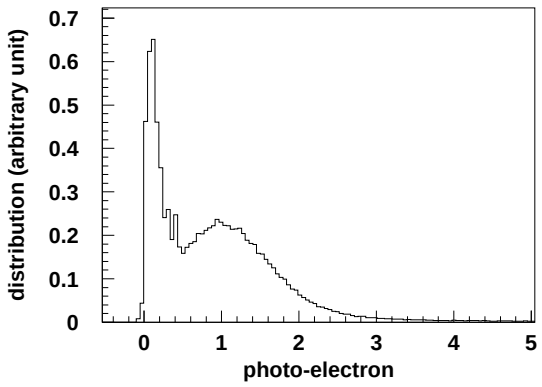

Figure 2.6: Single photoelectron distribution of a typical 20 inch PMT.

ing that experiment. The photocathode of the OD PMT is fitted with 60 cm × 60 cm × 1.3 cm wavelength shifter plate. The wavelength shifter increases the light collection efficiency by 60 %. Although the timing resolution of OD, which is about 11 nsec without the wavelength shifter, is degraded to about 15 nsec, it is still accurate enough for the function of the OD.

2.2.3 Water purification system

The water for the Super-Kamiokande experiment is produced from abundant spring water in the mine. The water in the tank is continuously circulated through the water purification system to keep the light attenuation length at roughly 100 m. It is also an important purpose of this system to remove the radioactive materials, especially radon (Rn), which become a background for solar neutrino observation. About 50 ton/hour water is constantly processed. The outline of the system is shown in Figure 2.7. The system consists of the following components.

- 1 μm mesh filter — removes dust and small particles. Such impurities reduce the water transparency.
- Heat exchanger — cools water to suppress the growth of bacteria. The water temperature in the detector is kept at 14 °C.
- Cartridge polisher — eliminates heavy ions which also reduce water transparency.
- Ultra-Violet sterilizer — kills bacteria.
- Radon-reduced air dissolve tank — dissolves radon-reduced air into the water to increase radon removal efficiency at the vacuum degasifier stage which follows.
- Reverse osmosis — removes particulates.
- Vacuum degasifier — removes dissolved gases in water, such as the oxygen and radon.

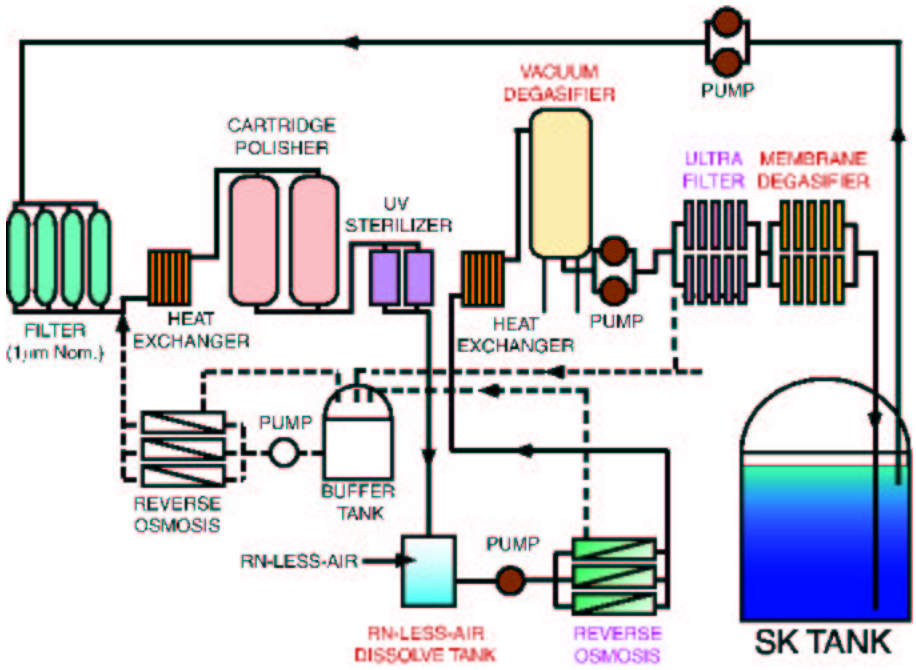

Figure 2.7: The water purification system for Super-Kamiokande.

- Ultra filter — removes minute particles of the order of 10 nm.
- Membrane degasifier — removes radon dissolved in water.

The typical number of particles larger than 0.2 μm is reduced to 6 particles/cc after purification.

2.2.4 Electronics and Data Acquisition System

Inner detector electronics and data acquisition

ID PMT signals are processed by custom built electronics modules called ATM (Analog-Timing-Module) of the TKO standard (TRISTAN KEK Online) [17, 18]. The ATM module can record the integrated charge and the arrival time information for each PMT signal with the functions of ADC and TDC.

Figure 2.8 shows the block diagram of the analog input part of the ATM module. Each PMT input channel of ATM has two switching pairs of QAC (Charge to Analog Converter) and TAC (Time to Analog Converter) so that two successive events, such as a muon and the subsequent decay electron, can be processed. Each PMT signal fed into ATM is amplified 100 times, and then divided into four signals. One of them is fed to the discriminator. When the pulse height of the PMT signal exceeds the threshold level, which is set to 0.25 p.e.s , a 400 nsec gate signal for QAC and a start signal for TAC are generated. At the same time, rectangular signal called HITSUM is sent to a global trigger module. Other two branches of the split PMT signal are fed to QAC. If a global trigger is issued, a stop signal is sent to TAC and the information in QAC and TAC is digitized by ADC. The digitized charge and timing information is stored in

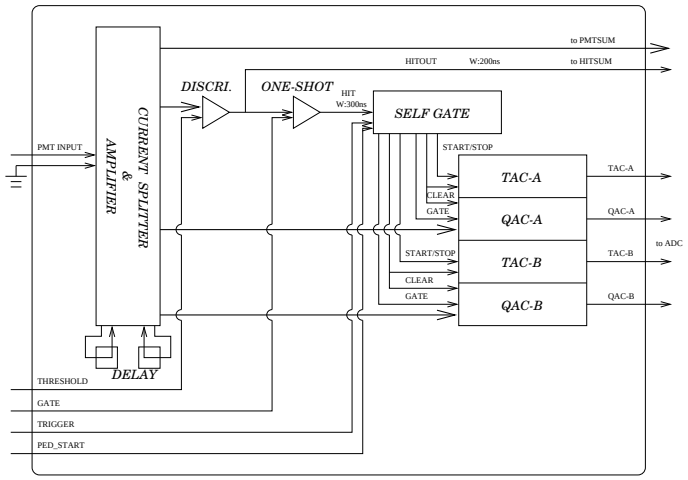

Figure 2.8: A block diagram of analog input part of ATM.

internal FIFO memory in ATM. If a global trigger is not issued within 1.3 μsec, the information is cleared. ATM has 450 pC dynamic range with a resolution of 0.2 pC, and 1.3 μsec dynamic range with a resolution of 0.4 nsec. The remaining one signal becomes an output signal of ATM called PMTSUM.

Figure 2.9 shows a schematic view of the ID data acquisition system. Signals from 12 PMTs are fed to an ATM board to be processed. There are in total 946 ATM boards installed in 48 TKO crates. The digitized data in ATM FIFO memory are sent to VME memory modules called SMP (Super Memory Partner) every 16 events. 48 SMP are installed in 8 VME crates, and one SMP module handles the data of 20 ATMs. The data in SMP memories are read out by 8 slave computers and sent to the online host computer.

Outer detector electronics and data acquisition

Figure 2.10 shows a schematic view of the OD data acquisition system [19]. The paddle cards distribute high voltage from the main frame to the OD PMTs. A coaxial cable is used to supply the high voltage to an OD PMT and to send a signal from the PMT. These cards also pick off the PMT signals through a high voltage capacitor. Signals from the OD PMTs are sent to QTC (Charge to Time Converter) modules. A QTC module converts the PMT signal to a rectangular pulse whose width is proportional to the input charge. At the same time, a rectangular HITSUM signal is generated by QTC and sent to a global trigger module. The threshold of QTC modules is set to 0.25 p.e.. If a global trigger is received, the leading edge and the width of the rectangular pulse are converted to the timing and charge information by a LeCroy 1877 multi-hit TDC module. TDC module can record up to 8 QTC pulses with a resolution of 0.5 nsec. The dynamic range is set to 16 μsec which starts from 10 μsec before the global trigger timing. The digitized data stored in TDC are read by a slave computer through VME memory module called DPM (Dual Port Memory) and then sent to the online host computer.

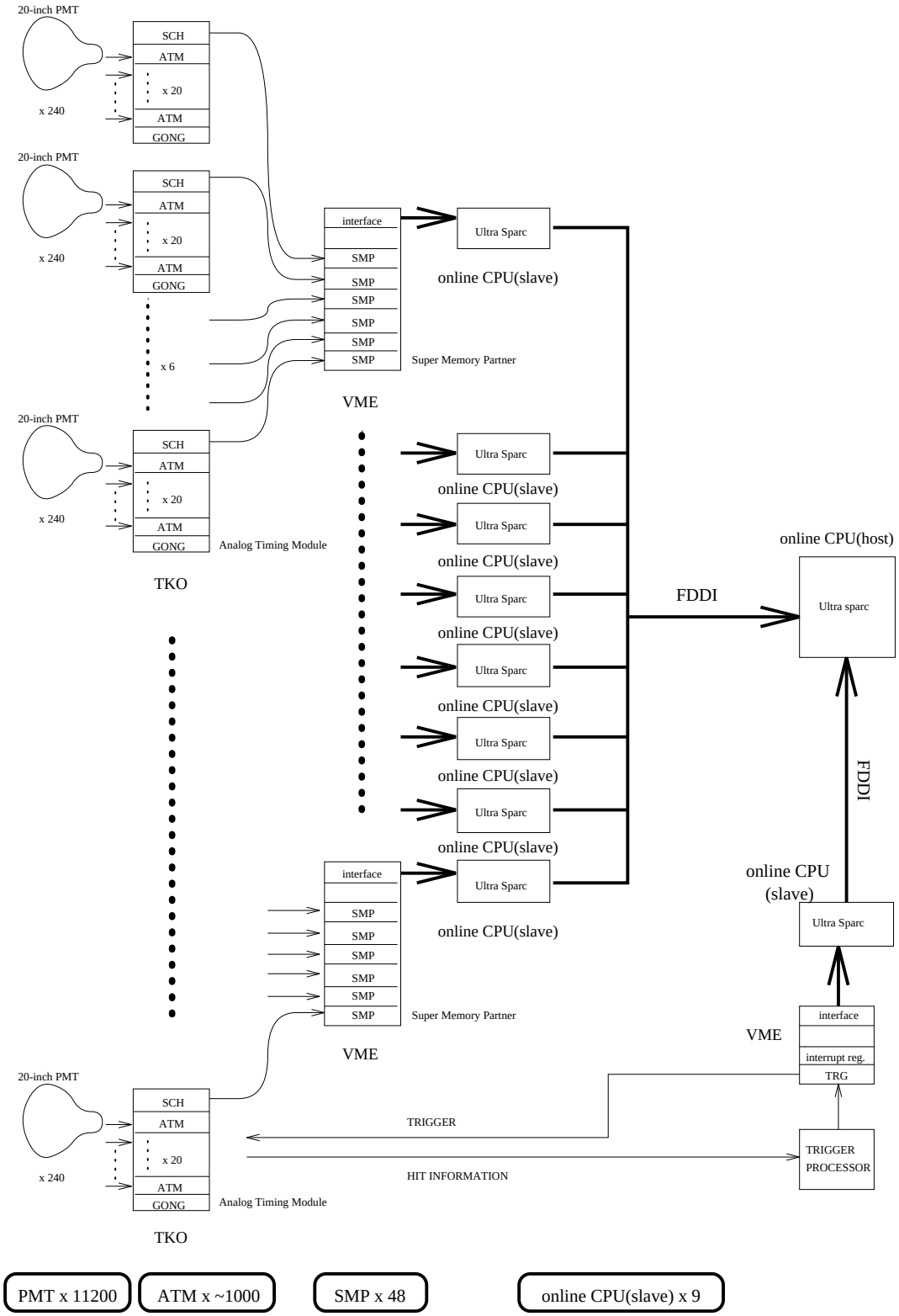

Figure 2.9: A schematic view of the inner detector data acquisition system.

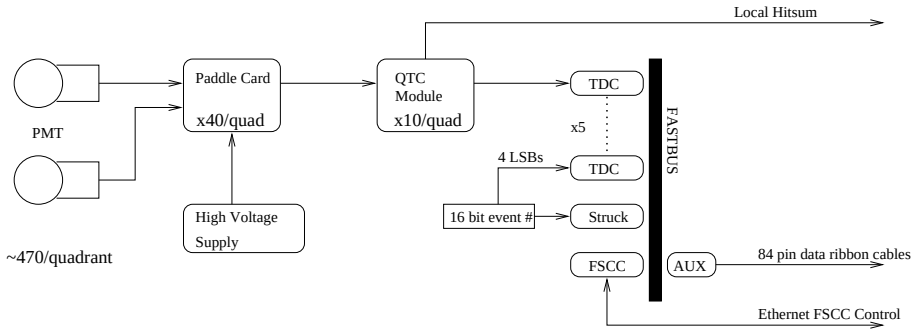

Figure 2.10: A schematic view of the outer detector data acquisition system.

Trigger

An ATM module generates a rectangular HITSUM signal with 11 mV in pulse height and 200 nsec in width each time an ID PMT signal exceeds the threshold. These signals are analog-summed over all PMTs to generate an ID-HITSUM signal. The pulse height of the ID-HITSUM signal is proportional to the number of hit PMTs within 200 nsec time window. There are three types of trigger signals derived from the ID-HITSUM signal. The high energy (HE) trigger is generated when the pulse hight of ID-HITSUM signal exceeds a threshold of -340 mV, which corresponds to 31 hits within a 200 nsec time window. The threshold for the low energy (LE) trigger is set to -320 mV, which corresponds to 29 hits. This is equivalent to a signal expected from a 5.7 MeV electron. The trigger rates for HE and LE triggers are ~ 5 Hz and ~ 11 Hz, respectively. The super low energy (SLE) trigger was implemented in May 1997 in order to lower the solar neutrino analysis threshold. The threshold is set to 4.6 MeV equivalent. The SLE triggered events are not used in atmospheric neutrino analysis.

The OD trigger is generated by a similar procedure. When an OD PMT signal exceeds a threshold, a QTC module generates a rectangular pulse with 20 mV in height and 200 nsec in width. These signals are also analog summed up to generate an OD-HITSUM signal. The threshold for the OD trigger is set to 19 hits within a 200 nsec time window.

These four types of trigger signals (HE, LE, SLE and OD) are fed to a hardware trigger module called TRG. The TRG module generates a global trigger signal when any one of the trigger signals is issued.

2.3 Calibration

2.3.1 Relative gain calibration

The high voltage value supplied to each PMT is adjusted to provide uniform gain for all PMTs in the ID. The uniformity of the PMT gain is necessary to determine the momentum without systematic difference depending on its vertex position or direction.

Figure 2.11 shows a schematic view of the relative gain calibration system. Light generated by a Xe lamp is passed through an ultraviolet (UV) filter and neutral density (ND) filter and then split into four. One is injected into a scintillator ball via an optical fiber. The others are used to monitor the intensity of the Xe light and to make a calibration trigger. The scintillator

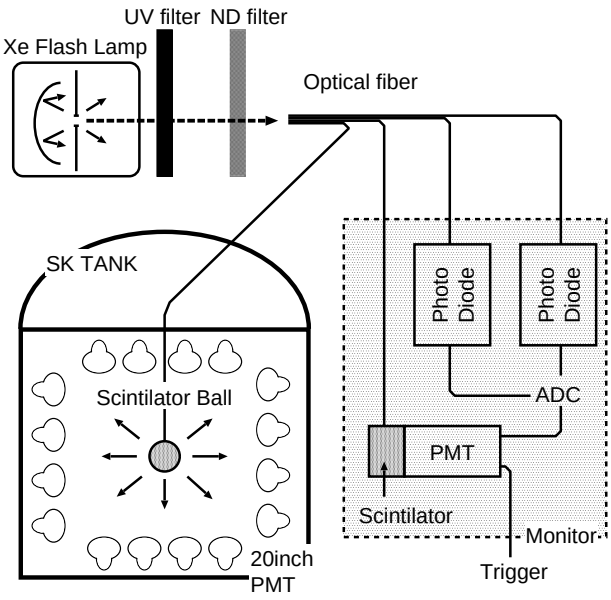

Figure 2.11: A schematic view of the relative gain measurement system using a Xe lamp.

ball is made of acrylic resin mixed with BBOT wavelength shifter and MgO powder diffuser. BBOT wavelength shifter absorbs UV light and emits light with a peak at 440 nm, which is a typical wavelength of Cherenkov light.

The high voltage value of each PMT is adjusted to give the same gain with the others. The relative gain G_i of the i-th PMT is obtained by :

$$G_i = \frac{Q_i}{Q_0 f(\theta)} \cdot l_i^2 \cdot \exp\left(\frac{l_i}{L}\right) \tag{2.4}$$

where Q_i is the charge detected by the i-th PMT, l_i is the distance from the light source to the PMT, $f(\theta)$ is the PMT acceptance as a function of the photon incidence angle θ, L is the attenuation length and Q_0 is the normalization factor. This measurement is performed for several positions of the scintillator ball, changing the voltage.

Figure 2.12 shows the relative gain distribution of all the PMTs after adjusting high voltage values. The relative gain spread is about 7 %. The remaining gain difference is corrected in software.

2.3.2 Absolute gain calibration

The absolute gain calibration is necessary to convert the charge detected by each PMT in pico Coulomb (pC) correctly into the number of photoelectrons. The absolute gain is determined using the charge distribution of single photoelectron signals.

The low energy gamma ray generated from neutron capture on Nickel nucleus is used as a calibration source to measure the single photoelectron distributions. The schematic view of the Nickel calibration source is shown in Figure 2.13. Neutrons produced by spontaneous fission of ^{252}Cf are captured on surrounding Ni wires in polyethylene vessel, and low energy ($6 \sim 9$ MeV) gamma rays are generated simultaneously. The number of hit PMT is about $50 \sim 80$ in total,

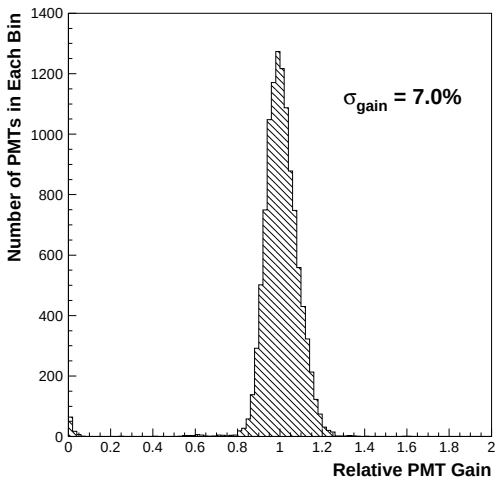

Figure 2.12: The relative gain distribution of all the ID PMTs, measured in 1996.

so that the number of p.e. detected by each PMT is at most one. The charge distribution of a typical PMT is also shown in Figure 2.13. The sharp peak near zero is caused by electrons that are emitted from the photocathode but miss the first dynode, and the peak around 2 pC corresponds to that of single photoelectrons. The mean value 2.055 pC is used as a constant to convert the PMT charge from pico Coulomb to the number of p.e.s.

2.3.3 Relative timing calibration

The relative timing calibration is important for the vertex position reconstruction. The timing response of the PMT depends on not only the length of the signal cable but also the detected charge because of the slewing effect of discriminator. The large signal tends to exceed the threshold earlier than the small one.

Figure 2.14 shows the schematic view of the relative timing calibration system. N_2 laser generator emits intense light with 337 nm wavelength within a time width of 3 nsec. The wavelength of the laser light is converted to 384 nm by a dye laser module. The PMT is most sensitive to this wavelength. Then the light is split into two. One is injected into a diffuser ball in the ID via an optical fiber and the other is used to monitor the light intensity. The schematic view of the diffuser ball is also shown in Figure 2.14. The laser light injected to the diffuser ball is first diffused by a TiO_2 diffuser tip at the center and then further diffused by the surrounding LUDOX silica gel made of 20 nm glass fragments.

The measurement is done for various intensity of the light using a variable attenuation filter. A scatter plot of the timing and the charge for a typical PMT is shown in Figure 2.15, which is called TQ-map. The dots represent the data and the circles represent the average timing for each charge bin with the errors. The TQ-map is made for all ID PMTs and used to correct the timing information.

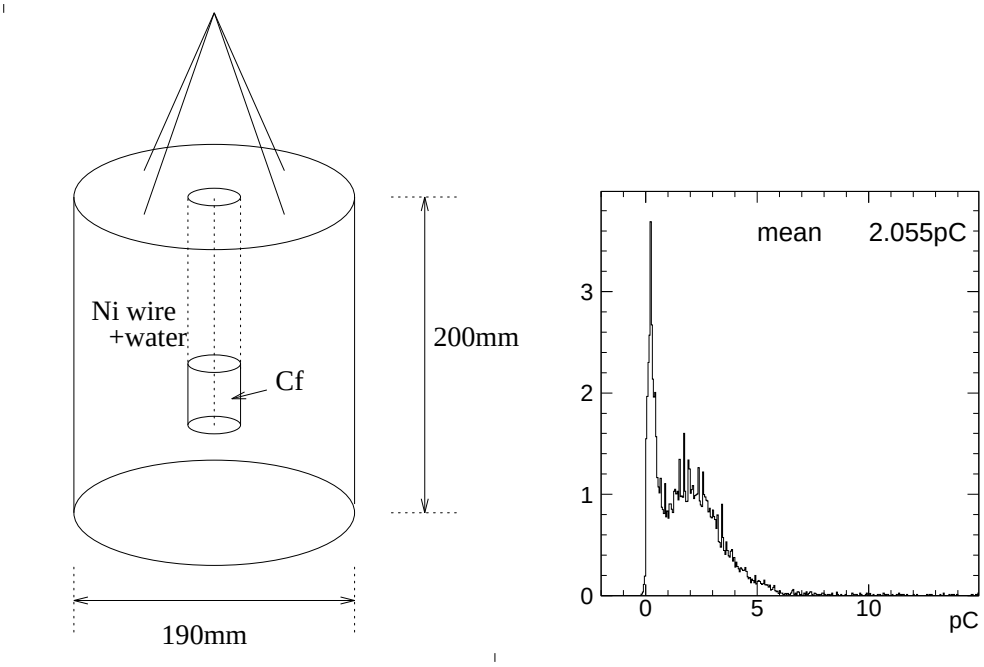

Figure 2.13: Schematic view of an Nickel calibration source (left) and charge distribution of a typical ID PMT (right).

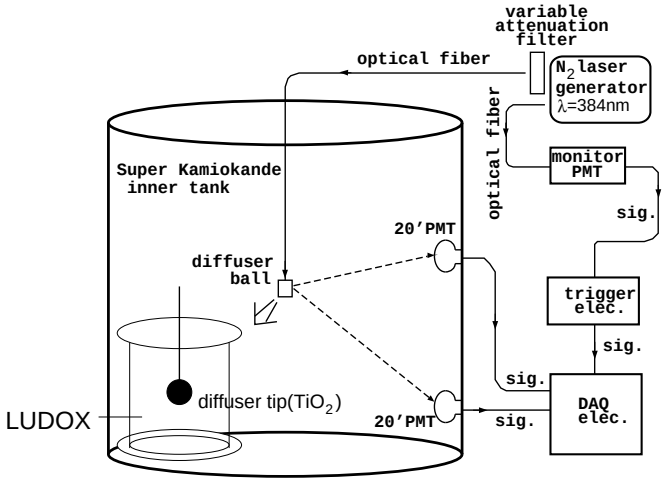

Figure 2.14: A schematic view of the timing measurement system using a laser.

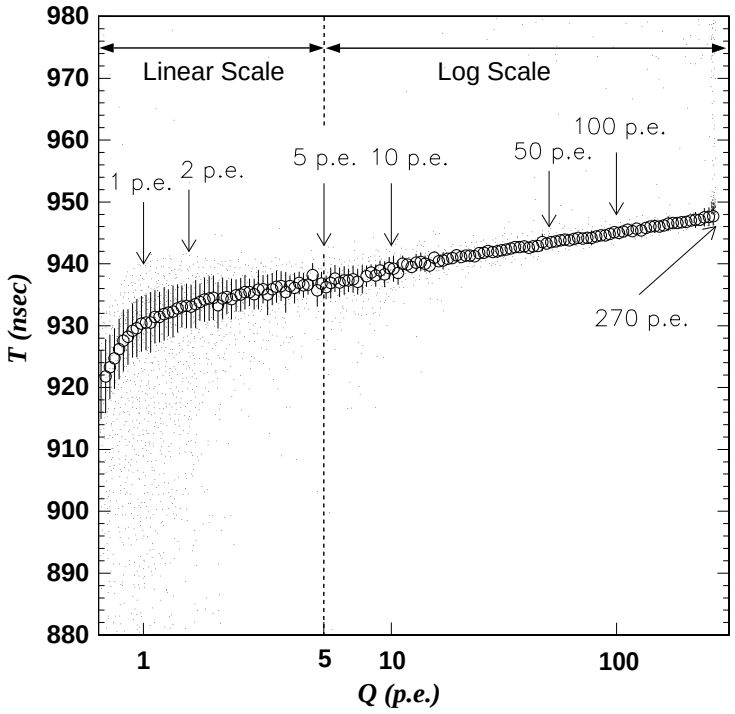

Figure 2.15: TQ-map, a measured two-dimensional plot of timing vs. charge distribution.

2.3.4 Water transparency measurement

Water transparency is the length scale of the optical attenuation in water, which represents the combined effect of absorption and scattering on the intensity of the light. Water transparency in Super-Kamiokande is measured using N_2 laser beam injected into the detector. The wavelength dependence of the attenuation length can be measured by changing the dye of the laser. The absorption and scattering coefficients are separately measured by this method. Further, the water transparency is independently measured using Cherenkov light from cosmic ray muons. The time variation of the water transparency can be monitored by this method without disturbing the normal data taking.

Light scattering measurement using a laser

The light attenuation length in water can be described as $L = (\alpha_{abs} + \alpha_{scat})^{-1}$, where α_{abs} and α_{scat} are the absorption coefficient and scattering coefficient, respectively. The absorption and scattering coefficients are separately measured using a N_2 laser [20]. Figure 2.16 shows a schematic view of the measurement system. Each laser, wavelength of 337, 371, 400 and 420 nm, fires every 6 seconds during normal data taking. The light from the laser is injected into the ID via an optical fiber toward the bottom of the tank. A typical event by the laser light is also shown in Figure 2.16. The PMT hits clustered at the bottom of the tank are due to the direct (unscattered) photons.

In the analysis, the detector is separated into 6 regions, top and 5 in barrel, as shown in

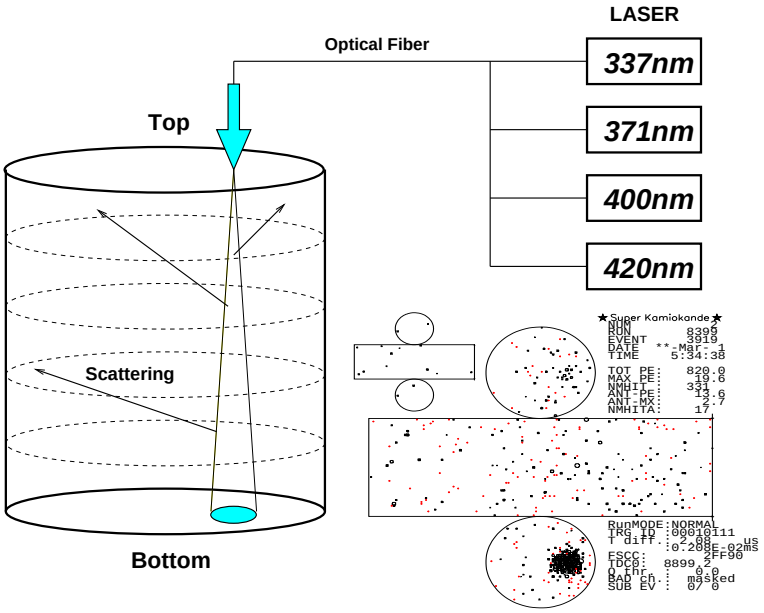

Figure 2.16: A schematic view of the scattering and absorption parameter measurement using laser systems, and a typical laser event.

Figure 2.16. The total charge of bottom PMTs is used for the normalization of the light intensity. Figure 2.17 shows the PMT hit timing distributions in each region for data and Monte Carlo simulation. These PMT hits on the top and barrel wall are due to the photons scattered in water, or the photons reflected by surfaces of bottom PMTs or black sheets. For the Monte Carlo simulation, the absorption and scattering coefficients are adjusted so that the PMT hit time distributions are in agreement with data. The attenuation length in water is calculated using the measured absorption and scattering coefficients.

The attenuation coefficients (L^{-1}) obtained by this method are plotted in Figure 2.18 with a star symbol. The lines shows a model used in Monte Carlo simulation, which are determined by fitting the measurements from this method.

Measurement using cosmic ray muons

Water transparency is also measured by using Cherenkov light from cosmic ray muons passing through the detector. Since the energy deposit of such a energetic muon is almost constant (about 2 MeV/cm), cosmic ray muons can be used as a calibration source.

Only vertical downward muons are selected for this measurement. The muon track is reconstructed by connecting the entrance and the exit points in the ID. Under the assumption that the light detected by each PMT is not scattered, the detected charge is expressed by :

$$Q = Q_0 \cdot \frac{f(\theta)}{l} \cdot \exp\left(-\frac{l}{L}\right) \tag{2.5}$$

where Q_0 is a constant, $f(\theta)$ is the PMT acceptance, l is the photon path length and L is the attenuation length. Figure 2.19 shows $\log(Q \cdot l / f(\theta))$ as a function l in a typical run. The attenuation length is estimated to be 95 m for this data set.

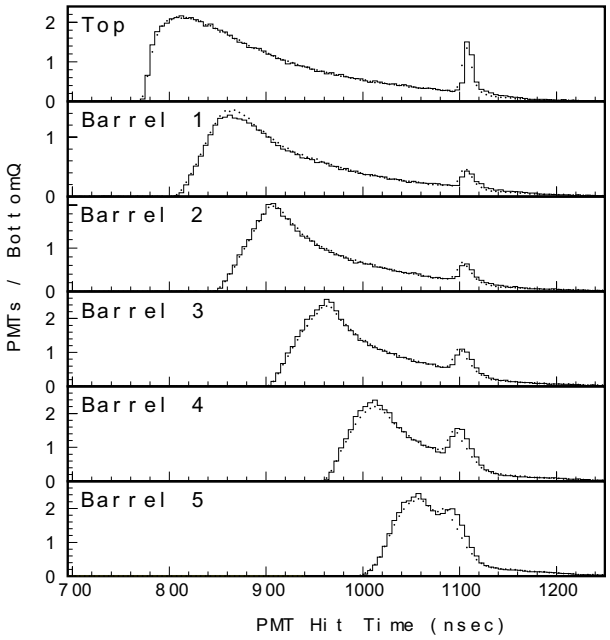

Figure 2.17: PMT hit time distributions of 337 nm-laser events in each detector region for the data (dots) and the Monte Carlo events which is tuned by the scattering and absorption parameters (histograms).

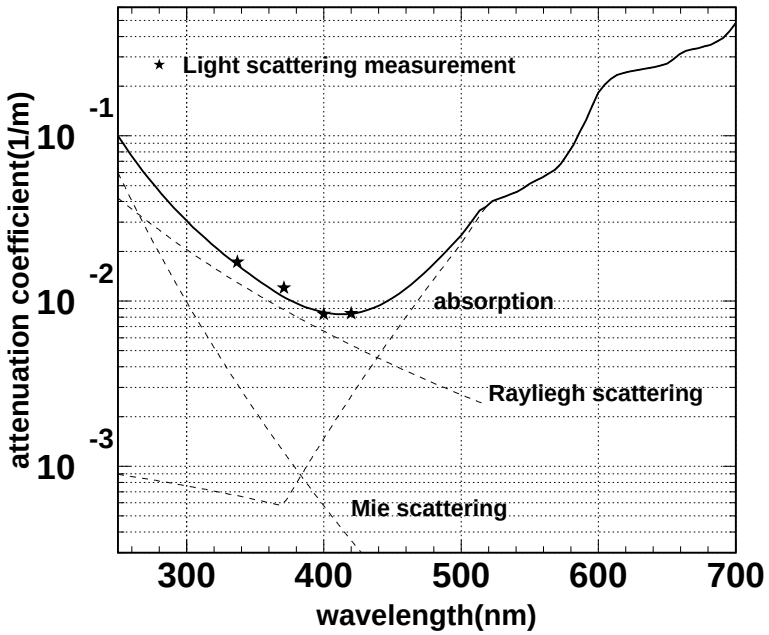

Figure 2.18: Wavelength dependence of attenuation coefficients ($L_{\rm atten}^{-1}$) obtained by the light scattering measurement (points) together with a model in the detector simulation (lines, see Section 3.5).

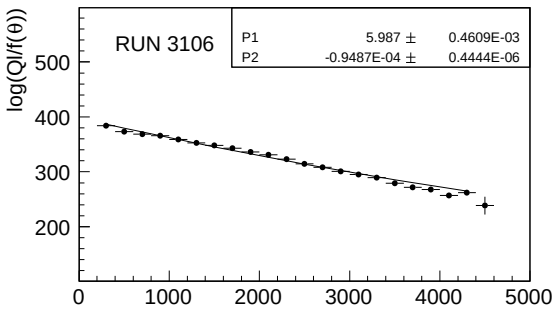

Figure 2.19: Effective observed charge ($\log(Ql/f(\theta))$) for through-going muons as a function of the photon path length (l) where Q is the detected charge and $f(\theta)$ is the PMT acceptance.

Since the cosmic ray muons are measured during the normal data taking, continuous check of the water transparency is possible by this method. Figure 2.20 shows the time variation of the attenuation length. This time variation is corrected in event reconstruction processes.

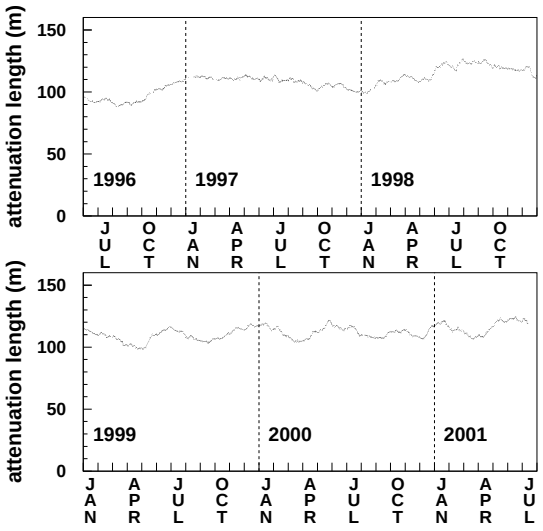

Figure 2.20: Time variation of water attenuation length.

2.3.5 Absolute Energy Calibration

The momentum of particle is determined by the charge information of PMTs based on the evaluation by Monte Carlo simulation. Since the systematic uncertainty in the absolute energy scale affect the atmospheric neutrino analysis, it is essential to understand how precise the Monte Carlo simulation reproduce the absolute energy scale. Four kind of methods are employed in momentum range from a few ten MeV/c to about 10 GeV/c by using independent calibration sources: decay electrons from stopping muons, π^0 events, low and high energy stopping muons.

Decay electrons

A large number of electron events produced by the decay of cosmic ray muons are available in Super-Kamiokande data. These electrons have a spread energy spectrum below 53 MeV. The absolute energy scale in this energy region is checked by comparing the energy spectrum of the decay electron between the observed data and the Monte Carlo simulation. Decay electrons are selected by the following criteria :

1. The time interval from a stopping muon event is 1.5 μsec to 8.0 μsec.
2. The number of hit PMT in a 50 nsec time window is greater than 60 .
3. The goodness of low energy fit is greater than 0.5 .
4. The vertex position is reconstructed more than 2 m away from the ID wall.

Figure 2.21 shows the momentum spectrum of decay electrons compared with the prediction from the Monte Carlo simulation. The effect of the nuclear Coulomb field caused by an atomic capture of the negative muon is taken into account in the simulation [21, 22]. The distribution of the data agrees well with the Monte Carlo prediction. The mean value of the data is 0.4 % higher than that of the Monte Carlo simulation.

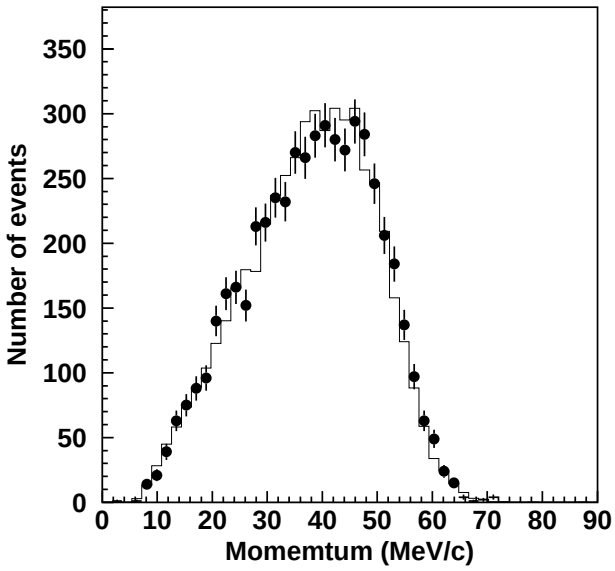

Figure 2.21: Reconstructed momentum distributions for decay electron events. The dots show the observed data and the histogram shows the expectation from Monte Carlo simulation.

Neutrino induced π^0 events

Invariant mass distribution of π^0 events produced by atmospheric neutrino interactions can be used for checking the energy scale over several hundred MeV. Invariant mass of π^0 is reconstructed by the momentum of two γ-rays, $P_{\gamma 1}$ and $P_{\gamma 2}$, and their opening angle θ as follows :

$$M_{\pi^0} = 2P_{\gamma 1}P_{\gamma 2}(1 - cos\theta) \tag{2.6}$$

Single π^0 events are selected from atmospheric neutrino sample by the following criteria :

1. Two Cherenkov rings are recognized and both of them are identified as electron-like.
2. Electrons from muon decay is not detected.
3. The vertex position is reconstructed more than 2 m away from the ID wall.

Figure 2.22 shows the invariant mass distribution of π^0 events, which is compared with the prediction from the Monte Carlo simulation. A peak from π^0 is clearly observed at around $135\,\mathrm{MeV}/c^2$. The peak position of the data is 1.6 % higher than that of the Monte Carlo simulation.

Low energy stopping muons

Cherenkov angle of charged particle is a function of the momentum :

$$\cos\theta_C = \frac{1}{n\beta} = \frac{1}{n}\sqrt{1 + \frac{m^2}{p^2}} \tag{2.7}$$

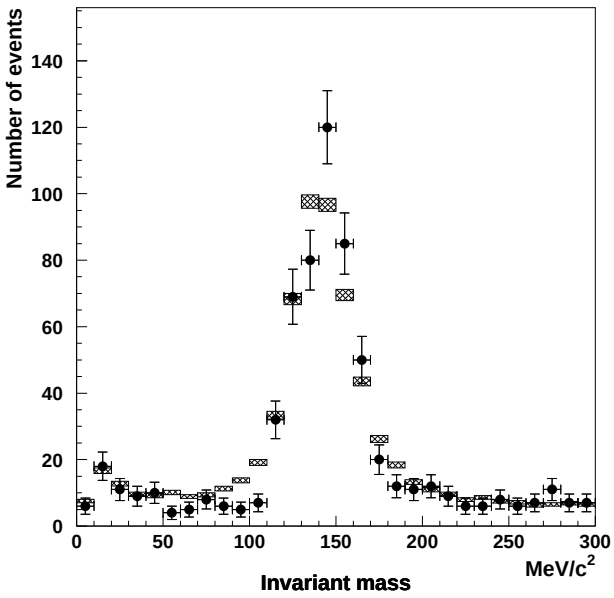

Figure 2.22: Invariant mass distribution of neutrino induced π^0 events for the observed data (dots) and the atmospheric neutrino Monte Carlo events (boxes). The peak position is fitted by a Gaussian distribution.

Since the Cherenkov angle largely depends on the momentum for low energy muons ($< 400\,\mathrm{MeV}/c$), the momentum can be estimated by measuring the Cherenkov angle. The momentum estimated from the Cherenkov angle (P_θ) is used to check the systematic uncertainty of the momentum determination by comparing it with the momentum derived from the detected charge ($\mathrm{P}_{p.e.}$). On the other hand, this method is not useful for electrons or high energy muons because the Cherenkov angle approaches a limit when the momentum is high compared to its mass. Stopping muon events are selected for this study by the following criteria :

1. The total number of p.e.s in the ID is less than 1500 p.e. .
2. The entrance point is on the top wall.
3. The direction is downward ($\cos\theta > 0.9$).
3. One decay electron event is detected.

Figure 2.23 show the scattered plot of the reconstructed Cherenkov opening angle and the momentum $\mathrm{P}_{p.e.}$ for the data and the Monte Carlo simulation. The momentum dependence of the Cherenkov opening angle can be seen in both figures. The energy scale of the data is compared with that of the Monte Carlo simulation by comparing the ratios of $\mathrm{p}_{p.e.}/\mathrm{p}_\theta$. Figure 2.24 show the averaged $\mathrm{p}_{p.e.}/\mathrm{p}_\theta$ for the data and the Monte Carlo simulation and the ratio as a function of the expected momentum p_θ. They agree within 1.5 %.

High energy stopping muons

For high energy muons, the momentum can be estimated from its range because the range of the muon track is approximately proportional to the momentum. The estimated momentum

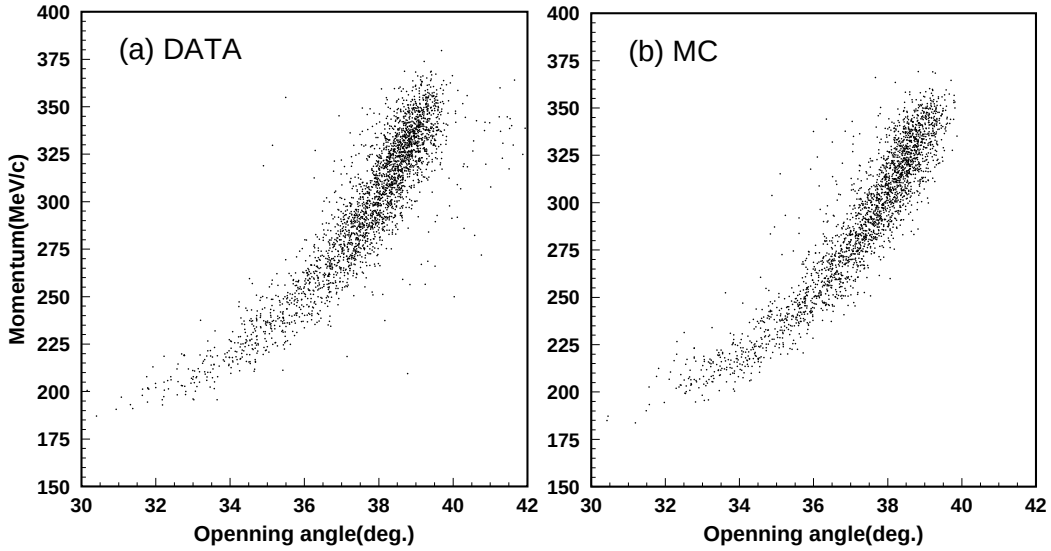

Figure 2.23: Scatter plot of the reconstructed Cherenkov opening angle and the reconstructed momentum $P_{p.e.}$ for (a) the data and (b) the Monte Carlo simulation. The momentum dependence of the Cherenkov opening angle is seen in both figures.

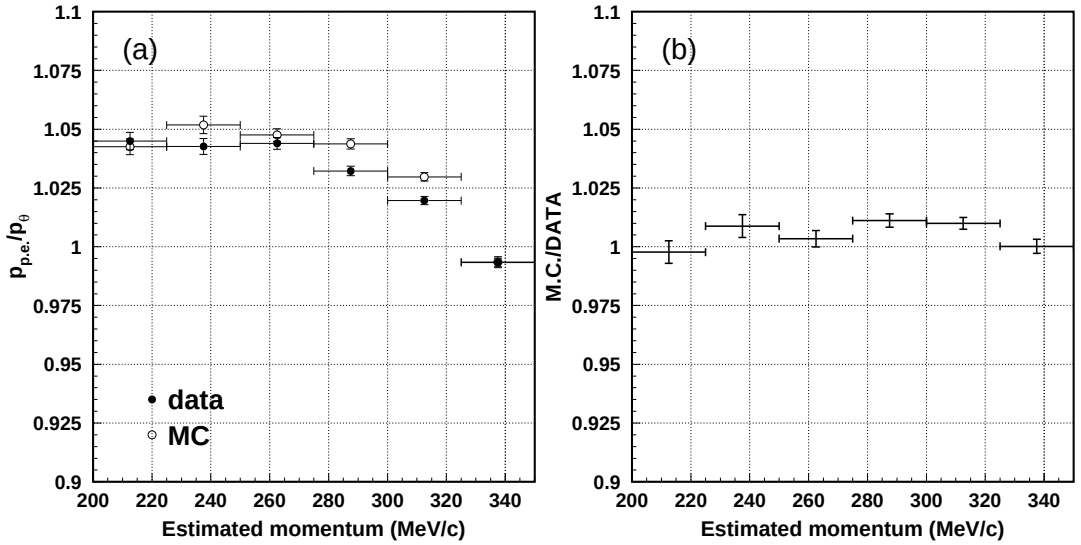

Figure 2.24: Figure (a) shows the averaged ratio of the momentum derived from the charge to that from the opening angle ($p_{p.e.}/p_\theta$) as a function of the momentum p_θ for the data (black points) and the Monte Carlo events (white points), and figure (b) shows the ratio of the data to the Monte Carlo events.

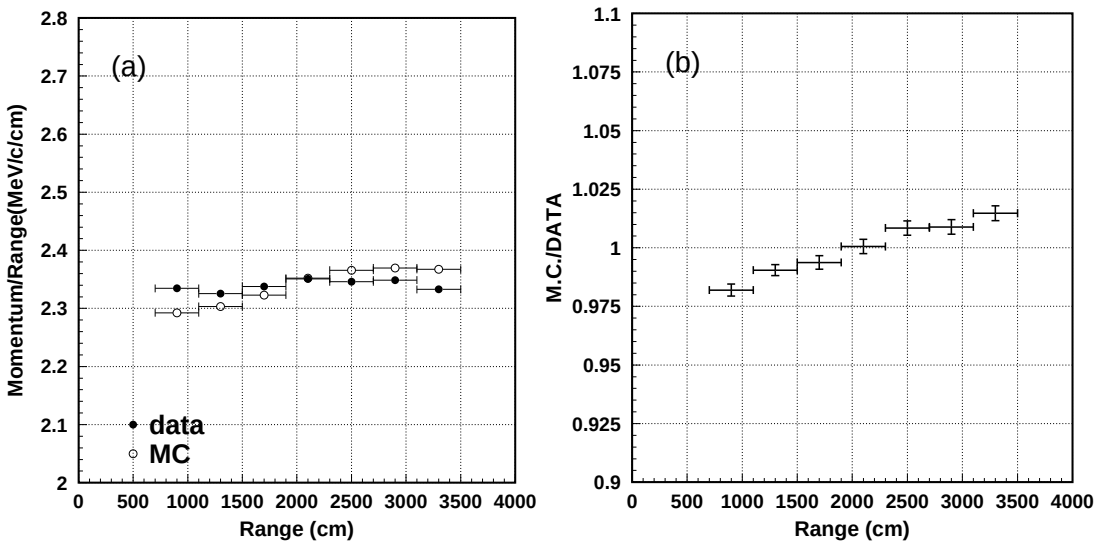

Figure 2.25: Figure (a) shows the range v.s. averaged momentum/range of stopping muon events for the data (black points) and the Monte Carlo events (white points), and figure (b) shows the ratio of the Monte Carlo events to the data.

from its range is used for checking the energy scale from 1 GeV/c up to 10 GeV/c. Stopping muon events are selected by the following criteria :

1. The entrance point is on the top wall.
2. The direction is downward ($\cos\theta > 0.94$).
2. One decay electron event is detected.
3. The reconstructed range of muon track is greater than 7 m.

The range of the muon is determined by the entrance position of the stopping muons and the vertex position of the subsequent decay electron. Figure 2.25 shows the averaged value of the ratio momentum/range as a function of the range for the data and the Monte Carlo simulation. The momentum loss per cm is about 2.3 MeV/c. The comparison of the momentum/range between the data and the Monte Carlo simulation is also shown in Figure 2.25. Although the momentum dependence is seen, the deviations from unity are less than 2 %.

Summary of the absolute energy calibration

Figure 2.26 shows the summary of the absolute energy calibration. The absolute energy scale is checked by various methods over a wide energy range. The uncertainty of the energy scale is estimated to be less than 2 % for the momentum range from a few ten MeV/c to about 10 GeV/c.

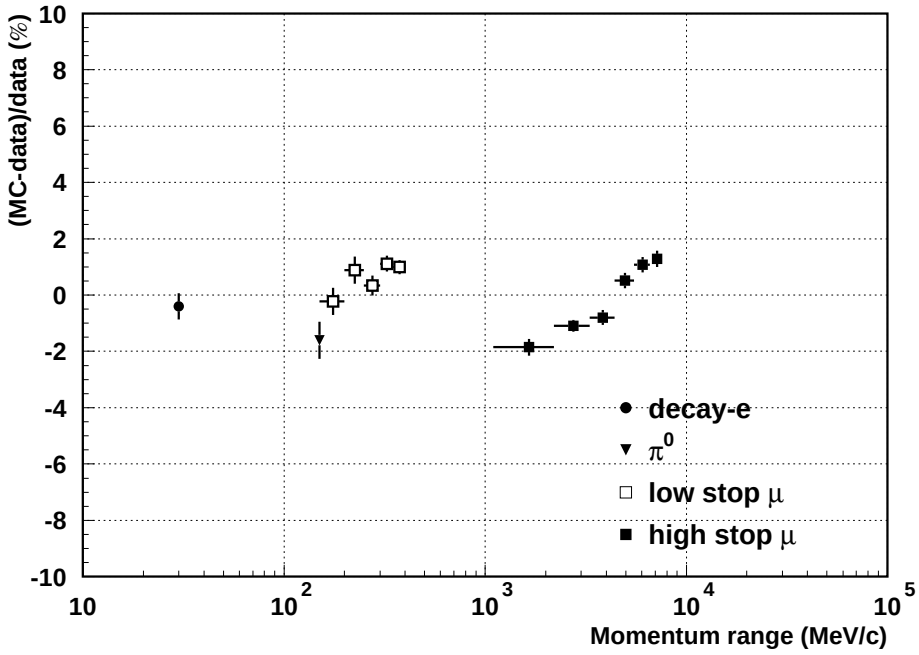

Figure 2.26: The summary of the absolute energy scale calibration. The horizontal axis shows the momentum range of each sources and the vertical axis shows the deviation of the data from the Monte Carlo events.

Chapter 3

Simulation

3.1 Overview

Expectation of atmospheric neutrino events in Super-Kamiokande is calculated by a Monte Carlo simulation, in which all of the important factors can be accurately simulated. Neutrino oscillation and the other physical features of atmospheric neutrinos are studied by comparing the observed data with the prediction from the Monte Carlo simulation.

Monte Carlo simulation is made of three constituents: neutrino flux, neutrino interactions and particle tracking in the detector. First, the expected number of events occured in the detector water during a certain period is calculated from a products of neutrino flux and cross-sections. The kinematics in the neutrino interactions are simulated, and then the generated particles are tracked in water by using a detector simulation program. The detailed descriptions are presented in this chapter.

3.2 Atmospheric Neutrino Flux

Among several detailed calculations of atmospheric neutrino flux at the Super-Kamiokande site, the flux calculated by M.Honda *et al.* [1, 2] (Honda flux) is adopted in our Monte Carlo simulation. In the calculation of neutrino flux, interactions and propagation of particles are treated in a 3-dimensional way, including the curvature of charged particles in geomagnetic field. In addition to that, neutrino flux from G.Battistoni *et al.* [24] (Fluka flux) and G.Barr *et al.* [25] (Bartol flux), which also adopt 3-dimensional calculations, are used to estimate the systematic uncertainties in the flux calculation.

The primary cosmic ray flux model as an input of the flux calculation is determined based on the experimental measurements. Current status of the measurements of cosmic ray proton flux is shown in Figure 3.1 with the model used in the Honda flux calculation. The primary cosmic ray spectrum has been precisely measured by BESS and AMS experiments up to 100 GeV/c [32, 33]. The effects of solar activity and geomagnetic field are taken into account in the calculation. The flux of low energy cosmic rays is modulated by solar activity. The difference of the cosmic ray flux at solar maximum and solar minimum is more than a factor of two for 1 GeV cosmic rays, while it decrease to $\sim 10\,\%$ for 10 GeV. The effect of geomagnetic field is represented as rigidity (= momentum/charge) cutoff. The geomagnetic field works as a shield, by which cosmic ray with lower momentum than the cutoff cannot arrive at the Earth. Cosmic ray flux above

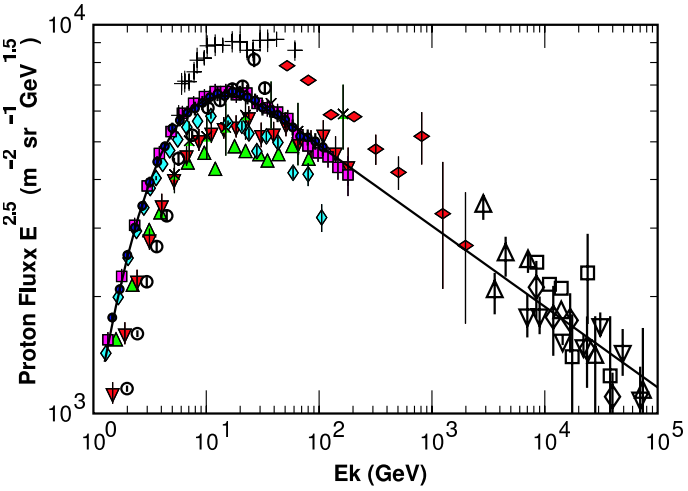

Figure 3.1: Measurements of primary cosmic ray proton flux and the model used in Honda flux calculation. The data are taken from Webber [27] (crosses), LEAP [28] (upward triangles), MASS1 [29] (open circles), CAPRICE [30] (vertical diamonds), IMAX [31] (downward triangles), BESS98 [32] (circles), AMS [33] (squares), Ryan [34] (horizontal diamonds), JACEE [35] (downward open triangles), Ivanenko [36] (upward open triangles), Kawamura [37] (open squares) and Runjob [38] (open diamonds).

100 GeV, which are responsible for ≥ 10 GeV neutrinos, is not affected by the solar activity nor the geomagnetic field.

Primary cosmic ray protons and nuclei interact with air nuclei, and secondary particles, mostly pions and some kaons, are generated in the atmosphere. The US Standard Atmosphere model is employed for the density structure of the atmosphere. The density structure of the the atmosphere is important because it is related to the zenith angle dependence of atmospheric neutrino flux. In the hadronic interactions, cosmic ray nuclei are treated as a bundle of independent nucleons by a superposition approximation, NUCRIN simulation code is used for the primary cosmic ray energies/nucleon < 5 GeV and dpmjet3 for > 5 GeV. Those mesons generated from hadronic interactions create atmospheric neutrinos when they decay in the atmosphere, as described in Section 1.1. The measurement of the secondary cosmic rays, such as atmospheric muons, have been carried out by the BESS [39] and CAPRICE [40] experiments. The accurately measured secondary cosmic ray flux is used to calibrate the calculation method including the hadronic interaction model. The observed muon flux at ground level is shown in Figure 3.2 with the prediction from the Honda flux calculation.

The direction averaged atmospheric neutrino flux and the flavor ratio at the Super-Kamiokande detector site are shown in Figure 3.3, in which the Honda flux, Fluka flux and Bartol flux are compared. The systematic uncertainty in the absolute flux is estimated to be about 20 %, while the uncertainty in the flavor ratios are smaller than 5 %.

The prominent features of the 3-dimensional calculation in comparison with the 1-dimensional one are (1) an enhancement of neutrino flux for near-horizontal direction and (2) lower production height of neutrinos in the atmosphere which is also prominent for near-horizontal direction. The first feature is explained as a difference of the effective area for primary cosmic rays which

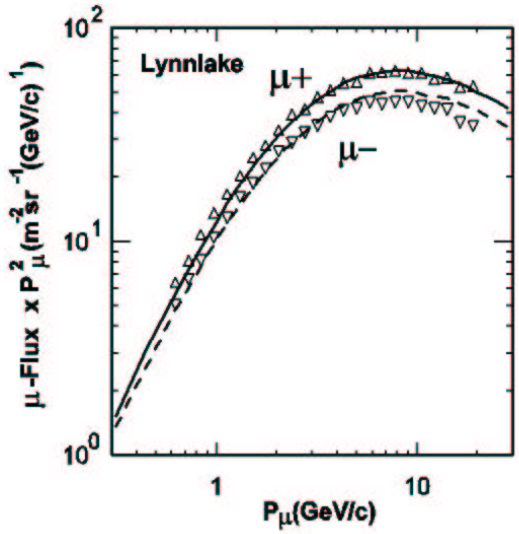

Figure 3.2: Secondary cosmic ray muon flux at Lynnlake observed by the BESS experiment [39] (points) and the prediction from the Honda flux calculation [41] (lines).

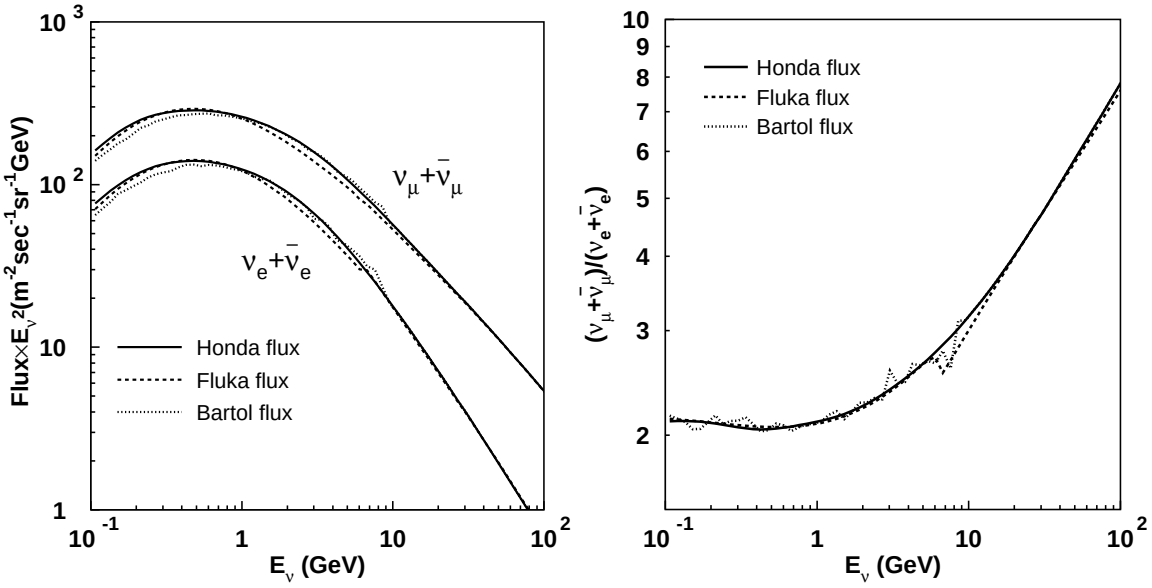

Figure 3.3: Predictions of the direction averaged atmospheric neutrino flux and the flavor ratio. Solid lines show the Honda flux, dashed lines show the Fluka flux and dotted lines show the Bartol flux.

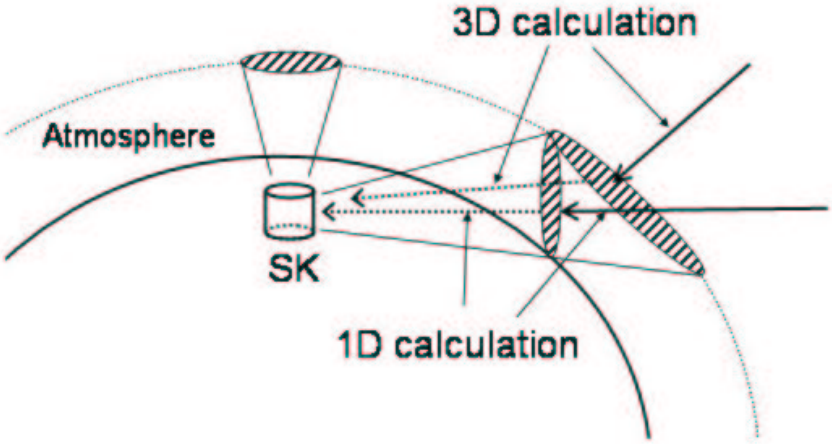

Figure 3.4: A schematic view of the effective areas of primary cosmic rays interacting with air nuclei for 1-dimensional and 3-dimensional calculations. Arrows written by solid lines show the primary cosmic rays and dotted lines show the neutrinos. The 3-dimensional calculation gives larger areas for near-horizontal direction.

generate horizontally incoming neutrinos, as illustrated in Figure 3.4. This effect is important for low energy neutrinos ($< 1\,\mathrm{GeV}$), in which transverse momentum of the secondary particles in hadronic interactions and the bending of muons in the geomagnetic field are considerable. Figure 3.5 shows the zenith angle distributions of the atmospheric neutrino flux from Honda flux, Bartol flux and neutrino flux from Honda *et al.* [23] (Honda-1D flux) using 1-dimensional approximation with older primary flux and hadronic interaction model. Since the geomagnetic field above Super-Kamiokande is stronger than the average, neutrino flux below a few GeV is predicted to be up-down asymmetry. This up-down asymmetry for low energy neutrinos is smeared due to the small angular correlation in neutrino interactions and cannot be observed in charged leptons. The reason of the second feature is explained as follows. The primary cosmic rays from horizontal direction travel a longer distance in atmosphere than the vertically incoming cosmic rays to reach the same altitude. Therefore, interaction vertex of the vertically incoming cosmic rays have a lower altitude compared to the horizontal one. Unlike a 1-dimensional calculation, the incidence angle of primary cosmic rays which produce horizontally going neutrinos is not restricted to be horizontal direction in a 3-dimensional calculation. As a result, production height of neutrinos in the 3-dimensional calculation is lower than that in the 1-dimensional calculation for near-horizontal direction. This effect is also prominent for low energy neutrinos ($< 1\,\mathrm{GeV}$). The simulations for neutrino production height from the Honda flux and Honda-1D flux are shown in Figure 3.6.

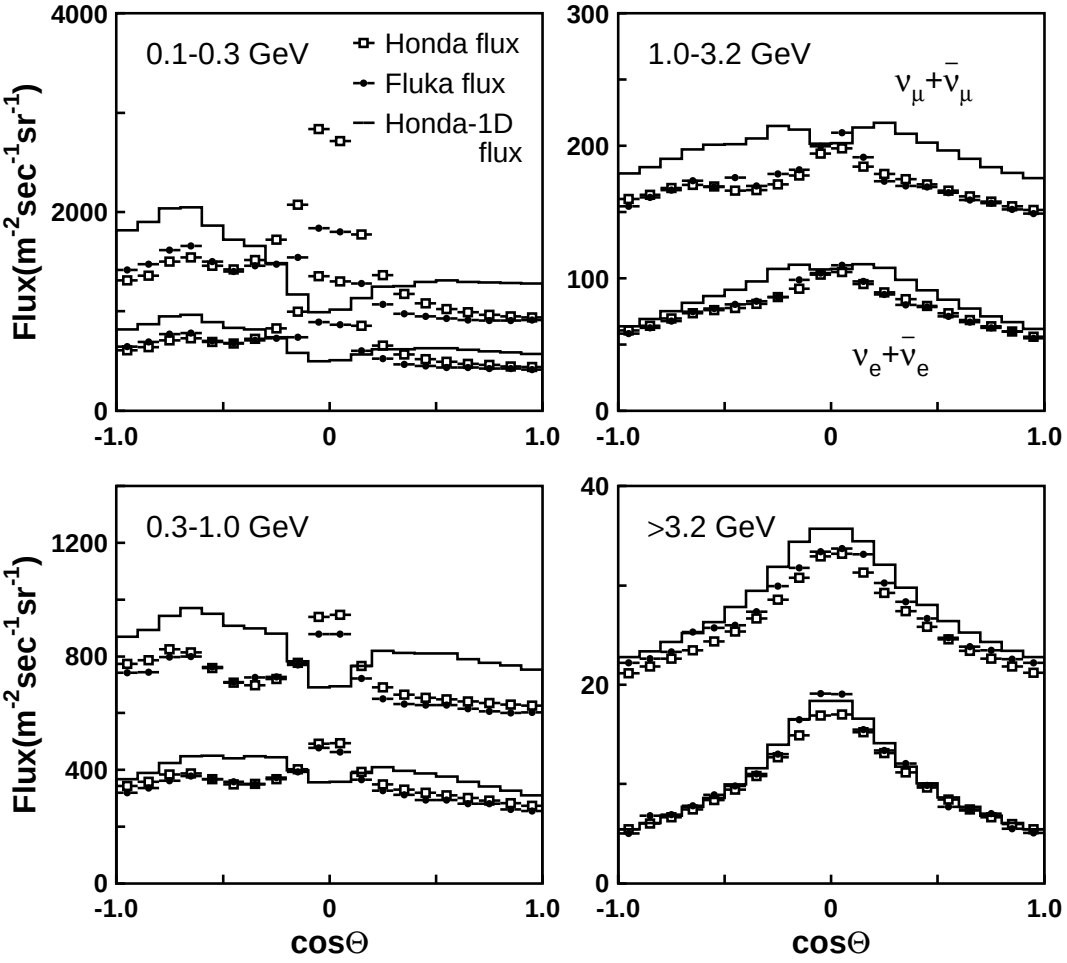

Figure 3.5: Zenith angle dependence of the atmospheric neutrino flux. Boxes show the Honda flux, dots show the Bartol flux and solid lines show the Honda-1D flux. The higher flux is for $\nu_\mu + \overline{\nu}_\mu$ and the lower flux for $\nu_e + \overline{\nu}_e$ in each plot. An enhancement of the neutrino flux is seen for near-horizontal directions at energies below 1 GeV in 3-dimensional calculations, the Honda flux and the Fluka flux. On the other hand, no enhancement is seen in the Honda-1D flux.

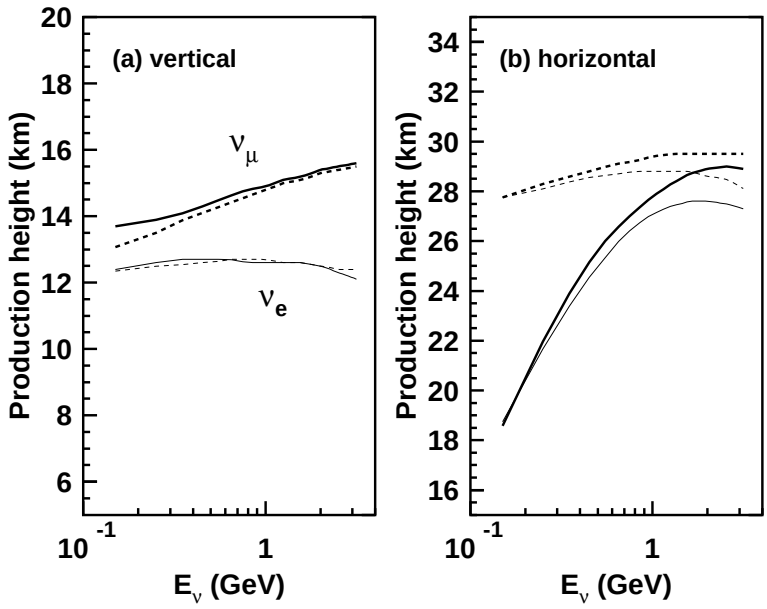

Figure 3.6: 50 % accumulation probability lines of neutrino production height for (a) near-vertical ($\cos\theta > 0.95$) and (b) near-horizontal ($|\cos\theta| < 0.05$) directions. Thick and thin solid lines are for ν_μ and ν_e by the 3-dimensional calculation, and thick and thin dashed lines are for ν_μ and ν_e by the 1-dimensional calculation, respectively.

3.3 Neutrino Interaction

Atmospheric neutrinos interact with nucleons and electrons in water. The neutrino interactions are treated by using NEUT program library in our Monte Carlo simulation. This library was first developed to study atmospheric neutrinos as a background of nucleon decay analysis in the Kamiokande experiment, and then it was inherited to the Super-Kamiokande experiment with various modifications. In the NEUT code, the following charged current (CC) and neutral current (NC) interactions are considered :

CC/NC (quasi-)elastic scattering	$\nu + N \rightarrow\ l + N'$
CC/NC single meson production	$\nu + N \rightarrow\ l + N' + meson$
CC/NC deep inelastic interaction	$\nu + N \rightarrow\ l + N' + hadrons$
CC/NC coherent pion production	$\nu + {}^{16}\mathrm{O} \rightarrow\ l + {}^{16}\mathrm{O} + \pi$

where N and N' are nucleons (proton or neutron) and l is a lepton, respectively.

Since the cross-section of neutrino-electron elastic scattering is about 10^3 times smaller than that of the neutrino-nucleon interactions at $\sim$1 GeV neutrino energy, this interaction mode is ignored in our simulation.

3.3.1 Elastic and Quasi-Elastic Scattering

The simulation of quasi-elastic scattering with a bound nucleon is based on the Smith & Moniz's model [42]. The cross-section for charged current quasi-elastic interaction is expressed as follows :

$$\begin{aligned}\frac{d^2\sigma}{dk_l d\Omega_l} &= \frac{G_F^2 k_l^2 \cos^2(\frac{1}{2}\chi)}{2\pi^2 M_T}\Big\{W_2 + \big[2W_1 + \frac{m_l^2}{M_T^2}W_\alpha\big]\tan^2(\frac{1}{2}\chi) \\ &\quad +(W_\beta + W_8)m_l^2/(M_T E_l \cos^2(\tfrac{1}{2}\chi)) \\ &\quad -2W_8/M_T \tan(\tfrac{1}{2}\chi)\sec(\tfrac{1}{2}\chi)\big[q^2\cos^2(\tfrac{1}{2}\chi) + |\boldsymbol{q}|^2\sin^2(\tfrac{1}{2}\chi) + m_l^2\big]^{\frac{1}{2}}\Big\} \qquad (3.1)\end{aligned}$$

where $\cos\chi = k_l/E_l\cos\theta_l$ with scattering angle θ_l, q is the 4-momentum transfer, G_F is the weak coupling constant, M_T is the target nuclear mass and the subscript l specifies the kinetic variables of scattered lepton, respectively. The factors W_j are given by the form of $W_{\mu\nu}$ in lab frame :

$$\begin{aligned}W_{\mu\nu} &= W_1\delta_{\mu\nu} - W_2\delta_{\mu4}\delta_{\nu4} + W_\alpha/M_T^2 q_\mu q_\nu \\ &\quad +iW_\beta/M_T(\delta_{\mu4}q_\nu + \delta_{\nu4}q_\mu) - iW_8/M_T\epsilon_{\mu\nu\sigma4}q_\sigma \qquad (3.2)\end{aligned}$$

The target state is described as a superposition of non-interacting neutron and proton Fermi gas with momentum distributions $n_{\rm n}(p)$ and $n_{\rm p}(p)$, and then $W_{\mu\nu}$ in the lab frame can be expressed in terms of the single nucleon matrix elements as follows :

$$W_{\mu\nu} = \int d\boldsymbol{p} f(\boldsymbol{p},\boldsymbol{q},\omega)\ T_{\mu\nu}, \qquad (3.3)$$

$$f(\boldsymbol{p},\boldsymbol{q},\omega) = \frac{M_T\Omega}{(2\pi)^3}\frac{\delta(E_p - E_{p'} + \omega)n_{\rm i}(p)(1-n_{\rm f}(p'))}{E_p E_{p'}}, \qquad (3.4)$$

$$T_{\mu\nu} = E_p E_{p'}\Omega^2 \sum_{\lambda\lambda'}\langle \boldsymbol{p'}\lambda'|j_\mu^{(+)}(0)|\boldsymbol{p}\lambda\rangle\langle \boldsymbol{p}\lambda|j_\nu^{(-)}(0)|\boldsymbol{p'}\lambda'\rangle \qquad (3.5)$$

$f(\boldsymbol{p},\boldsymbol{q},\omega)$ include relevant information of the nuclear state, which can be analytically evaluated for a simple relativistic Fermi gas model with flat momentum distribution $n_{\rm i}(p) = \theta(p_F - |\boldsymbol{p}|)$ where p_F is the Fermi surface momentum taken to be 225 MeV/c. Pauli exclusion principle is considered by the factor $(1 - n_{\rm f}(p'))$.

For quasi-elastic scattering, the current matrix element is expressed as follows :

$$\begin{aligned}\langle \boldsymbol{p'}\lambda'|j_\mu^{(+)}(0)|\boldsymbol{p}\lambda\rangle &= i\left(\frac{m^2\cos^2\theta_c}{E_p E_{p'}\Omega^2}\right)^{\frac{1}{2}}\bar{u}(\boldsymbol{p'}\lambda')\left\{\gamma_\mu F_V^1(q^2)\right. \\ &\quad \left. +\frac{i\sigma_{\mu\alpha}q_\alpha\xi F_V^2(q^2)}{2M_N} + \gamma_\mu\gamma_5 F_A(q^2) - iq_\mu\gamma_5 F_P\right\}u(\boldsymbol{p}\lambda) \qquad (3.6)\end{aligned}$$

where θ_c is the Cabbibo angle, the $F_V^1(q^2)$ and $F_V^2(q^2)$ are vector form factors, $F_A(q^2)$ is an axial vector form factor and $F_P(q^2)$ is a pseudoscalar form factor. Second-class currents are assumed to vanish as required by the V-A theory and fundamental symmetries. The vector form factors

are represented as follows :

$$F_V^1(q^2) = \left(1 - \frac{q^2}{4M_N^2}\right)^{-1} \left[G_E(q^2) - \frac{q^2}{4M_N^2} G_M(q^2)\right] \quad (3.7)$$

$$\xi F_V^2(q^2) = \left(1 - \frac{q^2}{4M_N^2}\right)^{-1} \left[G_E(q^2) - G_M(q^2)\right] \quad (3.8)$$

$$G_E(q^2) = (1+\xi)^{-1} G_M(q^2) = \left(1 - \frac{q^2}{M_V^2}\right)^{-2} \quad (3.9)$$

where M_N is the nucleon mass and $\xi \equiv \mu_p - \mu_n = 3.71$. The vector mass M_V is set to be 0.84 GeV. The axial vector form factor is given by :

$$F_A(q^2) = -1.23 \left(1 - \frac{q^2}{M_A^2}\right)^{-2} \quad (3.10)$$

The axial vector mass M_A is set to be 1.11 GeV from experimental data [43]. Figure 3.7 shows the angular difference between the muon direction and the neutrino direction (beam direction) measured by 1 kt water Cherenkov detector from K2K experiment with the Monte Carlo prediction using $M_A = 1.11$ and 1.01 for quasi-elastic scattering and single-meson production. The Monte Carlo simulation using $M_A = 1.11$ agrees with the observed data better than that for $M_A = 1.01$. The pseudoscalar form factor is given by

$$F_P(q^2) = \frac{2M_N F_A(q^2)}{M_\pi^2 - q^2} \quad (3.11)$$

where M_π is the pion mass.

For free nucleon target, the cross-section for charged current quasi-elastic interaction is given by the expression [44] :

$$\frac{d\sigma^{\nu(\bar{\nu})}}{dq^2} = \frac{M_N^2 G_F^2 \cos^2\theta_c}{8\pi E_\nu^2} \left[A(q^2) \mp B(q^2)\frac{s-u}{M_N^2} + C(q^2)\frac{(s-u)^2}{M_N^4}\right] \quad (3.12)$$

where s and u are Mandelstam variables and E_ν is the neutrino energy. Factors A, B and C are written as follows :

$$\begin{aligned} A(q^2) = {} & \frac{m^2 - q^2}{4M^2}\left[\left(4 - \frac{q^2}{M^2}\right)|F_A|^2 - \left(4 + \frac{q^2}{M^2}\right)|F_V^1|^2 \right. \\ & \left. - \frac{q^2}{M^2}|\xi F_V^2|^2\left(1 + \frac{q^2}{4M^2}\right) - \frac{4q^2 F_V^1 \xi F_V^2}{M^2} - \frac{m^2}{M^2}\left((F_V^1 + \xi F_V^2)^2 + |F_A|^2\right)\right] \quad (3.13) \end{aligned}$$

$$B(q^2) = \frac{q^2}{M^2}\left(F_A(F_V^1 + \xi F_V^2)\right) \quad (3.14)$$

$$C(q^2) = \frac{1}{4}\left(|F_A|^2 + |F_V^1|^2 - \frac{q^2}{4M^2}|\xi F_V^2|^2\right) \quad (3.15)$$

The cross-sections for neutral current elastic scattering are derived from the following rela-

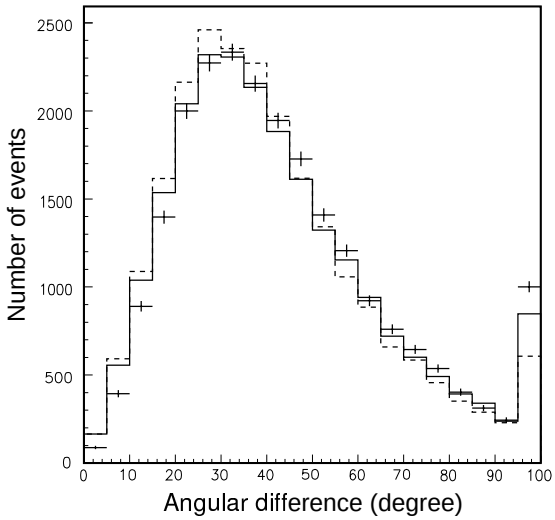

Figure 3.7: Angular difference between the muon direction and the neutrino direction (beam direction) observed in 1 kt detector from K2K experiment [43]. Points show the data and solid line (dashed line) shows the Monte Carlo events with $M_A = 1.11$ ($M_A = 1.01$) for quasi-elastic scattering and single-meson production.

tions [53, 54] :

$$\sigma(\nu p \to \nu p) = 0.153 \times \sigma(\nu n \to e^- p) \quad (3.16)$$
$$\sigma(\bar{\nu} p \to \bar{\nu} p) = 0.218 \times \sigma(\bar{\nu} p \to e^+ n) \quad (3.17)$$
$$\sigma(\nu n \to \nu n) = 1.5 \times \sigma(\nu p \to \nu p) \quad (3.18)$$
$$\sigma(\bar{\nu} n \to \bar{\nu} n) = 1.0 \times \sigma(\bar{\nu} p \to \bar{\nu} p) \quad (3.19)$$

Figure 3.8 shows the calculated cross-sections of (a) $\nu_\mu + n \to \mu^- + p$ and (b) $\overline{\nu}_\mu + p \to \mu^+ + n$ for (quasi-)free target together with the data from various experiments, and Figure 3.9 shows the comparison with that for the bound nucleons.

3.3.2 Single Meson Production

Single meson production is simulated based on the Rein & Sehgal's method [56]. This method assumes an intermediate baryon resonance :

$$\begin{aligned} \nu + N &\to l + N^* \\ N^* &\to N' + \text{meson} \end{aligned} \quad (3.20)$$

where N and N' are nucleons and N^* is a baryon resonance.

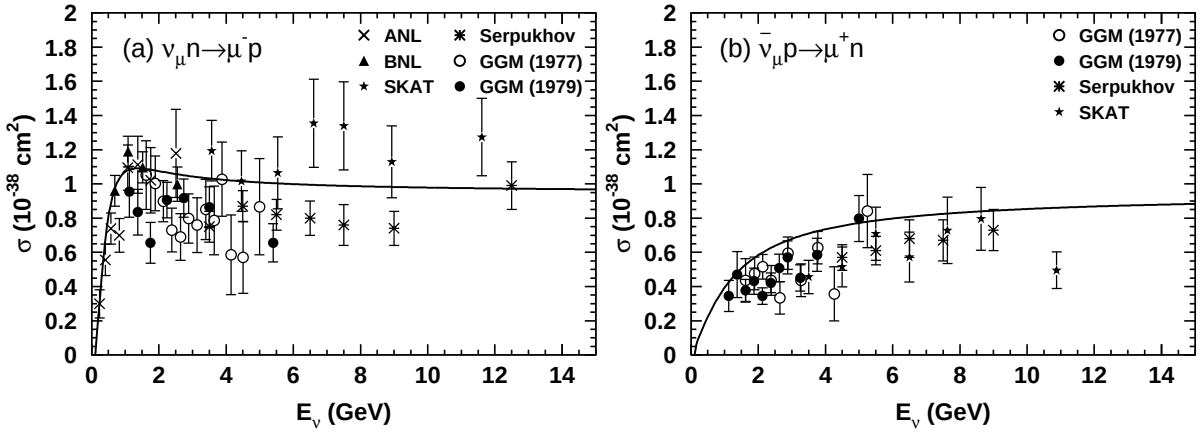

Figure 3.8: Cross-sections of (a) $\nu_\mu + n \to \mu^- + p$ and (b) $\overline{\nu}_\mu + p \to \mu^+ + n$ for (quasi-)free target. Solid lines show the result of our calculations and the points show the experimental data from ANL [47], Gargamelle [48, 49], BNL [50], Serpukhov [51] and SKAT [52].

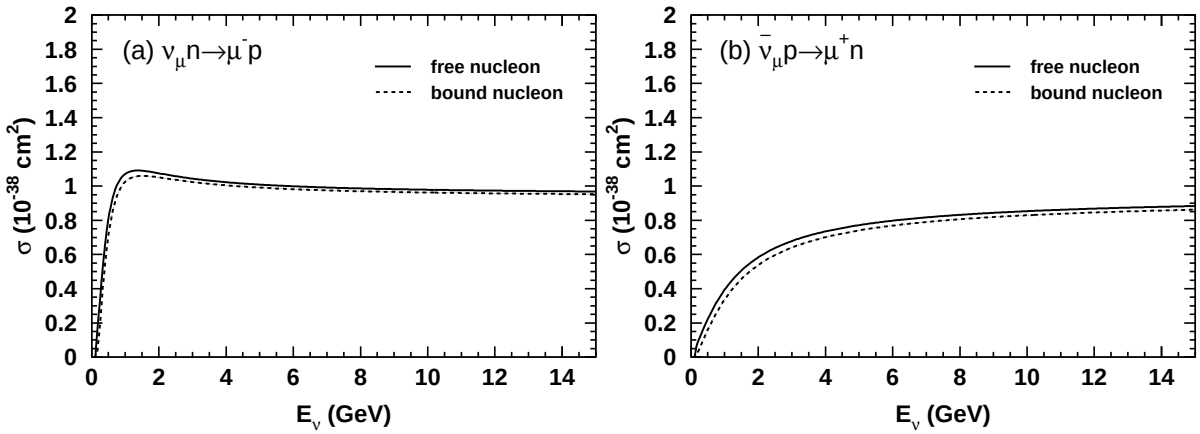

Figure 3.9: Calculated cross-sections of (a) $\nu_\mu + n \to \mu^- + p$ and (b) $\overline{\nu}_\mu + p \to \mu^+ + n$ for free nucleon target (solid lines) and for bound nucleon target in oxygen (dashed lines).

The differential cross-section of single resonance production with the mass M and the negligible width is written by :

$$\frac{d^2\sigma}{dq^2 dE_\nu} = \frac{1}{32\pi M_N E_\nu^2} \cdot \frac{1}{2} \sum_{spin} |T(\nu N \to l N^*)|^2 \, \delta(W^2 - M^2) \tag{3.21}$$

where W is the invariant mass of the hadronic system. $T(\nu N \to l N^*)$ is the amplitude of resonance production which is calculated using the FKR model [57]. The axial vector mass M_A is set to be 1.11 GeV. The differential cross-section for the resonance with finite width Γ can be derived by replacing the δ-function with a Breit-Wignar factor :

$$\delta(W^2 - M^2) \quad \to \quad \frac{1}{2\pi} \cdot \frac{\Gamma}{(W - M)^2 + \Gamma^2/4} \tag{3.22}$$

The cross-sections are calculated as a product of the amplitude of each resonance production and the probability of the resonance decay into one meson and an nucleon. Although the Rein & Sehgal's method was originally developed for single pion production, it is possible to extend the calculation to single K and single η production by changing the decay of the resonances. In our simulation, $\Delta(1232)$ and other 17 resonances which can be created in $W < 2.0\,\mathrm{GeV}/c^2$ are considered. Interference among those resonances is also taken into account. The calculated cross-sections for single pion productions are shown in Figures 3.10, 3.11 and 3.12 together with data from several experiments.

The decay kinematics of $\Delta(1232)$ is determined by the Rein & Sehgal's detailed method. For the other resonances, directional distribution of generated meson is set to be isotropic in the resonance rest frame. Pauli blocking effect is taken into consideration by requiring that the nucleon in the final state should have a momentum above the Fermi surface momentum. The pion-less Δ decay in ^{16}O nuclei ($NN^* \to NN$) is also considered assuming 20 % probability [58].

3.3.3 Deep inelastic scattering

The cross-section of charged current deep inelastic scattering is calculated by integrating the following equation in the range of the invariant mass $W > 1.3\,\mathrm{GeV}/c$ [68] :

$$\begin{aligned}
\frac{d^2\sigma^{\nu,\bar{\nu}}}{dx\,dy} &= \frac{G_F^2 M_N E_\nu}{\pi} \left((1 - y + \frac{y^2}{2} + C_1) F_2(x, q^2) \pm y(1 - \frac{y}{2} + C_2) x F_3(x, q^2) \right) \\
C_1 &= \frac{y M_l^2}{4 M_N E_\nu x} - \frac{x y M_N}{2 E_\nu} - \frac{m_l^2}{4 E_\nu^2} - \frac{m_l^2}{2 M_N E_\nu x} \\
C_2 &= -\frac{m_l^2}{4 M_N E_\nu x}
\end{aligned} \tag{3.23}$$

where $x = -q^2/(2M(E_\nu - E_l))$ and $y = (E_\nu - E_l)/E_\nu$ are Bjorken scaling parameters, M_N is the nucleon mass, m_l is the outgoing lepton mass, E_ν and E_l are the energy of incoming neutrino and outgoing lepton in the laboratory frame, respectively. The nucleon structure functions F_2 and xF_3 are taken from GRV94 [69].

In our simulation, the cross-section of deep inelastic scattering induced by neutral current are

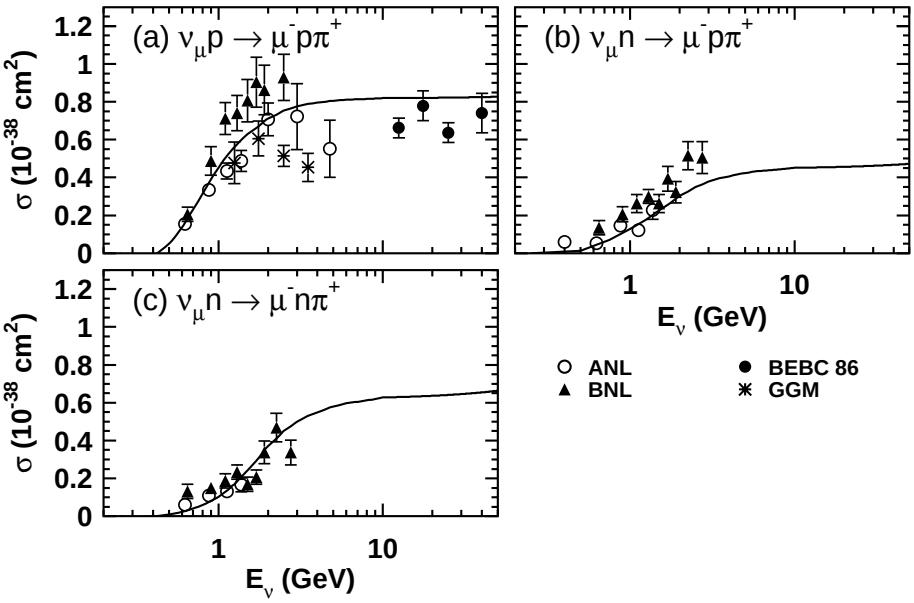

Figure 3.10: Cross-sections for charged current single pion productions of ν_μ. (a) $\nu_\mu p \to \mu^- p\pi^+$, (b) $\nu_\mu n \to \mu^- p\pi^0$, (c) $\nu_\mu n \to \mu^- n\pi^+$. Solid lines show our calculations. Experimental data are taken from ANL [59], BNL [60], BEBC [61] and Gargamelle [63].

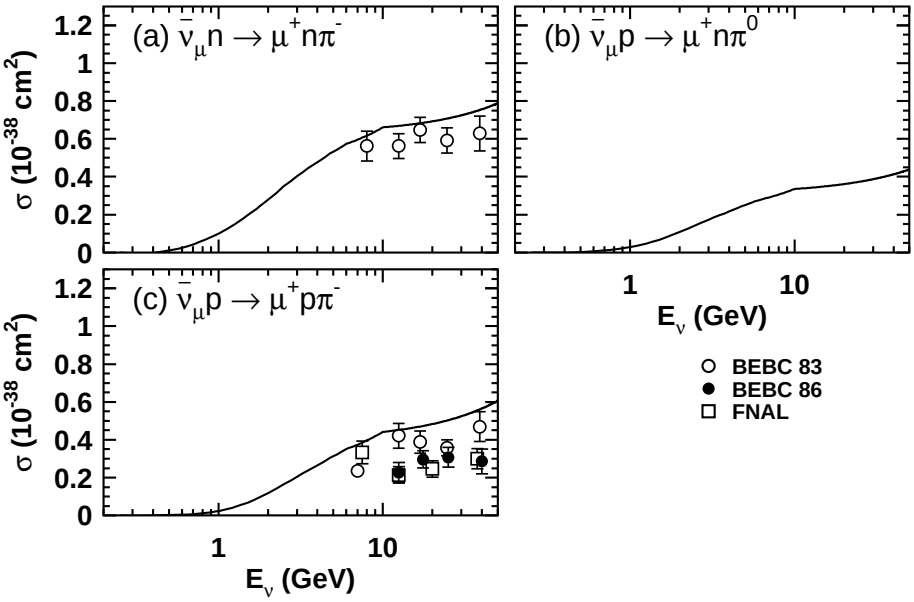

Figure 3.11: Cross-sections for charged current single pion productions of $\overline{\nu}_\mu$. (a) $\overline{\nu}_\mu n \to \mu^+ n\pi^-$, (b) $\overline{\nu}_\mu p \to \mu^+ n\pi^0$, (c) $\overline{\nu}_\mu p \to \mu^+ p\pi^-$. Solid lines show the result of our calculations. Experimental data are taken from BEBC [65, 61] and FNAL [66].

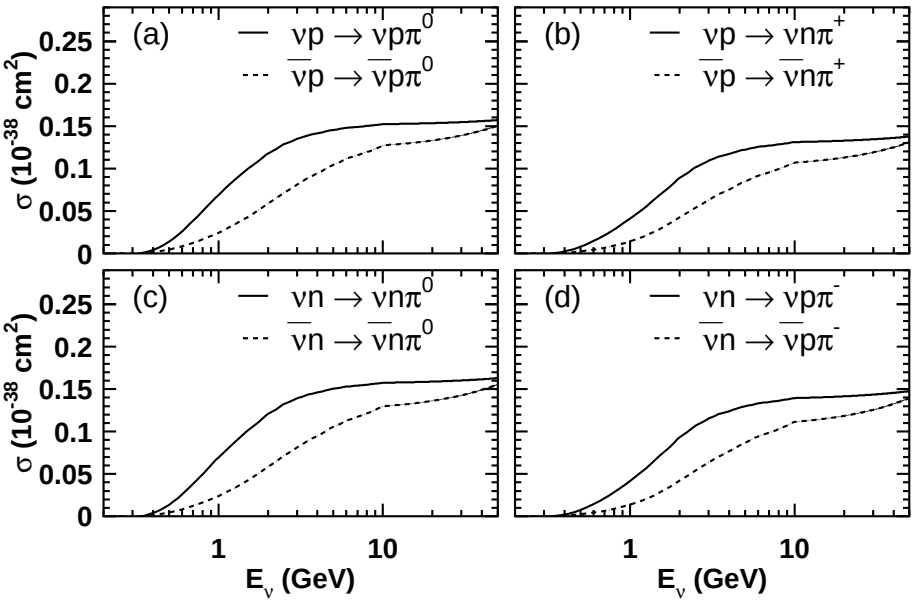

Figure 3.12: Cross-sections for neutral current single pion productions of ν_μ and $\overline{\nu}_\mu$. Solid(Dashed) lines show the result of our calculations for $\nu_\mu(\overline{\nu}_\mu)$ interactions.

assumed to have the following relations which are estimated from experimental results [74, 75] :

$$\frac{\sigma(\nu N \to \nu X)}{\sigma(\nu N \to \mu^- X)} = \begin{cases} 0.26 & (\ E_\nu < 3\,\mathrm{GeV}\ ) \\ 0.26 + 0.04\,(E_\nu/3 - 1) & (\ 3\,\mathrm{GeV} \le E_\nu < 6\,\mathrm{GeV}\ ) \\ 0.30 & (\ E_\nu \ge 6\,\mathrm{GeV}\ ) \end{cases} \tag{3.24}$$

$$\frac{\sigma(\bar{\nu} N \to \bar{\nu} X)}{\sigma(\bar{\nu} N \to \mu^+ X)} = \begin{cases} 0.39 & (\ E_\nu < 3\,\mathrm{GeV}\ ) \\ 0.39 - 0.02\,(E_\nu/3 - 1) & (\ 3\,\mathrm{GeV} \le E_\nu < 6\,\mathrm{GeV}\ ) \\ 0.37 & (\ E_\nu \ge 6\,\mathrm{GeV}\ ) \end{cases} \tag{3.25}$$

The kinematics of the hadronic system is simulated by two different methods according to the range of invariant mass. In the region of $1.3\,\mathrm{GeV}/c^2 < W < 2.0\,\mathrm{GeV}/c^2$, only pions are considered as outgoing mesons. The mean multiplicity of pions is estimated from the result of Fermilab 15-foot hydrogen bubble chamber experiment [70] :

$$\langle n_\pi \rangle = 0.09 + 1.83 \ln(W^2) \tag{3.26}$$

The number of pions in each event is determined by using KNO (Koba-Nielsen-Olsen) scaling. Since the range of W overlaps with that in single pion production, $n_\pi \ge 2$ is required in this W region. The forward-backward asymmetry of pion multiplicity in the hadronic center of mass system is included using the results from BEBC experiment [71] :

$$\frac{n_\pi^F}{n_\pi^B} = \frac{0.35 + 0.41 \ln(W^2)}{0.5 + 0.09 \ln(W^2)} \tag{3.27}$$

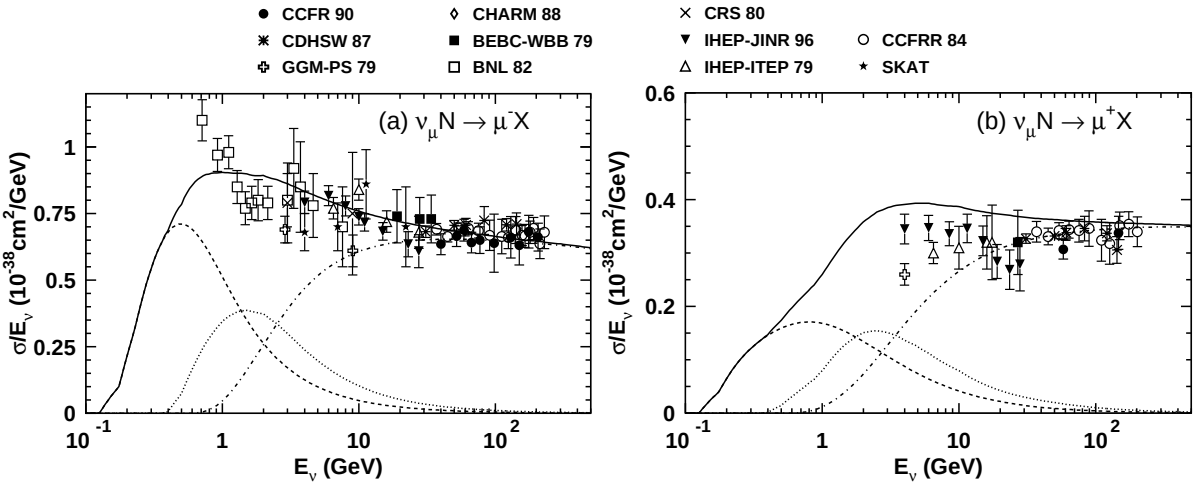

Figure 3.13: Total charged current cross-sections for (a) neutrinos and (b) anti-neutrinos. The results of our calculations are shown by solid lines, with the three contributions of quasi-elastic scattering (dashed lines), single meson productions (dotted lines) and deep inelastic scattering (dashed-dotted lines). Experimental data are taken from CCFR [76], CDHSW [77], Gargamelle [78, 79], CHARM [80], BNL [81], CRS [82], BEBC-WBB [83], IHEP-JINR [84], IHEP-ITEP [85], CCFRR [86] and SKAT [87].

In the region of $W > 2.0\,\mathrm{GeV}/c^2$, the kinematics of the hadronic system are calculated by using JETSET/GRV94 package [72]. This package treats not only π but also K, η, ρ and so on.

The total charged current cross-sections including quasi-elastic scattering, single meson productions and deep inelastic scattering are shown in Figure 3.13 for both neutrinos and anti-neutrinos.

3.3.4 Coherent Pion Production

Coherent pion production is a neutrino interaction with a nucleus, in which the nucleus remains intact without any change of its charge and isospin. One pion which has the same charge as the incoming weak current is produced in the reaction. Since the transferred momentum to the nucleus is small, the angular distribution of the outgoing leptons and pions are peaked in forward direction.

The cross-section and kinematics of coherent pion production is calculated based on the Rein & Sehgal's model [88]. The differential cross-section is expressed as follows :

$$\frac{d^3\sigma}{dQ^2dydt} = \frac{G_F^2 M_N}{2\pi^2} f_\pi^2 A^2 E_\nu (1-y) \frac{1}{16\pi} (\sigma_{total}^{\pi N})^2 (1+r^2) (\frac{M_A^2}{M_A^2+Q^2})^2 e^{-b|t|} F_{abs} \quad (3.28)$$

$$r = Re(f_{\pi N}(0))/Im(f_{\pi N}(0)) \quad (3.29)$$

where f_π is pion decay constant and taken to be $0.93\,m_\pi$, b is in the order of the nucleus transverse dimensions taken to be $80\,\mathrm{GeV}^{-2}$, A is the atomic number ($=16$ for oxygen), G_F is the weak coupling constant, M_N is the nucleon mass, M_A is the axial-vector mass, Q^2 is the square of the 4-momentum transfer of the lepton, and t is the square of the 4-momentum

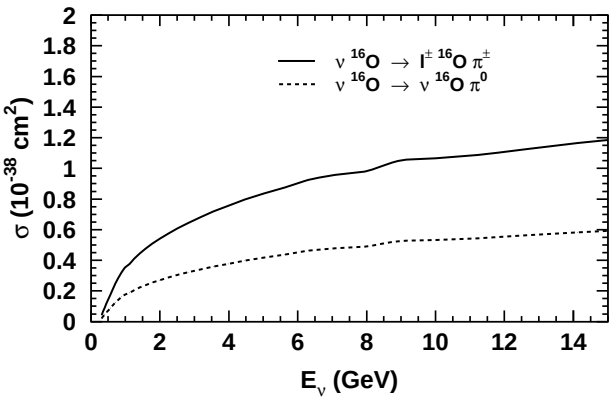

Figure 3.14: The cross-sections of coherent pion productions off the ^{16}O nucleus used in our Monte Carlo simulation. The solid line is for CC interactions, while the dashed line is for NC interactions.

transfer to the nucleus, respectively. F_{abs} is the factor to take the pion absorption in the nucleus into account. Fig. 3.14 shows the cross-sections for charged current and neutral current coherent pion productions used in our Monte Carlo simulation.

3.3.5 Nuclear Effects

For all hadrons generated in ^{16}O nucleus, the concept of formation zone is considered in our simulation. This is a distance (or time) from the neutrino interaction point to produce hadrons. The intermediate states are assumed to be non-bound quark states. The formation length of each hadron is expressed by :

$$L = p/\mu^2 \tag{3.30}$$

where p is the momentum of the hadron and $\mu^2 = 0.08\,\mathrm{GeV}^2$ is a fitted constant from the SKAT experiment [89]. The effect of this vertex shift reduce the interactions of generated hadrons in the nuclei.

Mesons and nucleons generated in ^{16}O nucleus often cause secondary interactions with nucleons before leaving the nucleus. The interactions of π's, K's, η's and ω's with nucleons in the nucleus are considered in our simulation. Among them, the simulation of pion is most important because the cross-section of pion production in a neutrino interaction is quite large compared with the others and the cross-section of pion-nucleon in nucleus is also large.

In our simulation, the following pion interactions in ^{16}O nucleus are considered : inelastic scattering, charge exchange and absorption. The neutrino interaction point in a nucleus is determined based on the Wood-Saxon type nucleon density distribution :

$$\rho(r) = \frac{Z}{A}\rho_0 \frac{1}{1+\exp(\frac{r-c}{a})} \tag{3.31}$$

We choose ρ_0=0.48 m_π^3, a=0.41 fm, c=2.69 fm, Z=8 and A=16 for ^{16}O nucleus. The cross-section of each interaction is calculated using the model by L.Salced *et al.* [90]. The mean free path of a pion depends on the momentum and the position in the nucleus. Fermi motion of nucleons in

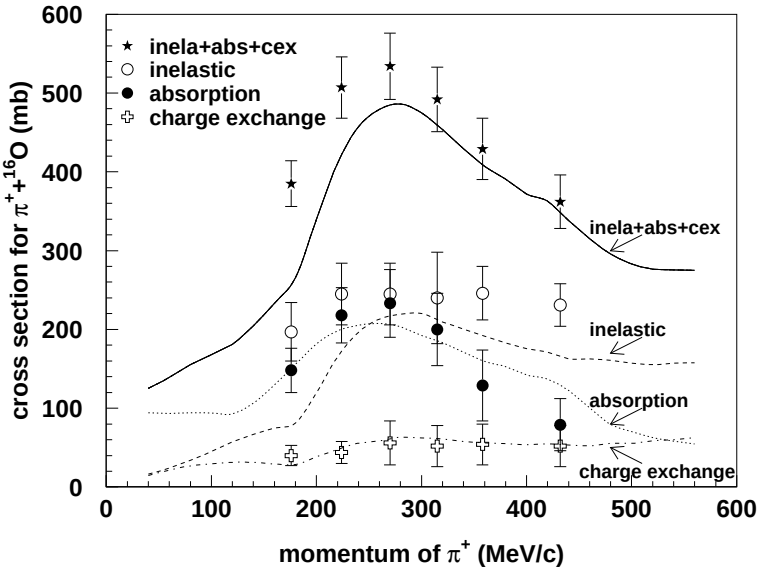

Figure 3.15: The cross-sections of $\pi^+ - ^{16}\mathrm{O}$ interactions. The lines show the results of our calculation based on [90] and the points show the experimental data [92]

the nucleus and the Pauli blocking effect are taken into consideration in the calculation. Fermi surface momentum is defined as follows :

$$p_F(r) = \left(\frac{3}{2}\pi^2\rho(r)\right)^{\frac{1}{3}} \tag{3.32}$$

The kinematics in the scattering is determined by using the results of $\pi - N$ phase shift analysis [91]. Figure 3.15 shows the calculated $\pi^+ - ^{16}\mathrm{O}$ interaction cross-sections together with experimental data. The result of our simulation agrees well with the experimental data.

3.4 Detector Simulation

The produced particles in neutrino interactions are fed into a detector simulation code, in which the tracks of particles, Cherenkov radiation, propagation of Cherenkov photons in water, and the response of PMTs and the readout electronics are simulated.

The detector simulator program has been developed based on GEANT package [93]. Table 3.1 lists various processes which are considered in our simulation program. For the hadronic interactions in water, CALOR package [94] is employed in our simulation code. This package is known to reproduce the pion interactions well including low energy region ($\sim 1\,\mathrm{GeV}/c$). For still lower energy region ($p_\pi \leq 500\,\mathrm{MeV}/c$), a custom program [95] based on experimental data from $\pi - {}^{16}\mathrm{O}$ scattering [96] and $\pi - p$ scattering [97] is used in our simulation code.

In connection with the propagation of charged particles, Cherenkov photons are generated according to Equation (2.2) and (2.3). For the propagation of Cherenkov photons in water, Rayleigh scattering, Mie scattering and absorption are considered in our simulation code. Cherenkov photons interact with small objects like molecule of water through Rayleigh scattering. The coefficient of Rayleigh scattering is known to have λ^{-4} dependence. If the size of the target object is roughly the same as or larger than the wavelength, Cherenkov photons interact through Mie scattering. Photons are scattered symmetrically in forward and backward directions in the case of Rayleigh scattering, while predominantly in forward direction in Mie scattering. Attenuation coefficients used in our simulation are shown in Figure 2.18, which are tuned to reproduce the measurement using laser system (Section 2.3.4). Light reflection and absorption on detector material, such as the surface of PMTs and black sheets, are also simulated using probability functions that depend on the photon incident angle estimated from direct measurements.

For the simulation of the PMT response, measured quantum efficiency is used. The total amount of p.e.s detected in each PMT is derived by summing up individual p.e. with a weight of a single p.e. distribution. The hit time of each PMT is smeared according to the PMT timing resolution. Properties of the electronics system, such as the time width of ADC gate and the signal threshold, are also taken into account.

3.5 Upward-Going Muon

The prediction of upward-going muon signals is also calculated by Monte Carlo method using the identical tools to that for the vertex contained events. The energy range and the target volume are extended for upward-going muons. The energy range of the atmospheric flux is extended up to 100 TeV, which is calculated by M.Honda *et al.* [1, 2] up to 7 TeV, and by L.V.Volkova [26] above that. The target volume of neutrino interactions is extended to the rock around the detector. The composition of the rock is set to be SiO_2 with the density $2.7\,\mathrm{g/cm^3}$. Neutrino interactions occur in the water of the OD are also considered, which amount to 6.6 % for upward stopping muons and 1.8 % for upward through-going muons. The output of the Monte Carlo simulation are passed through the same reduction and event reconstruction process as that for the observed data.

γ	(e^+, e^-) pair production
	Compton scattering
	Photoelectric effect
$e^{\pm}$	Multiple scattering
	Ionization and δ-rays production
	Bremsstrahlung
	Annihilation of positron
	Generation of Cherenkov radiation
$\mu^{\pm}$	Decay in flight
	Multiple scattering
	Ionization and δ-rays production
	Bremsstrahlung
	Direct (e^+, e^-) pair production
	Nuclear interaction
	Generation of Cherenkov radiation
Hadrons	Decay in flight
	Multiple scattering
	Ionization and δ-rays production
	Hadronic interactions
	Generation of Cherenkov radiation

Table 3.1: List of the processes considered in simulator.

Chapter 4

Data Reduction

4.1 Overview

In Super-Kamiokande, about 10^6 events/day are detected except for super low energy triggered events, while the number of the expected atmospheric neutrino events is about 10 events/day. The effective event selection is required to select neutrino events from a large quantity of data.

Atmospheric neutrino events observed in Super-Kamiokande are classified into four categories, fully contained (FC), partially contained (PC), upward stopping muons and upward through-going muons. Figure 4.1 shows the schematic view of each categories. Different reduction procedures are applied to select each sample. For FC and PC events, the vertices of neutrino interactions are inside the fiducial volume of the ID. If the tracks of entire particles are contained inside the ID, the event is classified into FC. If one of the particles exits the ID and deposits visible energy in the OD, the event is classified into PC. Muons produced by neutrino interaction in the rock surrounding the detector sometimes enter the ID. Among these neutrino induced muons, only background-free upward going muon events can be studied. The upward muon events are classified into two categories, upward stopping muons and upward through-going muons, according to whether the entering muons stop inside the ID or path through the ID.

The number of hit PMTs in the OD hit cluster (NHITAC, see Section 4.3.2) is used to

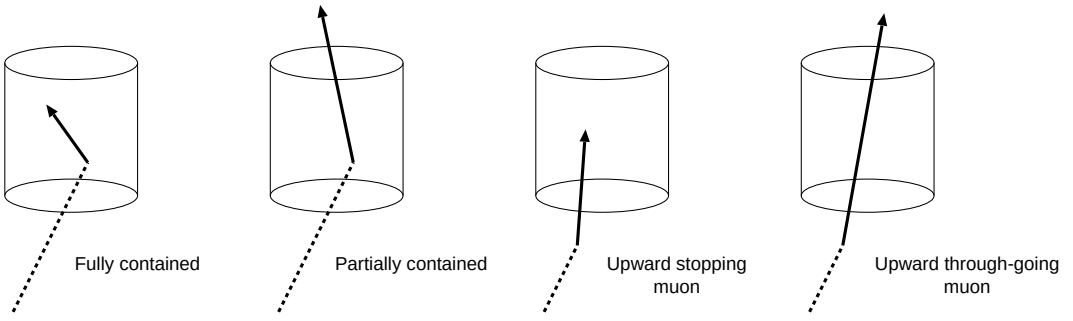

Figure 4.1: Categories of atmospheric neutrino events in Super-Kamiokande. Dashed lines show trajectories of primary neutrinos, and solid arrows show those of secondary charged particles.

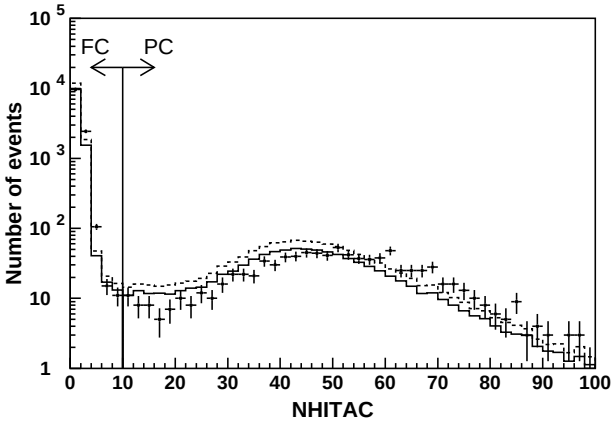

Figure 4.2: NHITAC distributions for FC and PC final samples. The points show the observed data, and histograms show the atmospheric neutrino Monte Carlo events assuming no oscillation (dashed lines) and $\nu_\mu \leftrightarrow \nu_\tau$ 2-flavor oscillation with $(\sin^2 2\theta,\ \Delta m^2) = (1.00,\ 2.0\times10^{-3}\,\mathrm{eV}^2)$ (solid lines).

separate FC and PC samples, where hit cluster means the spatial cluster of neighboring hit PMTs. Figure 4.2 shows the NHITAC distributions for both FC and PC final samples in the fiducial volume (more than 2 m away from the ID wall). The definitions of FC and PC events are as follows :

- FC sample

  NHITAC < 10

- PC sample

  NHITAC ≥ 10

The systematic uncertainty in the FC/PC separation was estimated to be 1.8 % by comparing the NHITAC distributions for the observed data and the Monte Carlo events.

The number of hit OD PMTs within 8 m from the exit position (NHITEX) is used to separate upward stopping and through-going muon samples. Figure 4.3 shows the NHITEX distributions for both upward stopping and through-going muon events. The definitions of upward stopping and through-going muon events are as follows :

- Upward stopping muon sample

  NHITEX < 10

- Upward through-going muon sample

  NHITEX ≥ 10

The systematic uncertainty in the stopping/through-going separation was estimated to be 0.76 % by comparing the NHITEX distributions for the observed data and the Monte Carlo events.

All of the event samples are used in this thesis for a neutrino oscillation analysis, although only FC and PC events are used for a L/E analysis. All reduction procedures for FC and PC samples are fully automated from the beginning to the final event selection. On the other hand, upward going muon events are selected one by one by physicists using a visual display after most of the background events are rejected by automated reduction processes. The detailed

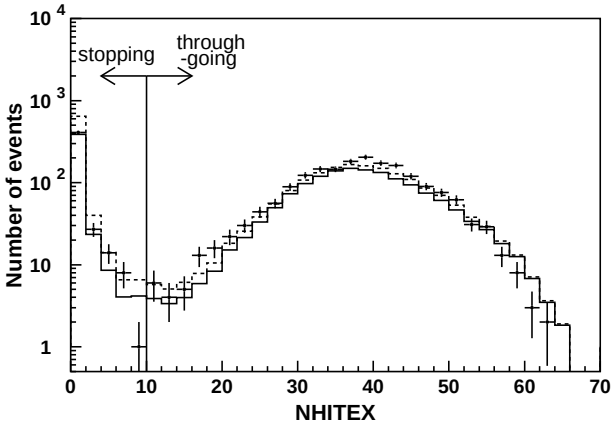

Figure 4.3: NHITEX distributions for upward stopping and through-going muon final samples. The points show the observed data, and histograms show the atmospheric neutrino Monte Carlo events assuming no oscillation (dashed lines) and $\nu_\mu \leftrightarrow \nu_\tau$ 2-flavor oscillation with $(\sin^2 2\theta,\ \Delta m^2) = (1.00,\ 2.0 \times 10^{-3}\,\mathrm{eV}^2)$ (solid lines).

explanations of the data reduction procedures for FC, PC and upward going muon events are described in this chapter.

4.2 Reduction for Fully Contained Sample

There are five steps in FC reduction process. The main sources of background are cosmic ray muons, low energy events from radioisotopes and electrical noise events. The cosmic ray muons are rejected using the OD activities.

4.2.1 First Reduction

The objective of the FC 1st reduction is to reduce the data to manageable size by simple and effective cuts. The selection criteria in the FC 1st reduction are the following :

(1) PE_{300} should be ≥ 200 p.e.
PE_{300} is the maximum number of total p.e.s observed by the ID PMTs in a sliding 300 nsec time window.

and

(2) NHITA_{800} should be ≤ 50
NHITA_{800} is the number of hit OD PMTs in a fixed 800 nsec time window from -400 nsec to $+400$ nsec before and after the trigger timing.

and

(3) TDIFF should be $> 100\,\mu$sec
TDIFF is a time interval to the previous event.

The low energy background events from radioisotopes are rejected by the first criterion. Figure 4.4 shows the PE_{300} distributions for the raw data and FC final samples. The 200 p.e.s cut corresponds to electron momentum of 22 MeV/c. Since events which have visible energy below 30 MeV are not used in the analysis, this cut is safe. The second cut removes a large part of the cosmic ray muon events. Figure 4.5 shows the NHITA_{800} distributions for the raw

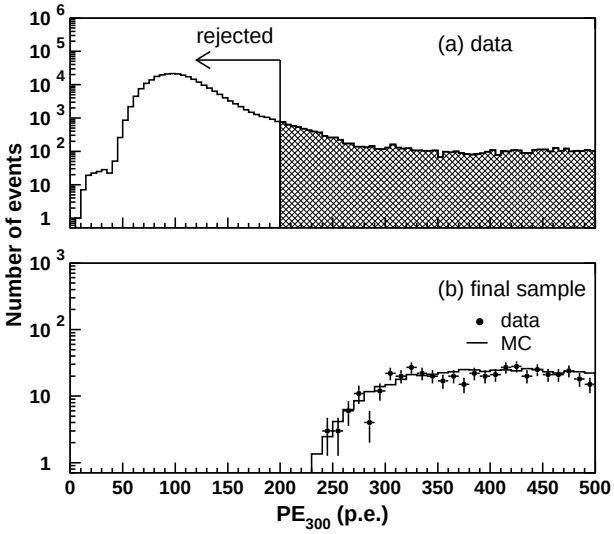

Figure 4.4: PE_{300} distribution for (a) the raw data and (b) the data and atmospheric neutrino Monte Carlo events (no oscillation) in FC final samples. The number of the Monte Carlo events in (b) is normalized to that of the data. The selection criterion is shown by an arrow.

data, fully contained atmospheric neutrino Monte Carlo events and final samples. The third cut eliminates the electron events from the decay of the cosmic ray muons stopped in the ID.

Besides these selection criteria, events within 30 μsec after the FC event candidates are selected to examine the presence of muon decay electrons. These events are attached to the fully contained event candidates as sub-events and not counted as a primary atmospheric neutrino event.

These cuts reduce the data size from 10^6 events/day to 3000 events/day.

4.2.2 Second Reduction

The aim of the FC 2nd reduction is to reject low energy events and cosmic muons furthermore. The criteria to select fully contained events are the following :

(1) $NHITA_{800}$ should be ≤ 25 if $PE_{tot} < 100{,}000$ p.e.
PE_{tot} is the total number of p.e.s observed in the ID.

and

(2) PE_{max}/PE_{300} should be < 0.5
PE_{max} is the maximum number of p.e.s observed by an ID PMT.

The first cut is similar to the second cut in the FC 1st reduction, but the threshold is tighter as shown by arrows written by solid lines in Figure 4.5. This cut is still safe for the fully contained events. The second cut removes low energy events and electrical noise events which have one large hit. Figure 4.6 shows the PE_{max}/PE_{300} distribution for the data after the FC 1st reduction, atmospheric neutrino Monte Carlo events and final samples. A PMT sometimes begins to flash because of a discharge around the dynode structure. The light emitted by such a problematic PMT causes an electrical noise event called flasher event. Since the flashing PMT tends to record a large charge, some of the flasher events are discarded by this criterion. The remaining flasher events are further removed by more elaborate methods in the following reduction stages.

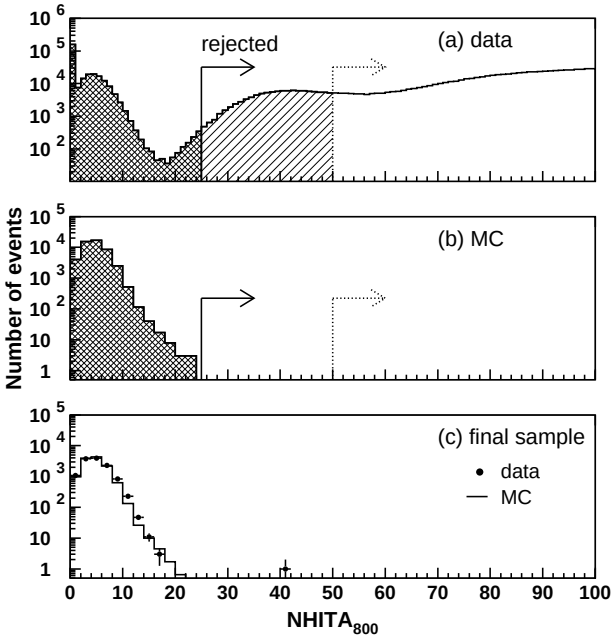

Figure 4.5: $NHITA_{800}$ distributions for (a) the raw data, (b) fully contained atmospheric neutrino Monte Carlo events whose vertex position is more than 2 m away from the ID wall and (c) final samples of the data and the Monte Carlo events. The number of the Monte Carlo events in (c) is normalized to that of the data. The arrows written by dotted (solid) lines show the selection criteria in the FC 1st (2nd) reduction.

The event rate after the FC 2nd reduction stage is 200 events/day.

4.2.3 Third Reduction

Most of the background events have been rejected by simple cuts in the FC 1st and 2nd reduction stages. The number of remaining background events is not so large at this stage but there are various sources of the background events. The purpose of the FC 3rd reduction is to eliminate cosmic ray stopping and through-going muons with small OD signals, flasher events, low energy events from radioisotopes and accidental coincidence events with algorithms dedicated to the specific background sources. The outline of the reduction algorithms are explained in the following sections.

The event rate after FC 3rd reduction is 45 events/day.

Through-going muon cut

Most of the cosmic ray muon events are eliminated in the FC 1st and 2nd reduction stages using the OD information. Therefore, the remaining cosmic ray muons have only a small number of hits in the OD. In order to distinguish these remaining muons from fully contained neutrino events, the number of hit OD PMTs near the entrance and the exit points are counted. Events which satisfy the following criteria are identified as through-going muons and rejected :

(1) $PE_{max} > 230$ p.e.

and

(2) goodness of through-going muon fit > 0.75

and

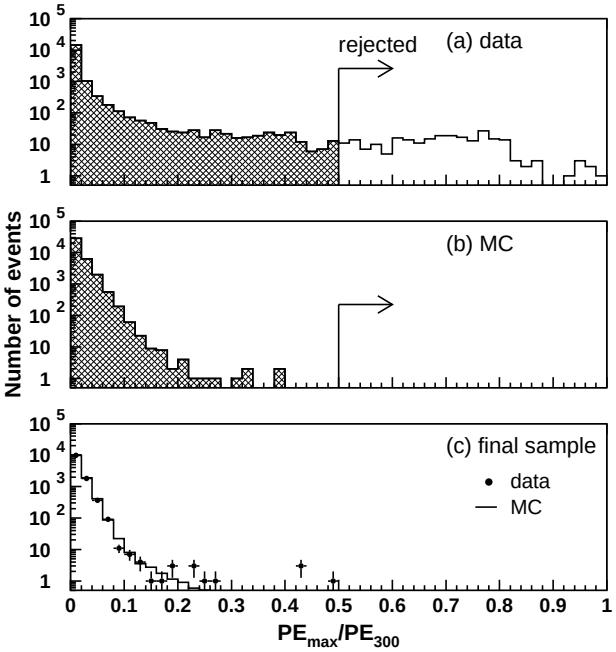

Figure 4.6: PE_{max}/PE_{300} distribution for (a) the data after the FC 1st reduction, (b) fully contained atmospheric neutrino Monte Carlo events and (c) final samples of the data and the the Monte Carlo events. The number of the Monte Carlo events in (c) is normalized to that of the data. The selection criteria are shown by arrows.

(3) $NHITA_{in} \geq 10$ or $NHITA_{out} \geq 10$
$NHITA_{in}$ ($NHITA_{out}$) is the number of hit OD PMTs located within 8 m from the entrance (exit) point in a fixed 800 nsec time window.

Through-going muon fit is specially made to reconstruct the track of through-going muons. The entrance and the exit points are determined as the positions of the earliest hit ID PMT with some neighbor hits and the center of the saturated ID PMTs, respectively. The goodness of through-going muon fit is defined as :

$$goodness = \frac{1}{\sum_i \frac{1}{\sigma_i^2}} \times \sum_i \frac{1}{\sigma_i^2} \exp\left(-\frac{(t_i - T_i)^2}{2(1.5 \times \sigma_i)^2}\right) \quad (4.1)$$

where t_i and σ_i are the observed hit time of the i-th PMT and its resolution, and T_i is the hit time expected from the entering time of muon and its track. Figure 4.7 shows the number of hit OD PMTs near the entrance and the exit points for the data after the FC 2nd reduction, atmospheric neutrino Monte Carlo events and final samples satisfying the first two conditions, PE_{max} >230 p.e. and goodness>0.75 .

Stopping muon cut

The procedure similar to through-going muon cut is used to remove stopping muon events. Events which satisfy the following criteria are rejected as stopping muons :

(1) $NHITA_{in} \geq 10$
or
$NHITA_{in} \geq 5$ if goodness of stopping muon fit > 0.5

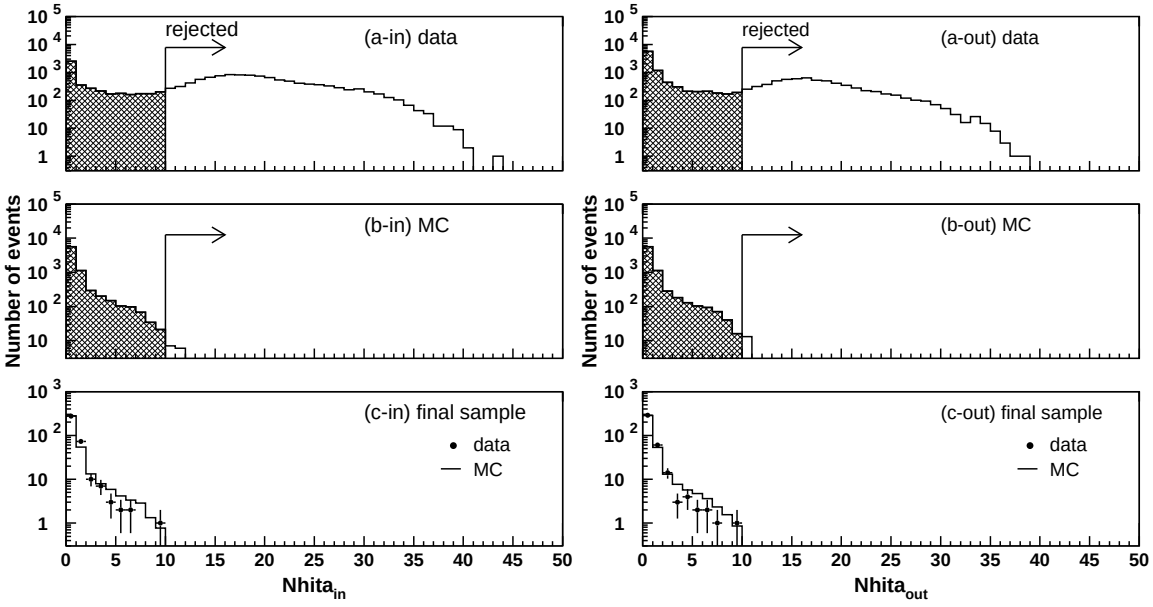

Figure 4.7: Number of hit OD PMTs (left) within 8 m of the entrance point of muons and (right) within 8 m of the exit position for (a) the data after FC 2nd reduction, (b) fully contained atmospheric neutrino Monte Carlo events and (c) final samples. The number of the Monte Carlo events in (c) is normalized to that of the data. The selection criteria are shown by arrows.

> $\mathrm{NHITA_{in}}$ is the number of hit OD PMTs located within 8 m from the entrance point in a fixed 800 nsec time window.

Stopping muon fit reconstructs the entrance position by the same way as through-going muon fit. The direction of muon is reconstructed to maximize the total number of p.e.s inside a cone with half opening angle 42°. The goodness is defined by Equation (4.1), which is the same as that of through-going muon fit. Figure 4.8 shows the number of hit OD PMTs near the entrance point for the data after the FC 2nd reduction, atmospheric neutrino Monte Carlo events and final samples satisfying the condition, goodness>0.5 . Most of the real FC neutrino events have the goodness of stopping muon fit of less than 0.5 .

Cable hole muon cut

Signal and HV supply cables are taken out from the detector tank through twelve cable holes. Four of them are located above the ID side-wall structure. These cable holes made inefficiency of the OD to the cosmic ray muons that penetrate through them at the beginning of the experiment. To compensate for the inefficiency of the OD, 2 m × 2.5 m plastic scintillation counters, referred to as veto counters, were installed over the four cable holes in April, 1997. A schematic view of a cable-hole muon and the veto counter is shown in Figure 4.9. Events satisfying the following criteria are rejected as cable hole muons :

(1) One veto counter hit.

and

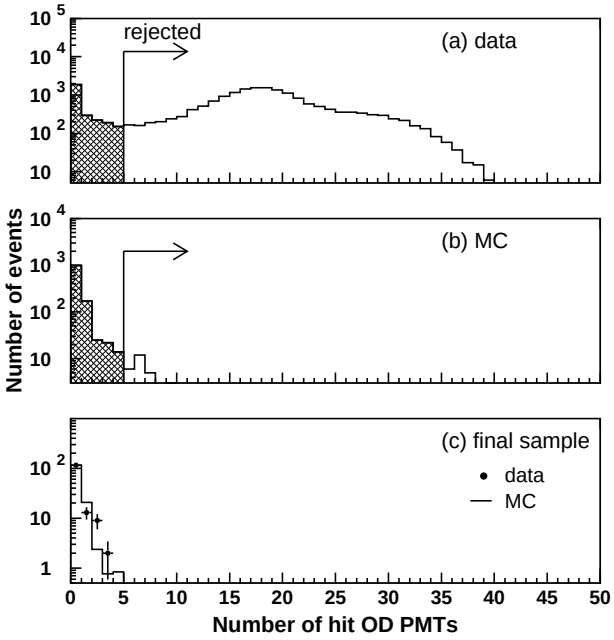

Figure 4.8: Number of hit OD PMTs near the entrance point of muons for (a) the data after FC 2nd reduction, (b) fully contained atmospheric neutrino Monte Carlo events and (c) final samples. The number of the Monte Carlo events in (c) is normalized to that of the data. The selection criteria are shown by arrows.

(2) $L_{veto} < 4\,m$
L_{veto} is the distance from the cable hole to the the reconstructed vertex.

Figure 4.10 shows the reconstructed vertex distribution for the FC 1-ring μ-like events before and after the installation of veto counters. Cable hole muons are well eliminated by veto counters as shown in this figure.

Accidental coincidence event cut

Sometimes a low energy event and the following cosmic ray muon occur in a single trigger gate by accident. These events are not rejected in the former reduction stages because of the absence of the OD activities on the trigger timing and the large number of total p.e.s in the ID due to the muons. The accidental coincidence events are removed by the following cuts :

(1) $NHITA_{off} \geq 20$
$NHITA_{off}$ is the number of hit OD PMTs in a fixed 500 nsec off-timing window from +400 nsec to +900 nsec after the trigger timing.

and

(2) $PE_{off} > 5000$ p.e.
PE_{off} is the number of p.e.s observed by ID PMTs in a fixed 500 nsec off-timing window from +400 nsec to +900 nsec.

Flasher event cut

Most of the flasher events have a broad hit timing distribution compared with that of the neutrino events. The cut criteria to eliminate these flasher events are :

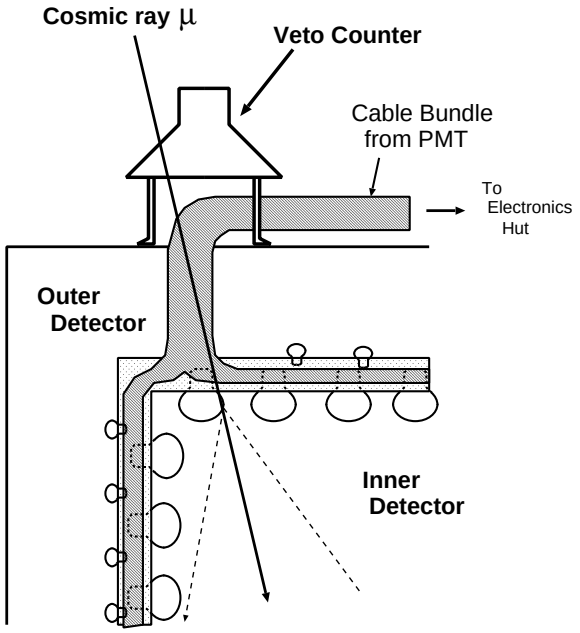

Figure 4.9: A schematic view of a cable-hole muon and a veto counter.

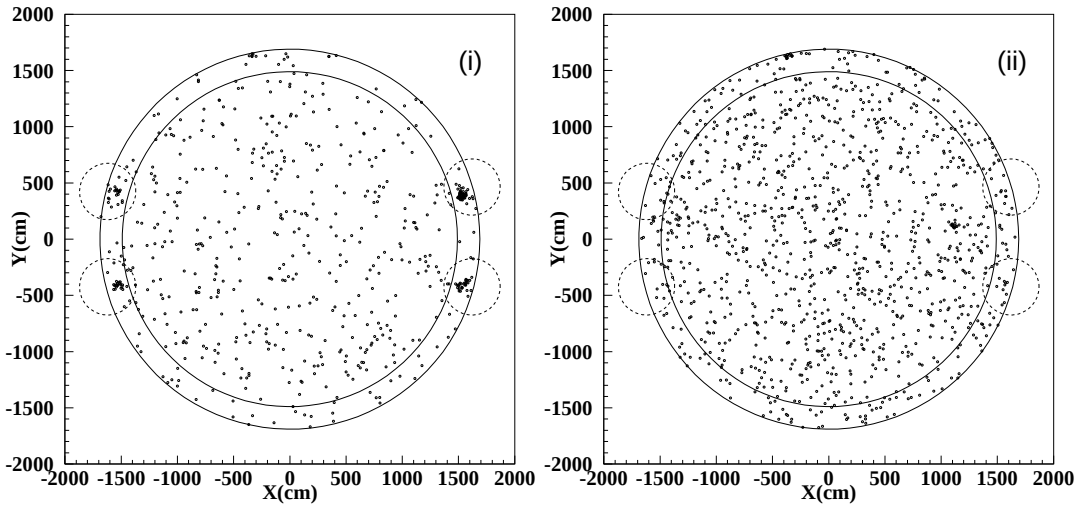

Figure 4.10: Reconstructed vertex distribution for the fully contained 1-ring μ-like events (i) before the installation of the veto counters and (ii) after installation. The outer solid circle shows the ID wall and the inner solid circle shows the fiducial volume (2 m from the wall). Small dashed circles indicate the positions of the veto counters. Four clusters are clearly seen around cable holes for data without veto counters, while no cluster is visible for data after the installation.

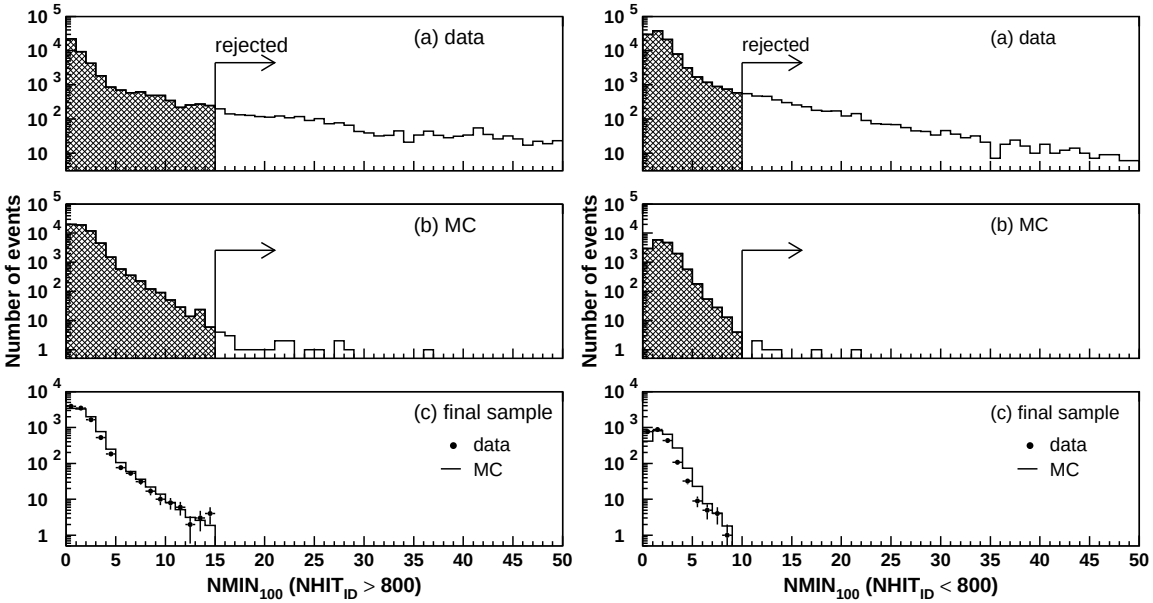

Figure 4.11: $NMIN_{100}$ distributions (left) for the events with more than 800 hit PMTs in the ID and (right) less than 800 hit PMTs. Three figures show (a) the data after FC 2nd reduction, (b) fully contained atmospheric neutrino Monte Carlo events and (c) final samples, respectively. The number of the Monte Carlo events in (c) is normalized to that of the data. The selection criteria are shown by arrows.

(1) $NMIN_{100} \geq 14$
or
$NMIN_{100} \geq 10$ if the number of hit ID PMTs < 800
$NMIN_{100}$ is the minimum number of hit ID PMTs in a sliding 100 nsec time window from +300 nsec to +800 nsec.

The $NMIN_{100}$ distributions for the data after the FC 2nd reduction, atmospheric neutrino Monte Carlo events and final samples are shown in Figure 4.11. The remaining flasher events after this cut are further removed in the next reduction stage.

Low energy event cut

The main sources of the remaining low energy events are the decay of radioisotopes and the electrical noise. Events satisfying the following criteria are removed as low energy background events :

(1) $NHIT_{50} < 50$
$NHIT_{50}$ is the number of hit ID PMTs in a sliding 50 nsec time window.

where $NHIT_{50}$ is counted after subtracting the time of flight (TOF) of each observed photon assuming all photons are generated at a point. The vertex is determined as the position at which the timing residual distribution is peaked. The cut $NHIT_{50}$=50 corresponds to visible energy of 9 MeV.

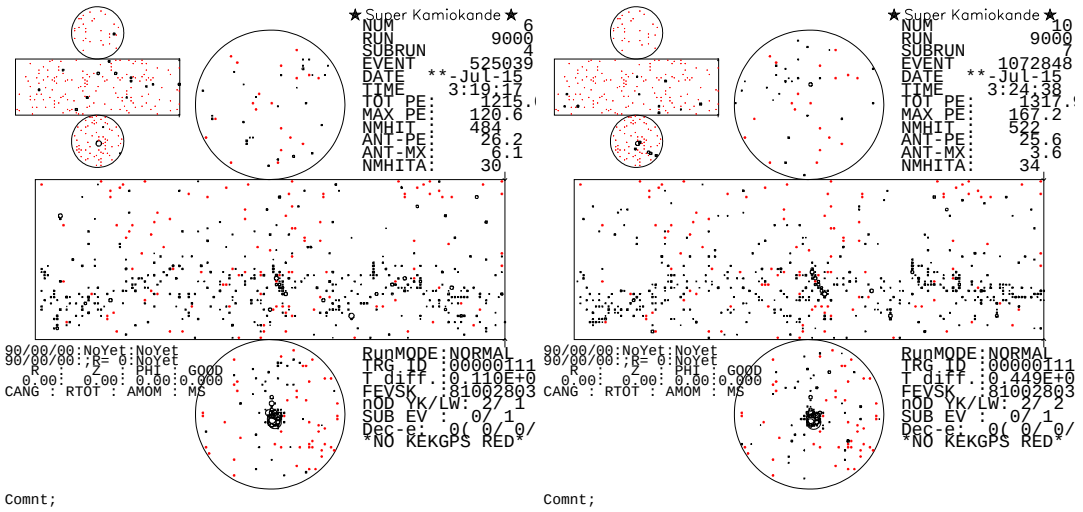

Figure 4.12: Visual displays of typical successive flasher events. The time interval between these two events is about 20 minutes.

4.2.4 Fourth Reduction

As described in the previous reduction stage, electric discharge in a PMT cause a background event called flasher event. The FC 4th reduction is dedicated to reject the flasher events, which are the main part of the remaining background events after the FC 3rd reduction. The rejection is done by a pattern matching algorithm based on its characteristic that the flasher events are likely to repeat with similar hit patterns. Figure 4.12 shows the visual displays of typical successive flasher events. These two events have a similar hit pattern with the time interval of about 20 minutes. Of course, neutrino events are unlikely to repeat in such a way. The algorithm of the FC 4th reduction is as follows.

First, the inner detector walls are divided into 1450 square patches including $6 \sim 9$ PMTs. Two events, A and B, are compared by using the charge in each patch. Their correlation is defined by :

$$r = \frac{1}{N} \sum_i \frac{\left(Q_i^A - \langle Q^A \rangle\right) \times \left(Q_i^B - \langle Q^B \rangle\right)}{\sigma_A \times \sigma_B} \tag{4.2}$$

where N is the number of the patches, and $\langle Q^{A(B)} \rangle$ and $\sigma_{A(B)}$ are the averaged charge and its standard deviation for event A and B, respectively. If the distance between the PMTs with the maximum pulse heights in the two compared events, $\mathrm{DIST}_{\max}$, is less than 75 cm, an offset value is added to the estimator r as follows :

$$r = r + 0.15 \qquad \text{if} \quad \mathrm{DIST}_{\max} < 75\,\mathrm{cm} \tag{4.3}$$

If the estimator r exceeds the threshold, events A and B are recognized as matched events. The threshold is defined by :

$$r > r_{th} = 0.168 \times \log_{10}((\mathrm{PE}_{\mathrm{tot}}^A + \mathrm{PE}_{\mathrm{tot}}^B)/2.) + 0.130, \tag{4.4}$$

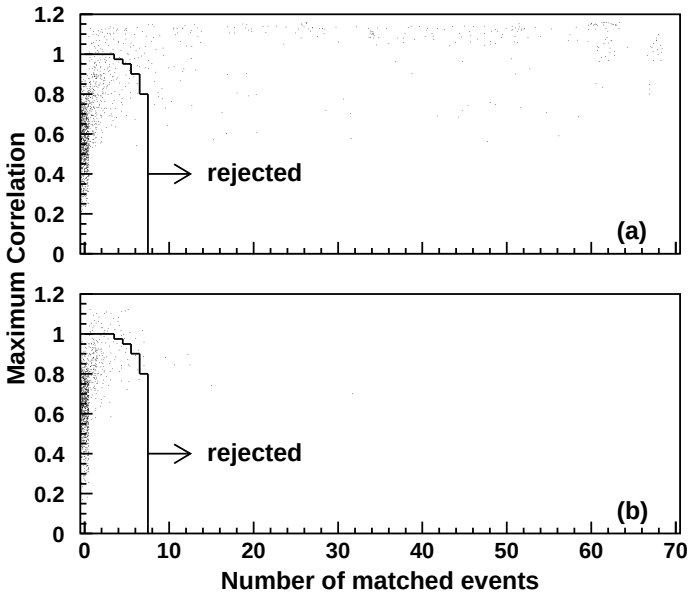

Figure 4.13: Scatter plots of N_{match} and the maximum value of the estimator r for (a) the data after the FC 3rd reduction and (b) atmospheric neutrino Monte Carlo events. The cut criteria are shown by arrows.

where PE_{tot} is the total number of p.e.s observed in the ID.

The same calculations are made over 10,000 events before and after the target event, and the number of matched events are counted (N_{match}). Figure 4.13 shows the scatter plots of N_{match} and the maximum value of the estimator r for the data after the FC 3rd reduction and atmospheric neutrino Monte Carlo events. For the Monte Carlo events, the data which were removed as flasher events in this reduction stage are mixed, and the estimator r is calculated. The cut criteria are also shown in Figure 4.13.

The event rate after the FC 4th reduction is 18 events/day.

4.2.5 Fifth Reduction

The purpose of the FC 5th reduction is the final rejection of the remaining background events for FC sample. The remaining background events are removed by various types of cuts specialized in each background source. Finally, 16 events/day are left as FC events after the five reduction stages.

Stopping muon cut

The remaining stopping muons are rejected by a similar cut as that in the FC 3rd reduction stage, but the entrance of the stopping muon is reconstructed by a different method. Events satisfying the following criteria are rejected :

(1) $NHITA_{in} \geq 5$
$NHITA_{in}$ is the number of hit OD PMTs located within 8 m from the entrance point in a sliding 200 nsec time window from -400 nsec to $+400$ nsec.

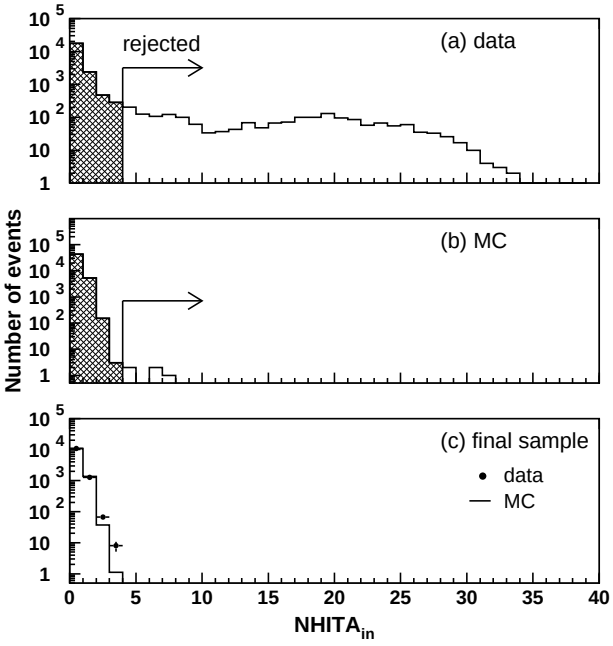

Figure 4.14: NHITA$_{in}$ distribution for (a) the data after FC 4th reduction and (b) fully contained atmospheric neutrino Monte Carlo events, and (c) final samples. The number of the Monte Carlo events in (c) is normalized to that of the data. The selection criteria are shown by arrows.

The vertex position is determined by TDC-fit as the point at which the timing residual distribution of hit PMTs has the sharpest peak (see Section 5.2.3). The timing residual for each PMT is calculated in TDC-fit taking the direction and the track length of the charged particle into consideration. The entrance position is estimated by a backward extrapolation from the reconstructed vertex. Figure 4.14 shows the NHITA$_{in}$ distribution for the data after the FC 4th reduction, atmospheric neutrino Monte Carlo events and final samples.

Invisible muon cut

An invisible muon event is an event caused by a combination of a cosmic ray muon with momenta below the Cherenkov threshold and the subsequent decay electron. These events are characterized by a low energy signal from decay electron and a signal in the OD before the trigger timing. Events which satisfy the following cut criteria are rejected as invisible muons :

(1) $PE_{tot} < 1000$ p.e.
PE_{tot} is the total number of p.e.s observed in the ID.

and

(2) $NHITAC_{early} > 4$
$NHITAC_{early}$ is the maximum number of hit PMTs in the OD hit cluster in a sliding 200 nsec time window from -8800 nsec to -100 nsec.

and

(3) $NHITAC_{early} + NHITAC_{500} > 9$ if $DIST_{clust} < 500$ cm
$NHITAC_{early} > 9$ otherwise

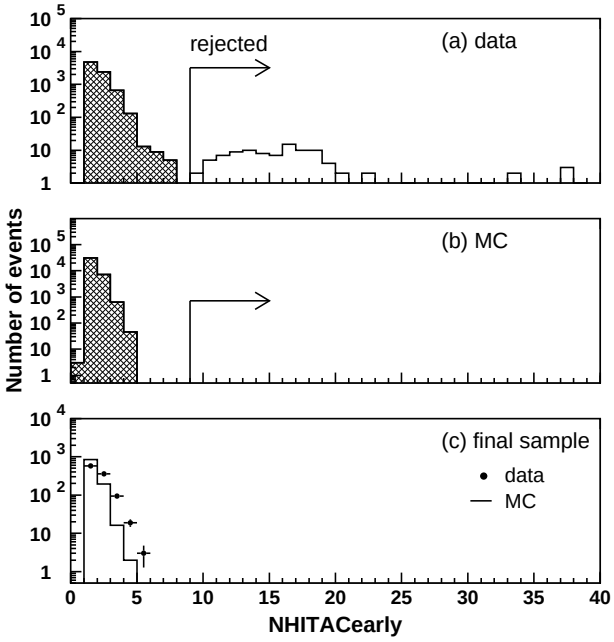

Figure 4.15: $\mathrm{NHITAC_{early}}$ distribution for (a) the data after FC 4th reduction and (b) fully contained atmospheric neutrino Monte Carlo events, and (c) final samples, satisfying conditions $\mathrm{PE_{tot}} < 1000\,\mathrm{p.e.}$ and $\mathrm{DIST_{clust}} > 500\,\mathrm{cm}$. The number of the Monte Carlo events in (c) is normalized to that of the data. The selection criteria are shown by arrows.

$\mathrm{NHITAC_{500}}$ is the number of hit PMTs in the OD hit cluster in a fixed 500 nsec time window from -100 nsec to $+400$ nsec.
$\mathrm{DIST_{clust}}$ is a distance between two OD hit clusters, which are used for the $\mathrm{NHITAC_{early}}$ and the $\mathrm{NHITAC_{500}}$.

Figure 4.15 shows the $\mathrm{NHITAC_{early}}$ distribution for the data after the FC 4th reduction, fully contained atmospheric neutrino Monte Carlo events and final samples, satisfying conditions $\mathrm{PE_{tot}} < 1000\,\mathrm{p.e.}$ and $\mathrm{DIST_{clust}} > 500\,\mathrm{cm}$. Although the number of hit PMTs in off-timing window for data is larger than that for the Monte Carlo simulation, the cut is safe for FC sample.

Coincidence muon cut

Events satisfying the following cut criteria are rejected as accidental coincidence of a low energy event and a muon event :

(1) $\mathrm{PE_{500}} < 300\,\mathrm{p.e.}$
$\mathrm{PE_{500}}$ is the total number of p.e.s observed in the ID in a fixed 500 nsec time window from -100 nsec to $+400$ nsec.

and

(2) $\mathrm{PE_{late}} \geq 20$
$\mathrm{PE_{late}}$ is the maximum number of hit OD PMTs in a 200 nsec sliding time window from $+400$ nsec to $+1600$ nsec.

Figure 4.16 shows the $\mathrm{PE_{late}}$ distribution for the data after the FC 4th reduction, fully contained atmospheric neutrino Monte Carlo events and final samples, satisfying the first condition $\mathrm{PE_{500}} < 300\,\mathrm{p.e.}$. The cut is safe for FC sample.

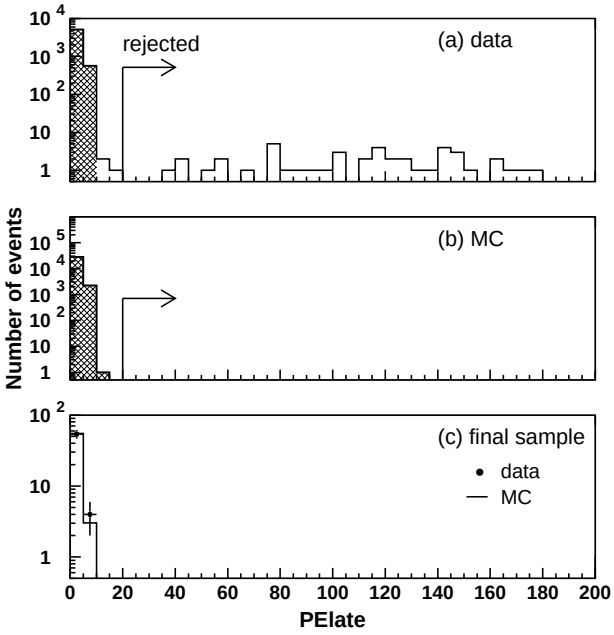

Figure 4.16: PE_{late} distribution for (a) the data after FC 4th reduction and (b) fully contained atmospheric neutrino Monte Carlo events, and (c) final samples, satisfying a condition $PE_{500} < 300$ p.e.. The number of the Monte Carlo events in (c) is normalized to that of the data. The selection criteria are shown by arrows.

Long tail flasher cut

This is a stricter version of flasher cut in the FC 3rd reduction stage. Events satisfying the following criterion are removed as flasher events :

(1) $NMIN_{100} > 5$ if the goodness of point fit < 0.4
$NMIN_{100}$ is the minimum number of the hit ID PMTs in a sliding 100 nsec time window from +300 nsec to +800 nsec.

The explanation of point fit is described in Section 5.2.1.

4.2.6 Efficiency and Background for FC Sample

Detection efficiency of the atmospheric neutrino events through the FC reduction process is estimated by the fully contained atmospheric neutrino Monte Carlo events. The definition of the FC event is : (1) vertex of neutrino interaction should be inside the fiducial volume, (2) number of hit PMTs in the highest charge OD cluster (NHITAC) should be ≤ 9, and (3) visible energy assuming electrons (E_{vis}) should be > 30 MeV. The detection efficiency is estimated to be 99.4 %. The systematic uncertainty of the detection efficiency for FC sample is estimated to be less than 1 %.

The background for the FC sample mainly originates from cosmic ray muons, flasher events and neutrons from the rock around the detector. These background events are strongly rejected by requiring fiducial volume cut. The contaminations of those backgrounds are estimated as shown in Table 4.1 [99].

	Sub-GeV		Multi-GeV	
	e-like(%)	μ-like(%)	e-like(%)	μ-like(%)
Cosmic ray μ	—	0.07	—	0.09
Flashing PMT	0.42	—	0.16	—
Neutron event	0.1	—	0.1	—

Table 4.1: Summary of the estimated upper limit of the contamination of each background.

4.3 Reduction for Partially Contained Sample

Data reduction for the PC sample is completely different from that for the FC sample. Since PC events are required to have the OD activities by its definition, it is rather difficult to eliminate cosmic ray muon backgrounds. The reduction stream for the PC sample consists of five steps and all of the reduction procedures are fully automated.

4.3.1 First Reduction

The objective of the PC 1st reduction is to reject the through-going cosmic ray muons and low energy events by simple and effective cuts. Not only atmospheric neutrino events but also stopping muons remain. The selection criteria in the PC 1st reduction are as follows :

(1) PE_{tot} should be ≥ 1000 p.e.
PE_{tot} is the number of p.e.s observed in the ID.

and

(2) TWIDA should be ≤ 260 nsec
TWIDA is the width of the hit timing distribution in the OD PMTs.

and

(3) NCLSTA should be ≤ 1
NCLSTA is the number of the hit clusters in the OD.

Exiting particles in the PC sample, mostly muons, must have at least 2 m track length in the ID, which corresponds to the momentum deposit of 500 MeV/c for muons. Therefore, the first cut, $PE_{tot} \geq 1000$ p.e. corresponds to 310 MeV/c for muons, is safe for the PC sample.

Most of the through-going muons are rejected by the second and the third criteria. Since through-going muons pass thorough the OD twice by the definition, a broad hit timing distribution and two hit clusters are expected in the OD. The hit cluster means the spatial cluster of neighboring hit PMTs. A hit cluster is formed around the PMT which detects more than 8 p.e. and the clusters within 8 m are merged. The TWIDA and the NCLSTA distributions for the raw data, atmospheric neutrino Monte Carlo events and final samples of the data and the Monte Carlo events are shown in Figure 4.17 and Figure 4.18, respectively.

The event rate after the PC 1st reduction is 14000 events/day.

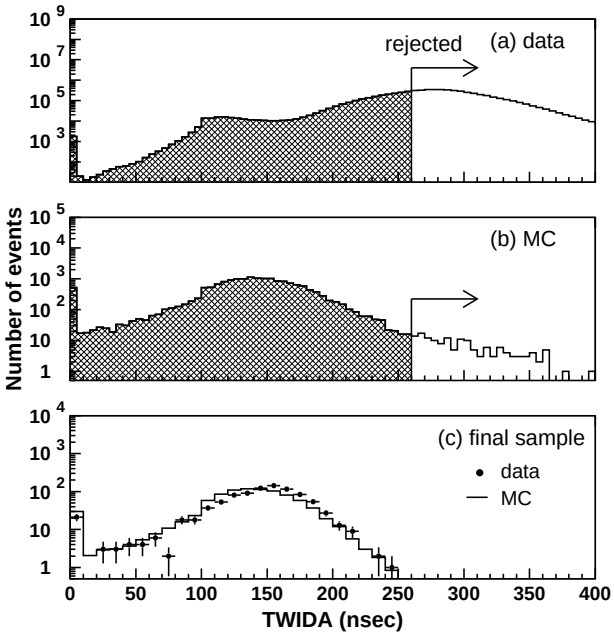

Figure 4.17: TWIDA distributions for (a) the raw data, (b) partially contained atmospheric neutrino Monte Carlo events whose vertex position is more than 2 m away from the ID wall and (c) final samples of the data and the Monte Carlo events. The number of the Monte Carlo events in (c) is normalized to that of the data. The selection criteria are shown by arrows.

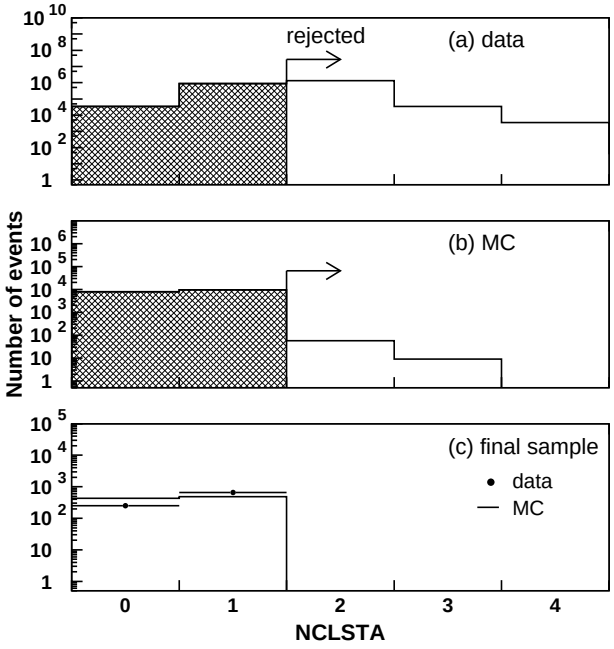

Figure 4.18: NCLSTA distributions for (a) the raw data, (b) partially contained atmospheric neutrino Monte Carlo events and (c) final sample of the data and the Monte Carlo events. The number of the Monte Carlo events in (c) is normalized to that of the data. The selection criteria are shown by arrows.

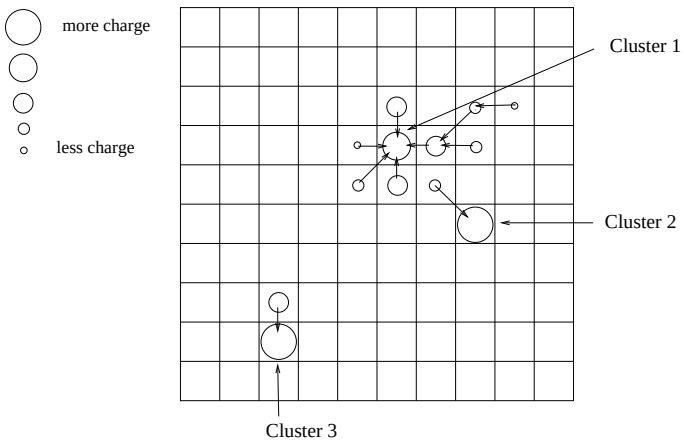

Figure 4.19: A schematic view of the algorithm to find hit clusters in the PC 2nd reduction. The circles represent the charge observed in each patch. The size of the circle is proportional to the number of p.e.s . The arrows represent the vector charge gradient, which point to the highest charge among the neighboring patches.

4.3.2 Second Reduction

Remaining through-going muons and the stopping muons are removed in the PC 2nd reduction based on the information of the hit clusters obtained by a different method from that in the PC 1st reduction. Figure 4.19 illustrates the algorithm to find hit clusters. The OD (ID) walls are divided into 11×11 (21×21) patches and the charge observed in each patch is counted. The clusters are formed by looking for the charge gradient to the neighboring patches. Events satisfying the following criteria remain after the PC 2nd reduction :

(1) NCLSTA2 should be ≤ 1
NCLSTA2 is the number of the OD hit clusters including more than 6 hit PMTs.

and

(2) $\mathrm{NHITAC_{min}}$ should be < 7
$\mathrm{NHITAC_{min}}$ is the minimum number of hit PMTs among top (or bottom) and side regions in the OD hit cluster.

and

(3) $\mathrm{PE_{200}}$ should be > 1000 p.e.s if NCLSTA2 $= 1$
$\mathrm{PE_{200}}$ is the number of the observed p.e.s within 200 cm from the highest charge PMT in the ID hit cluster closest to the OD hit cluster.

The second cut reject corner clipping muons, which left the hit PMTs in both top (or bottom) and side regions in the OD. In the third cut, the number of p.e.s in the ID hit cluster located behind the OD hit cluster is used for the primary rejection of the stopping muons. Figure 4.20 shows the scatter plots of the NCLSTA2 and the $\mathrm{PE_{200}}$ for the data and atmospheric neutrino

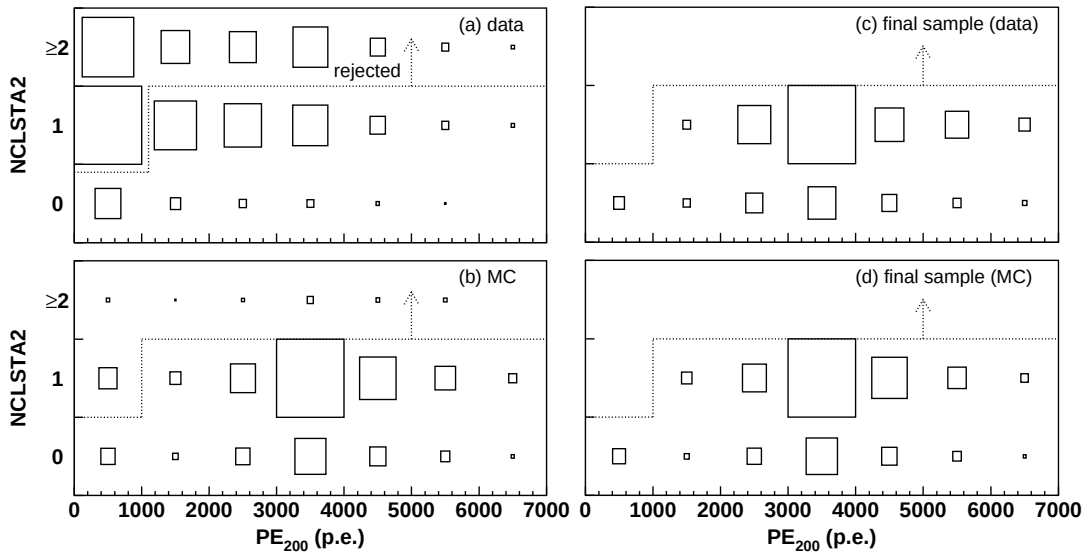

Figure 4.20: Scatter plots of NCLSTA2 and PE_{200} for (a) the data and (b) partially contained atmospheric neutrino Monte Carlo events after the PC 1st reduction and (c) final samples of the data and (d) the Monte Carlo events. The size of the boxes shows the number of the events in each bin. The cut criteria are shown by the dashed lines and arrows.

Monte Carlo events after the PC 1st reduction, and final samples, and Figure 4.21 shows the $NHITAC_{min}$ distributions for the same samples.

The event rate after the PC 2nd reduction is 2000 events/day.

4.3.3 Third Reduction

The aim in this reduction stage is to reject flasher events and cosmic ray stopping muons. Flasher events are rejected by the same way as that in the FC 3rd reduction, in which the broad timing distribution of the flasher events is used for cut. Events which satisfy the following criteria are rejected as flasher events :

(1) $NMIN_{100} > 14$
or
$NMIN_{100} > 9$ if the number of hit ID PMTs < 800
$NMIN_{100}$ is the minimum number of hit ID PMTs in a sliding 100 nsec time window from +300 nsec to +800 nsec.

Stopping muons are removed by the number of hit OD PMTs near the entrance position. Simple vertex and direction fitter called point fit is applied. The vertex position is determined by point fit as the point where the timing residual distribution of hit PMTs has the sharpest peak assuming the photons are emitted from a point source (see Section 5.2.1). The direction of the ring is determined by summing up the charge weighted vector for all PMTs, and the entrance position is estimated by a backward extrapolation from the reconstructed vertex. Events satisfying the following criteria are rejected as stopping muons :

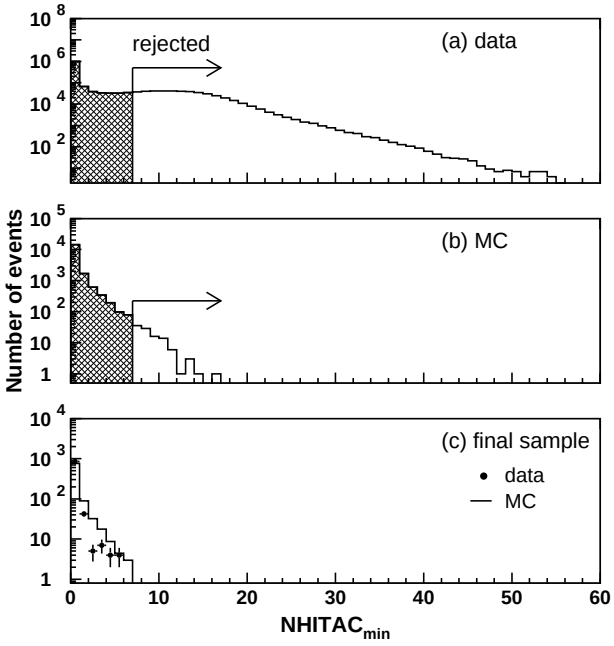

Figure 4.21: NHITAC$_{\rm min}$ distributions for (a) the data, (b) partially contained atmospheric neutrino Monte Carlo events after the PC 1st reduction and (c) final sample of the data and the Monte Carlo events. The selection criteria are shown by arrows.

(1) NHITA$_{\rm in}$ > 10
NHITA$_{\rm in}$ is the number of hit OD PMTs located within 8 m from the entrance point in a fixed 500 nsec time window.

The NHITA$_{\rm in}$ distributions for the data and atmospheric neutrino Monte Carlo events after the PC 2nd reduction, and final samples are shown in Figure 4.22.

The event rate after the PC 3rd reduction is 100 events/day.

4.3.4 Fourth Reduction

PC 4th reduction is dedicated to reject cosmic ray muons, which pass through the PC 3rd reduction due to the relatively small OD activities. The two types of event reconstruction tools are used in this reduction stage, that is a point fit and a though going muon fit. The through going muon fit determines the entrance point as the position of the earliest hit cluster in the ID. For the PC events, the entrance point can not be correctly determined by the through-going muon fit because they are generated inside the ID, and the goodness tends to be worse compared with the through-going muon events. On the other hand, the vertex position and the direction can be well estimated by the point fit for both the PC events and the cosmic ray muons. The selection criteria in the PC 4th reduction are as follows :

(1) $\vec{d}_{\rm pfit} \cdot \vec{d}_{\rm PMT}$ should be > -0.8
$\vec{d}_{\rm pfit}$ is the reconstructed direction by point fit, and $\vec{d}_{\rm PMT}$ is the direction from the reconstructed vertex to the earliest saturated PMT.

and

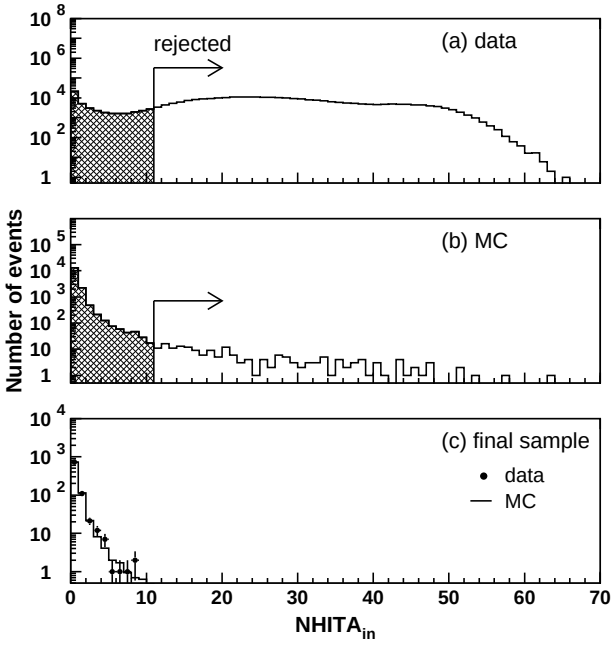

Figure 4.22: NHITA$_{in}$ distributions for (a) the data and (b) atmospheric neutrino Monte Carlo events after the PC 2nd reduction and (c) final samples. The number of the Monte Carlo events in (c) is normalized to that of the data. The selection criteria are shown by arrows.

(2) DCORN should be $> 150\,\mathrm{cm}$
DCORN is the distance from the reconstructed vertex by the point fit to the nearest fringe of the ID.

and

(3) TLMU should be $> 30\,\mathrm{m}$ if goodness of through-going muon fit > 0.85
TLMU is the track length of a muon estimated from the entrance and the exit points.

The first cut eliminate cosmic ray stopping muons which are likely to have $\vec{d}_{\mathrm{pfit}}$ and $\vec{d}_{\mathrm{PMT}}$ in opposite direction. The second cut aims to reject corner clipping muons. The distribution of the $\vec{d}_{\mathrm{pfit}} \cdot \vec{d}_{\mathrm{PMT}}$ and the DCORN are shown in Figure 4.23 and Figure 4.24, respectively. Through-going muons which have long track length are rejected by the third cut. Figure 4.25 shows the scatter plots of the TLMU and the goodness of the through-going muon fit for the data and atmospheric neutrino Monte Carlo events after the PC 3rd reduction, and final samples. The events in the upper-right box region are rejected as through-going muons.

The event rate after the PC 4th reduction is 20 events/day.

4.3.5 Fifth Reduction

The aim of the 5th reduction stage is the final rejection of the remaining background events for the PC sample. This is done by some elaborate criteria specialized for each background source. The event rate after the PC 5th reduction is 0.8 events/day.

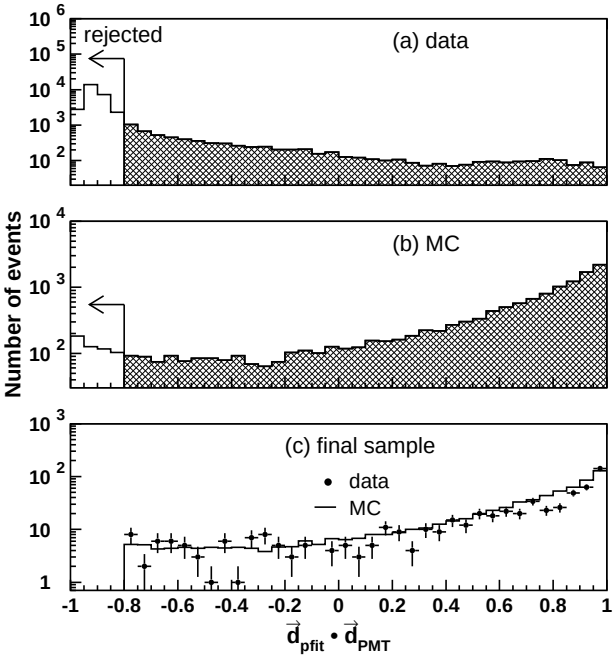

Figure 4.23: $\vec{d}_{\rm pfit} \cdot \vec{d}_{\rm PMT}$ distributions for (a) the data and (b) partially contained atmospheric neutrino Monte Carlo events after the PC 3rd reduction and (c) final samples. The number of the Monte Carlo events in (c) is normalized to that of the data. The selection criteria are shown by arrows.

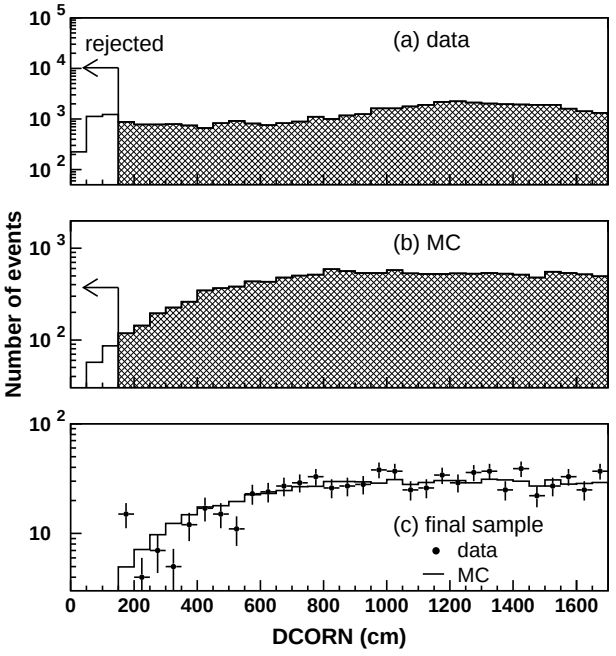

Figure 4.24: DCORN distributions for for (a) the data and (b) partially contained atmospheric neutrino Monte Carlo events after the PC 3rd reduction and (c) final samples. The number of the Monte Carlo events in (c) is normalized to that of the data. The selection criteria are shown by arrows.

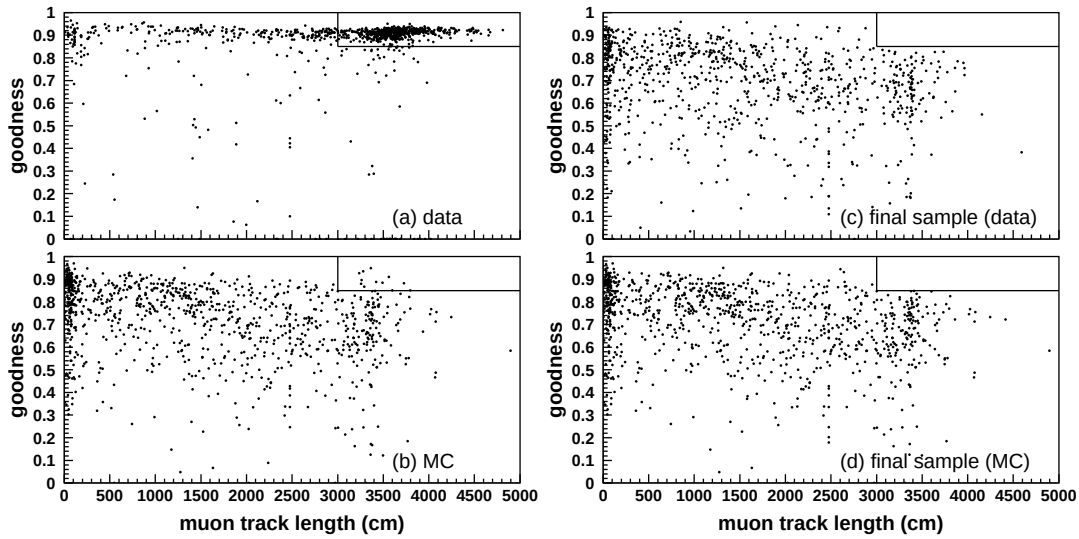

Figure 4.25: Scatter plots of muon track length and goodness of through-going muon fit for (a) the data and (b) partially contained atmospheric neutrino Monte Carlo events after the PC 3rd reduction, and (c) final samples of the data and (d) the Monte Carlo. The events in the upper-right box region are rejected as through-going muons.

Low energy event cut

Events satisfying the following criteria are removed as the remaining low energy background events :

(1) $\mathrm{PE_{tot}} < 3000$ p.e.
$\mathrm{PE_{tot}}$ is the total number of p.e.s observed in the ID.

The requirement of total photoelectrons > 3000 p.e., which corresponds to muon momentum of $500\,\mathrm{MeV}/c$, is safe for PC events because the exiting muons must have at least momentum of $700\,\mathrm{MeV}/c$ to reach the OD.

Through-going muon cut

The remaining through-going muons are removed by investigating the existence of two OD hit clusters and the existence of hit OD PMTs near the entrance and the exit points. The first cut uses the OD hit cluster information obtained by the algorithm in the PC 2nd reduction. Events satisfying the following criteria are removed as through-going muons :

(1) $\mathrm{DIST_{clust}} > 20\,\mathrm{m}$
$\mathrm{DIST_{clust}}$ is the distance between the highest charge OD hit cluster and the second highest one.

and

(2) $\mathrm{PEAC_{2nd}} \geq 10$ p.e.
$\mathrm{PEAC_{2nd}}$ is the number of p.e.s detected in the second highest charge OD hit cluster.

Through-going muons are also removed by the same clustering algorithm as that in the PC 2nd reduction with different parameters. The OD walls are divided into 6×6 patches using spherical coordinate centering on ring direction, which is estimated by the sum of the charge weighted vectors for all hit ID PMTs, while the division is 11×11 in the PC 2nd reduction. The aims of these change is not to mis-reconstruct one cluster into two clusters by the boundary effect of the patches. The charge threshold for each PMT is also changed to 0.5 p.e. from 2.0 p.e. to detect smaller signals than identified in the PC 2nd reduction. The cut criterion to reject through-going muons is the following :

(1) NCLSTA5 ≥ 2
NCLST5 is the number of OD hit clusters which contain more than 9 hit PMTs.

Figure 4.26 shows the NCLSTA5 distributions for the data and atmospheric neutrino Monte Carlo events after the PC 4th reduction, and final samples.

Cosmic ray muon sometimes enters from the edge on top, passes along the ID wall, and exits from the edge at the bottom. Such through-going muon events tend to pass through the former reduction stages because the light collection efficiency around the edge of the OD is inferior and the accuracy of the event reconstruction is relatively worse for those events. To reject the through-going muons which graze the ID wall, the number of hit OD PMTs and the observed p.e.s in 8 m radius spheres centered at the top and the bottom edges or fringes are counted. Events satisfying the following criteria are rejected as through-going muons :

(1) $\mathrm{NHITA_{top}} \geq 7$ and $\mathrm{NHITA_{bottom}} \geq 7$
$\mathrm{NHITA_{top}}$ ($\mathrm{NHITA_{bottom}}$) is the maximum number of hit OD PMTs in a 8 m radius sphere centered at the top (bottom) edge.

and

(2) $\mathrm{PEA_{top}} \geq 10$ p.e. and $\mathrm{PEA_{bottom}} \geq 10$ p.e.
$\mathrm{PEA_{top}}$ ($\mathrm{PEA_{bottom}}$) is the number of p.e.s detected in the same sphere as that for the $\mathrm{NHITA_{top}}$ ($\mathrm{NHITA_{bottom}}$)

and

(3) $0.75 < \mathrm{TDIFFA} \times c/40\,\mathrm{m} < 1.5$
TDIFFA is a time interval between the averaged hit timing in the top and the bottom spheres.

The scatter plots of the $\mathrm{PEA_{top}}$ and the $\mathrm{PEA_{bottom}}$ for the data and atmospheric neutrino Monte Carlo events are shown in Figure 4.27. The events in the upper-right region are the candidates of the through-going muons.

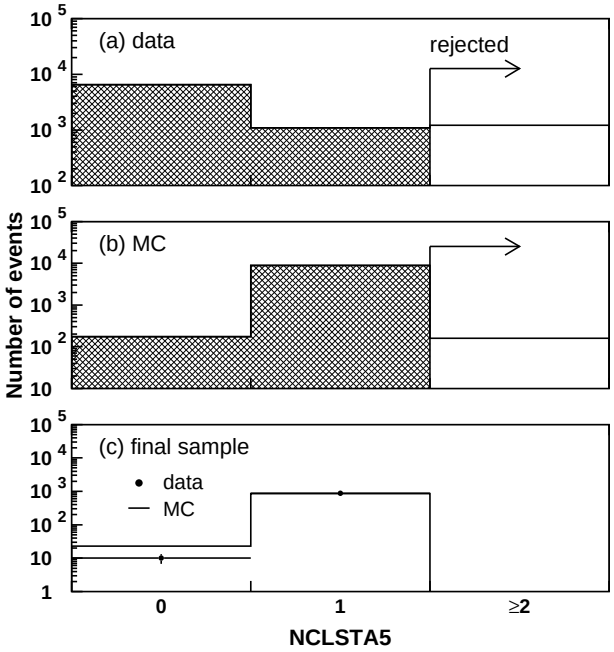

Figure 4.26: NCLSTA5 distributions for (a) the data and (b) partially contained atmospheric neutrino Monte Carlo events after the PC 4th reduction, and (c) final samples. The number of the Monte Carlo events in (c) is normalized to that of the data. The cut criteria are shown by arrows.

The remaining through-going muons are removed by the number of hit OD PMTs near the entrance and the exit points. The vertex position and the ring direction are reconstructed by a precise fit (MS-fit) using the Cherenkov ring pattern (see Section 5.5). The entrance and the exit points on the detector wall are estimated by an extrapolation. The cut criteria are as follows :

(1) $\mathrm{NHITA_{in}} \geq 5$ and $\mathrm{NHITA_{out}} \geq 5$
$\mathrm{NHITA_{in}}$ ($\mathrm{NHITA_{out}}$) is the number of hit OD PMTs within 8 m from the entrance (exit) point.

and

(3) $0.75 < \mathrm{TDIFFA} \times c/40\,\mathrm{m} < 1.5$
TDIFFA is a time interval between the averaged hit timing of the OD PMTs near the entrance and the exit points.

Stopping muon cut

Three types of stopping muon cuts are applied. In the first cut, the number of hit OD PMTs near the entrance position is counted. The entrance position of the stopping muons are estimated by reconstructing the vertex position and direction using MS-fit and back extrapolating to the wall. Events satisfying the following criteria are rejected as stopping muons :

(1) $\mathrm{NHITA_{in}} \geq 10$
$\mathrm{NHITA_{in}}$ is the number of OD hit PMTs within 8 m from the reconstructed entrance.

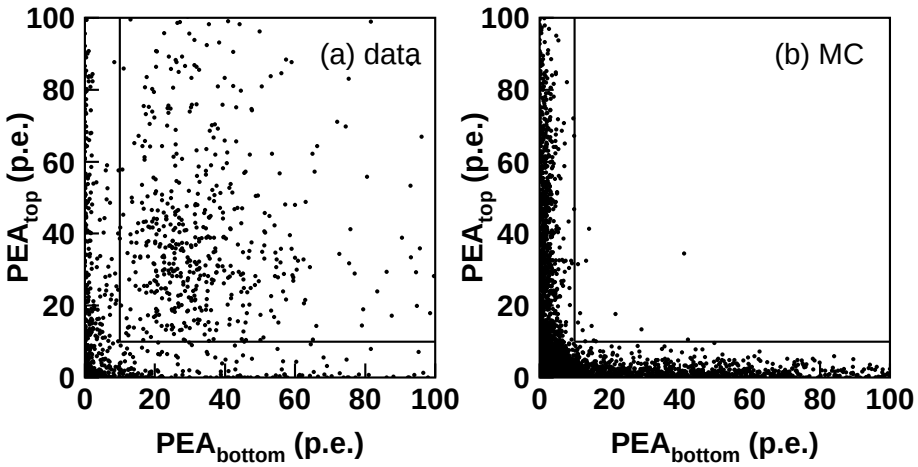

Figure 4.27: Scatter plots of PEA_{top} and PEA_{bottom} for for (a) the data and (b) partially contained atmospheric neutrino Monte Carlo events after the PC 4th reduction. The events in the upper-right region are the candidates of through-going muons.

The second stopping muon cut is done by comparing the direction to the OD hit cluster from the vertex and the direction of the ring. The vertex and the direction is estimated by two different fitters, TDC-fit using the hit timing information and MS-fit using the ring pattern. In case of the stopping muon event, the opening angle between the direction to the OD hit cluster and the ring direction is expected to be large, while it is expected to be small in case of the PC event. The cut criterion is the following :

(1) $\Theta_{\text{TDC-fit}} > 90^\circ$ or $\Theta_{\text{MS-fit}} > 90^\circ$

$\Theta_{\text{TDC-fit}}$ ($\Theta_{\text{MS-fit}}$) is the opening angle between the direction to the OD hit cluster and the ring direction reconstructed by TDC-fit (MS-fit).

Figure 4.28 shows the $\Theta_{\text{TDC-fit}}$ and the $\Theta_{\text{MS-fit}}$ distributions for the data and atmospheric neutrino Monte Carlo events after the PC 4th reduction, and final samples.

Stopping muons are further removed using the charge inside a 42° cone in the ID. The vertex and direction are determined by stopping muon fit, which estimate the entrance as the position of the earliest hit cluster in the ID. The entrance position can not be reconstructed correctly for the PC events since the vertex of the PC events are not on the wall. Events satisfying the following criteria are rejected as stopping muons :

(1) goodness of stopping muon fit > 0

and

(2) $PE_{cone}/PE_{tot} \geq 0.6$
PE_{cone} is the number of p.e.s observed by ID PMTs located inside a 42° cone.
PE_{tot} is the total number of p.e.s observed in the ID.

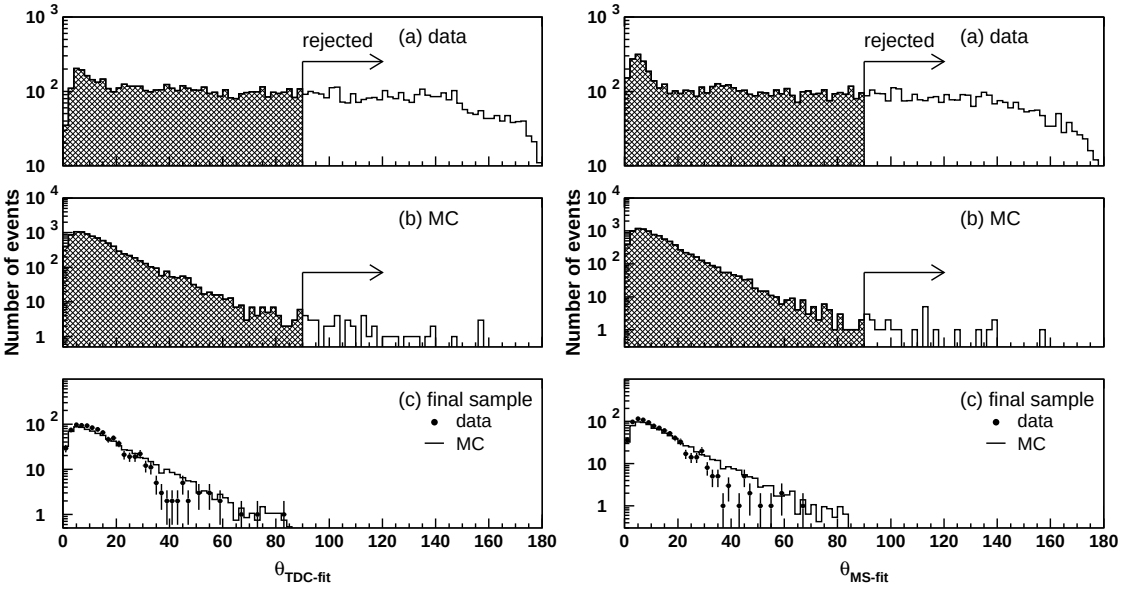

Figure 4.28: $\Theta_{\text{TDC-fit}}$ (left) and $\Theta_{\text{MS-fit}}$ (right) distributions for (a) the data and (b) partially contained atmospheric neutrino Monte Carlo events after the PC 4th reduction, and (c) final samples. The number of the Monte Carlo events in (c) is normalized to that of the data. The cut criteria are shown by arrows.

and

(3) $\text{NHITA}_{\text{in}} > 6$
NHITA_{in} is the number of hit OD PMTs within 8 m from the entrance position.

Figure 4.29 shows scatter plots of the NHITA_{in} and the $\text{PE}_{\text{cone}}/\text{PE}_{\text{tot}}$ for the data and partially contained atmospheric neutrino Monte Carlo events after the PC 4th reduction, and final samples of the data and the Monte Carlo events, satisfying the first condition goodness of stopping muon fit > 0.

Cable hole muon cut

Veto scintillation counters are placed over the four cable holes on top of the detector. Unlike the FC event selection, simple condition that only requiring veto counter hit is inapplicable for the PC event selection. Cut criteria for cable hole muons are as follows :

(1) One veto counter hit.

and

(2) $\vec{d}_{\text{ring}} \cdot \vec{d}_{\text{veto-vertex}} > -0.8$
$\vec{d}_{\text{ring}}$ is the reconstructed ring direction by TDC-fit, and $\vec{d}_{\text{veto-vertex}}$ is the direction from the hit veto counter to the reconstructed vertex.

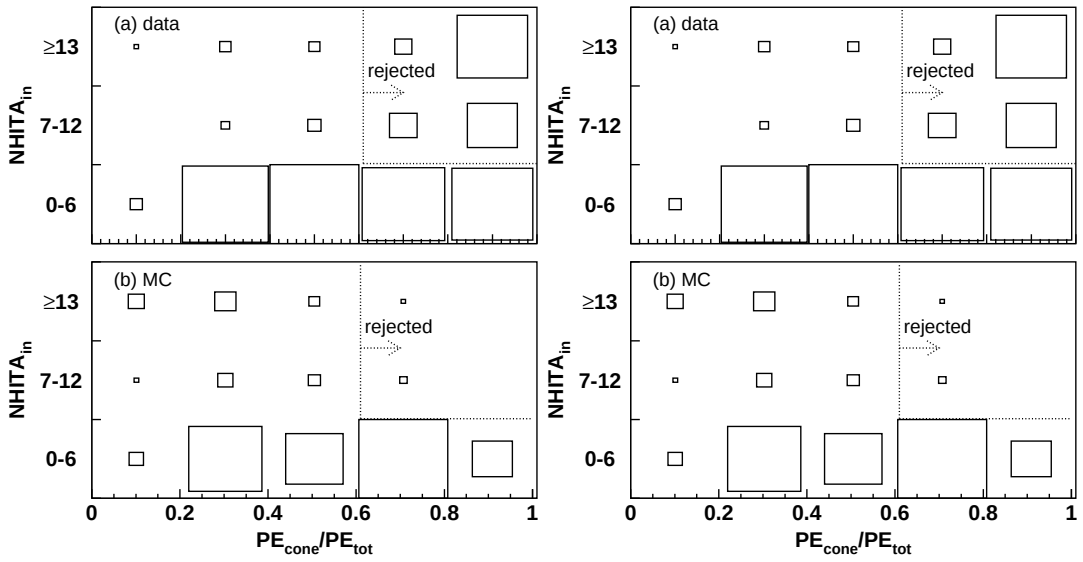

Figure 4.29: Scatter plots of $\mathrm{NHITA_{in}}$ and $\mathrm{PE_{cone}/PE_{tot}}$ for (a) the data and (b) partially contained atmospheric neutrino Monte Carlo events after the PC 4th reduction and (c) final samples of the data and (d) the Monte Carlo events. The size of the boxes shows the number of the events in each bin. The cut criteria are shown by the dashed lines and arrows.

4.3.6 Efficiency and Background for PC Sample

Detection efficiency of the atmospheric neutrino events through the PC reduction process is estimated by the partially contained atmospheric neutrino Monte Carlo events. The definition of the PC events is : (1) vertex of neutrino interaction should be inside the fiducial volume, (2) number of hit PMTs in the highest charge OD cluster (NHITAC) should be$\geq$ 10, and (3) total number of p.e.s in the ID should be > 3000 p.e.s . The detection efficiencies are estimated to be 99.0, 94.2, 93.2, 87.9 and 84.6 % after PC 1st, 2nd, 3rd, 4th and 5th reduction stage, respectively. The systematic uncertainty in the detection efficiency for PC sample is estimated by comparing the distribution of each cut variable of the data with that of the Monte Carlo events. The uncertainty is estimated to be 3.2 %.

The remaining background for PC sample is cosmic ray muons. After all reduction process, the remaining events are scanned by physicists and the contamination of background is estimated to be 0.2 % in the fiducial volume, 200 cm away from the ID wall.

4.4 Reduction for Upward-Going Muon Sample

The event rate of neutrino induced upward-going muons is predicted to be a few events/day in Super-Kamiokande, while that of the downward-going cosmic ray muons reaches 2×10^5 events/day. Since the upward-going muons are identical to the cosmic ray muons except for the direction, it is impossible to eliminate cosmic ray muon background completely. Therefore, the strategy of the reduction process is different from that of the FC and PC reduction. The automated reduction process for upward-going muon sample is first applied. Low energy background events and downward-going cosmic ray muons are rejected by the automated reduction

process. The remaining background after the automated process, mainly horizontally-going cosmic ray muons, are rejected one by one by physicists using a visual display. In spite of the careful reduction process, the contamination of cosmic ray muon background is unavoidable due to the multiple scattering of the muons and the resolution of the event reconstruction. The contamination of the background is estimated by an extrapolation from the zenith angle distributions of downward-going muons, then the estimated contaminations are subtracted from the final samples.

4.4.1 Automated Reduction for Upward-Going Muon Sample

Low energy cut

Since the energy range of upward-going muons used in analysis is restricted to the region above 1.6 GeV, low energy events from radioactive sources can be strongly rejected by a simple cut. Events satisfying the following cut are rejected :

(1) $PE_{tot} < 8000$ p.e.
PE_{tot} is the total number of p.e.s observed in the ID.

The 8000 p.e.s cut, which corresponds to muon momentum of 1 GeV/c, is safe for upward-going muons.

Ultra high energy cut

Since it is difficult to reconstruct the direction for extremely high energy event, in which almost all ID PMTs have hit signals, those events are rejected. Events satisfying the following cut are rejected :

(1) $PE_{tot} > 1750{,}000$ p.e.
PE_{tot} is the total number of p.e.s observed in the ID.

Zenith angle cut

In order to eliminate downward-going cosmic ray muons, seven different fitters specialized to fit stopping muons, through-going muons and Bremsstrahlung events are used. The logic of the zenith angle cut is as follows :

(1) Apply a muon fitter.

(2) If the event is classified as upward and the goodness of fit is above the threshold, the event is saved.

(3) If the event is classified as downward and the goodness of fit is above the threshold, the event is rejected.

(4) If the event is classified as horizontal and the goodness of fit is above the threshold, or if the goodness of fit is below the threshold, the judgment is suspended.

(5) Go to (1) and apply the next muon fitter.

This sequence continues until the event has passed through all the fitters or has been classified. If no fitter gives a goodness above the threshold, the event is rejected, while if at least one fitter classifies the event as horizontal, the event is saved. Detailed description about the seven muon fitters and the definition of the goodness can be found in Ref. [100].

4.4.2 Scanning

About half of the remaining candidate events are horizontal muons. In order to eliminate those background events, the data are scanned by physicists using a visual display and upward-going muon events are selected one by one. All events are checked by two independent scanners not to miss neutrino events. The possibility to miss a upward-going event is at most 1 % by a scanner. Therefore, the efficiency of scanning is estimated to be almost 100 %.

4.4.3 Efficiency and Background for Upward-Going Muon Sample

Detection efficiencies through the data reduction process are estimated by the upward-going muon Monte Carlo events to be 96.2% for upward stopping muons and 97.2% for upward through-going muons. These efficiencies are almost constant for the zenith angle except for the most horizontal bin ($-0.1 < \cos\Theta < 0$), in which more events are lost by the zenith angle cut due to the fitter resolution of the direction. The systematic uncertainty in the data reduction process for upward-going sample is estimated by comparing the distribution of each cut variable of the data with that of the Monte Carlo events. The estimated errors are 1.25 % for upward stopping muons and 0.54 % for upward through-going muons.

The final samples of upward-going muons still contain cosmic ray muon background in the most horizontal bin ($-0.1 < \cos\Theta < 0$). Because of the resolution of the fitter resolution and multiple scattering of muons in the nearby rock, some of the down-going cosmic ray muons appear to be upward-going muons. The contamination of the cosmic ray muon background for the upward stopping muon sample is relatively larger than that for the upward through-going muon sample because of the larger scattering angles in rock due to the lower momentum of the muons and the lower angular resolution of the event reconstruction. Figure 4.30 shows the angular difference between the reconstructed muon direction and the true muon direction at the generated point in the neutrino interaction for upward stopping and through-going muon Monte Carlo events. The resolutions of the muon direction are 2.5° and 1.4° for upward stopping and through-going muons taking into account the scattering of the muons and the fitter performance. The event reconstruction algorithm is explained in Section 5.8.

The contaminations of the cosmic ray muon background events are estimated by an extrapolation from the zenith angle distributions of downward-going muons. The numbers of the background events are subtracted from the most horizontal zenith angle bin ($-0.1 < \cos\Theta < 0$) for upward stopping and through going samples. Figure 4.31 shows the scatter plots of the zenith angle and the azimuth angle of muon direction for the remaining data before the cut by scanning. Clusters of events are seen in the regions zenith angle $\cos\Theta > 0$ (downward) and azimuth angle at $\phi = 120°$, $\phi = 180°$ and $\phi = 270°$ because the thickness of the mountain rock which cover the detector is thin for those directions. In order to estimate the contamination of the background events for the thinner-mountain region, stopping and through-going muon samples are divided into two in azimuth angle of the directions. Figure 4.32 shows the azimuth angle distributions for stopping and through-going muons, in which region (2) shows

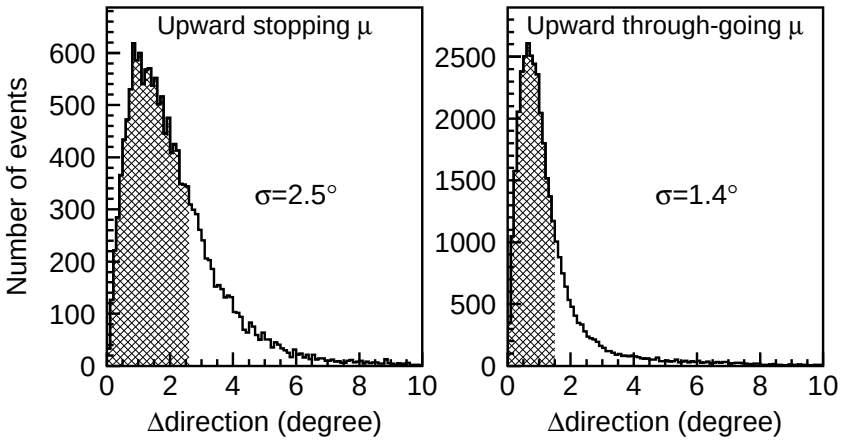

Figure 4.30: Angular difference between the reconstructed muon direction and the true muon direction generated in the neutrino interaction for upward stopping muon (left) and through-going muon Monte Carlo events (right). The resolution is defined as the width in which 68 % of the events are included

the thinner-mountain direction, which is defined as the region $60^\circ < \phi < 310^\circ$ for stopping muons and $60^\circ < \phi < 240^\circ$ for through-going muons, and the region (1), defined as the rest of region (2), shows the thicker-mountain direction.

Figure 4.33 shows the zenith angle distributions for stopping and through-going muon samples. Region (1) and (2) are normalized to the range of the azimuth angle. The zenith angle distributions are flat for upward-going muons ($\cos\Theta < 0$). While the number of events in the region (2) exponentially increase with the cosine of zenith angle for downward-going muons ($\cos\Theta > 0$). The contaminations of the cosmic ray muons into the upward-going direction are estimated by an extrapolation from the upward-going direction in the region (2) using (*exponential* + *constant*) function. The numbers of background events in the range of $-0.1 < \cos\Theta < 0$ are estimated to be 40.3 ± 13.7 for upward stopping muon and 14.4 ± 7.2 for upward through-going muon for 1645.9 days live-time, respectively. The errors represent the statistical uncertainties of the fitting.

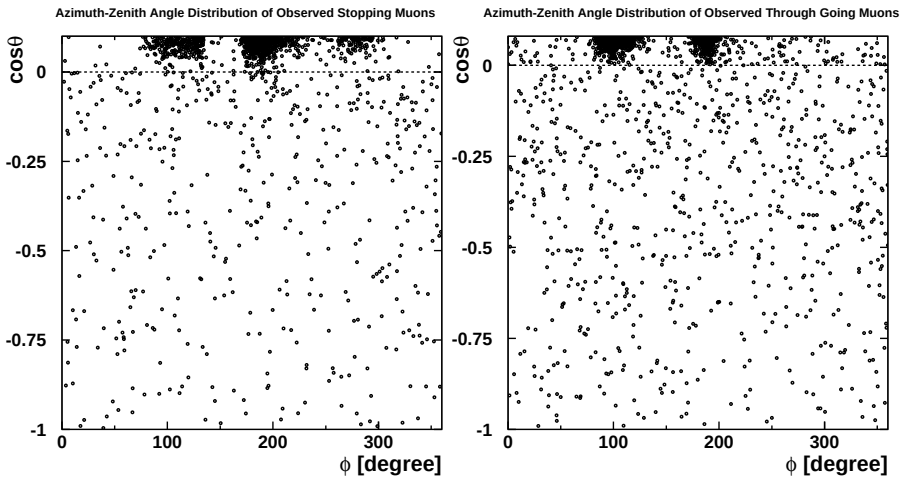

Figure 4.31: Scatter plots of the zenith angle and the azimuth angle of the muon directions for stopping (left) and through-going muon data (right). Vertical axis shows the cosine of zenith angle and horizontal axis shows the azimuth angle of the muon direction.

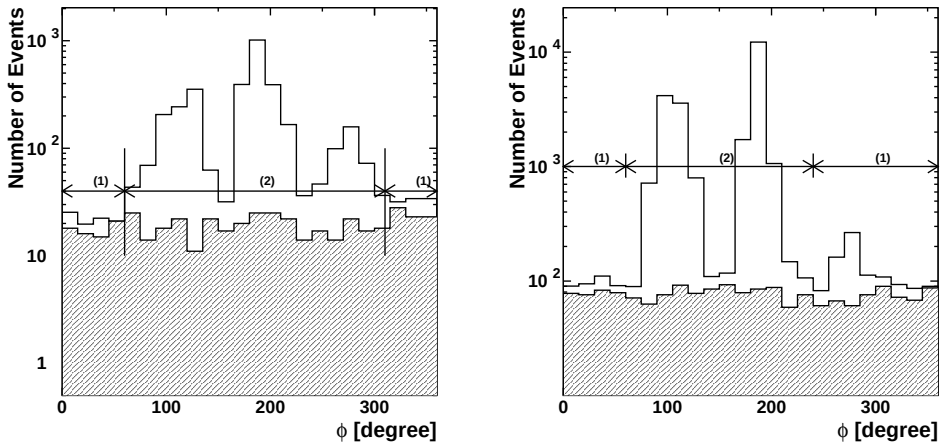

Figure 4.32: Azimuth angle distributions for stopping (left) and through-going muons (right). Region (2) shows the thinner-mountain direction and region (1) shows the thicker-mountain direction. White histograms show the distributions of downward-going muons ($0 < \cos\Theta < 0.1$) and the hatched histograms show the upward-going muons ($\cos\Theta < 0$). Peaks due to the contamination from cosmic ray muons are seen in region (2) for downward-going muons.

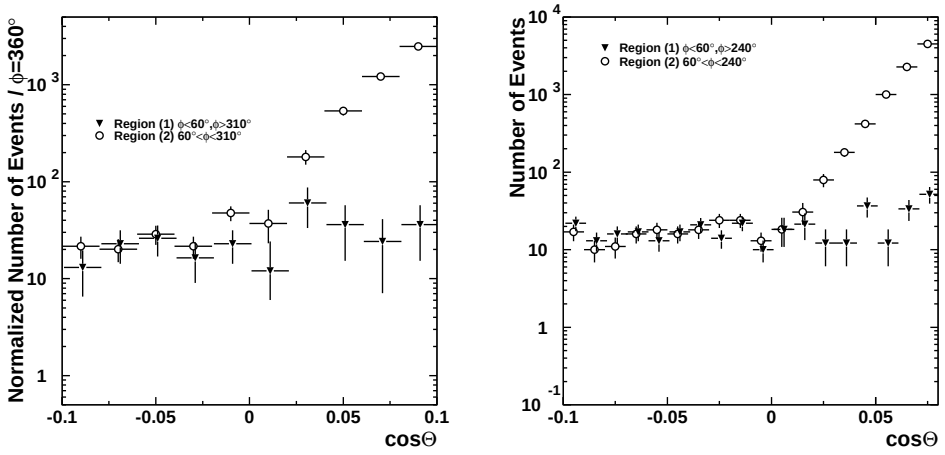

Figure 4.33: Zenith angle distributions for stopping muons (left) and through-going muons (right). Reverse triangles show those for region (1) (thicker-mountain direction) and open circles show those for region (2) (thinner-mountain region).

Chapter 5

Event Reconstruction

5.1 Overview

Event reconstruction process is applied to the atmospheric neutrino events which pass through the data reduction. The same programs are used for both the observed data and the atmospheric neutrino Monte Calro events. The event reconstruction process is fully automated. The detailed explanations of the procedures are described in this chapter.

The outline of the reconstruction process for FC and PC events is the following :

(1) Vertex Fitting

The vertex position is determined as the point at which the timing residual distribution of hit PMTs has the sharpest peak. The direction and the outer edge of the dominant ring is estimated, and the track length of the charged particle is taken into account in the calculation of the time residual.

(2) Ring Counting

With the knowledge of the vertex position and the direction of the dominant ring, the other possible rings are searched. The ring candidates are tested whether the ring is true or not by a likelihood method, and the number of rings is determined.

(3) Particle Identification

Each ring is classified into two types, a showering type ($e^{\pm}, \gamma$) and non-showering type ($\mu^{\pm}, \pi^{\pm}$), by the ring pattern and the opening angle. The showering type and non-showering type are commonly called e-like and μ-like, respectively.

(4) Precise Vertex Fitting (only for single-ring event)

The precise vertex position is obtained by the Cherenkov ring pattern assuming the particle type, a non-showering type or a showering type. This precise vertex fitter is called MS-fit.

(5) Momentum Determination

The momentum of each ring is determined from the charge detected inside a Cherenkov cone. The conversion from the charge to the momentum is determined based on a Monte Calro simulation and the detector calibration.

(6) Ring Number Correction

Rings which have low momentum and overlapped with the other energetic rings are discarded as fitting mistakes.

5.2 Vertex Fitting

First, the vertex position is reconstructed using timing information of hit PMTs. The vertex fitting algorithm consists of three steps.

5.2.1 Point-Fit

Vertex position is roughly estimated in the first step assuming all of the photons are emitted at the same time from a point source. The photon time of flight is subtracted from the hit timing for each PMT. The vertex is estimated as the point where the timing residual distribution is peaked. This vertex reconstruction algorithm is called point-fit, and the goodness of the fit is defined as follows :

$$G_p = \frac{1}{N} \sum_i \exp\left(- \frac{(t_i - t_0)^2}{2\,(1.5 \times \sigma)^2} \right) \tag{5.1}$$

where N is the number of hit PMTs, t_i is the time residual of the i-th PMT, t_0 is the mean value of t_i, and σ is the PMT timing resolution taken to be 2.5 nsec. The numerical factor 1.5 is chosen to optimize the fitter performance. The fitter searches for the vertex point which gives the maximum value of G_p.

The particle direction is also roughly estimated by summing up the charge weighted vector over all PMTs :

$$\vec{d_0} = \sum_i q_i \times \frac{\vec{P_i} - \vec{O_0}}{|\vec{P_i} - \vec{O_0}|} \tag{5.2}$$

where $\vec{d_0}$ is the particle direction, $\vec{O_0}$ is the vertex position obtained by point fit, $\vec{P_i}$ is the position and q_i is the detected charge of the i-th PMT. The vertex position and the particle direction estimated by point fit are used in the next step.

5.2.2 Ring Edge Search

The direction and the outer edge of the dominant ring is measured in this step. To determine the direction of the ring, the estimator $Q(\theta_{\rm edge})$ is defined as follows :

$$Q(\theta_{\rm edge}) = \frac{\displaystyle\int_0^{\theta_{\rm edge}} {\rm PE}(\theta) d\theta}{\sin\theta_{\rm edge}} \times \left(\left. \frac{d{\rm PE}(\theta)}{d\theta} \right|_{\theta=\theta_{\rm edge}} \right)^2 \times \exp\left(- \frac{(\theta_{\rm edge} - \theta_{\rm exp})^2}{2\sigma_\theta^2} \right) \tag{5.3}$$

where $\theta_{\rm exp}$ and σ_θ are the Cherenkov opening angle expected from the charge within the cone and its resolution, respectively. ${\rm PE}(\theta)$ is the angular distribution of the observed charge as a function of the opening angle θ from the particle direction. The observed charge is corrected for the effect from a water transparency and a PMT acceptance. The ring edge position $\theta_{\rm edge}$ is determined to satisfy the following two conditions :

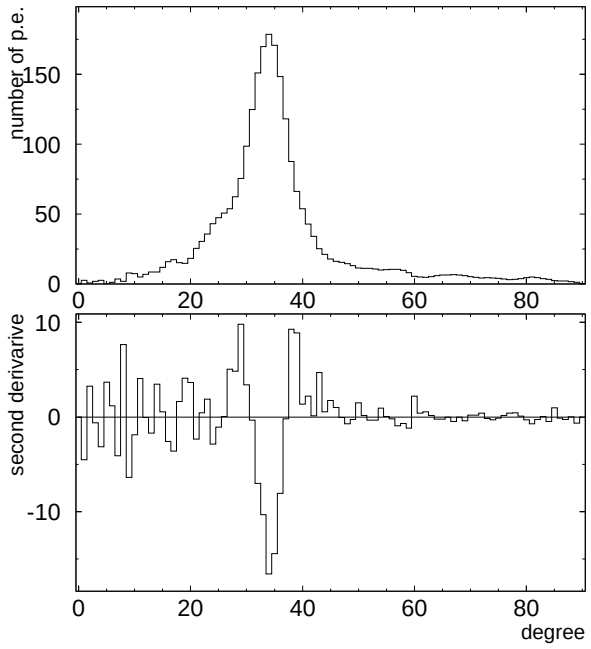

Figure 5.1: (i) The typical PE(θ) distribution and (ii) its second derivative.

(1) $\theta_{\rm edge} > \theta_{\rm peak}$

(2) $\left.\dfrac{d^2{\rm PE}(\theta)}{d^2\theta}\right|_{\theta_{\rm edge}} = 0$

where $\theta_{\rm peak}$ is the opening angle by which PE(θ) takes maximum. PE(θ) distribution and the second derivative of PE(θ) for a typical event are shown in Figure 5.1.

The estimator $Q(\theta_{\rm edge})$ is calculated changing the ring direction around $\vec{d_o}$ which is estimated by point fit. The direction of the ring is selected to maximize the estimator $Q(\theta_{\rm edge})$, and the ring edge position is simultaneously deterimined.

5.2.3 TDC-Fit

The vertex position is more precisely estimated in this step by TDC-fit. Unlike point-fit which assume a point light source, the track length of the charged particle and the scattered Cherenkov photons are taken into account in the TDC-fit.

The time residual of the i-th PMT is calculated by :

$$t_i = \begin{cases} t_i^0 - \dfrac{1}{c} \times |\vec{X}_i - \vec{O}| - \dfrac{n}{c} \times |\vec{P}_i - \vec{X}_i| & \text{for PMTs inside the Cherenkov ring} \\ t_i^0 - \dfrac{n}{c} \times |\vec{P}_i - \vec{O}| & \text{for PMTs outside the Cherenkov ring} \end{cases} \tag{5.4}$$

where $\vec{O}$ is the vertex position, $\vec{X}_i$ is the position at which Cherenkov photons are emitted toward the i-th PMT, n is the refractive index of water, $\vec{P}_i$ is the position and t_i^0 is the hit timing of the i-th PMT, respectively.

The estimator of the TDC-fit consists of three parts which are calculated by the different way based on the position of the PMT. For the hit PMTs inside the Cherenkov ring, the fitting estimator G_I is defined by :

$$G_I = \sum_i \frac{1}{\sigma_i^2} \exp\left(-\frac{(t_i - t_0)^2}{2\,(1.5 \times \sigma)^2}\right) \tag{5.5}$$

where σ_i is the timing resolution of the i-th PMT depending on the detected p.e.s, σ is the timing resolution for the average p.e.s of all hit PMTs and t_i is the time residual of the i-th PMT calculated by Equation (5.4).

For the hit PMTs outside the Cherenkov ring, the definition of the estimator changes with the time residual. If the hit timing is later than t_0, where t_0 is the mean of the t_i, the contribution from the scattered photons are considered. The definitions of the estimator for hit PMTs outside the Cherenkov ring are as follows :

$$G_{O1} = \sum_i \frac{1}{\sigma_i^2}\left(\exp\left(-\frac{(t_i - t_0)^2}{2\,(1.5 \times \sigma)^2}\right) \times 2 - 1\right) \qquad (\text{ for } t_i \le t_0\ ) \tag{5.6}$$

$$G_{O2} = \sum_i \frac{1}{\sigma_i^2}\left(\max\left[\exp\left(-\frac{(t_i - t_0)^2}{2\,(1.5 \times \sigma)^2}\right)\ ,\ G_{\mathrm{scatt}}(t_i, t_0)\right] \times 2 - 1\right) \qquad (\text{ for } t_i > t_0\ ) \tag{5.7}$$

where

$$G_{\mathrm{scatt}}(t_i, t_0) = \frac{R_q}{1.5^2} \times \exp\left(-\frac{(t_i - t_0)^2}{2\,(1.5 \times \sigma)^2}\right) + \left(1 - \frac{R_q}{1.5^2}\right) \times \exp\left(-\frac{t_i - t_0}{60\mathrm{nsec}}\right) \tag{5.8}$$

R_q is the fraction of the charge detected inside the Cherenkov ring. The numerical factors in the equations are choozen to optimize the fitter performance.

Then total estimator of TDC fit is obtained by :

$$G_T = \frac{G_I + (G_{O1} \text{ or } G_{O2})}{\sum_i \frac{1}{{\sigma_i}^2}} \tag{5.9}$$

The vertex position and the ring direction are determined to maximize the G_T.

The resolutions of the TDC-fit are estimated to be 57 cm and 60 cm for FC single-ring Sub-GeV e-like and μ-like events, 103 cm and 76 cm for FC single-ring Multi-GeV e-like and μ-like events, 67 cm for FC multi-ring μ-like events and 83 cm for PC events, respectively. For single-ring events, the vertex positions are more precisely estimated later by MS-fit using the ring pattern.

5.3 Ring Counting

Several energetic particles are sometimes generated from an atmospheric neutrino interaction, which make more than one Cherenkov rings in the detector. The number of the Cherenkov rings and the direction of each ring are determined by a ring counting algorithm described in this section. The algorithm consists of two steps. First, the possible ring candidates are selected, then the candidates are checked whether the ring is true or not by a likelihood method.

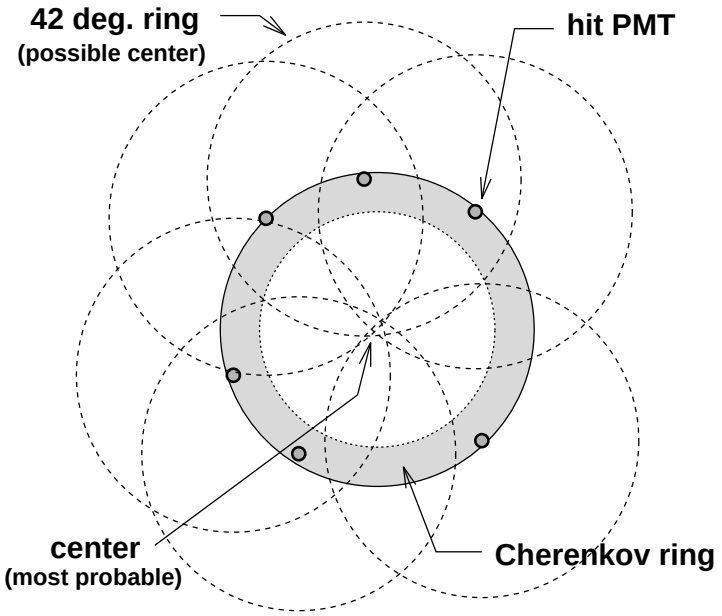

Figure 5.2: A basic concept to find ring candidates. The most intersecting point is recognized as the direction of a Cherenkov ring.

5.3.1 Ring Candidate Search

The ring candidates are searched by a pattern recognition method called Hough transformation after subtracting the expected charge from other established rings for each PMT [102]. Figure 5.2 illustrates the basic concept to find other possible rings, in which a spherical coordinate centered on the vertex position is considered. The shaded circle in this figure represents the Cherenkov ring image projected to a plane perpendicular to the ring direction. Hit PMTs are picked up and vertual circles (dashed line) centered on the position of the hit PMT are drawn with 42 ° half angle. As a result of this procedure, the direction of a Cherenkov ring is identified as a intersection point of these rings. In practice, instead of drawing virtual circles, expected charge distribution function $f(\theta)$ with the weight of the observed charge is mapped on a (Θ, Φ) plane for each hit PMT. As a result of this Hough transformation method, ring center candidates are visible as the peaks of charge on the map. A typical charge map is shown in Figure 5.3. The position of the two peaks correspond to the directions of Cherenkov rings.

5.3.2 Ring Candidate Test

The ring candidates are tested by a likelihood method. Suppose N rings are already found in the event, the test of the $(N+1)$-th ring candidate is carried out by comparing the likelihood (L_N) for the assumption of N rings with the likelihood (L_{N+1}) for $N+1$ rings including the candidate ring. The likelihood function for the assumption of $N+1$ rings is defined as :

$$L_{N+1} = \sum_i \log \left(prob \left(q_i^{\rm obs} , \sum_{n=1}^{N+1} \alpha_n \cdot q_{i,n}^{\rm exp} \right) \right) \tag{5.10}$$

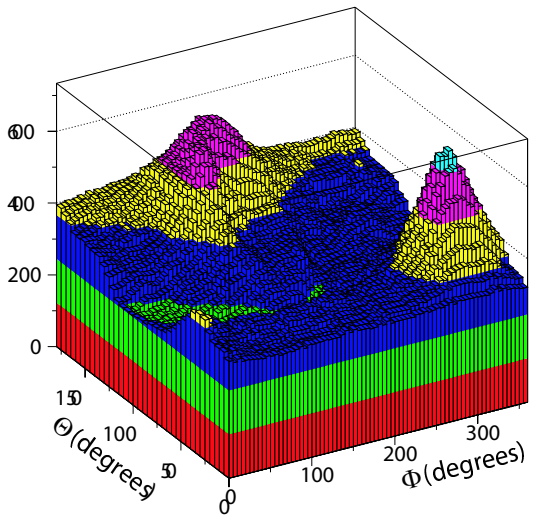

Figure 5.3: A typical charge map. Peaks correspond to the directions of Cherenkov rings from the vertex position.

where the summation is made over hit PMTs inside N+1 Cherenkov rings. $q_i^{\rm obs}$ is the observed p.e.s in the i-th PMT and $\alpha_n \cdot q_{i,n}^{\rm exp}$ is the expected p.e.s in the i-th PMT from the n-th ring. The L^{N+1} is maximized by changing the scale factors α_n (n=1 , $\cdots$, N+1) with a constraint of lower momentum limit. The probability function in Equation (5.10) is defined by :

$$prob\,(q_{\rm obs}\,,\,q_{\rm exp}) = \begin{cases} \dfrac{1}{\sqrt{2\pi}\,\sigma}\exp\left(-\dfrac{(q_{\rm obs}-q_{\rm exp})^2}{2\,\sigma^2}\right) & (\text{for } q_i^{\rm exp} > 20 \text{ p.e.}) \\ \text{convolution of a single p.e. distribution} \\ \text{and a Poisson distribution} & (\text{for } q_i^{\rm exp} < 20 \text{ p.e.}) \end{cases} \tag{5.11}$$

where σ is the resolution for $q_{\rm exp}$.

If no candidate satisfies $L^{N+1} \geq L^N$, the number of rings is determined to be N and the ring counting procedure is finalized. For the ring candidates satisfying $L^{N+1} \geq L^N$, following four evaluation functions are calculated :

F_1 : The difference $L(N+1) - L(N)$ corrected for the total p.e.s. When the difference is large, the candidate is probable.

F_2 : The average of the expected p.e.s around the edge of the (N+1)-th ring, in which PMTs overlapped with other N rings are not considered. When the average p.e.s ($Q_{\rm edge}$) is large, the candidate is probable.

F_3 : The average of the expected p.e.s ($Q_{\rm out}$) over the PMTs located outside the (N+1)-th ring and off the other N rings. When the difference $Q_{\rm edge} - Q_{\rm out}$ is large, the candidate is probable.

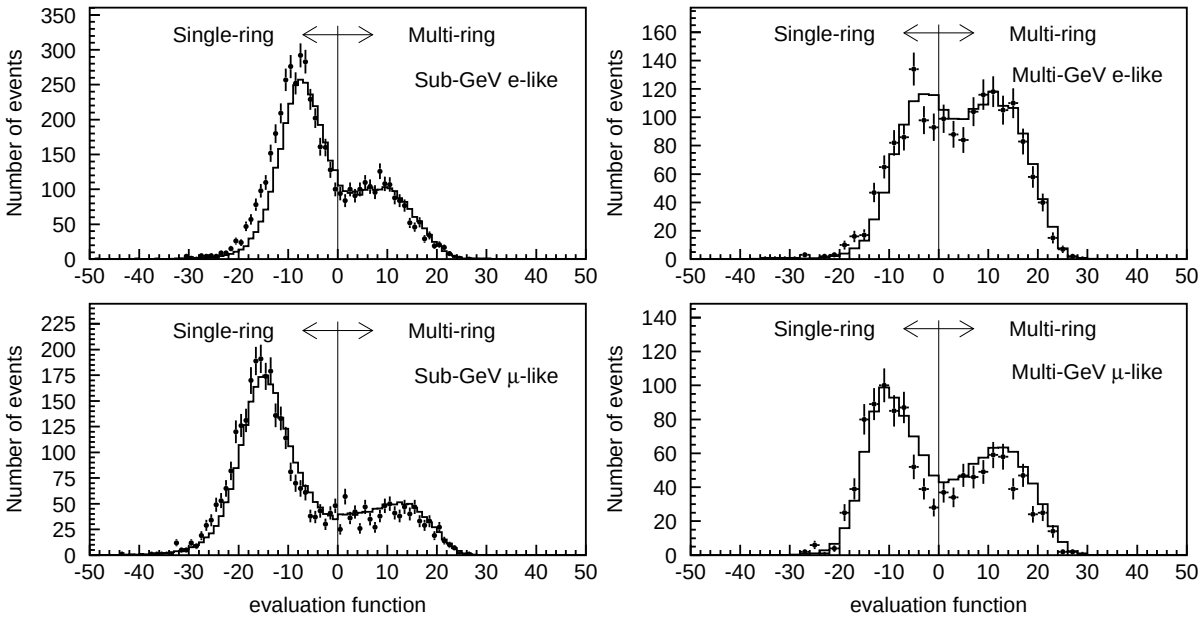

Figure 5.4: Evaluation function distributions for the most probable ring candidates in FC Sub-GeV e-like and μ-like events (left), and Multi-GeV e-like and μ-like events (right). The points show the observed data and the histgrams show the atmospheric neutrino Monte Calro events assuming 2-flavor $\nu_\mu \leftrightarrow \nu_\tau$ oscillation with $(\sin^2 2\theta,\ \Delta m^2) = (1.00,\ 2.0 \times 10^{-3}\,\mathrm{eV}^2)$. Ring candidates satisfying $F > 0$ are identified as the 2nd ring.

F_4 : The residual p.e.s from the expectation with N rings. The amount of the residual p.e.s is evaluated by summing up the charge weighted vector for all PMTs. When the absolute value of the vector sum is large, the candidate is probable.

The final evaluation function F for the candidate ring is made as the linear sum of F_1, F_2, F_3 and F_4 with optimized weights. The candidate which satisfies $F \geq 0$ is selected as $(N+1)$-th ring. If there is no candidate which satisfies $F \geq 0$, the number of rings is finally determined to be N. If a ring candidate satisfies $F \geq 0$, it is identified as the $(N+1)$-th ring and the ring search program starts the same calculation for the $(N+2)$-th ring. Figure 5.4 shows the distributions of the evaluation function F for the 2nd ring candidates for both observed data and the atmospheric neutrino Monte Calro events, in which 2-flavor $\nu_\mu \leftrightarrow \nu_\tau$ oscillation is assumed with $(\sin^2 2\theta,\ \Delta m^2) = (1.00,\ 2.0 \times 10^{-3}\,\mathrm{eV}^2)$.

The systematic uncertainties of the ring counting, which are related to the uncertainties of a water transparency or the tracking of hadrons in water, are estimated by comparing the evaluation function distributions for the observed data with that for the Monte Calro events. The estimated uncertainties of the single-ring/multi-ring separations are 5.4 % and 2.0 % for e-like and μ-like events with momentum of the 1st ring less than 400 MeV/c, 3.1 % and 1.2 % with greater than 400 MeV/c in Sub-GeV samples, and 13.4 % and 5.2 % for Multi-GeV samples, respectively.

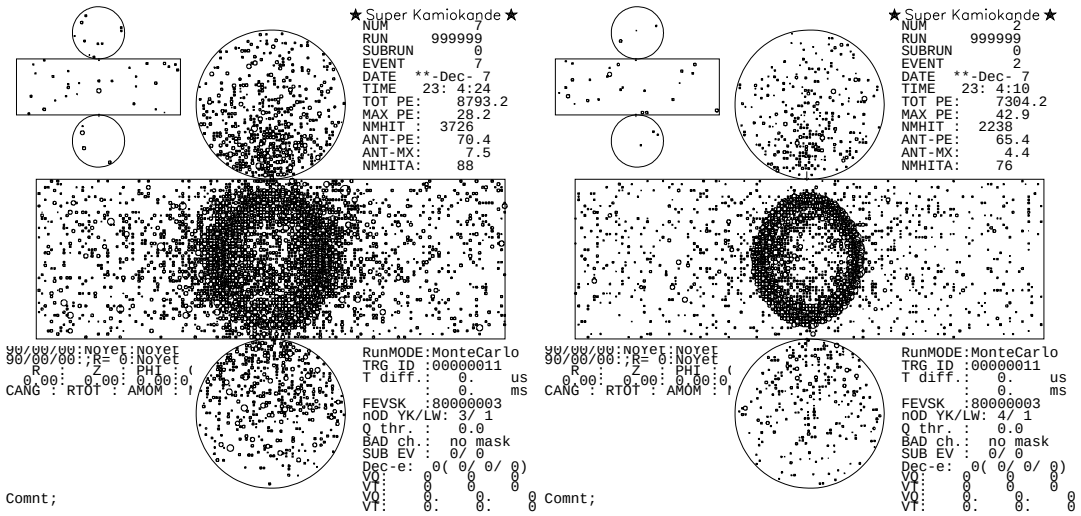

Figure 5.5: Visual display of typical electron (left) and muon (right) Monte Carlo events with momentum of 1 GeV/c. An electron make a diffused ring, while the ring from a muon has a sharp edge.

5.4 Particle Identification

The particle identification program classify the Cherenkov rings into two types according to the ring pattern and the opening angle. An electron or a gamma ray make a diffused ring because of the electromagnetic shower and the multiple scattering. These diffused rings are identified as a showering type (e-like). On the other hand, Cherenkov ring from a muon or a charged pion has a sharp ring edge, and identified as a non-showering type (μ-like). Figure 5.5 shows the visual displays of typical electron (left) and muon (right) Monte Carlo events with momentum of 1 GeV/c. The observed charge distribution is compared with the expectation from an electron or a muon. One of two particle types which reproduces the observed charge distribution better is selected.

5.4.1 Expected Charge Distributions

The expected p.e.s in the i-th PMT from an electron is calculated as follows :

$$q_i^{\rm exp}(e) = \alpha_e \times Q^{\rm exp}(p_e, \theta_i) \times \left(\frac{R}{r_i}\right)^{1.5} \times \frac{1}{\exp(r_i/L)} \times f(\Theta_i) + q_i^{\rm scatt} \tag{5.12}$$

where

α_e : normalization factor

r_i : distance from the vertex to the i-th PMT

θ_i : opening angle between the i-th PMT direction and the ring direction

L : light attenuation length in water

$f(\Theta_i)$: correction for the PMT acceptance as a function of the photon incidence angle Θ_i

R : radius of the virtual sphere (16.9 m)

$Q^{\rm exp}(p_e, \theta_i)$: expected p.e. distribution from an electron as a function of the opening angle and the electron momentum

$q_i^{\rm scatt}$: expected p.e.s for the i-th PMT from scattered photons

The angular distribution of the expected p.e. $Q^{\rm exp}(p_e, \theta_i)$ is made beforehand by a Monte Carlo simulation. In practice, the table contains the expected number of p.e.s observed in a 50 cm-diameter circular area located on a inside surface of a 16.9 m-radius sphere. The distance dependence of the light intensity is taken into account by a factor $(R/l_i)^{1.5}$, in which a power index is determined by a Monte Carlo simulation. In addition to the direct photons, the expectation from scattered photons are also considered.

In the case of muon, the expected p.e.s in i-th PMT is analytically calculated as follows :

$$q_i^{\rm exp}(\mu) = \left(\alpha_\mu \times \frac{\sin^2\theta_{x_i}}{r_i \left(\sin\theta_{x_i} + r_i \cdot \frac{d\theta}{dx}\Big|_{x=x_i} \right)} + q_i^{\rm knock} \right) \times \frac{1}{\exp(r_i/L)} \times f(\Theta_i) + q_i^{\rm scatt} \qquad (5.13)$$

where

α_μ : normalization factor

x : track length of the muon

x_i : track length of the muon at which Cherenkov photons are emitted toward the i-th PMT

θ : Cherenkov opening angle of the muon traveling at x

θ_{x_i} : Cherenkov opening angle of the muon traveling at x_i

$q_i^{\rm knock}$: expected p.e.s. for the i-th PMT from knock-on electrons

In the equation, $\sin^2\theta$ comes from the Cherenkov angle dependence of the Cherenkov light intensity. The term $r(\sin\theta + r(d\theta/dx))$ comes from the area where Cherenkov photons are emitted to. The Cherenkov angle shows a decrease of $d\theta$ while a muon travels a distance of dx, and Cherenkov photons are emitted to the area of $2\pi r \sin\theta(dx\sin\theta + rd\theta)$ as shown in Figure 5.6. The contribution from knock-on electrons $q_i^{\rm knock}$ is estimated by a Monte Carlo simulation.

5.4.2 Estimation of the Particle Type

The definition of likelihood for the n-th ring is expressed by :

$$L_n(e \text{ or } \mu) = \prod_{\theta_i < (1.5\times\theta_c)} prob\left(q_i^{\rm obs} \ , \ q_{i,n}^{\rm exp}(e \text{ or } \mu) + \sum_{n' \neq n} q_{i,n'}^{\rm exp} \right) \qquad (5.14)$$

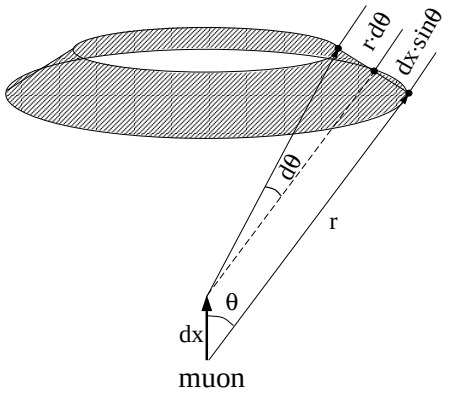

Figure 5.6: A schematic view of Cherenkov radiation from a muon. Cherenkov photons are emitted to the area of $2\pi r \sin\theta(dx \sin\theta + r d\theta)$ while a muon travels the distance of dx.

where the product is made over the PMTs inside the n-th ring. $q_i^{\rm obs}$ is the observed p.e.s in the i-th PMT, $q_{i,n}^{\rm exp}(e \text{ or } \mu)$ is the expected p.e.s from the n-th ring assuming an electron or a muon (Equation (5.12), (5.13)) and $q_{i,n'}^{\rm exp}$ is the expected p.e.s from the n'-th ring without any assumption of the particle type. The function *prob* gives the probability to detect $q_i^{\rm obs}$ in the i-th PMT when $q_i^{\rm exp}$ is expected (Equation (5.11)). The $q_{i,n}^{\rm exp}(e)$ and $q_{i,n}^{\rm exp}(\mu)$ is optimized by changing the direction and the opening angle of the n-th ring to give the maximum likelihood value.

In order to combine with another estimator which uses the Cherenkov opening angle, the likelihood for the ring pattern is translated into a χ^2 parameter :

$$\chi_n^2(e \text{ or } \mu) = -2 \log L_n(e \text{ or } \mu) + \text{constant} \tag{5.15}$$

The probability from the ring pattern is given by :

$$P_n^{\rm pattern}(e \text{ or } \mu) = \exp\left(- \frac{\left(\chi_n^2(e \text{ or } \mu) - \min\left[\chi_n^2(e)\,,\, \chi_n^2(\mu)\right] \right)^2}{2\,\sigma_{\chi_n^2}^2} \right) \tag{5.16}$$

The resolution of the χ^2 distribution is approximated by $\sigma_{\chi_n^2} = \sqrt{2N}$, where N is the number of PMTs used in the calculation.

The probability from the Cherenkov opening angle is given by :

$$P_n^{\rm angle}(e \text{ or } \mu) = \exp\left(- \frac{\left(\theta_n^{\rm obs} - \theta_n^{\rm exp}(e \text{ or } \mu) \right)^2}{2\,(\delta\theta_n)^2} \right) \tag{5.17}$$

where $\theta_n^{\rm obs}$ and $\delta\theta_n$ are the reconstructed opening angle of the n-th ring and the fitting error. $\theta_n^{\rm exp}(e \text{ or } \mu)$ is the expected opening angle of the n-th ring, which is estimated from the reconstructed momentum with assuming an electron or a muon.

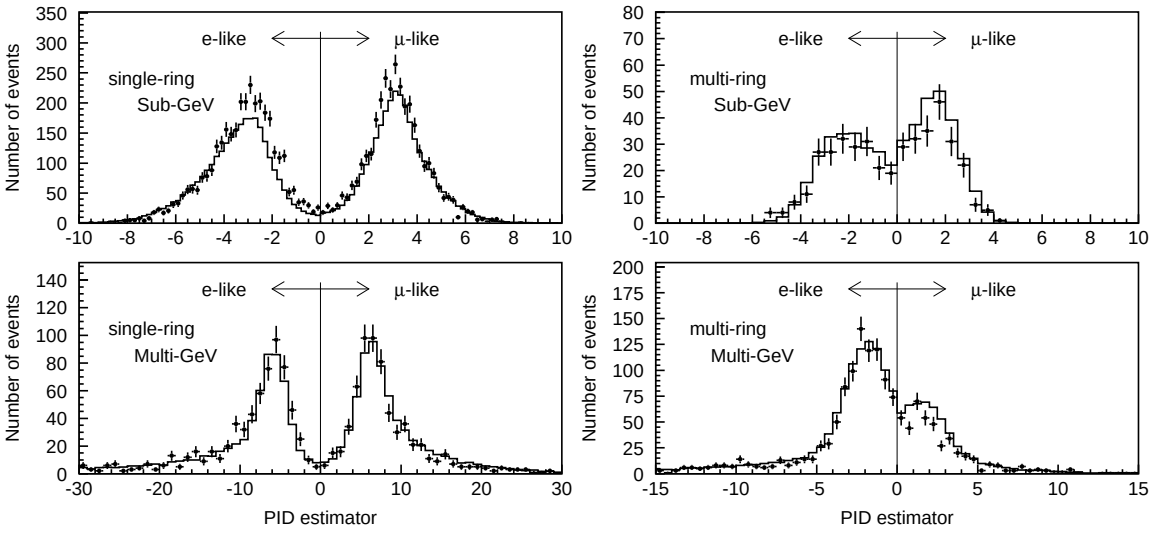

Figure 5.7: The distribution of the PID parameter, $P \equiv \sqrt{-\log P_n(\mu)} - \sqrt{-\log P_n(e)}$ for the FC single-ring events and multi-ring events. The points show the observed data and the histograms show the atmospheric neutrino Monte Calro events assuming 2-flavor $\nu_\mu \leftrightarrow \nu_\tau$ oscillation with $(\sin^2 2\theta,\ \Delta m^2) = (1.00,\ 2.0 \times 10^{-3}\,\mathrm{eV}^2)$. Rings satisfying $P < 0$ ($P \geq 0$) are identified as e-like (μ-like).

The definition of the probability used for the particle identification is different in single-ring event and multi-ring event. The definitions are as follows :

$$P_1(e \text{ or } \mu) = P_1^{\text{pattern}}(e \text{ or } \mu) \times P_1^{\text{angle}}(e \text{ or } \mu) \quad (\text{ for single-ring event }) \tag{5.18}$$

$$P_n(e \text{ or } \mu) = P_n^{\text{pattern}}(e \text{ or } \mu) \quad (\text{ for multi-ring event }) \tag{5.19}$$

For a single-ring event, the final probability is defined as the product of the probabilities from the ring pattern and the opening angle. On the other hand, only the probability from the ring pattern is used for a muli-ring event. This is because the estimation of the opening angle works relatively worse in case of a multi-ring event.

The distributions of the PID estimator $P \equiv \sqrt{-\log P_n(\mu)} - \sqrt{-\log P_n(e)}$ are shown in Figure 5.7 for single-ring events (left) and multi-ring events (right). The peaks in the μ-like region and the e-like region are clearly separated especially for single-ring events. The performance of the particle identification algorithm is examined using the atmospheric neutrino Monte Carlo events. The misidentifying probabilities are estimated to be 0.8 % and 0.7 % for ν_e and ν_μ quasi-elastic scattering events.

The systematic uncertainties of the particle identification are estimated as 0.5 % in Sub-GeV and 0.4 % in Multi-GeV both for e-like and μ-like events, and 5.4 % and 3.2 % fot Sub-GeV and Multi-GeV multi-ring μ-like events by comparing the PID estimator distributions for the observed data with that for the atmospheric neutrino Monte Calro events.

5.5 Precise Vertex Fitting

TDC-fit, vertex fitting algorithm using timing information (Section 5.2), gives a relatively worse vertex resolution in the longitudinal directions for single-ring events. This is because a vertex shift along the ring direction changes the TOFs evenly for all hit PMTs, and the estimator of the fitting doesn't change so much. To obtain more precise vertex position, the vertex position is estimated by MS-fit using the ring pattern for single-ring events. On the other hand, the result from TDC-fit is used for multi-ring events.

In the MS-fit, the observed charge distribution is compared with the expected charge distribution by a likelihood method changing the vertex position and the ring direction. The definition of the likelohood is the same as that is used in the particle identification algorithm, in which the particle type and the Cherenkov opening angle are determined. After the modification of the vertex position and the ring direction, the vertex position is further adjusted perpendicularly to the ring direction to give a miximum goodness which is defined in TDC-fit (Equation (5.9)). These processes are iterated until the changes in the vertex position and the ring direction become less than 5 cm and 0.5°, respectively.

The performance of the fitting algorithm, TDC-fit or MS-fit, is examined by applying it to the atmospheric neutrino Monte Carlo sample. Figure 5.8 shows the distance between the true vertex and the reconstructed vertex for FC single-ring events, FC multi-ring μ-like events and PC events. The vertex resolutions are estimated to be 27 cm and 24 cm for single-ring Sub-GeV e-like and μ-like events, 49 cm and 24 cm for single-ring Multi-GeV e-like and μ-like events, 67 cm for multi-ring μ-like events and 64 cm for PC events. Figure 5.9 shows the angular difference between the true electron or muon direction and the reconstructed direction for CC quasi-elastic scattering events in the atmospheric neutrino Monte Calro sample. The angular resolutions are estimated to be 3.4° and 1.9° for e-like events and μ-like events. The resolution is defined as the width where 68 % of the events are included.

5.6 Momentum Determination

The momentum of each particle is estimated by the observed p.e.s inside a cone with half opening angle of 70°. In order to determine the momentum for individual rings, the observed p.e.s in hit PMTs are separated to the contribution from each ring. The separation of the observed p.e.s is carried out based on the expected p.e. distribution from each ring as a function of the opening angle θ and uniform in azimuthal angle ϕ. The observed p.e.s in the i-th PMT from the n-th ring are estimated as :

$$q_{i,n}^{\rm obs} = q_i^{\rm obs} \times \frac{q_{i,n}^{\rm exp}}{\sum_{n'} q_{i,n'}^{\rm exp}} \tag{5.20}$$

where $q_{i,n}^{\rm obs}$ is the fractional p.e.s from the n-th ring in the i-th PMT, $q_i^{\rm obs}$ is the observed p.e.s in the i-th PMT and $q_{i,n}^{\rm exp}$ is the expected p.e.s .

To calculate the total number of p.e.s inside the 70° cone, the number of p.e.s in each PMT is corrected for the light attenuation in water and the acceptance of the PMT as follows :

$$RTOT_n = \frac{G_{\rm MC}}{G_{\rm data}} \left[\alpha \times \sum_{\substack{\theta_{i,n}<70^\circ \\ -50{\rm nsec}<t_i<250{\rm nsec}}} \left(q_{i,n}^{\rm obs} \times \exp\left(\frac{r_i}{L}\right) \times \frac{\cos\Theta_i}{f(\Theta_i)} \right) - \sum_{\theta_{i,n}<70^\circ} S_i \right] \tag{5.21}$$

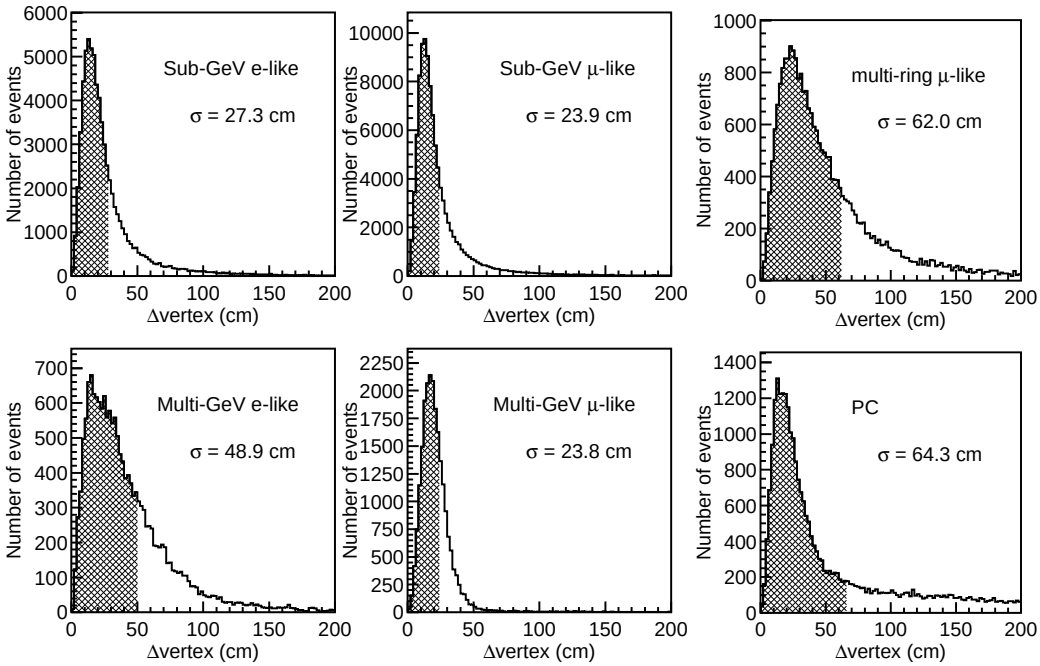

Figure 5.8: Distance between the true vertex and the reconstructed vertex for FC single-ring events, FC multi-ring μ-like events and PC events in the atmospheric neutrino Monte Calro sample.

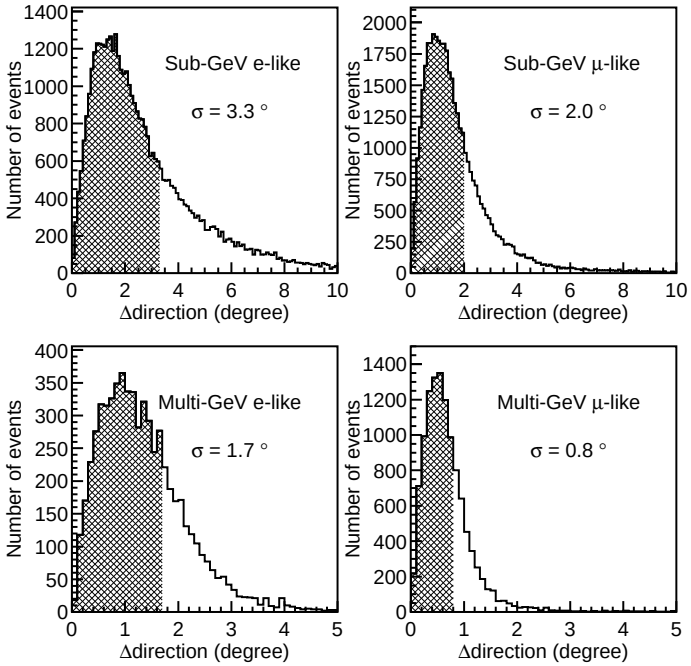

Figure 5.9: Angular difference between the true electron or muon direction and the reconstructed direction for CC quasi-elastic scattering events in the atmospheric neutrino Monte Calro sample.

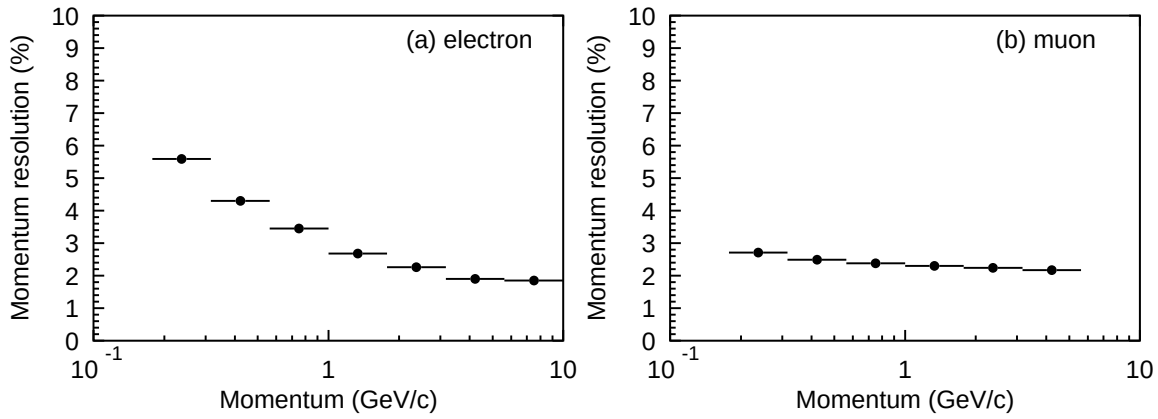

Figure 5.10: Momentum resolution for (a) electron and (b) muon estimated by the Monte Calro simulation as a function of the true momentum.

where

α	: normalization factor
$G_{\rm data}$, $G_{\rm MC}$	: relative PMT gain parameter for the data and the Monte Calro simulation
$\theta_{i,n}$	: opening angle between the n-th ring direction and the i-th PMT direction
t_i	: TOF subtracted hit timing of the i-th PMT position
L	: light attenuation length in water
r_i	: distance from the vertex position to the i-th PMT
$f(\Theta_i)$	: correction function for the PMT acceptance as a function of the photon incidence angle Θ_i
S_i	: expected p.e.s for the i-th PMT from scattered photons

The summation is restricted inside the time window from -50 nsec to +250 nsec around the peak of the TOF subtracted hit timing distribution to reject the effect from muon decay electrons. For the attenuation length in water L, the continuous measurement using cosmic ray through-going muons (Section 2.3.4) is used to correct the time variation for the observed data. Figure 5.10 shows the momentum resolution for electron and muon estimated from the Monte Calro simulation as a function of the true momentum. The resolution is defined as 1 σ width of the Gaussian fit. The absolute energy scale is calibrated using the four independent calibration sources as described in Section 2.3.5. The uncertainty of the energy scale is estimated to be less than 2 % for the momentum range from a few ten MeV/c to about 10 GeV/c.

5.7 Ring Number Correction

Finally, the number of rings is corrected in this stage. Miss fitted rings tend to have low momentum and overlapped with the other energetic rings. There are two cuts. The first rejection criteria are as follows :

(1-a) $E_A < E_B$
E_A and E_B are the visible energy of ring-A and ring-B, respectively.

and

(1-b) $\theta_{A-B} < 30^\circ$
θ_{A-B} is the opening angle between the directions of ring-A and ring-B.

and

(1-c) $E_A \cos\theta_{A-B} < 60\,\mathrm{MeV}$

The second criteria are the following :

(2-a) $E_A / \sum_i E_i < 0.05$

and

(2-b) $E_A < 40\,\mathrm{MeV}$

If one of two criteria is satisfied, the ring-A is discarded as a fitting mistake.

The performance of the ring counting algorithm and the effect of the ring correction are examined using quasi-elastic scattering events producing an electron or a muon in the atmospheric neutrino Monte Calro sample. Figure 5.11 shows the efficiency of single-ring identification as a function of the electron and the muon momentum, where efficiency is defined as (the number of quasi-elastic scattering events identified as a single-ring event)/(the number of quasi-elastic scattering events). The white circles in this figure show the efficiency before the ring correction and the black points show the final result. Since the high energy electron events make a diffused Cherenkov ring by the electromagnetic shower, the efficiency for such events is lower than that for the others.

5.8 Event Reconstruction for Upward-Going Muon Sample

Event reconstruction process for upward-going muons is different from that for FC and PC events. The outline of the event reconstruction process for upward-going muons is described in this section. The same program is used for both observed data and atmospheric neutrino Monte Carlo events which pass through the data reduction process. The event reconstruction process for upward-going muons is fully automated. The reconstructed directions by the automated process are used in analysis.

There are three fitters for upward-going muons : OD-fit, TDC-fit and Upmu-fit. The result of the most appropriate fitter is selected according to the track length, the total p.e.s in the ID, the angular difference between the directions reconstructed by two of three different fitters and the number of OD hit clusters. Upmu-fit is applied to determine the entrance and the direction.

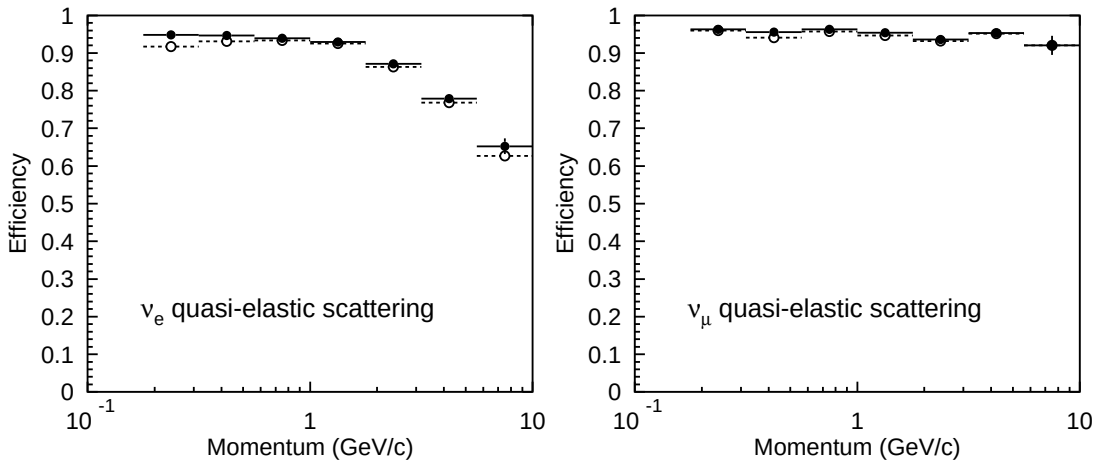

Figure 5.11: Efficiency identified as single-ring event for ν_e (left) and ν_μ (right) quasi-elastic scattering events in the atmospheric neutrino Monte Calro sample as a function of the electron and the muon momentum. White points show the efficiency before the ring number correction and black points show the final result.

If larger p.e.s are observed compared to the expectation from the track length of the muon due to bremsstrahlung, OD-fit or TDC-fit is selected. The detailed description about the determination of the fitter can be found in Ref. [101]. The explanation of OD-fit and Upmu-fit are described below, while the explanation of TDC-fit has already described in Section 5.2. Figure 5.12 shows the angular difference between the reconstructed muon direction and the true entering direction of the muon to the ID for upward stopping and through-going muon Monte Carlo events. The angular resolutions are estimated to be 1.1° for upward stopping muons and 1.0° for upward through-going muons.

5.8.1 OD-fit

OD-fit can be applied when there are more than two OD hit clusters. Through-going muons are expected to have two OD hit clusters, while stopping muons have only one OD hit cluster.

The direction of muon is determined using OD signals by OD-fit. The entrance point is determined as the position of OD hit cluster which has the earliest hit timing, and the exit point is determied as position of the highest charge OD hit cluster. The resolution of OD-fit is estimated to be 3.8°. OD-fit gives a better performance than the other fitters for the extremely high energy events which hit almost all PMTs in the ID and do not make clear Cherenkov ring.

5.8.2 Upmu-fit

Upmu-fit is a vertex and direction reconstruction algorithm which is based on MS-fit (Section 5.5) and optimized for upward-going muons. The modifications from MS-fit for upward-going muons are as follows :

(1) Event vertex is restricted to the surface of the ID wall.

(2) Particle type is fixed as muon.

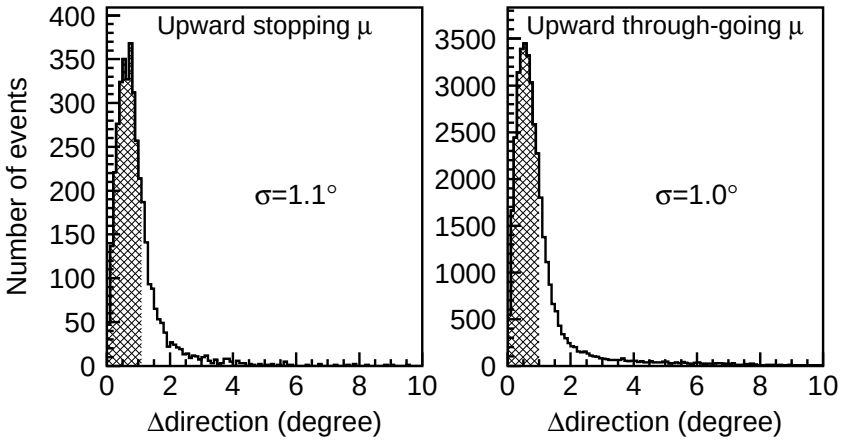

Figure 5.12: Angular difference between the reconstructed muon direction and the t rue entering direction of the muon to the ID for upward stopping muon (left) and through-going muon Monte Carlo events (right). The resolution is defined as the width in which 68 % of the events are included

(3) A function to evaluate the sharpness of the Cherenkov ring is added to the likelihood function.

The additional function is defined as follows :

$$R_{cone} = 1 - \frac{N_{hit}^{42}}{N_{all}^{42}} + \frac{N_{hit}^{70}}{N_{all}^{70}} \tag{5.22}$$

where N_{hit}^{42} and N_{all}^{42} are the number of hit PMTs and the number of PMTs inside a half opening angle of 42° cone, and N_{hit}^{70} and N_{all}^{70} are the number of hit PMTs and the number of PMTs between 42° and 70° cones. The second term in Equation (5.22) shows the fraction of hit PMTs inside the Cherenkov ring, and the third term shows the fraction of the hit PMTs outside the ring. When the direction of the muon is well reconstructed, $N_{hit}^{42}/N_{all}^{42}$ takes a larger value and $N_{hit}^{70}/N_{all}^{70}$ takes a smaller velue, therefore R_{cone} takes smaller value. The likelihood of the fit is translated into a χ^2 parameter by :

$$\chi^2 = (-2 \log L + constant)/R_{cone} \tag{5.23}$$

The vertex position and the direction of the muon are determined to minimize the χ^2.

Chapter 6

Data summary

1489.2 days exposure data for FC and PC, and 1645.9 days data for upward-going muons were accumulated in Super-Kamiokande during SK-I running period from April, 1996 till July, 2001. Although the observation period is the same, the live time of the upward-going muon events is larger than that of FC and PC events because the reconstruction of long path length muon is less sensitive to the detector condition. The observed data used in this thesis is summarized in this chapter together with the Monte Carlo prediction. The statistics of the Monte Carlo simulation are equivalent to the exposure of 100 years equivalent for all samples, that is FC, PC and upward-going muon events. In most cases, neutrino oscillations are not taken into account in the Monte Carlo events described in this chapter.

6.1 Event Summary

Final samples of FC and PC events are selected by requiring the following criteria after data reduction and event reconstruction processes :

- FC sample
  (1) Number of hit PMTs in the OD hit cluster (NHITAC) < 10
  (2) Distance from event vertex to the nearest ID wall (D_{wall}) $> 200\,\mathrm{cm}$
  (3) Visible energy assuming electrons (E_{vis}) $> 30\,\mathrm{MeV}$
  (4) $p_\mu > 200\,\mathrm{MeV}/c$ for single-ring μ-like events and $p_e > 100\,\mathrm{MeV}/c$ for single-ring e-like events
  (5) The most energetic ring is identified as μ-like and the momentum $p_\mu > 600\,\mathrm{MeV}/c$ and $E_{vis} > 600\,\mathrm{MeV}$ for multi-ring μ-like events
- PC sample
  (1) NHITAC ≥ 10
  (2) $D_{wall} > 200\,\mathrm{cm}$
  (3) $E_{vis} > 350\,\mathrm{MeV}$

FC and PC samples are separated by the number of hit PMTs in the OD hit cluster (NHITAC, see Chapter 4). The fiducial volume for the FC and PC samples defined by $D_{wall} > 200\,\mathrm{cm}$

corresponds to 22.5 kton and the exposure of the detector amounts to 91.7 kton·yr in the fiducial volume. The visible energy (E_{vis}) is defined as the sum of the energy of each ring assuming all rings are produced by electrons. The third criterion for the FC sample, $E_{vis} > 30$ MeV, is required to reject remaining low energy background events. For PC events, the requirement of $E_{vis} > 350$ MeV, which corresponds to muon momentum of 530 MeV/c, is safe for PC events because the exiting muons must have at least momentum of 700 MeV/c to reach the OD.

Final samples of upward stopping and through-going muons are selected by requiring the following criteria after data reduction and event reconstruction processes :

- Upward stopping muon sample

  (1) Number of hit OD PMTs within 8 m from the exit point (NHITEX) < 10

  (2) Fitted direction is upward (zenith angle $\cos\Theta \leq 0$)

  (3) $p_\mu \geq 1.6$ GeV/c (equivalent to track length of 7 m for muon)

- Upward through-going muon sample

  (1) NHITEX ≥ 10

  (2) Fitted direction is upward (zenith angle $\cos\Theta \leq 0$)

  (3) Distance from the entrance point to the exit point ≥ 7 m

Upward stopping and through going muon samples are separated by the number of hit OD PMTs near the exit point (NHITEX, see Chapter 4). The third criterion is required to keep the performance of the event reconstruction. The track length is determined by connecting the entrance and exit points for upward through-going muons. The momentum of upward stopping muon is determined from the observed charge by the same way as that for FC and PC events (see Section 5.6).

The event summary of the atmospheric neutrino data in the final samples is shown in Table 6.1 together with the Monte Carlo predictions. FC events are separated into two at the visible energy of 1330 MeV. The sample with $E_{vis} < 1330$ MeV is referred to "Sub-GeV", and the sample with $E_{vis} > 1330$ MeV is referred to "Multi-GeV". The PC sample is classified into Multi-GeV sample. The FC sample is classified into "single-ring" and "multi-ring" events according to the number of identified rings. The "single-ring" events are classified into "e-like" and "μ-like" events by the result of particle identification. For the "multi-ring" events, the particle type of the most energetic ring is used to classify the events and only "μ-like" events are used in neutrino oscillation analysis. Table 6.2 and 6.3 show the fraction of each neutrino interaction mode in the final samples of atmospheric neutrino Monte Carlo events. The fractions of CC ν_μ interactions in μ-like events are estimated to be 94.5 % for Sub-GeV single-ring, 90.5 % for Sub-GeV multi-ring, 99.4 % for Multi-GeV single-ring and 94.9 % for Multi-GeV multi-ring sample. The fraction for the other samples are 97.2 % for PC, 98.7 % for upward stopping muon and 99.8 % for upward through-going muon sample.

6.2 Vertex Distributions

Figure 6.1 shows the reconstructed vertex distributions for the FC and PC samples projected to Z and $R^2 = (X^2 + Y^2)$ axes. Points show the observed data and histograms show the

	Data	Monte Carlo	Data/MC
FC Sub-GeV			
single-ring	6580	7286.1	0.90
e-like	3353	2959.2	1.13
μ-like	3227	4327.0	0.75
multi-ring			
μ-like	208	331.2	0.63
FC multi-GeV			
single-ring	1397	1605.0	0.87
e-like	746	688.5	1.08
μ-like	651	916.5	0.71
multi-ring			
μ-like	439	723.2	0.61
PC	911	1143.8	
Upward-going muon			
stopping	417.7	721.4	0.58
through-going	1841.6	1684.4	1.09

Table 6.1: Summary of atmospheric neutrino events for 1489.2 days FC and PC samples and 1645.9 days upward stopping and through-going muon samples. Number of the Monte Carlo events are normalized by the live time of the data.

		Sub-GeV			Multi-GeV			PC
		1-ring e-like	1-ring μ-like	multi-ring μ-like	1-ring e-like	1-ring μ-like	multi-ring μ-like	
CC $\nu_e + \overline{\nu}_e$	Q.E.	69.4%	0.4%	0.8%	37.8%	0.1%	0.2%	0.3%
	single meson	14.4%	0.1%	1.6%	24.4%	0.1%	0.5%	0.4%
	multi π	2.4%	0.0%	1.2%	18.5%	0.2%	1.7%	1.2%
	coherent π	1.7%	0.0%	0.1%	2.1%	0.0%	0.0%	0.0%
	total	87.9%	0.5%	3.7%	82.8%	0.4%	2.4%	1.9%
CC $\nu_\mu + \overline{\nu}_\mu$	Q.E.	0.8%	73.4%	8.6%	0.9%	50.7%	4.1%	18.7%
	single meson	1.0%	16.6%	45.1%	1.1%	30.0%	30.5%	22.0%
	multi π	0.5%	2.5%	33.7%	4.8%	15.8%	58.7%	54.8%
	coherent π	0.1%	1.8%	3.1%	0.1%	2.9%	1.6%	1.7%
	total	2.4%	94.5%	90.5%	6.9%	99.4%	94.9%	97.2%
NC		9.7%	5.0%	5.8%	10.3%	0.2%	2.7%	0.9%

Table 6.2: Fraction of each neutrino interaction mode in FC and PC atmospheric neutrino Monte Carlo events.

		upward stopping μ	upward through-going μ
CC $\nu_e + \overline{\nu}_e$	Q.E.	0.1%	0.0%
	single meson	0.1%	0.0%
	multi π	0.7%	0.1%
	coherent π	0.0%	0.0%
	total	0.9%	0.1%
CC $\nu_\mu + \overline{\nu}_\mu$	Q.E.	13.9%	3.4%
	single meson	20.2%	6.6%
	multi π	64.3%	89.8%
	coherent π	0.3%	0.0%
	total	98.7%	99.8%
NC		0.4%	0.1%

Table 6.3: Fraction of each neutrino interaction mode in upward stopping and through-going muon Monte Carlo events.

atmospheric neutrino Monte Carlo events assuming no oscillation (dashed lines) and 2-flavor $\nu_\mu \leftrightarrow \nu_\tau$ oscillation with $(\sin^2 2\theta,\ \Delta m^2) = (1.00,\ 2.0 \times 10^{-3}\,\mathrm{eV}^2)$ (solid lines). The live time of the Monte Carlo events are normalized to that of the observed data. The vertex distributions of the data and the Monte Carlo events with neutrino oscillation agree well in fiducial volume, which are shown by arrows. Although there are excesses of the data at the top of the ID in Z distributions (the highest bin) for Multi-GeV single-ring μ-like and PC events due to cosmic ray muons, the contamination to the fiducial volume is not seen.

6.3 Number of Rings and Momentum Distributions

Figure 6.2 shows the distributions of the number of rings for the FC data and the atmospheric neutrino Monte Carlo events assuming no oscillation and 2-flavor $\nu_\mu \leftrightarrow \nu_\tau$ oscillation with $(\sin^2 2\theta,\ \Delta m^2) = (1.00,\ 2.0 \times 10^{-3}\,\mathrm{eV}^2)$, and Figure 6.3 shows the momentum distributions for FC single-ring e-like and μ-like events. The shape of the data and the Monte Carlo events with neutrino oscillation agree well, while the absolute number of events is smaller than the Monte Carlo events without oscillation.

6.4 Flavor Ratio

The result of particle identification indicates us the neutrino flavor as shown in Table 6.2, and the ratio of the number of e-like events and μ-like events gives a test of ν_μ/ν_e flux ratio in atmospheric neutrinos by comparing to that of the Monte Carlo events. The double ratio of the μ/e ratios is defined by :

$$R(\mu/e) \equiv (N_\mu/N_e)_{Data}/(N_\mu/N_e)_{MC} \tag{6.1}$$

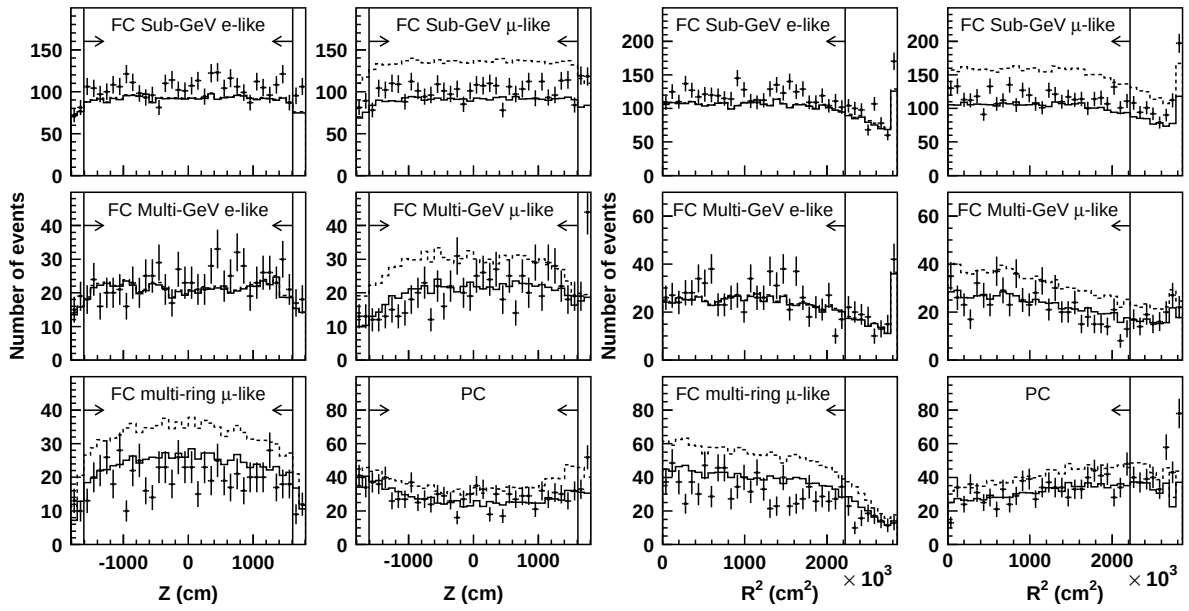

Figure 6.1: Vertex distributions for FC and PC events projected to Z axis (six figures on the left) and R^2 axis (six figures on the right). Events which have vertices 200 cm away from barrel (top and bottom) wall are plotted in left (right) figures. Points and the error bars show the data and the statistical errors. Histograms show the Monte Carlo events assuming no oscillation (dashed lines) and 2-flavor $\nu_\mu \leftrightarrow \nu_\tau$ oscillation with $(\sin^2 2\theta,\, \Delta m^2) = (1.00,\, 2.0 \times 10^{-3}\,\mathrm{eV}^2)$ (solid lines). The live time of the Monte Carlo sample is normalized to that of the data. Arrows show the fiducial volume.

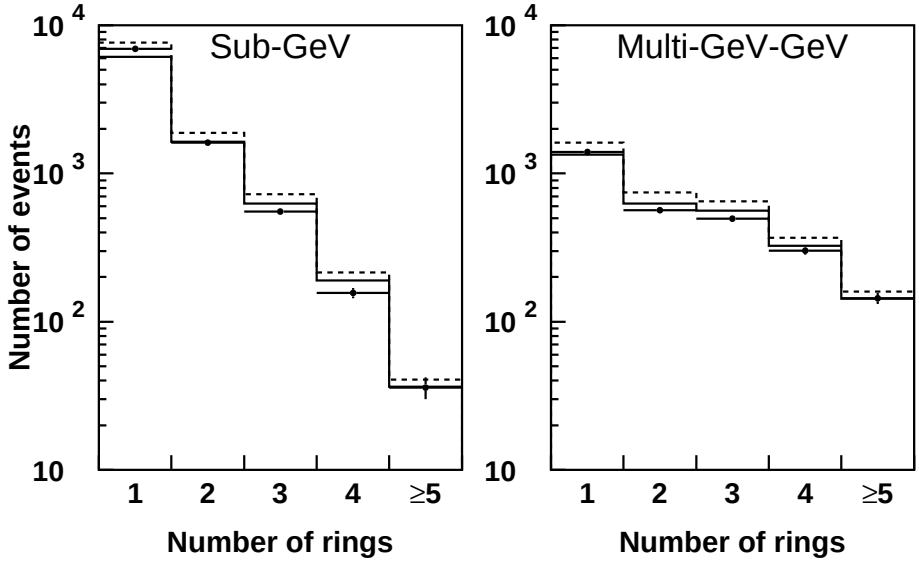

Figure 6.2: Number of rings distributions for the FC data (points) and the atmospheric neutrino Monte Carlo events assuming no oscillation (dashed lines) and 2-flavor $\nu_\mu \leftrightarrow \nu_\tau$ oscillation with $(\sin^2 2\theta,\, \Delta m^2) = (1.00,\, 2.0 \times 10^{-3}\,\mathrm{eV}^2)$ (solid lines).

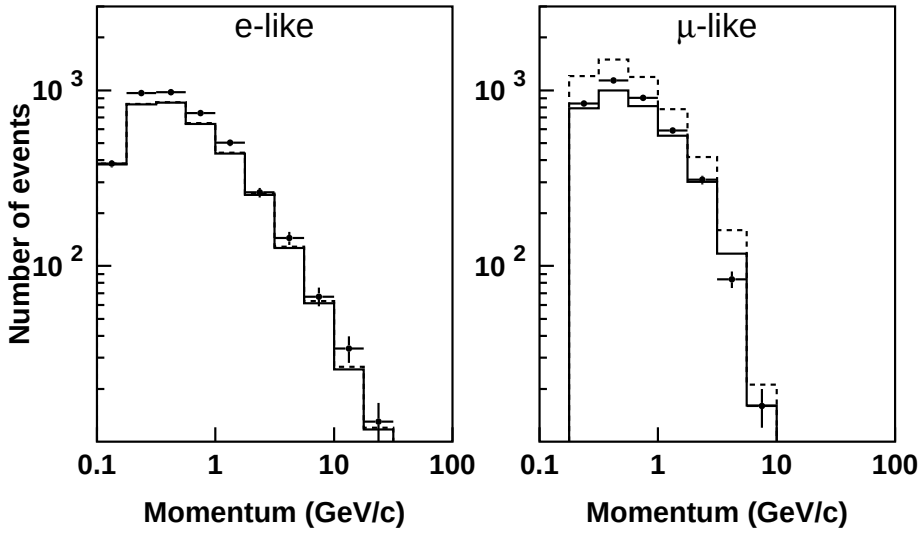

Figure 6.3: Momentum distributions for the FC single-ring events for the data (points) and the atmospheric neutrino Monte Carlo events assuming no oscillation (dashed lines) and 2-flavor $\nu_\mu \leftrightarrow \nu_\tau$ oscillation with $(\sin^2 2\theta,\ \Delta m^2) = (1.00,\ 2.0 \times 10^{-3}\,\mathrm{eV}^2)$ (solid lines).

where N_e and N_μ are the number of e-like and μ-like events, respectively. The double ratio should take a unity if the observed data agrees with the prediction.

The obtained double ratio for Sub-GeV and Multi-GeV samples are as follows :

$$R(\mu/e) = \begin{cases} 0.658\ ^{+0.016}_{-0.016}(stat) \pm 0.038(syst) & \text{(sub-GeV)} \\ \\ 0.700\ ^{+0.032}_{-0.030}(stat) \pm 0.085(syst) & \text{(multi-GeV)} \end{cases} \tag{6.2}$$

where PC events are included in the Multi-GeV μ-like sample. Systematic uncertainty in the double ratio R are estimated to be 5.8 % for Sub-GeV and 12.2 % for Multi-GeV events. The sources of the systematic uncertainties in R are listed in Table 6.4, which include both theoretical and experimental errors. The explanation about each source of the systematic errors is described in Section 7.2.

In Figure 6.4, the left-hand figures show the momentum distributions for FC single-ring e-like and μ-like events, and the N_μ/N_e ratio, and the right-hand figures show the ratio of the data to the Monte Carlo events and the double ratio R as a function of the momentum. The number of PC events is also shown for the comparison. Although the systematic error in absolute event rate is large (± 20 % from the prediction of the atmospheric neutrino flux and the cross section of neutrino interaction), there are deficits for FC μ-like and PC events and excesses for e-like events in all momentum regions. The double ratio R takes smaller value than unity in all momentum range. Figure 6.5 shows the visible energy distribution for FC multi-ring μ-like events and the ratio of the data to the Monte Carlo events. The number of the data for multi-ring μ-like events is also small compared to the Monte Carlo prediction.

	Sub-GeV(%)	Multi-GeV + PC(%)
Prediction of ν_μ/ν_e ratio	4.4	4.4
E_ν spectral index	0.8	0.8
ν interaction		
quasi-elastic scattering	0.5	0.8
single-meson productio	0.2	0.2
deep-inelastic scattering	0.2	1.4
coherent-pion production	0.4	0.2
NC/CC ration	1.0	2.0
Hadron simulation	0.5	1.0
FC reduction	<1.0	<1.0
PC reduction	0.0	1.4
Non-ν background	<0.5	<0.3
μ/e separation	1.0	0.8
Single-ring/multi-ring separation	2.9	10.6
Fiducial volume cut	0.6	1.4
Energy calibration	0.5	1.2
MC statistics	0.5	0.9
Total	5.8	12.2

Table 6.4: Sources of the systematic errors in double ratio R for the Sub-GeV and Multi-GeV+PC samples.

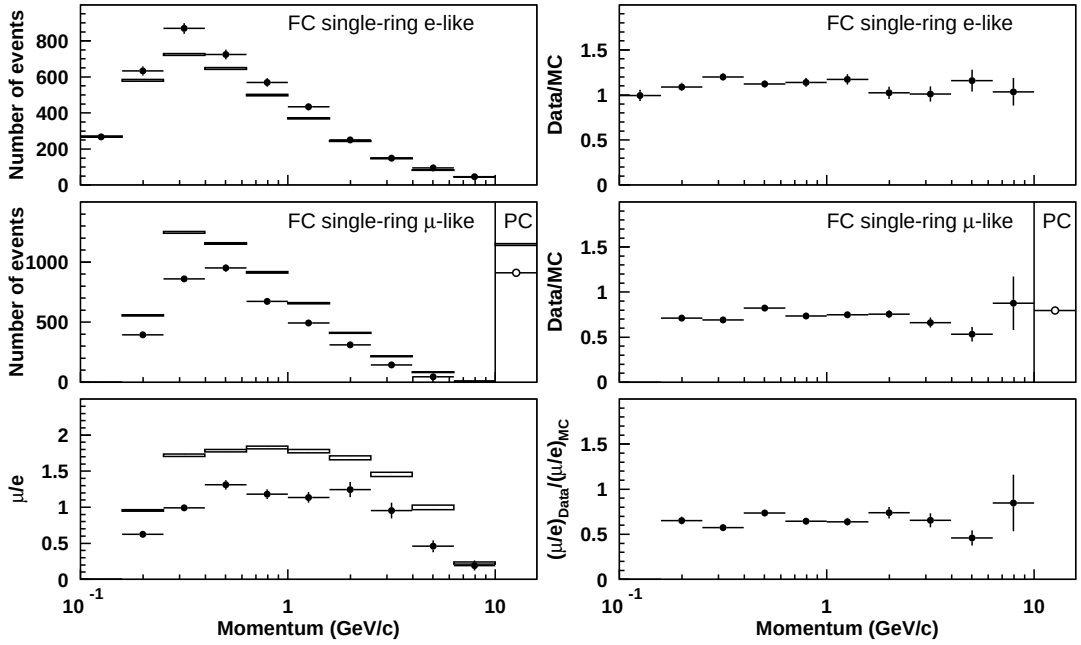

Figure 6.4: The left-hand figures show the momentum distributions for FC single-ring e-like (upper left) and μ-like events (center left), and the N_μ/N_e ratio (lower left), and the right-hand figures show the ratio of the data to Monte Carlo events (upper right and center right) and the double ratio R (lower right) as a function of the momentum, in which the live time of the Monte Carlo sample is normalized to that of the data. The number of PC events is also shown for the comparison. Points show the data and box histograms show the Monte Carlo events with their statistical errors.

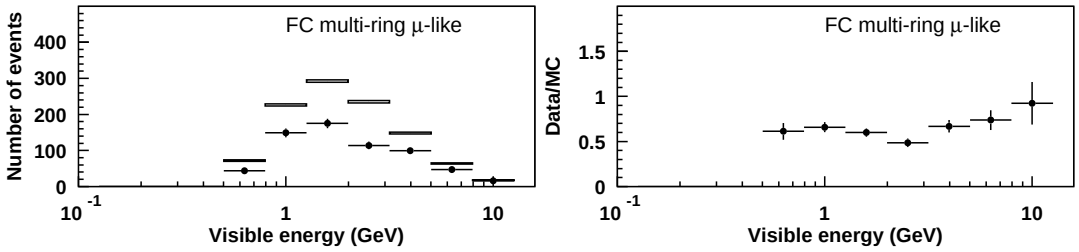

Figure 6.5: Visible energy distributions for FC multi-ring μ-like (left), and the ratio of the data to Monte Carlo events (right). Points show the data and box histograms show the Monte Carlo events with their statistical errors. The live time of the Monte Carlo sample is normalized to that of the data.

6.5 Zenith Angle Distributions

Figure 6.6 shows the zenith angle distributions for the FC single-ring e-like and μ-like + PC samples for various energy regions, where horizontal axis shows cosine of the zenith angle of the particle direction. Zenith angle $\cos\Theta = -1$ indicates upward-going direction and $\cos\Theta = +1$ indicates downward-going. The Sub-GeV samples are separated into two at the momentum of 400 MeV/c for both the e-like and μ-like samples. Since the angular correlation between neutrinos and charged leptons is not good in the momentum range below 400 MeV/c, the zenith angle distribution becomes flat although the prediction of the neutrino flux is not flat. The enhancements in the horizontal direction for the Multi-GeV samples are explained by the higher neutrino flux due to the higher decay probability of high energy muons in the atmosphere.

Comparing the zenith angle distributions of the data with that of the Monte Carlo predictions, there are clear deficits of μ-like events especially in upward-going events in high energy regions, while the data and Monte Carlo predictions agree well for the e-like samples.

Figure 6.7 shows the zenith angle distributions for the FC multi-ring μ-like sample. The FC multi-ring sample is separated into Sub-GeV and Multi-GeV samples. The direction of the multi-ring event is determined by the sum of the momentum weighted vectors toward the ring directions over all identified rings. Deficits in upward-going events are also clearly seen for multi-ring μ-like events.

Figure 6.8 shows the zenith angle distributions for the upward stopping and through-going muons. Although the observed flux of the upward-going muons is systematically lower than the prediction, the shape of the zenith angle distribution of the upward through-going muons clearly disagrees with the Monte Carlo prediction. The ratio of the number of the upward stopping muons to the upward through-going muons $N_{stop}/N_{through}$ is also shown in Figure 6.8 for the data and the atmospheric neutrino Monte Carlo events. Systematic uncertainties in the prediction of the upward-going muon events are largely canceled by taking the ratio. The ratio $N_{stop}/N_{through}$ of the data is clearly small compared to the prediction.

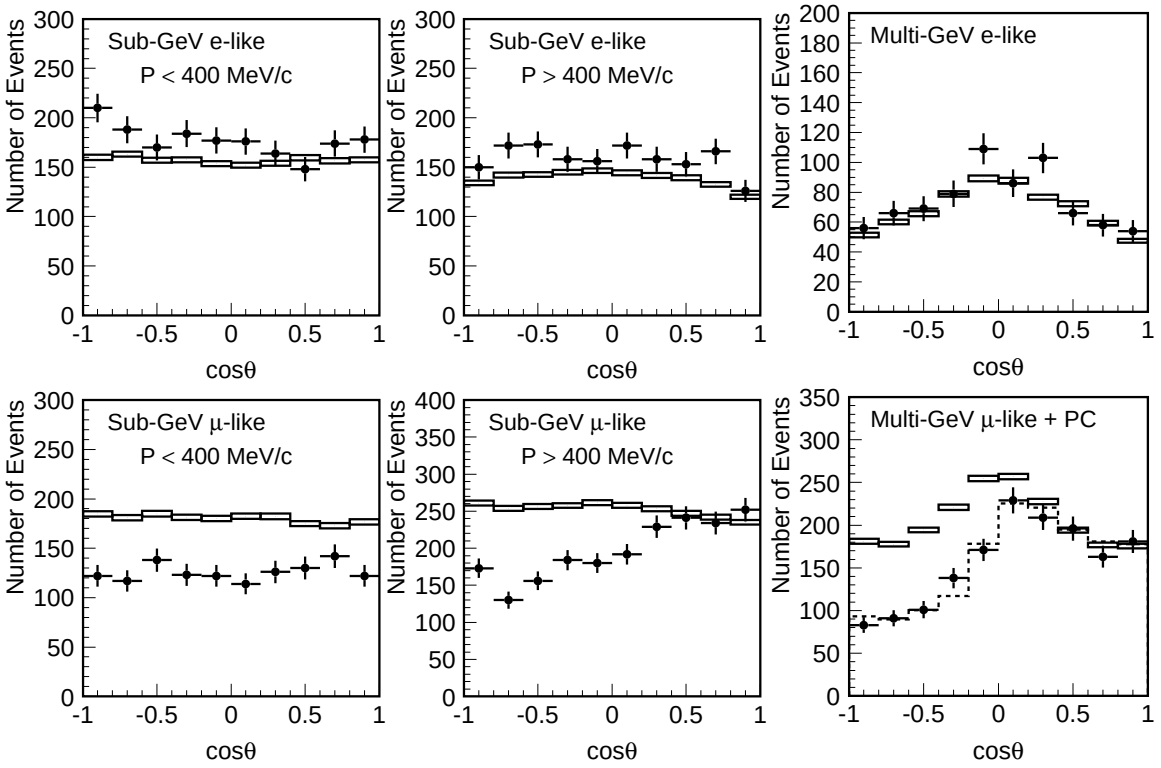

Figure 6.6: Zenith angle distributions for the FC single-ring e-like and μ-like + PC samples. The horizontal axis shows cosine of zenith angle of particle direction. Zenith angle $\cos\Theta = -1$ ($\cos\Theta = +1$) indicates upward-going (downward-going) direction. Points show the data and box histograms show the Monte Carlo predictions with their statistical errors. PC events are included in the Multi-GeV μ-like sample in lower right figure.

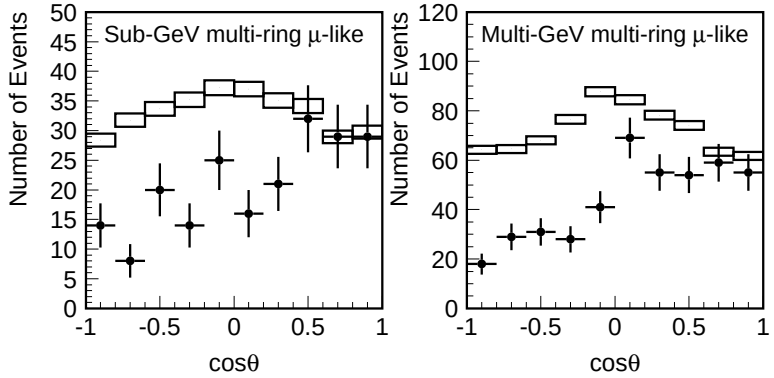

Figure 6.7: Zenith angle distributions for the FC multi-ring μ-like sample. The horizontal axis shows cosine of zenith angle of the particle direction. Zenith angle $\cos\Theta = -1$ ($\cos\Theta = +1$) indicates upward-going (downward-going) direction. Points show the data and box histograms show the Monte Carlo predictions with their statistical errors.

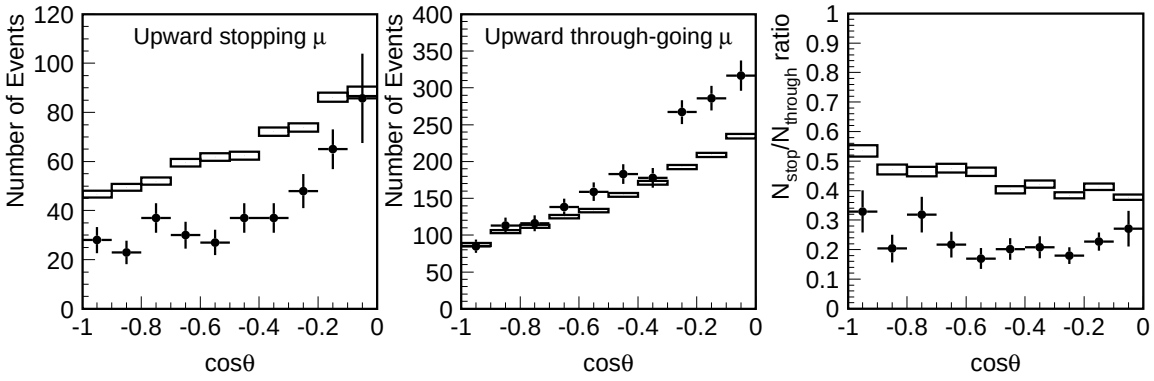

Figure 6.8: Zenith angle distributions for the upward stopping and through-going muon samples (two figures on the left) and the ratio of the number of upward stopping muons to the upward through-going muons $N_{stop}/N_{through}$ (right-hand figure). The horizontal axis shows cosine of zenith angle of the particle direction. Zenith angle $\cos\Theta = -1$ ($\cos\Theta = 0$) indicates upward-going (horizontal-going) direction. Points show the data and box histograms show the Monte Carlo predictions. Error bars for the data contain the statistical errors for all bins and the systematic errors due to subtraction of the contamination of cosmic ray for the most horizontal bins, while only statistical errors are considered in the Monte Carlo predictions.

Chapter 7

Neutrino Oscillation Analysis

Deficit of upward going μ-like events strongly indicates atmospheric neutrino oscillations. In this chapter, a fit to the FC, PC, upward stopping and through-going muon data is carried out assuming 2-flavor $\nu_\mu \leftrightarrow \nu_\tau$ oscillation. Since the observed zenith angle distributions of e-like events agree with the predictions, 2-flavor $\nu_\mu \leftrightarrow \nu_\tau$ oscillation is considered to be dominant in the atmospheric neutrino oscillations. A χ^2 test is carried out to evaluate the agreement of the fit to the observed data, in which systematic errors are taken into account. As the data are well explained by $\nu_\mu \leftrightarrow \nu_\tau$ oscillations, confidence intervals can be derived for the oscillation parameters Δm^2 and $\sin^2 2\theta$.

7.1 Analysis Method

In the analysis, the FC single-ring, FC multi-ring μ-like, PC, upward stopping muon and upward through-going muon samples are used and the whole sample is divided into 180 bins by particle type, momentum and zenith angle as shown in Figure 7.1. The FC and PC samples are divided into 10 bins equally spaced between $\cos\Theta = -1$ and $\cos\Theta = +1$, where $\cos\Theta$ is cosine of zenith angle of particle direction. Zenith angle $\cos\Theta = -1$ ($\cos\Theta = +1$) indicates the upward-going (downward-going) directions. The FC single-ring e-like and μ-like samples were divided into 7 and 6 equally spaced momentum bins in the logarithmic scale, and the FC multi-ring sample is separated at $E_{vis} = 1330\,\mathrm{MeV}$ into Sub-GeV and Multi-GeV samples. The upward stopping and upward through-going muon samples are divided into 10 bins equally spaced between $\cos\Theta = -1$ and $\cos\Theta = 0$. In total 180 observable variables are considered in the calculation of χ^2 with their associated sets of the observations and the Monte Carlo predictions.

The definition of χ^2 is as follows :

$$\chi^2 = \sum_{i=1}^{180} \frac{\left(N_i^{\mathrm{obs}} - N_i^{\mathrm{exp}}(1 + \sum_{j=1}^{37} f_j^i \cdot \epsilon^j)\right)^2}{(\sigma_i^{stat})^2} + \sum_{j=1}^{37} \left(\frac{\epsilon^j}{\sigma_j^{sys}}\right)^2 \tag{7.1}$$

In the first sum, N_i^{obs} is the number of observed events in the i-th bin, N_i^{exp} is the expected number of events from Monte Carlo simulation, and σ_i^{stat} combines the statistical uncertainties in the data and the Monte Carlo simulation. In the χ^2 calculation, the values of N_i^{exp} are re-calculated to account for neutrino oscillations and systematic variations due to uncertainties in

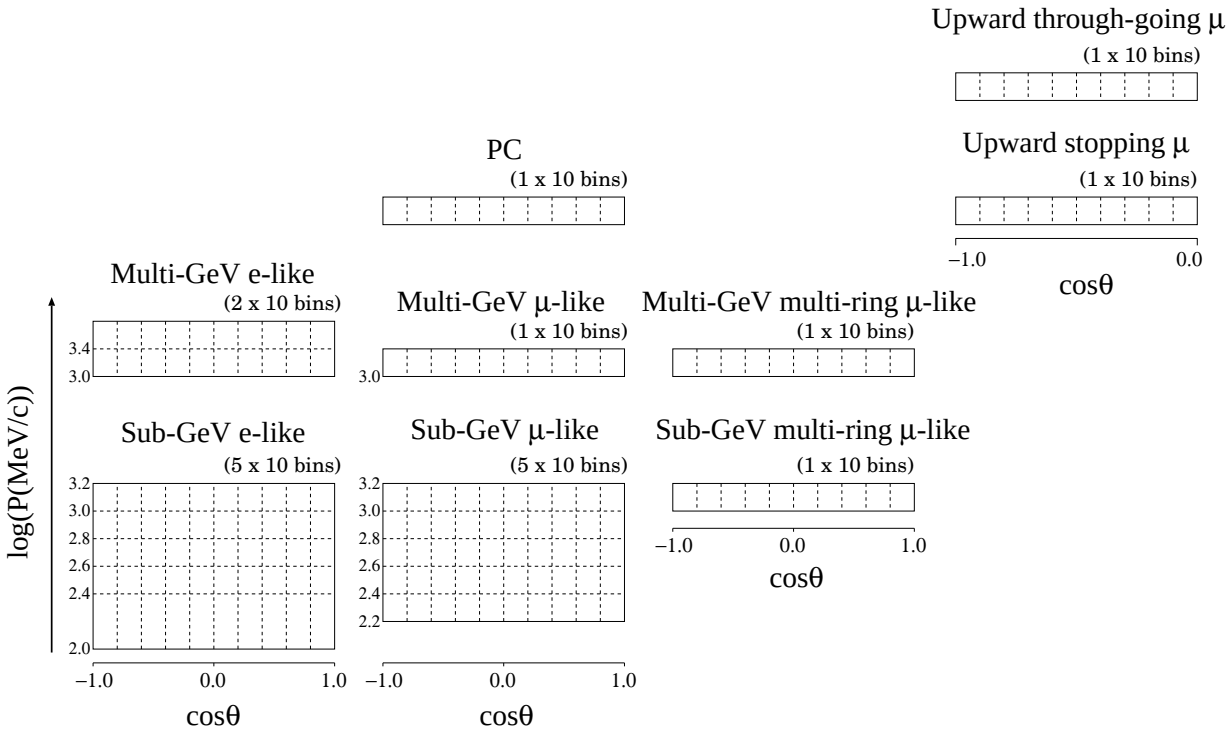

Figure 7.1: Definition of the binning for neutrino oscillation analysis. There are 180 bins divided by particle type, momentum and zenith angle : 70 for the FC single-ring e-like sample, 60 for the FC single-ring μ-like sample, 20 for the FC multi-ring μ-like sample, 10 for the PC sample, 10 for the upward stopping muon sample and 10 for the upward through-going muon sample.

the neutrino flux model, neutrino interaction model, and detector performance. The systematic uncertainties are represented by 37 parameters ϵ_j. The parameter f_j^i represents the fractional change in the predicted event rate in the i-th bin due to a variation of the parameter ϵ_j. The second sum in the χ^2 definition represents the contributions from the variables which parameterize the systematic uncertainties in the expected neutrino rates. These variables are listed in Tables 7.1, 7.2, 7.3 and 7.4 with their estimated uncertainties and the resulting best-fit values. The explanations about the systematic error sources are described in the next section. During the fit, these parameters are adjusted to minimize χ^2 for each choice of oscillation parameters $\sin^2 2\theta$ and Δm^2.

A global scan is carried out on a $(\sin^2 2\theta, \log \Delta m^2)$ grid minimizing χ^2 with respect to 37 systematic error parameters. At each grid point, the local minimum of χ^2 can be derived by solving linear equations [103]. At the minimum χ^2 location, $\frac{\partial \chi^2}{\partial \epsilon_j} = 0$ is realized for each of the parameters ϵ_j. As a result, the minimization of χ^2 in Equation 7.1 is equivalent to solving the following $k = 1, 37$ linear equations:

$$\sum_{j=1}^{37} \left[\frac{1}{(\sigma_j^{sys})^2} \delta_{jk} + \sum_{i=1}^{180} \left(\frac{N_i^{\rm exp} \cdot N_i^{\rm exp} \cdot f_j^i \cdot f_k^i}{(\sigma_i^{stat})^2} \right) \right] \cdot \epsilon_k = \sum_{i=1}^{180} \frac{(N_i^{\rm obs} - N_i^{\rm obs}) \cdot N_i^{\rm exp} \cdot f_k^i)}{(\sigma_i^{stat})^2} \qquad (7.2)$$

where σ_j^{sys} is the estimated uncertainty in the parameter ϵ_j.

7.2 Systematic Uncertainties

7.2.1 Systematic Uncertainties in Atmospheric Neutrino Flux

Several detailed calculations of atmospheric neutrino flux at the Super-Kamiokande detector site have been reported. Systematic uncertainties in the prediction of the atmospheric neutrino flux are estimated by comparing the Honda flux [1, 2] with the other calculations, the Fluka flux [24] and the Bartol flux [25]. Systematic uncertainties in the prediction of atmospheric neutrino flux are listed in Table 7.1 with their estimated 1-σ errors and the best-fit values from neutrino oscillation analysis.

Absolute normalization

Absolute normalization uncertainty in the prediction of atmospheric neutrino flux is roughly estimated to be 20 % below 100 GeV and 30 % above, which comes from the uncertainty in the primary cosmic ray flux and the hadronic interaction models used in the calculation. The absolute normalization parameter is treated as a free parameter in this analysis because of the large uncertainty.

Flavor ratio

The flavor ratio $(\nu_\mu + \overline{\nu}_\mu)/(\nu_e + \overline{\nu}_e)$ of the atmospheric neutrino flux is predicted from independent flux calculations within 5 % difference. To consider the energy dependence, the systematic uncertainty in the flavor ratio of the atmospheric neutrino flux is treated separately for Sub-GeV and Multi-GeV. The systematic errors are 5 % for both $E_\nu < 1.33$ GeV and $E_\nu > 1.33$ GeV. In the low energy range, this uncertainty mainly comes from the estimation of pion

			uncertainty (%)	best-fit (%)
(A) Systematic uncertainties in neutrino flux				
Absolute normalization			free	17.5
Flavor ratios	$E_\nu < 1.33\,\mathrm{GeV}$		5.0	-2.3
	$E_\nu > 1.33\,\mathrm{GeV}$		5.0	-5.1
Anti-neutrino/neutrino ratio	$\overline{\nu}_e/\nu_e$		5.0	1.8
	$\overline{\nu}_\mu/\nu_\mu$		5.0	-1.6
Up/down ratio	$< 400\,\mathrm{MeV}$	e-like	0.4	-0.1
		μ-like	0.8	-0.2
	$> 400\,\mathrm{MeV}$	e-like	1.7	-0.4
		μ-like	2.1	-0.5
	Multi-GeV	e-like	0.7	0.2
		μ-like	0.7	0.2
	PC		0.1	0.0
	Sub-GeV	multi-ring μ	1.0	0.3
	Multi-GeV	multi-ring μ	0.2	0.1
Horizontal/vertical (3D)	$< 400\,\mathrm{MeV}$	e-like	0.5	0.0
		μ-like	0.4	0.0
	$> 400\,\mathrm{MeV}$	e-like	2.4	0.0
		μ-like	2.5	0.0
	Multi-GeV	e-like	2.0	0.0
		μ-like	3.1	-0.1
	PC		0.8	0.0
	Sub-GeV	multi-ring μ	2.0	0.0
	Multi-GeV	multi-ring μ	3.1	-0.1
Horizontal/vertical (K/π)	upmu		3.0	0.4
L_ν (production height)			10.0[a]	-1.0
Energy spectrum			0.05[b]	0.047
Sample-by-sample normalization	FC Multi-GeV		5.0	-5.8
	PC + upward stopping μ		5.0	-3.0

Table 7.1: Summary of systematic uncertainties in the prediction of the atmospheric neutrino flux. Estimated uncertainty and the best-fit value are listed for each error.

[a] 10 % uncertainty in atmospheric density structure
[b] 0.05 uncertainty in spectral index of neutrino energy

	uncertainty (%)	best-fit (%)
(B) Systematic uncertainties in neutrino interaction		
Quasi-elastic scattering and single-meson production (M_A)	10.0[a]	-1.7
Quasi-elastic scattering (nuclear effect)	1.0[b]	-0.83
Quasi-elastic scattering (total cross-section)	10.0	4.7
Single-meson production (total cross-section)	10.0	-4.8
Multi-pion production (a few GeV region)	1.0[c]	1.94
Multi-pion production (total cross-section)	5.0	2.4
Coherent pion production (total cross-section)	30.0	-0.5
NC/CC ratio	20.0	5.5

Table 7.2: Summary of systematic uncertainties in neutrino interactions. Estimated uncertainty and the best-fit value are listed for each error.

[a] 10 % uncertainty in M_A value
[b] Difference from the Oset model is set to 1.0
[c] Difference from the Bodek model is set to 1.0

			uncertainty (%)	best-fit (%)
(C) Systematic uncertainties in event selection				
Reduction for fully contained event			1.0	0.1
Reduction for partially contained event			3.2	0.4
Detection efficiency	upward stopping μ		1.3	-0.2
	upward through-going μ		0.5	-0.1
FC/PC relative normalization			2.6	1.0
μ/e ratio[a]	Sub-GeV		0.9	-0.2
	Multi-GeV		2.6	-0.5
Up/down ratio (non-neutrino background)	Sub-GeV	e-like	1.0	-0.5
		μ-like	0.2	0.0
	Multi-GeV	e-like	0.6	0.0
		μ-like	0.4	0.0
Separation of upward stopping and through-going muon			0.8	-0.1
Charged current ν_τ interaction			50.0[b]	-1.5

Table 7.3: Summary of systematic uncertainties in event selection. Estimated uncertainty and the best-fit value are listed for each error.

[a] Small systematic error sources that are not listed in Tables 7.1, 7.2, 7.3 and 7.4 are included. They are non-neutrino background, hadron simulator and fiducial volume.
[b] 50 % of the expected charged current ν_τ interaction.

			uncertainty (%)	best-fit (%)
(D) Systematic uncertainties in event reconstruction				
Single-ring/multi-ring separation	$< 400\,\mathrm{MeV}$	e-like	5.4	2.1
		μ-like	2.0	0.8
	$> 400\,\mathrm{MeV}$	e-like	3.1	1.2
		μ-like	1.2	0.5
	Multi-GeV	e-like	13.4	5.2
		μ-like	5.2	2.0
	Sub-GeV	multi-ring μ	3.4	-1.3
	Multi-GeV	multi-ring μ	6.1	-2.4
Particle identification	Sub-GeV	e-like	0.5	0.3
		μ-like	0.5	-0.3
	Multi-GeV	e-like	0.4	0.2
		μ-like	0.4	-0.2
	Sub-GeV	multi-ring μ	5.4	-3.3
	Multi-GeV	multi-ring μ	3.2	-2.0
Energy calibration for FC event			2.0^a	0.0
Energy cut for upward stopping muon			1.1	
Up/down symmetry of energy calibration			0.6^b	-0.2

Table 7.4: Summary of systematic uncertainties in event reconstruction. Estimated uncertainty and the best-fit value are listed for each error.

[a] 2 % uncertainty in absolute energy scale

[b] 0.6 % uncertainty in up/down symmetry of energy calibration

spectrum in the primary hadronic interactions, which affects decay probabilities of secondary muons in atmosphere. On the other hand, in the high energy range, the uncertainty mainly comes from the K/π production ratio.

Anti-neutrino/neutrino ratio

Systematic uncertainty of anti-neutrino to neutrino ratio comes from π^+/π^- ratio in hadronic interaction in the flux calculation. The uncertainties are estimated to be 5 % for $\overline{\nu}_e/\nu_e$ and $\overline{\nu}_\mu/\nu_\mu$, separately.

Up/down ratio

As described in Section 3.2, the neutrino flux below a few GeV has up/down asymmetry because of the rigidity cutoff by the geomagnetic field, while flux above a few GeV is up/down symmetric. The systematic uncertainty in the up/down ratio of atmospheric neutrino flux is derived from the treatment of the geomagnetic field in the calculation. Since the up/down asymmetry in low energy neutrino flux is largely canceled due to the small angular correlation in neutrino interactions, the uncertainty of flux calculation does not directly affect the zenith angle distributions observed in Super-Kamiokande. The systematic uncertainties of up/down ratio are estimated by comparing the predictions of zenith angle distributions in Super-Kamiokande from independent flux calculations. The systematic error parameters are listed in Table 7.1. These evaluated systematic errors are treated as correlated.

Horizontal/vertical ratio

The source of the uncertainties in horizontal/vertical ratio of atmospheric neutrino flux changes with the neutrino energy. For relatively lower energy neutrinos below 10 GeV, the uncertainties come from the difference in 3-dimensional calculation method for each calculation. For higher energy neutrinos, the uncertainties are derived from the generated K/π ratio in hadronic interactions in the atmosphere. Therefore, the systematic errors in horizontal/vertical ratio are considered separately for the FC + PC samples and the upward-going muon samples, and the parameters in each are treated as correlated errors. The estimated errors are listed in Table 7.1.

Neutrino flight length

The systematic uncertainty in neutrino flight length is not directly related to the prediction of the atmospheric neutrino flux, but the uncertainty effects the oscillation probabilities of neutrinos because of its L/E dependence. The effect on the prediction from the neutrino flight length is estimated with typical oscillation parameters $(\sin^2 2\theta,\ \Delta m^2) = (1.0,\ 2.0 \times 10^{-3}\,\mathrm{eV}^2)$. The systematic uncertainty is negligible for upward-going neutrinos which pass through the Earth because the flight length for those neutrino can be easily calculated from the geometry. For downward-going and horizontally-going neutrinos, the production height of the neutrinos must be considered to calculate the flight length. The neutrino production height can be calculated by a Monte Carlo method. The uncertainty of the neutrino production height is related to the structure of the atmosphere. To estimate the systematic uncertainty in the production height and neutrino flight length, the calculation is carried out by changing the density structure of

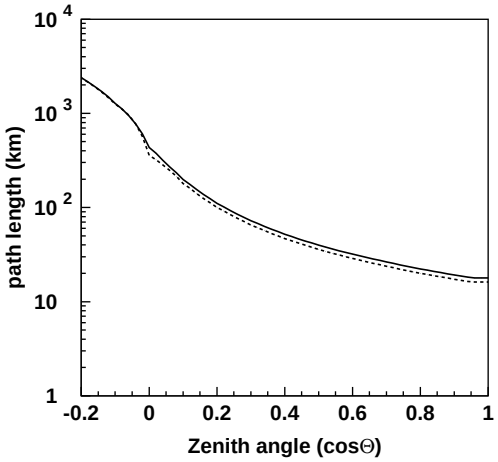

Figure 7.2: Neutrino flight length as a function of zenith angle. Solid line shows the flight length used in analysis and dashed line shows that for the compressed density structure of atmosphere by 10 %.

atmosphere by 10 %. Figure 7.2 shows the comparison of the flight length used in the analysis with that for the compressed density structure of atmosphere by 10 %. The effect of this difference is considered as the systematic error.

Energy spectrum

The spectrum of primary cosmic ray is well fit to the form E^{γ}. The spectral index for the primary proton flux used is $\gamma = 2.74$. The systematic uncertainty in the spectral index is estimated to be 0.05 .

Sample-by-sample normalization

Figure 7.3 shows the comparison of energy spectra predicted from independent calculations (left) and energy spectrum of parent neutrinos for each sample (right). The flux ratio is fluctuated with the energy. Although uncertainties in the absolute normalization and energy spectra have already been introduced, those errors cannot explain the fluctuation of the flux ratio. The flux difference for each sample is considered as the remaining uncertainty in the prediction of the atmospheric neutrino flux, and evaluated as the systematic uncertainty in the sample-by-sample relative normalization. The systematic error in sample-by-sample normalization is estimated to be ± 5 %. In order not to double-count the errors with the energy spectrum, only the FC Multi-GeV and the PC+upward stopping muon samples are adjusted by the errors. Since the energy spectrum for the PC sample has peak around 10 GeV, and which is almost the same as the upward stopping muon sample as shown in Figure 7.3, the PC and upward stopping muon samples are simultaneously adjusted by this error.

7.2.2 Systematic Uncertainties in Neutrino Interaction

cross-sections and kinematics in neutrino interactions are theoretically predicted, and measured by several experiments. Systematic uncertainties in neutrino interactions are listed in Table 7.2 with their estimated 1-σ errors and the best-fit values of neutrino oscillation analysis. The details of the errors are described below.

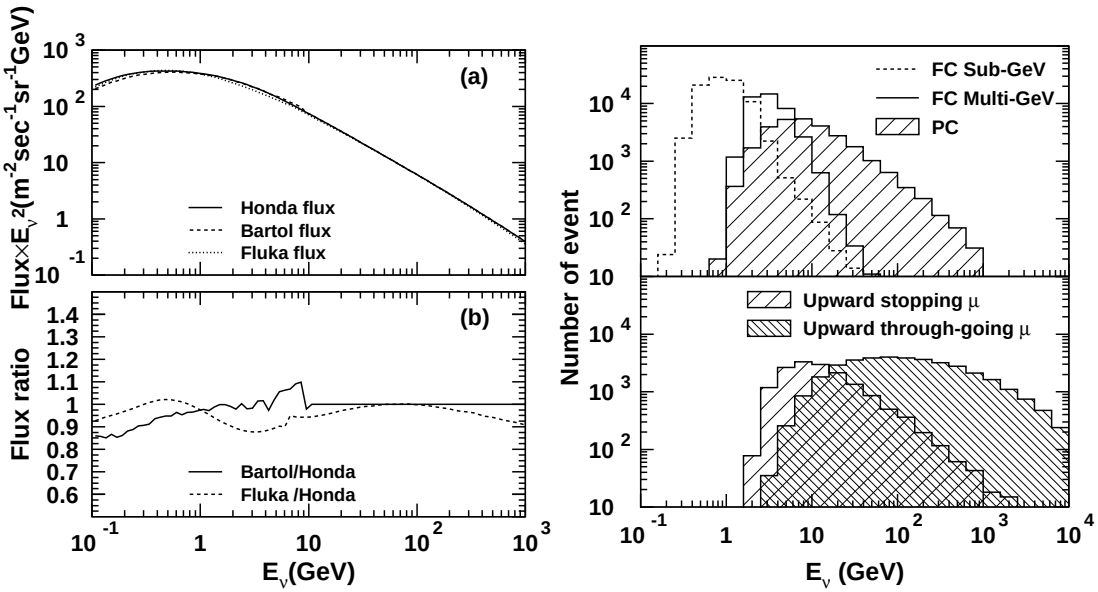

Figure 7.3: Comparison of energy spectra predicted from independent calculations (left) and energy spectrum of parent neutrinos for each sample (right). In the left-hand figures, the Honda flux is compared with the Fluka flux and the Bartol flux. The upper figure (a) shows the absolute flux for each calculation and the lower one (b) is the ratio of the Honda flux to the others. The calculation of Bartol flux is in progress, and the flux above 10 GeV has not presented yet. In the right-hand figures, the energy spectrum of the parent neutrinos for each muon sample is shown. The energy spectrum for the PC sample has a peak around 10 GeV, which is almost the same as that of the upward stopping muon sample.

Quasi-elastic scattering and single-meson production (M_A)

The cross-section and kinematics in quasi-interaction scattering and single-meson production have a dependence on the axial vector mass M_A. The value of M_A is set to be 1.11 in our simulation based on experimental data, but the uncertainty of the value is estimated to be 10 %. Figure 7.4 shows the effect from the uncertainty in the M_A value as a function of the angular difference between the direction of incident neutrino and out-going lepton, in which ratios of the angular distributions for quasi-elastic scattering and single-meson production in atmospheric neutrino Monte Carlo events using $M_A = 1.01$ to that for $M_A = 1.11$ are plotted.

Quasi-elastic scattering (nuclear effect)

In quasi-elastic neutrino interaction with bound nucleon target in ^{16}O, the Fermi motion of the nucleons and Pauli exclusion principle are taken into account. R.A.Smith and E.J.Moniz'z relativistic Fermi gas model is employed in the Monte Carlo simulation, in which the momentum distribution of nucleons are assumed to be flat up to the Fermi surface momentum [42]. The Fermi surface momentum is set to be 225 MeV/c and the nucleon potential is set to 27 MeV/c. These configuration and the calculation of kinematic in neutrino interaction are thought to have uncertainties. The systematic error in the nuclear effect is estimated by comparing with the independent model of S.K.Singh and E.Oset [44]. The 1-σ error is defined to be the difference in the predicted cross-sections by [42] and [44].

Multi-pion production (a few GeV region)

The prediction of the cross-sections for multi-pion production agree with the experimental data within 5 % for energies above a few ten GeV, while the uncertainties in lower energy region are relatively large. Systematic uncertainty in multi-pion production is estimated by comparing with the model presented from A. Bodek and U. K. Yang [73]. The difference of the models depends on the square of 4-momentum transfer q^2, and is large in a few GeV region. The 1-σ error is defined to be the difference in the predicted cross-section by [68] and [73].

Total cross-sections

Systematic uncertainties comes from the other sources are conservatively estimated by changing the total cross-section of quasi-elastic scattering by 10 %, single-pion production by 10 %, multi-pion production by 5 % and coherent-pion production by 30 %. Although the uncertainty in coherent-pion is large, the effect to the analysis is small because the fraction of the coherent-pion production is small for each sample. In addition, a 20 % uncertainty in the NC/CC ratio is taken into account.

7.2.3 Systematic Uncertainties in Event Selection

FC and PC reduction

Systematic uncertainties of the FC and PC reduction efficiencies are estimated by comparing the distribution of each cut variable of the data with that of the Monte Carlo events. The estimated uncertainties are 1 % and 3.2 % for FC and PC reduction, respectively.

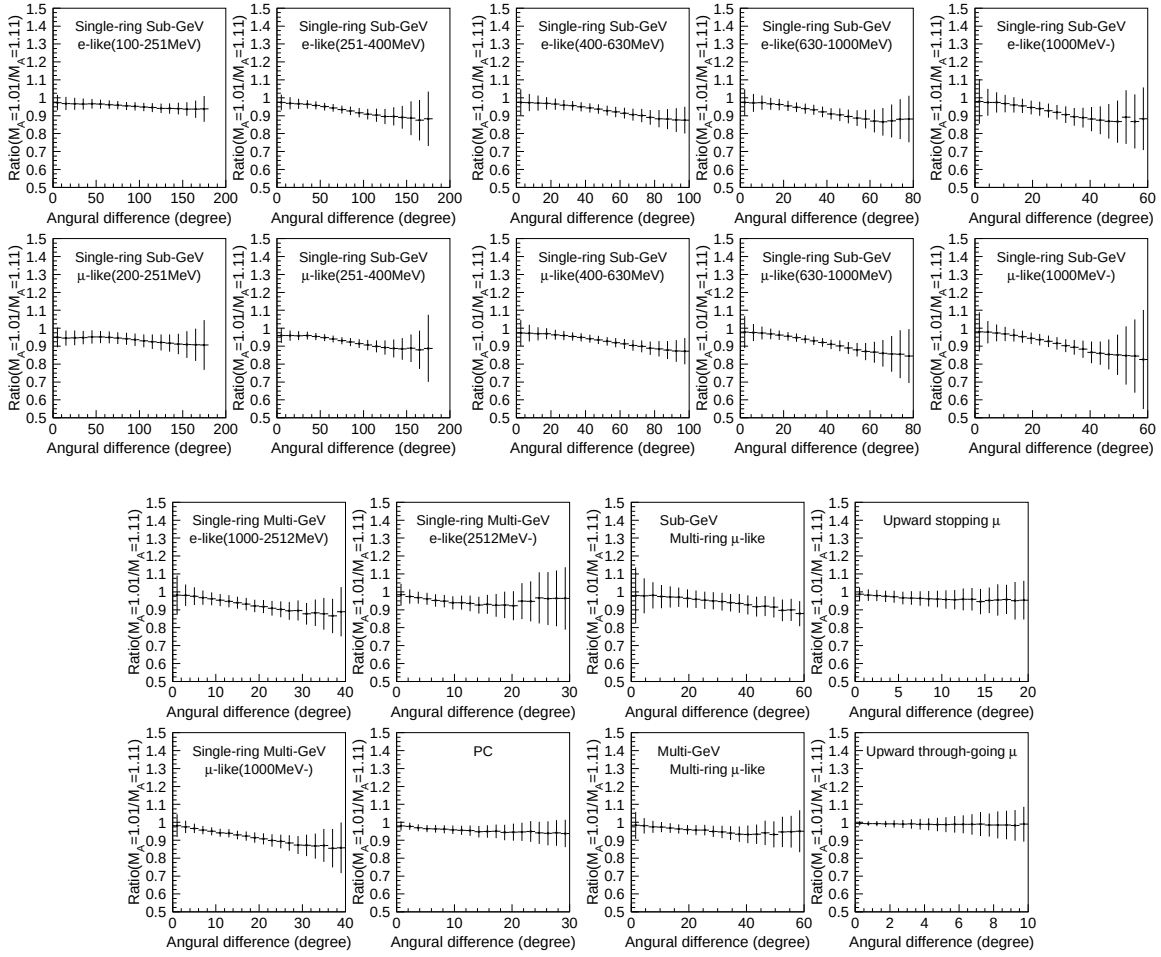

Figure 7.4: Ratios of angular distributions for quasi-elastic scattering and single-meson production in atmospheric neutrino Monte Carlo events using $M_A = 1.01$ to that for $M_A = 1.11$. The horizontal axis shows the angular difference between the direction of incident neutrino and out-going lepton. The higher value of M_A gives smaller angular correlation. Since the fractions of quasi-elastic scattering and single-meson production are small, the effect of the uncertainty in M_A becomes small for the upward-going muon sample.

FC/PC relative normalization

The uncertainty of FC/PC relative normalization include small sources that are not listed in Tables 7.1, 7.2, 7.3 and 7.4. The largest uncertainty comes from the uncertainty of FC/PC separation. The FC and PC events are separated by the number of hit PMTs in the OD hit PMT cluster (NHITAC). The uncertainty of the FC/PC separation is estimated to be 1.8 % by comparing NHITAC distribution of the data with that of the Monte Carlo events as shown in Section 4.1. The other errors are fiducial volume, non-neutrino background and hadron simulation. The uncertainty of FC and PC relative normalization is 2.6 % in total.

Separation of upward stopping and through-going muon

The upward stopping and through-going muons are separated by the number of hit OD PMTs within 8 m from the exit point (NHITEX). The uncertainty of the separation of upward stopping and through-going muons is estimated to be 0.76 % by comparing NHITEX distribution of the data with that of the Monte Carlo events as shown in Section 4.1.

Charged current ν_τ interaction

In 2-flavor $\nu_\mu \leftrightarrow \nu_\tau$ oscillation analysis, the number of charged current ν_τ interactions in the FC single-ring e-like samples is considered, while the contamination in the μ-like sample is negligible. The systematic uncertainty in the cross-section of charged current ν_τ interaction is estimated to be 50 % from the result of τ detection in Super-Kamiokande [104].

7.2.4 Systematic Uncertainties in Event Reconstruction

Single-ring/multi-ring separation

The number of rings is determined in event reconstruction process using an evaluation function for possible ring candidates (see Section 5.3). The number of rings for the FC sample is used in neutrino oscillation analysis to separate the single- and multi-ring samples. The systematic error in single-ring/multi-ring separation comes from the uncertainties in a water transparency and tracking of hadrons in water. The uncertainties are estimated by comparing the evaluation function distributions for the observed data with that for the Monte Carlo events. The estimated errors are shown in Table 7.4 with their best-fit values. Since the differences of the evaluation function distributions in the Monte Carlo events from that of the data have the same direction for all energy regions, the uncertainties in single-ring/multi-ring separation are treated as correlated.

Particle identification

Particle identification is carried out by a likelihood method (see Section 5.4). The uncertainty in the performance of the classification affects the number of e-like and μ-like events, and the result of the neutrino oscillation analysis. The errors for the particle identification are estimated by comparing the likelihood distributions for the observed data with that for the Monte Carlo events. The estimated errors are shown in Table 7.4 with their best-fit values. The uncertainties in particle identification are treated as correlated because the differences of the likelihood distributions from that of the data have the same direction for all energies.

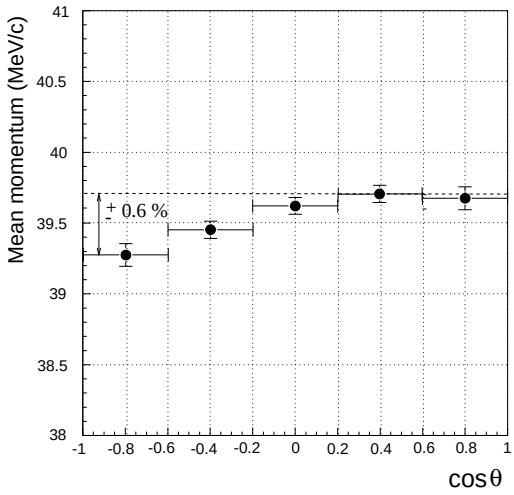

Figure 7.5: Mean momentum of muon decay electrons as a function of the zenith angle of the direction.

Energy calibration for FC event

The absolute energy scale is checked using several sources over a wide energy range from a few ten MeV/c to about 10 GeV/c as shown in Section 2.3.5. The systematic uncertainty of the energy scale is estimated to be less than 2 %.

Energy cut for upward stopping muon

For the upward stopping muon sample, an energy cut of $p_\mu \geq 1.6\,\mathrm{GeV}/c$ is applied to keep a good performance of the event reconstruction. The systematic uncertainty of the cut is estimated to be 1.1 % by changing the energy scale by 2 %.

Up/down symmetry of energy calibration

The difference of the energy scale for upward-going and downward-going event is measured using decay electrons from cosmic ray stopping muons. Figure 7.5 shows the mean momentum for muon decay electrons as a function of the zenith angle of the direction. The up/down asymmetry of the energy scale is estimated to be 0.6 %.

7.3 Result of 2-Flavor $\nu_\mu \leftrightarrow \nu_\tau$ Oscillation Analysis

As the result of the global scan on the oscillation parameter grid, the minimum χ^2 value, $\chi^2_{min} = 176.2/177$ d.o.f., is obtained at $(\sin^2 2\theta,\ \Delta m^2) = (1.00,\ 2.1 \times 10^{-3}\,\mathrm{eV}^2)$, where θ is the mixing angle and $\Delta m^2 = m_3^2 - m_2^2$ is the difference of the squared mass of ν_3 and ν_2. The best-fit values of the systematic error parameters ϵ_j obtained at the global minimum are summarized in Tables 7.1, 7.2, 7.3 and 7.4. Including unphysical parameter region ($\sin^2 2\theta > 1$) in the scan, the minimum χ^2 value is obtained at $(\sin^2 2\theta,\ \Delta m^2) = (1.02,\ 2.1 \times 10^{-3}\,\mathrm{eV}^2)$. The minimum χ^2 value, $\chi^2_{min} = 175.9/177$ d.o.f., including the unphysical parameter region is lower than the

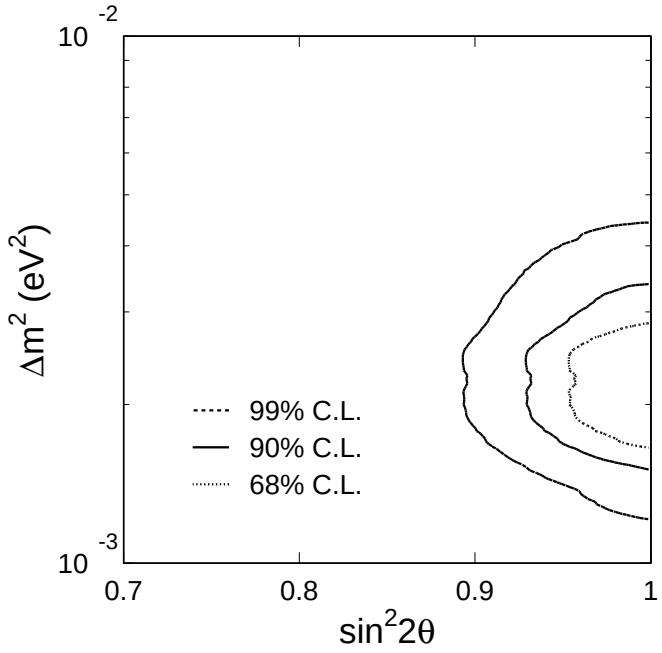

Figure 7.6: Allowed oscillation parameters for 2-flavor $\nu_\mu \leftrightarrow \nu_\tau$ oscillations. The horizontal axis shows $\sin^2 2\theta$ and the vertical axis shows Δm^2. Three contours correspond to the 68 % (dotted line), 90 % (solid line) and 99 % (dashed line) C.L. allowed regions, respectively.

minimum in the physical region by 0.32 . Assuming no oscillation, χ^2 value takes 491.1 for 179 d.o.f. . The hypothesis of no oscillation is strongly rejected.

Figure 7.6 shows the contour plots of the allowed regions of the neutrino oscillation parameters $(\sin^2 2\theta, \Delta m^2)$. Three contours correspond to the 68%, 90% and 99% confidence levels (C.L.) allowed regions which are defined to be $\chi^2 = \chi^2_{min}$ +2.62, 5.00, and 9.63 based on the minimum in the physical region, respectively. These intervals are derived by using the 2-dimensional Gaussian approximation from the minimum in the unphysical region [105]. The 90 % allowed parameter region is :

$$1.5 \times 10^{-3}\,\mathrm{eV}^2 \;<\; \Delta m^2 < 3.4 \times 10^{-3}\,\mathrm{eV}^2 \tag{7.3}$$

$$0.92 \;<\; \sin^2 2\theta \tag{7.4}$$

Figure 7.7 shows the $\chi^2 - \chi^2_{min}$ distributions as a function of $\sin^2 2\theta$ and Δm^2, which are sliced at $\Delta m^2 = 2.1 \times 10^{-3}\,\mathrm{eV}^2$ and $\sin^2 2\theta = 1.00$.

Figure 7.8 shows the zenith angle distributions for the FC single-ring e-like and μ-like + PC samples, Figure 7.9 shows those for the FC multi-ring μ-like samples, and Figure 7.10 shows those for the upward stopping and through-going muon samples. The data are compared with the Monte Carlo expectation (no oscillations, box histograms) and the best-fit expectation for 2-flavor $\nu_\mu \leftrightarrow \nu_\tau$ oscillations (dashed lines). The 2-flavor $\nu_\mu \leftrightarrow \nu_\tau$ oscillation hypothesis provides a consistent explanation to all data samples.

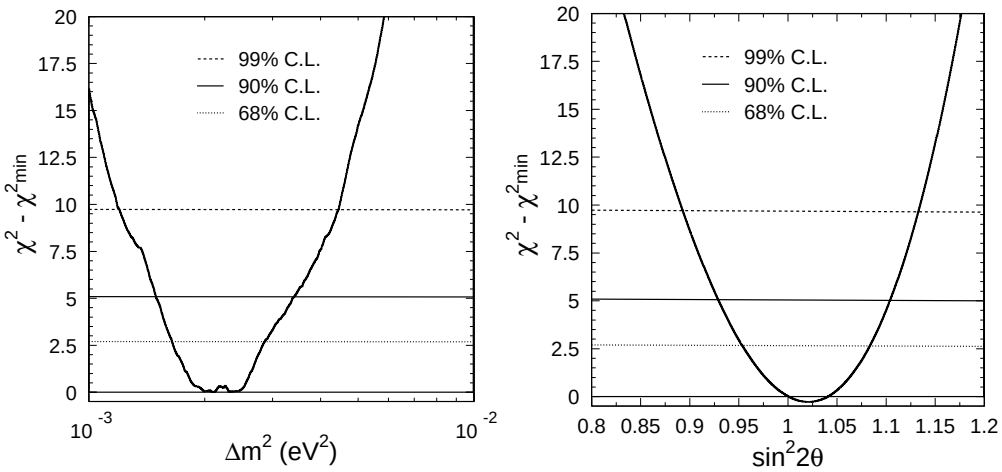

Figure 7.7: $\chi^2 - \chi^2_{min}$ distributions as a function of Δm^2 (left) and $\sin^2 2\theta$ (right), in which χ^2_{min} is the minimum value of χ^2 in physical parameter region. $\sin^2 2\theta$ is set to be 1.00 in the left-hand figure and Δ^2_m is set be $2.1 \times 10^{-3}\mathrm{eV}^2$ in the right-hand figure. Three horizontal lines correspond to the 68 % (dotted line), 90 % (solid line) and 99 % (dashed line) C.L. intervals, respectively.

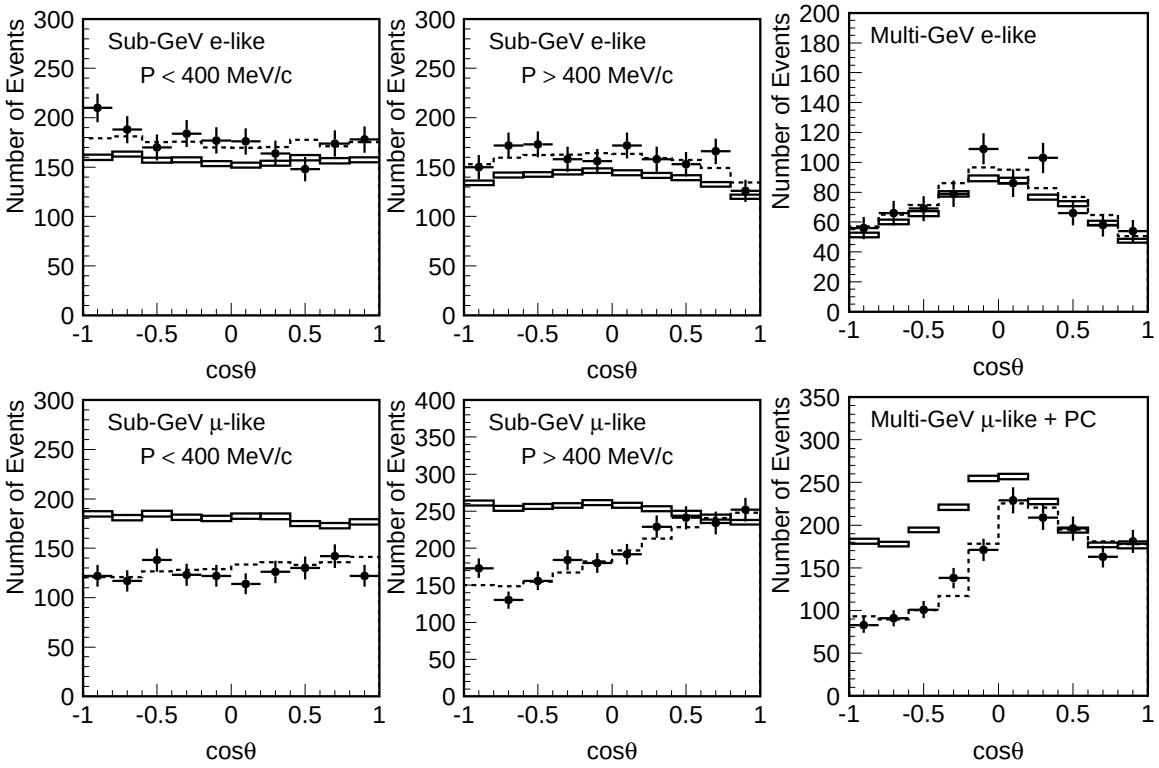

Figure 7.8: Zenith angle distributions of the observed data (points with statistical errors) together with the expectations from no oscillation Monte Carlo(box histograms with Monte Carlo statistical errors) and the best-fit expectation for $\nu_\mu \leftrightarrow \nu_\tau$ oscillations (dashed lines) for the FC single-ring e-like and μ-like + PC samples.

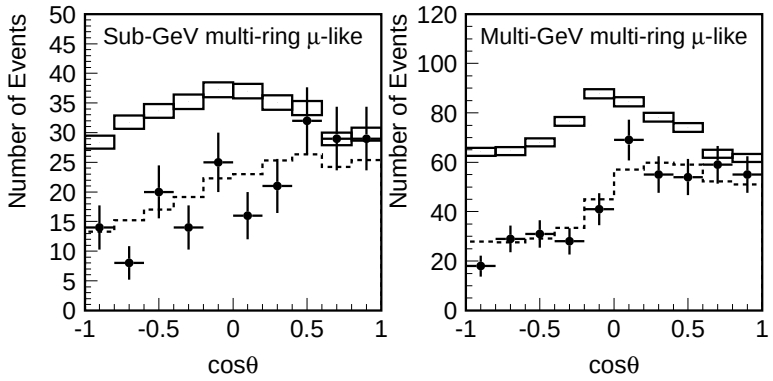

Figure 7.9: Zenith angle distributions of the observed data (points with statistical errors) together with the expectations from no oscillation Monte Carlo(box histograms with Monte Carlo statistical errors) and the best-fit expectation for $\nu_\mu \leftrightarrow \nu_\tau$ oscillations (dashed lines) for the FC multi-ring μ-like samples.

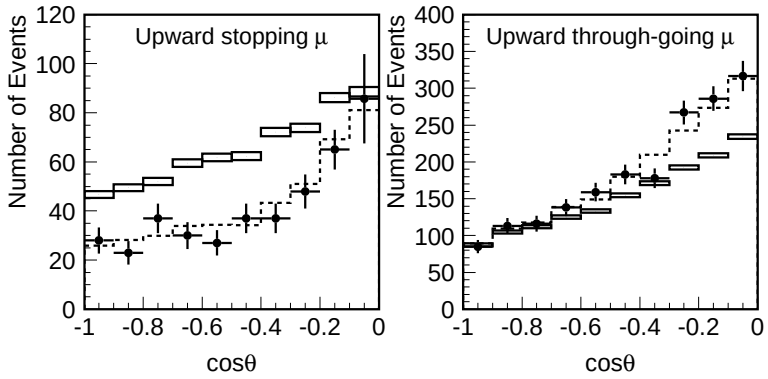

Figure 7.10: Zenith angle distributions of the observed data (points) together with the expectations from no oscillation Monte Carlo(box histograms with Monte Carlo statistical errors) and the best-fit expectation for $\nu_\mu \leftrightarrow \nu_\tau$ oscillations (dashed lines) for the upward stopping and through-going muon samples. Error bars for the data contain the statistical errors for all bins and the systematic errors due to subtraction of cosmic ray background for the most horizontal bins

Chapter 8

L/E Analysis

8.1 Outline of L/E Analysis

In 2-flavor $\nu_\mu \leftrightarrow \nu_\tau$ oscillations, survival probability of ν_μ is expressed by :

$$P(\nu_\mu \to \nu_\mu) = 1 - \sin^2 2\theta \sin^2 \left(\frac{1.27 \Delta m^2(\mathrm{eV}^2) L_\nu(\mathrm{km})}{E_\nu(\mathrm{GeV})} \right) \tag{8.1}$$

where E_ν is the neutrino energy, L_ν is the flight length of neutrino, θ is the mixing angle, and Δm^2 is the mass-squared difference of neutrino mass eigenstates ν_2 and ν_3. The survival probability of ν_μ as a function of the L_ν/E_ν is shown in Figure 8.1 with a solid line, in which $(\sin^2 2\theta,\ \Delta m^2) = (1.00,\ 2.0 \times 10^{-3}\,\mathrm{eV}^2)$ are assumed. The survival probabilities predicted from the other models that can explain the deficit of muon neutrinos are also shown in Figure 8.1 with a dashed line (neutrino decay [106], see Section 8.8.1) and a dotted line (neutrino decoherence [108], see Section 8.8.2) with typical parameters. Although the survival probabilities are different between oscillations and the other models, any clear difference cannot be seen in the zenith angle distributions (see Figure 8.2 and 8.3).

The survival probability of ν_μ can be studied by comparing the reconstructed L_ν/E_ν distribution of the data with the prediction from atmospheric neutrino Monte Carlo events. Although the survival probability distribution is smeared because of the finite resolution of reconstructed L_ν/E_ν, it could be possible to observe the first dip in case of neutrino oscillations by selecting the events which are expected to have high resolution of L_ν/E_ν.

First, E_ν and L_ν are estimated for each events from the reconstructed energy and the direction. The relations between the reconstructed energy and the E_ν are determined based on the Monte Carlo simulation, and the L_ν is estimated from the zenith angle of the reconstructed direction. Then, the resolution of L_ν/E_ν is calculated using the Monte Carlo simulation for each point in $(E, \cos\Theta)$ coordinate, where E and $\cos\Theta$ are the reconstructed energy and cosine of zenith angle. High L_ν/E_ν resolution events are selected based on a cut criterion on the resolution of L_ν/E_ν on the $(E, \cos\Theta)$ plane. FC μ-like and PC events are used in this analysis. In general, FC events have better energy resolution compared to PC events, while PC events have better angular correlation with the parent neutrinos. Both samples have advantages and disadvantages for this analysis.

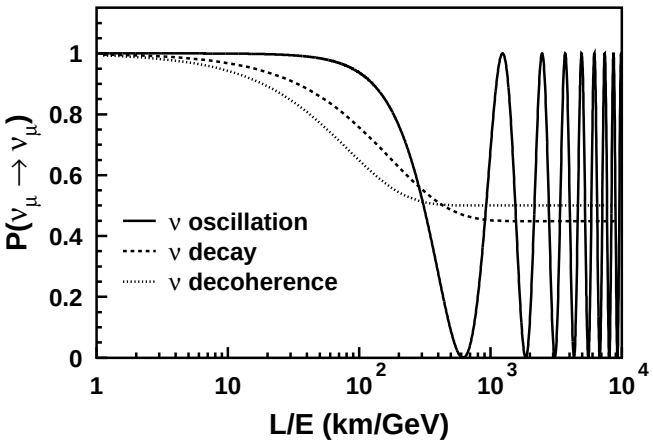

Figure 8.1: Survival probabilities of ν_μ as a function of the L_ν/E_ν. Solid line shows the prediction from neutrino oscillation, dashed line shows neutrino decay and dotted line shows neutrino decoherence.

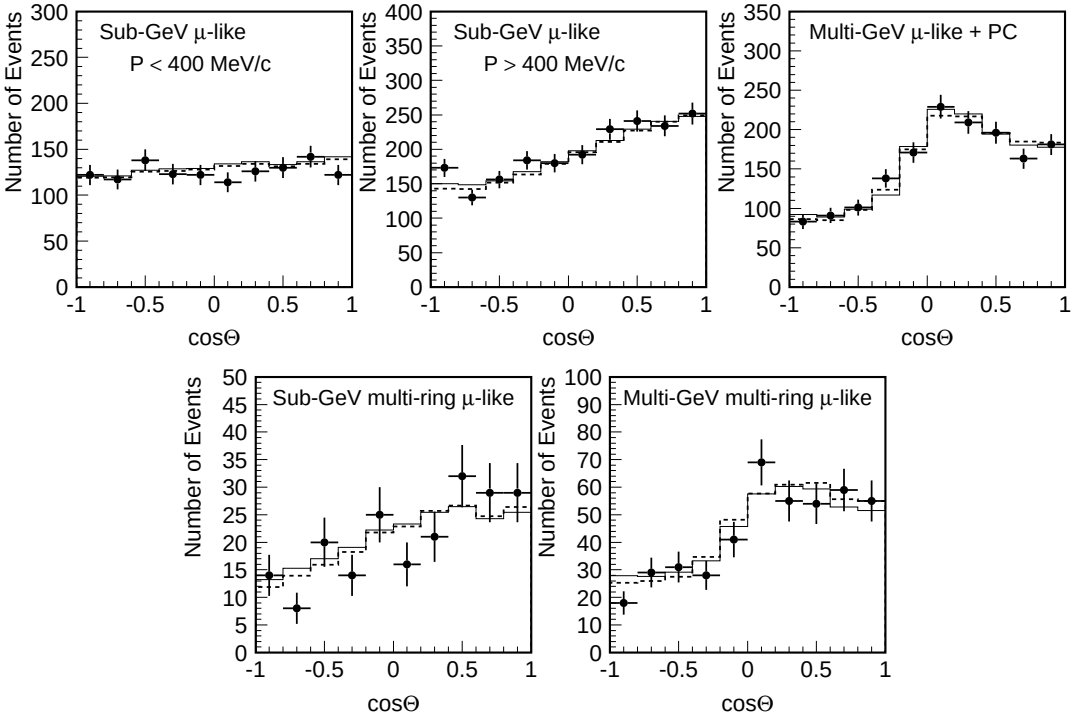

Figure 8.2: Zenith angle distribution of the observed muon sample (points) together with the atmospheric neutrino Monte Carlo events assuming neutrino oscillation with the best-fit parameters obtained by the standard oscillation analysis described in Section 7.3 (thin solid lines), and neutrino decay with typical parameters (dashed lines).

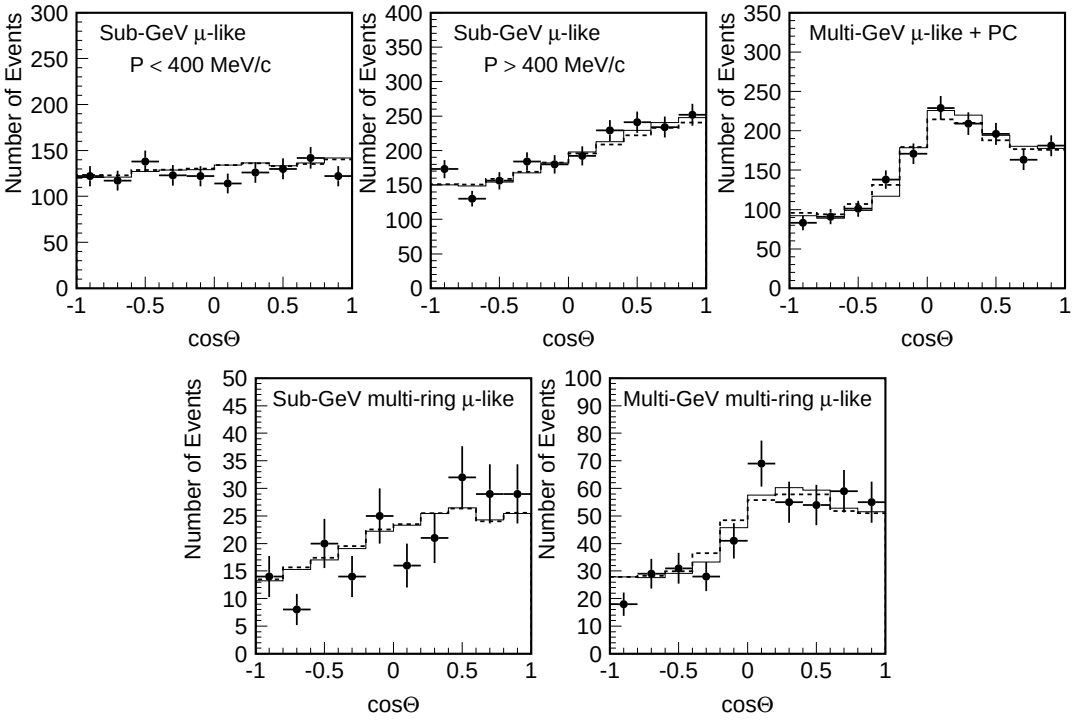

Figure 8.3: Zenith angle distribution of the observed muon sample (points) together with the atmospheric neutrino Monte Carlo events assuming neutrino oscillation with the best-fit parameters obtained by the standard oscillation analysis (thin solid lines), and neutrino decoherence with typical parameters (dashed lines).

8.2 Event Summary for L/E Analysis

FC and PC data observed in SK-I running period are used in L/E analysis. Although the live-time of the data is the same as that in the standard neutrino oscillation analysis using zenith angle distributions (see Chapter 7), the selection criteria and the event classification for the L/E analysis are different from that for the standard oscillation analysis. The data used in the L/E analysis are summarized in this section together with the Monte Carlo prediction. The amount of the Monte Carlo simulation is equivalent to the exposure of 100 years for both FC and PC samples.

The primary cuts for L/E analysis are as follows :

- FC single-ring sample
  (1) Distance from event vertex to the nearest top and bottom walls of the ID should be > 150 cm, and to the nearest barrel wall should be > 100 cm
  (2) Number of hit PMTs in the OD hit cluster (NHITAC) should be < 10
  (3) Visible energy assuming electrons (E_{vis}) should be > 30 MeV
  (4) Ring should be identified as μ-like and $p_\mu > 200$ MeV/c
- FC multi-ring sample
  (1) Distance from event vertex to the nearest top and bottom walls of the ID should be > 150 cm, and to the nearest barrel wall should be > 100 cm
  (2) NHITAC should be < 10
  (3) E_{vis} should be > 30 MeV
  (5) The most energetic ring should be identified as μ-like and $p_\mu > 600$ MeV/c and $E_{vis} > 600$ MeV
- PC OD stopping sample
  (1) Distance from event vertex to the nearest ID wall should be > 200 cm
  (2) NHITAC should be ≥ 10
  (3) E_{vis} should be > 350 MeV
  (4) The maximum number of p.e.s observed in the OD in a sliding 500 nsec time window from -400 nsec to $+600$ nsec (PE_{anti}) should be $< PE_{exp}/1.5$, where PE_{exp} is the expected number of p.e.s in the OD from the potential track length in the OD
  (5) The most energetic ring or the second one should be identified as μ-like
- PC OD through-going sample
  (1) Distance from event vertex to the nearest ID wall should be > 200 cm
  (2) NHITAC should be ≥ 10.
  (3) E_{vis} should be > 350 MeV.
  (4) PE_{anti} should be $> PE_{exp}/1.5$

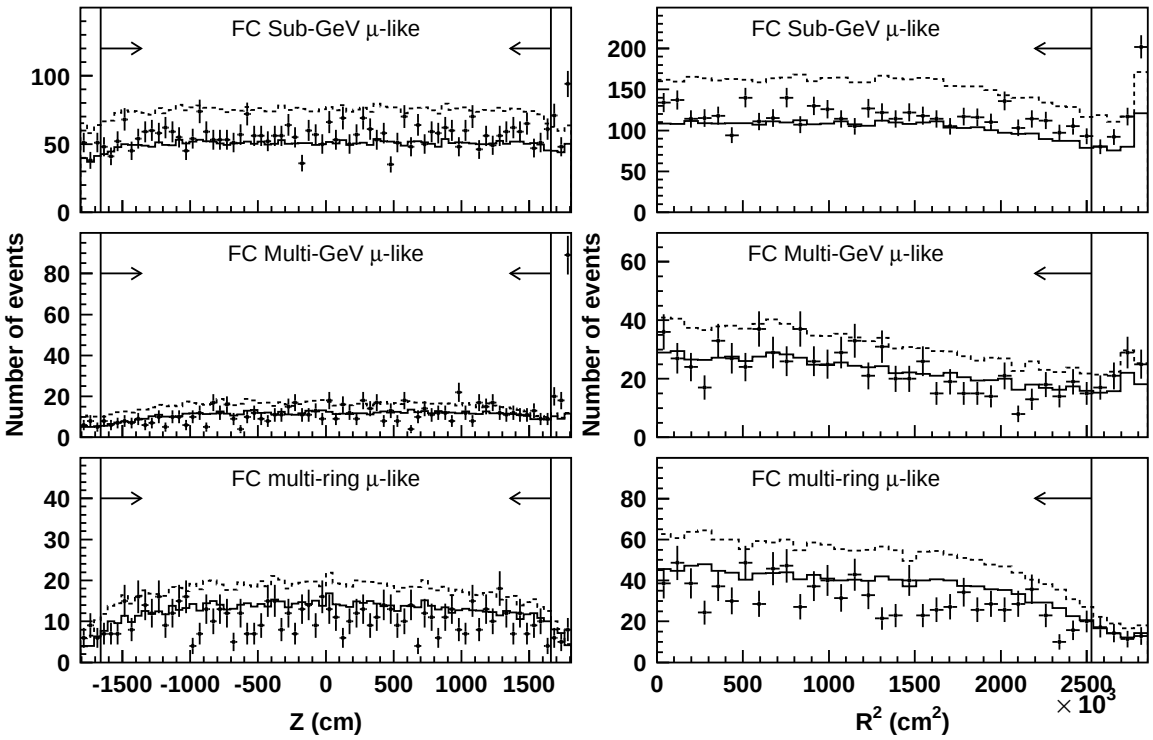

Figure 8.4: Vertex distributions for FC events projected to Z axis (the figures on the left) and R^2 axis (the figures on the right). Events which have the vertex 150 cm away from barrel wall are plotted in the figures on the left, and events which have the vertex 100 cm away from the top and bottom wall are plotted in the figures on the right. Points and the error bars show the data and the statistical errors. Histograms show the Monte Carlo events assuming no oscillation (dashed lines) and oscillation with $(\sin^2 2\theta,\ \Delta m^2) = (1.00,\ 2.0 \times 10^{-3}\,\mathrm{eV}^2)$ (solid lines). Arrows in each figure show the fiducial volume in L/E analysis.

The fiducial volume is expanded for the FC sample from that in the standard analysis in order to increase the statistics of the data, especially for high energy muons. Figure 8.4 shows the reconstructed vertex distributions for the FC sample projected to Z and $R^2 = (X^2 + Y^2)$ axes. Points show the observed data and histograms show the atmospheric neutrino Monte Carlo events assuming no oscillation (dashed lines) and 2-flavor $\nu_\mu \leftrightarrow \nu_\tau$ oscillation with $(\sin^2 2\theta,\ \Delta m^2) = (1.00,\ 2.0 \times 10^{-3}\,\mathrm{eV}^2)$ (solid lines). The live-time of the Monte Carlo events is normalized to that of the observed data. Although there are excesses of the data at the top of the ID in Z distributions, the vertex distributions of the data and Monte Carlo events with neutrino oscillation agree well in fiducial volume and the contamination of the cosmic ray muons is not seen.

To reconstruct the energy and the direction as accurately as possible and apply more efficient cut for each event, the PC sample is separated into two categories using the OD information, "OD stopping events" and "OD through-going events". Muons in the "OD stopping events" are assumed to have stopped in the OD. While the energetic muons in the "OD through-going events" are assumed to have pass through the OD and deposit a fraction of energy to the outside

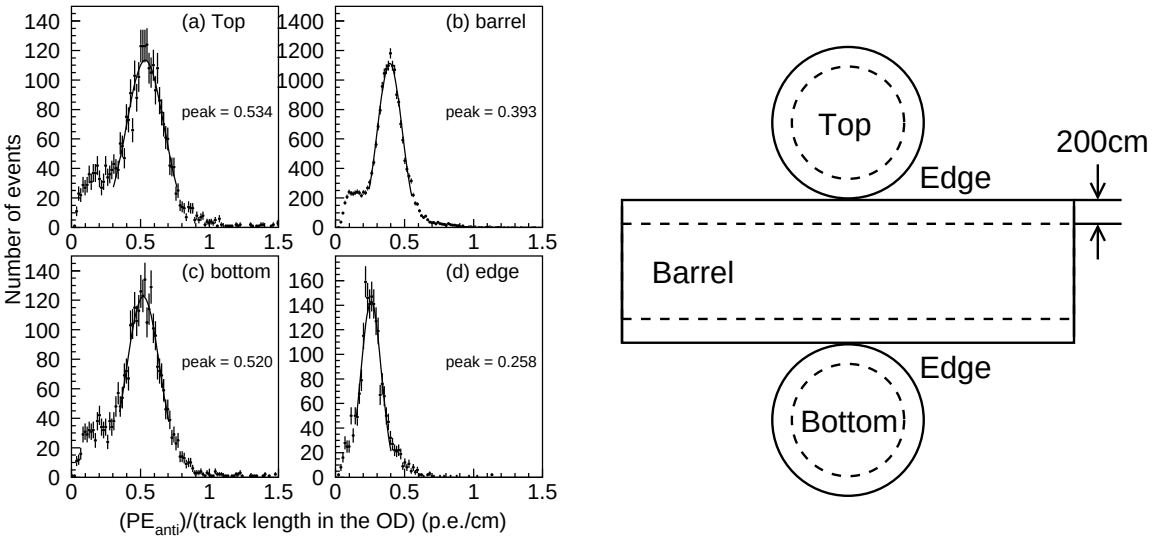

Figure 8.5: Observed p.e.s divided by the track length in the OD for the Monte Carlo simulation for (a) top part of the OD, (b) barrel part, (c) bottom part and (d) edge part (figures on the left), and a schematic view of the division of the OD (right-hand figure). The light collection efficiency of the edge part is relatively lower than the other parts.

of the detector. The observed p.e.s in the OD (PE_{anti}) is compared with the expectation from the potential track length in the OD (PE_{exp}). The potential track length of the exiting muon is estimated from the reconstructed vertex, direction and the detector structure assuming the muon path through the OD. The conversion from the track length to the expected p.e.s changes with the exit point of the muon. Figure 8.5 shows the observed p.e.s divided by the track length in the OD for the Monte Carlo simulation (the left-hand figure), in which the outer detector is divided into four parts as shown in the right-hand figure. The conversion factors to estimate the PE_{exp} are taken from the fitted peaks. The light collection efficiency at the edge of the OD is relatively lower than the other parts. Figure 8.6 shows the scatter plot of the $\mathrm{PE}_{anti}/\mathrm{PE}_{exp}$ and the energy escaped from the ID for the atmospheric neutrino Monte Carlo events (the left-hand figure), and the $\mathrm{PE}_{anti}/\mathrm{PE}_{exp}$ distributions for the data and the Monte Carlo simulation (the right-hand figure) with the criteria to separate OD stopping and OD through-going events. The linear relation between the $\mathrm{PE}_{anti}/\mathrm{PE}_{exp}$ and the escaped energy is clearly seen in the left-hand figure. The peak at $\mathrm{PE}_{anti}/\mathrm{PE}_{exp} = 1.0$ in the right-hand figure indicates the muons pass through the OD. Figure 8.7 shows the escaped energy of energetic muons for OD stopping, OD through-going and all PC events. The sharp peak in OD stopping events at less than 1 GeV means the separation is successfully made. The fifth criterion for OD stopping events aims to reject $\nu_e + \overline{\nu}_e$ CC and NC interactions. The fraction of the $\nu_\mu + \overline{\nu}_\mu$ CC interactions in the OD stopping events increases to 95.1 % from 89.3 % after the cut. That criterion is not necessary for OD through-going events in which the fraction of the $\nu_\mu + \overline{\nu}_\mu$ CC interactions is more than 99 % without any cut.

The event summary for L/E analysis after the primary cuts are shown in Table 8.1 together with the Monte Carlo prediction and the fraction of $\nu_\mu + \overline{\nu}_\mu$ CC interactions.

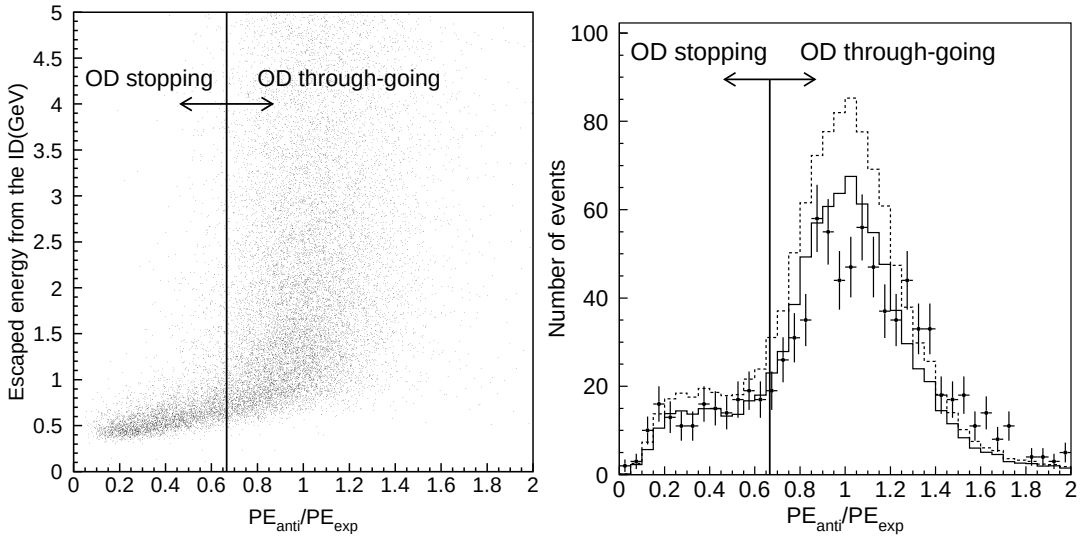

Figure 8.6: Scatter plot of $\mathrm{PE}_{anti}/\mathrm{PE}_{exp}$ and escaped energy from the ID for the atmospheric neutrino Monte Carlo events (the left-hand figure), and the $\mathrm{PE}_{anti}/\mathrm{PE}_{exp}$ distributions for the data and the Monte Carlo simulation (the right-hand figure). Criteria to separate OD stopping and OD through-going events are shown by arrows.

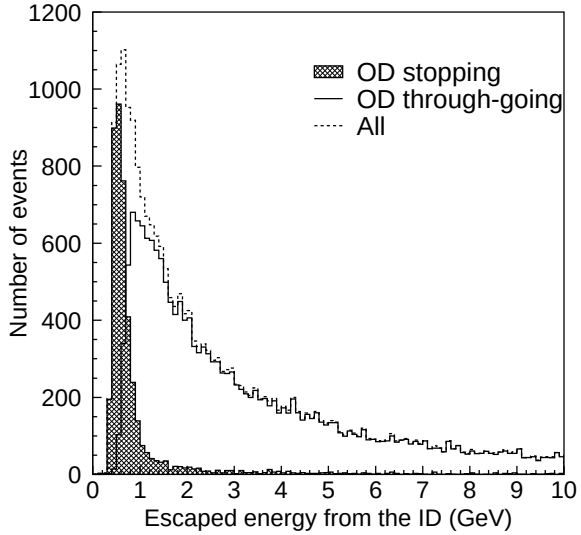

Figure 8.7: Escaped energy of energetic muons for OD stopping (hatched histogram), OD through-going (solid line) and all PC events (dashed line). Sharp peak in OD stopping events at less than 1 GeV indicates the separation is successfully made.

	Data	Monte Carlo	$\nu_\mu + \overline{\nu}_\mu$ CC
FC			
single-ring μ-like	4445	5971.8	(95.1 %)
multi-ring μ-like	702	1159.5	(93.4 %)
PC			
OD stopping	147	176.1	(95.0 %)
OD through-going	740	938.4	(99.0 %)

Table 8.1: Summary of atmospheric neutrino events after the primary cuts for L/E analysis. Only μ-like events are used in L/E analysis. Number of the Monte Carlo events are normalized by the live time of the data. Neutrino oscillation is not included in the Monte Carlo events. Numbers in the parentheses show the fraction of $\nu_\mu + \overline{\nu}_\mu$ CC interactions in each sample.

8.3 Reconstruction of E_ν

Energy of neutrino is estimated from the total energy of charged particles, which is denoted as E_{vis2}, using the polynomial expression as a function of $\log(E_{vis2})$ based on the Monte Carlo simulation.

8.3.1 Energy Reconstruction of Charged Particles

First, the total energy of charged particles is reconstructed. The procedure is different for each category.

FC Single-ring Sample

Energy of charged particle for the FC single-ring sample is equivalent to the energy of muon :

$$E_{vis2} = E_\mu \tag{8.2}$$

where E_μ is the reconstructed energy of muon.

FC Multi-ring Sample

In case of FC multi-ring events, the total energy of charged particles is reconstructed with the assumption that the most energetic ring is originated from a muon via CC interaction and the rest of the rings are due to charged pions for μ-like rings and electrons for e-like rings. With this assumption, the total energy of charged particles is determined by the summation of the energies of all rings :

$$E_{vis2} = E_\mu + \sum_{i=2}^{n} (E_\pi^i \text{ or } E_e^i) \tag{8.3}$$

where n is the number of rings, E_π^i and E_e^i are the energy of the i-th ring assuming charged pion and electron, respectively. Energy of charged pion (more precisely, energy of non-interacting pion) is reconstructed by the following procedure.

Energy of muon and charged pion can be written by :

$$E_\mu = (E_\mu - E_\mu^{th}) + E_\mu^{th} \tag{8.4}$$

$$E_\pi = (E_\pi - E_\pi^{th}) + E_\pi^{th} \tag{8.5}$$

where E_μ^{th} and E_π^{th} are the energy threshold for muon and pion to emit Cherenkov photons in water :

$$E_\mu^{th} = 160\,\mathrm{MeV} \tag{8.6}$$

$$E_\pi^{th} = 212\,\mathrm{MeV} \tag{8.7}$$

Assuming dE/dx in water is a constant and independent to the energy and the particle type, the number of the emitted Cherenkov photons is proportional to the track length. Then, energy deposits from a muon and a pion estimated from the same ring satisfy the following relationship :

$$E_\mu - E_\mu^{th} = E_\pi - E_\pi^{th} \tag{8.8}$$

then,

$$E_\pi = (E_\mu - E_\mu^{th}) + E_\pi^{th} = E_\mu + (E_\pi^{th} - E_\mu^{th}) \tag{8.9}$$

As a result, the energy of non-interacting pion is estimated by :

$$E_\pi = E_\mu + 52\,\mathrm{MeV} \tag{8.10}$$

PC sample

In case of PC events, the total energy of charged particles is estimated as the sum of the following three parts :

$$E_{vis2} = E_{inner} + E_{dead} + E_{anti} \tag{8.11}$$

where E_{inner}, E_{dead} and E_{anti} are the energy deposit in each detector region.

E_{inner} is the total energy of the charged particles observed in the ID. Before the reconstruction of the E_{inner}, the number of rings for PC events is corrected. Since the incoming neutrinos have high energy ($\sim$10 GeV) and produce a charged lepton (mostly muon) and other particles (mostly pions) in parallel for PC events, more than two Cherenkov rings are likely to overlap and be mis-reconstructed as one ring. These mis-reconstructed ring can be recognized by comparing the track length and the reconstructed momentum of the particle. Figure 8.8 shows the P_μ/D_{inner} distribution for quasi-elastic (QE) interactions and non-QE interactions in the atmospheric neutrino Monte Carlo PC single-ring sample, where P_μ is the reconstructed momentum of the muon and D_{inner} is the track length in the ID estimated from the reconstructed vertex and direction. P_μ distribution of non-QE interactions has a broad tail due to overlapping pions and/or the other particles. These overlapping rings make energy resolution worse. If the most energetic muon ring satisfies $P_\mu/D_{inner} > 3.0\,\mathrm{MeV/cm}$, the ring is separated to a muon ring with momentum estimated from the track length in the ID as $D_{inner} \times dE/dx$, where $dE/dx = 2.4\,\mathrm{MeV/cm}$, and an electron ring. The expected charge from the muon is subtracted from the ring, and the remaining charge is used to reconstruct the momentum of the

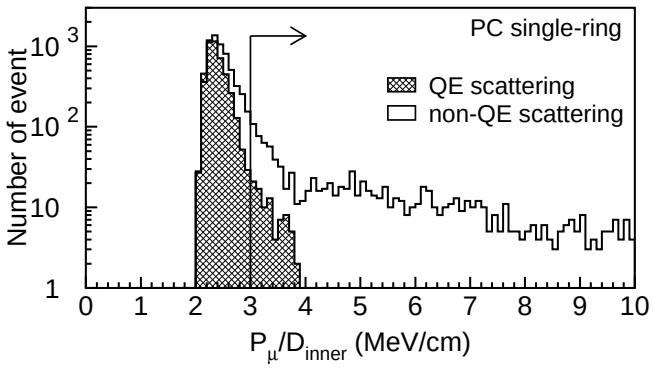

Figure 8.8: P_μ/D_{inner} distribution for quasi-elastic (QE) interactions (hatched histogram) and non-QE interactions (white histogram) in the atmospheric neutrino Monte Carlo PC single-ring sample. Events at the right from the arrow are divided into two rings, a muon ring and an electron ring.

electron. After that, E_{inner} is reconstructed by the same way as that for the FC single-ring or FC multi-ring events according to the number of rings including the overlapped one.

E_{dead} is the energy deposit in the dead region which exists between the ID and the OD (see Section 2.2.1). Since an energetic muon penetrates the dead zone by the definition of the PC sample, the energy deposit in the dead zone can be estimated from the track length in the dead zone and the dE/dx of muon. E_{dead} is estimated by :

$$E_{dead} = D_{dead} \times dE/dx \tag{8.12}$$

where D_{dead} is the track length in the dead zone estimated from the vertex position and the ring direction, and dE/dx of muon is taken to be 2.4 MeV/cm.

E_{anti} is the energy deposit in the OD. E_{anti} is determined by a similar way with that for the E_{dead}. The track length in the OD is estimated from the reconstructed vertex and direction assuming the muon stopped at the half range in the OD for OD stopping events and assuming the muon penetrates the OD for OD through-going events. E_{anti} is estimated by :

$$E_{anti} = 0.5 \times D_{anti} \times dE/dx \quad \text{(for OD stopping events)} \tag{8.13}$$

$$E_{anti} = D_{anti} \times dE/dx \quad \text{(for OD through-going events)} \tag{8.14}$$

where D_{anti} is the track length in the OD assuming that the muon penetrates the OD, and dE/dx of muon is taken to be 2.4 MeV/cm.

8.3.2 Reconstruction of Neutrino Energy

Energy of neutrino is estimated from the total energy of charged particles (E_{vis2}) using the polynomial expression as a function of the $\log(E_{vis2})$. The function is made by fitting the ratio of E_ν and E_{vis2} for each sample based on the Monte Carlo simulation. The fitting function take the following form :

$$E_\nu^{rec} = E_{vis2} \times (a + b \times x + c \times x^2 + d \times x^3) \tag{8.15}$$

$$x = \log(E_{vis2}) \tag{8.16}$$

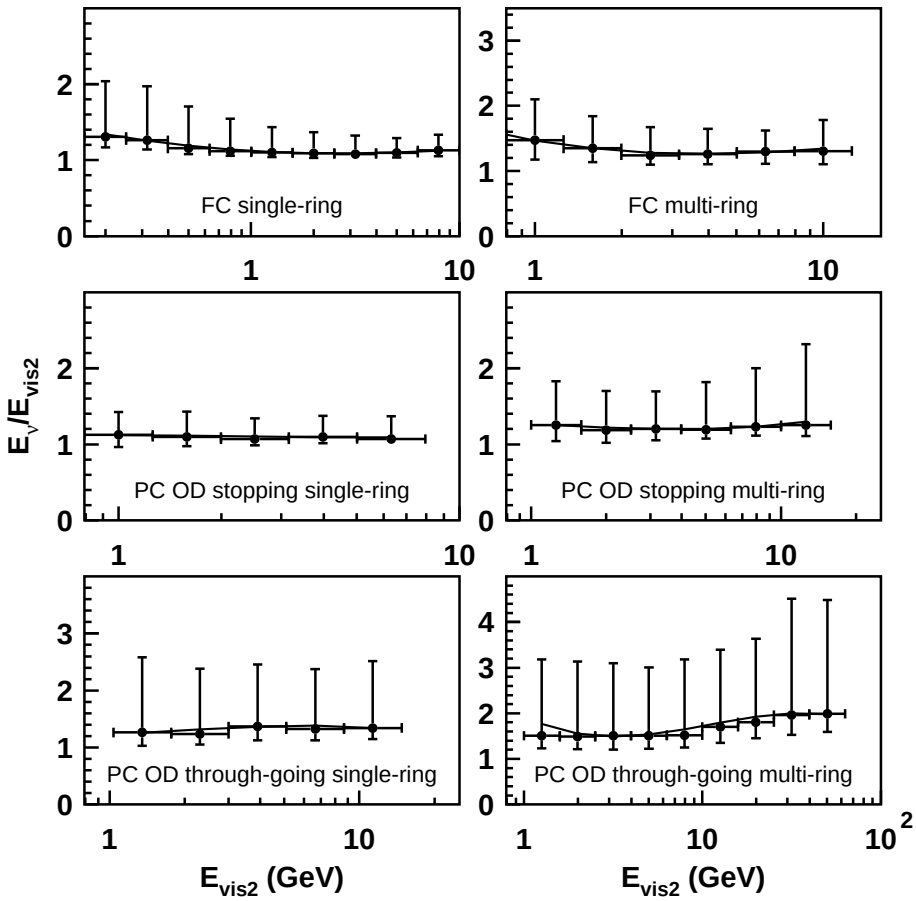

Figure 8.9: Fitting results to reconstruct neutrino energy from total energy of charged particles for the FC single-ring, FC multi-ring, PC OD stopping single-ring, PC OD stopping multi-ring, PC OD through-going single-ring and PC OD through-going multi-ring sample. Points show the peak point of the E_ν/E_{vis2} distributions, and the error bars show the range which include 68 % of the events. Solid lines show the result of fitting.

where E_ν^{rec} is the reconstructed energy of neutrinos.

Figure 8.9 shows the fitting results for each sample: FC single-ring; FC multi-ring; PC OD stopping single-ring; PC OD stopping multi-ring; PC OD through-going single-ring; and PC OD through-going multi-ring. Since the relations between E_ν and E_{vis2} are different for single-ring and multi-ring events, the polynomial functions are separately made. Figure 8.10 shows the E_ν/E_ν^{rec} distributions in atmospheric neutrino Monte Carlo simulation and Figure 8.11 shows the resolution of the neutrino energy for each sample as a function of the lepton momentum for FC single-ring events and E_{vis2} for FC multi-ring events. The resolutions are 30 % and 17 % for FC single-ring Sub-GeV and Multi-GeV samples, 27 % and 22 % for FC multi-ring Sub-GeV and Multi-GeV samples, 24 % and 66 % for PC OD stopping and through-going samples, respectively.

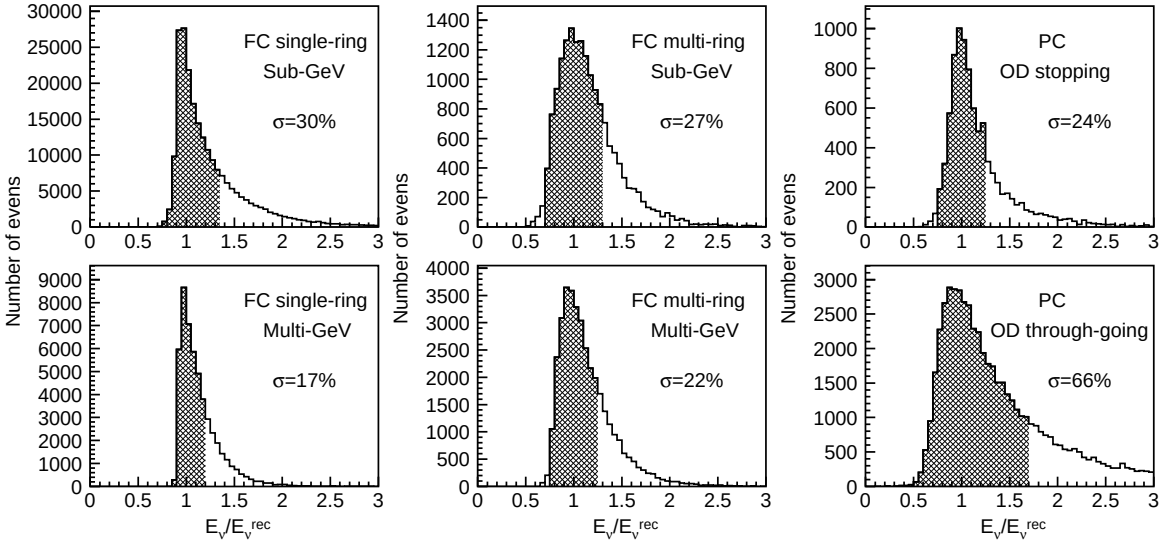

Figure 8.10: E_ν/E_ν^{rec} distributions for FC single-ring, FC multi-ring and PC OD stopping and through-going samples. The resolution of energy reconstruction is defined as the width in which 68 % of the events are included.

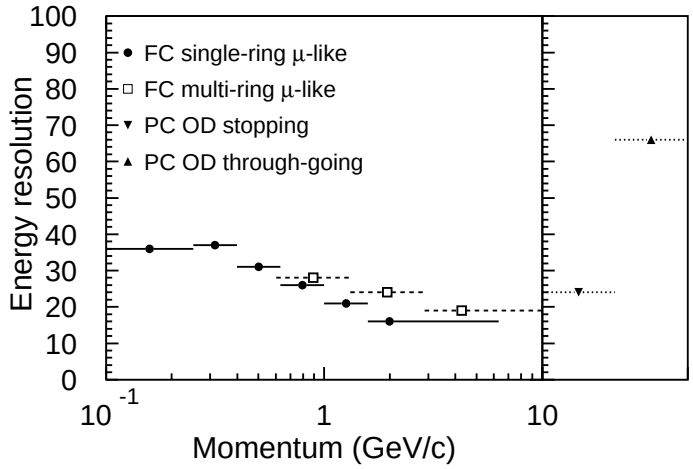

Figure 8.11: Resolution of neutrino energy for each sample as a function of the lepton momentum for FC single-ring events and E_{vis2} for FC multi-ring events.

8.4 Reconstruction of L_ν

Flight length of neutrino is determined from the neutrino incident zenith angle, although the energy and the flavor are also involved. First, the direction of neutrino is estimated for each sample by a different way. Then, the neutrino flight length is calculated from the zenith angle of the reconstructed direction.

8.4.1 Reconstruction of Neutrino Direction

FC Single-ring Sample

The direction of neutrino for FC single-ring sample is simply assumed to be the same as the reconstructed direction of muon. Zenith angle of neutrino is reconstructed as follows :

$$\cos\Theta_\nu^{rec} = \cos\Theta_\mu \tag{8.17}$$

where $\cos\Theta_\mu$ and $\cos\Theta_\nu^{rec}$ are cosine of the reconstructed zenith angle of muon and neutrino, respectively.

FC Multi-ring Sample

In case of FC multi-ring events, the direction of the neutrino is estimated as the sum of the momentum weighted directions over all identified rings. The zenith angle of the neutrino is reconstructed as follows :

$$\cos\Theta_\nu^{rec} = \cos\Theta_{sum} \tag{8.18}$$

$$\vec{d}_{sum} = p_\mu \cdot \vec{d}_1 + \sum_{i=2}^{n} (p_\pi \text{ or } p_e) \cdot \vec{d}_i \tag{8.19}$$

where n is the number of rings, p_μ, p_e and p_π are the momentum of muon, electron and charged pion, $\vec{d}_i$ is the direction of the i-th ring, and $\vec{d}_{sum}$ and $\cos\Theta_{sum}$ are the direction and the cosine of zenith angle of the momentum weighted vector sum, respectively.

PC Sample

In case of PC events, the direction of neutrino is estimated as the direction of the muon for single-ring events. For PC multi-ring events, the direction of neutrino is estimated as the sum of the momentum weighted directions with a factor for energetic muon ring. Direction and zenith angle of neutrino is estimated as follows :

$$\cos\Theta_\nu^{rec} = \cos\Theta_\mu \qquad \text{for single-ring events} \tag{8.20}$$

$$\cos\Theta_\nu^{rec} = \cos\Theta_{sum} \qquad \text{for multi-ring events} \tag{8.21}$$

$$\vec{d}_{sum} = \alpha \cdot p_\mu \cdot \vec{d}_1 + \sum_{i=2}^{n} (p_\pi \text{ or } p_e) \cdot \vec{d}_i \tag{8.22}$$

where α is the numerical factor taken to be 2.0 for OD stopping events and 4.0 for OD through-going events, which are optimized to get the best performance of the reconstruction.

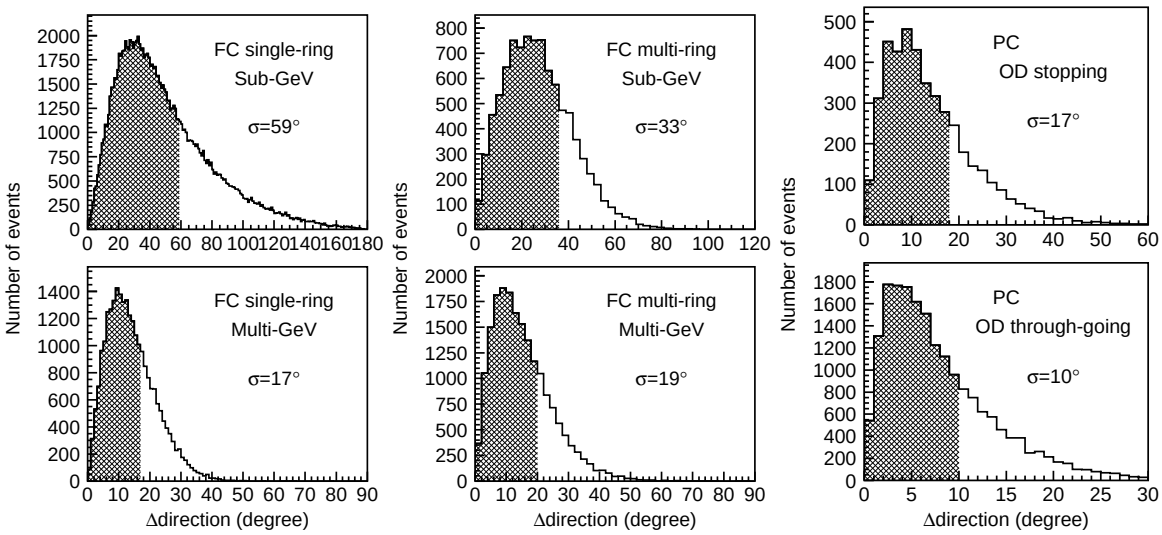

Figure 8.12: Angular difference between the true neutrino direction and the reconstructed direction. The resolution is defined as the width in which 68 % of the events are included.

Figure 8.12 shows the angular difference between the true neutrino direction and the reconstructed one and Figure 8.13 shows the angular resolution of the neutrino direction for each sample as a function of the lepton momentum for FC single-ring events and E_{vis2} for FC multi-ring events.

8.4.2 Reconstruction of Neutrino Flight Length

The flight length of neutrino is strongly related to the zenith angle, especially for the upward going neutrinos. The production height of neutrinos in the atmosphere should be considered for downward and horizontally going neutrinos. The relation between zenith angle and flight length for ν_μ and the probability distribution of the neutrino flight length for horizontally going neutrinos is shown in Figure 8.14, based on the Honda flux calculation. In the L/E analysis, the neutrino flight length is estimated from the reconstructed zenith angle and neutrino energy, assuming ν_μ interactions.

8.5 L/E Resolution Cut

8.5.1 Resolution map

Neutrino energy and flight length are reconstructed as described in the previous sections and L_ν/E_ν can be reconstructed. Figure 8.15 shows the reconstructed L/E distribution for the data and the Monte Carlo events assuming neutrino oscillation with $(\sin^2 2\theta,\ \Delta m^2) = (1.00,\ 2.0 \times 10^{-3}\ \mathrm{eV}^2)$ in the left-hand figure and L/E contour plots on $(\cos\Theta_\nu, E_\nu)$ coordinates in the right-hand figure. The peak below 100 (km/GeV) in L/E distribution comes from the downward-going events and that above 1000 (km/GeV) is due to upward-going events. Events which have L/E

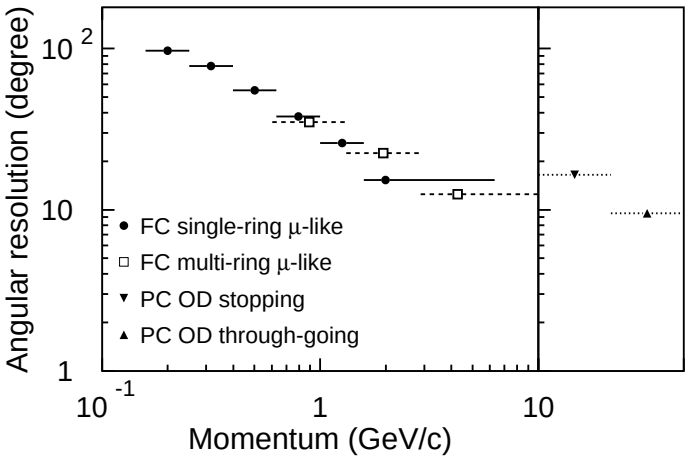

Figure 8.13: Angular resolution of neutrino direction for each sample as a function of the lepton momentum for FC single-ring events and E_{vis2} for FC multi-ring events.

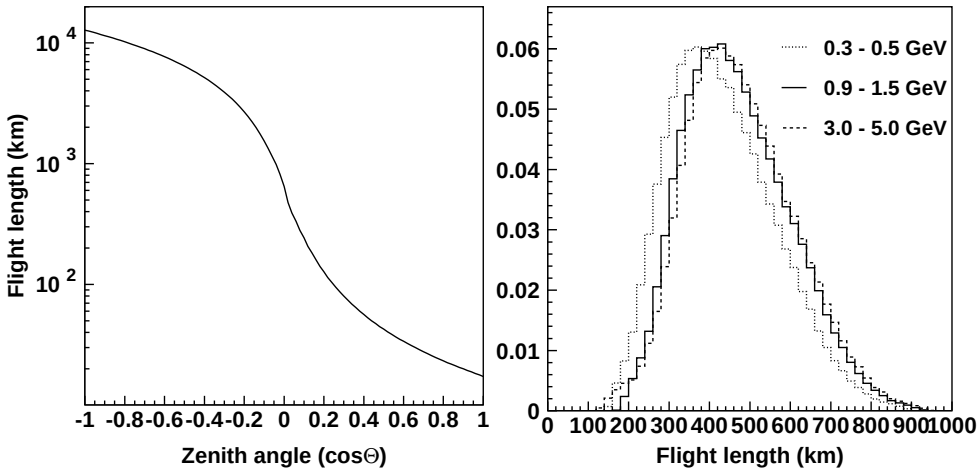

Figure 8.14: Mean neutrino flight length as a function of the zenith angle for 1 GeV ν_μ (left), and the probability distribution of flight length for horizontally going muon neutrinos with energy of $0.3-0.5$ GeV (dotted line), $0.9-1.5$ GeV (solid line) and $3.0-5.0$ GeV (dashed line), respectively (right).

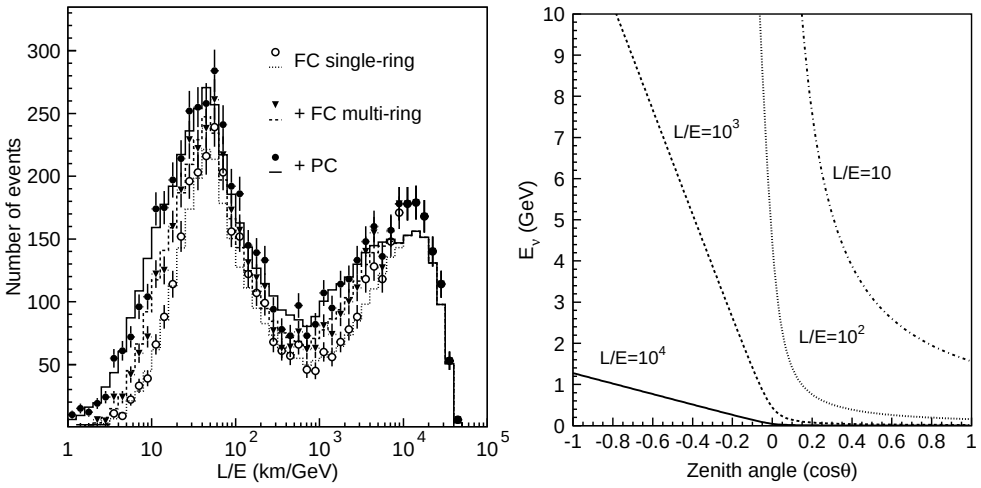

Figure 8.15: Fraction of each sample as a function of the reconstructed L/E for the data (points) and the Monte Carlo events (lines) assuming neutrino oscillation with $(\sin^2 2\theta,\ \Delta m^2) = (1.00,\ 2.0 \times 10^{-3}\,\mathrm{eV}^2)$ (left), and L/E contours on $(\cos\Theta_\nu, E_\nu)$ coordinates (right).

between 100 and 1000 (km/GeV) originate in horizontally going events and high energy upward-going events as indicated in the right-hand figure. Since the statistics of the lower energy events are larger than that of the higher energy events, the numbers of the events which have L/E between 10 and 100 (km/GeV) and between 1000 and 10000 (km/GeV) are larger than the other regions.

In order to determine cuts to select events which are expected to have high resolution of L/E, resolutions of the L/E are calculated on each point in $(\cos\Theta_\nu^{rec}, E_\nu^{rec})$ coordinates. Since the L_ν/L_ν^{rec} and E_ν/E_ν^{rec} have asymmetric distributions, the peak of the $(L_\nu/E_\nu)/(L_\nu^{rec}/E_\nu^{rec})$ is shifted from unity. The shifts make the L/E resolution worse, and the sample-by-sample difference of the shifts of L/E smear the information of L/E. In order to avoid this, reconstructed L/E are corrected as $(L/E)' = \delta_{L/E} \cdot (L/E)$, where $\delta_{L/E}$ is the correction factor of L/E. The correction factor is chosen to give the best L/E resolution. Figure 8.17 shows contours of the resolution of L/E on $(\cos\Theta_\nu^{rec}, E_\nu^{rec})$ coordinate, which are used for selection criteria in L/E analysis. Extremely high energy events ($E_{vis2} > 10\,\mathrm{GeV}$ for FC single-ring events and $E_{vis2} > 50\,\mathrm{GeV}$ for FC multi-ring and PC events) are not used in this analysis because the statistics of such events are small and it is impossible to estimate the resolution of L/E. The $(L_\nu/E_\nu)/(L_\nu^{rec}/E_\nu^{rec})$ distributions for FC single-ring, FC multi-ring, PC OD stopping and PC OD through-going events are shown in Figure 8.16, in which dashed lines show the events after primary cuts and solid lines show the events satisfying $\Delta(L/E) < 70\,\%$. In Figure 8.18, the left-hand figure shows the L/E distribution with L/E resolution cut, $\Delta(L/E) < 70\,\%$, for atmospheric neutrino Monte Carlo events assuming no oscillation (dashed line) and $\nu_\mu \leftrightarrow \nu_\tau$ oscillation with $(\sin^2 2\theta,\ \Delta m^2) = (1.00,\ 2.0 \times 10^{-3}\,\mathrm{eV}^2)$ (solid line), and the right-hand figure shows the ratio of the Monte Carlo with neutrino oscillation to that without oscillation. A dip due to first maximum oscillation probability is clearly seen in Monte Carlo simulation events in case of neutrino oscillation. The cut value is determined in the next section.

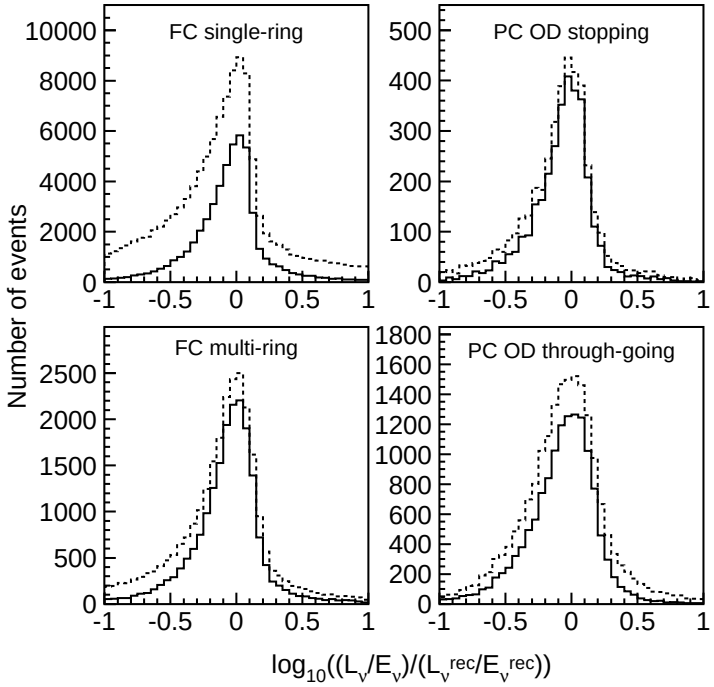

Figure 8.16: $\log((L_\nu/E_\nu)/(L_\nu^{erc}/E_\nu^{rec}))$ distributions for FC single-ring (upper left), FC multi-ring (lower left), PC OD stopping (upper right) and PC OD through-going events (lower right) without any cut (dashed lines) and with resolution cut $\Delta(L/E) < 70\,\%$ (solid lines).

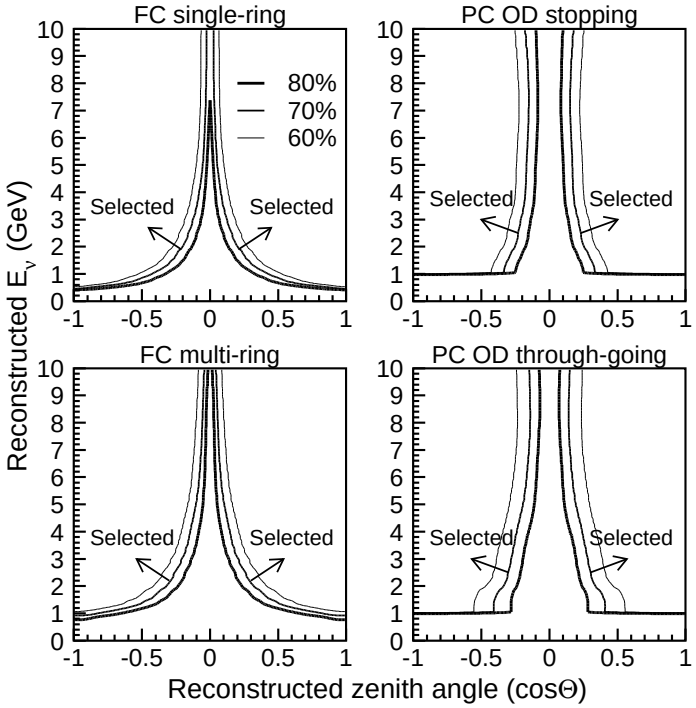

Figure 8.17: Contour plots of L/E resolution in ($\cos\theta_n^{rec}$, E_ν^{rec}) coordinate for FC single-ring (upper left), FC multi-ring (lower left), PC OD stopping (upper right) and PC OD through-going samples (lower right). Lines with three kinds of thickness correspond to the L/E resolution of 60, 70 and 80 %, respectively.

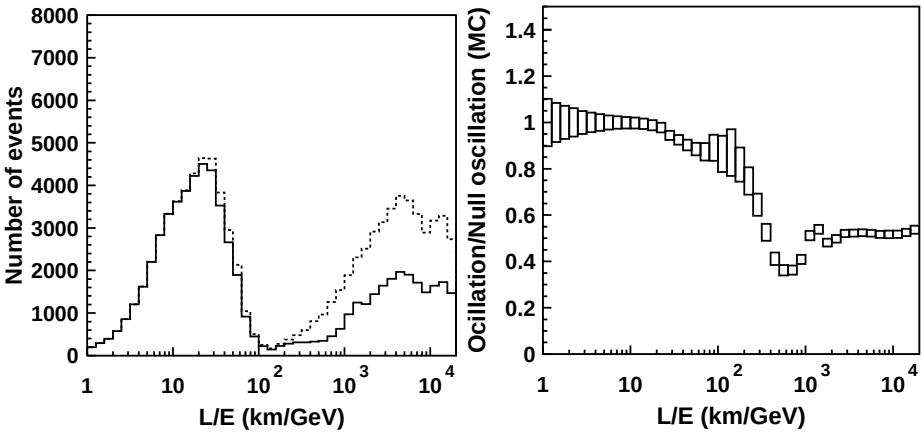

Figure 8.18: The left-hand figure shows L/E distribution with L/E resolution cut, $\Delta(L/E) < 70\,\%$, for atmospheric neutrino Monte Carlo events assuming no oscillation (dashed line) and $\nu_\mu \leftrightarrow \nu_\tau$ oscillation with $(\sin^2 2\theta,\ \Delta m^2) = (1.00,\ 2.0 \times 10^{-3}\,\mathrm{eV}^2)$ (solid line). The right-hand figure shows the ratio of the two distributions (Oscillation)/(Null oscillation), in which the height of the boxes show the statistical errors of Monte Carlo events (100 yr).

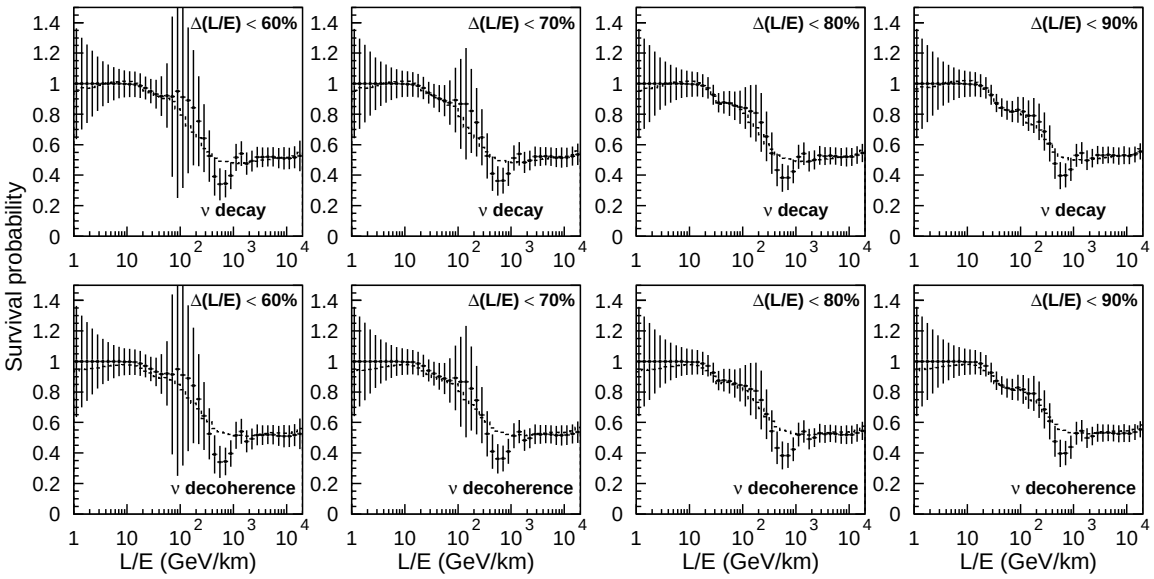

Figure 8.19: Survival probabilities as a function of reconstructed L/E for atmospheric neutrino Monte Carlo events, in which points show the probabilities assuming neutrino oscillation with $(\sin^2 2\theta,\ \Delta m^2) = (1.00,\ 2.0 \times 10^{-3}\,\mathrm{eV}^2)$, the error bars show the statistical errors normalized to the live time of the data (1489.2 days), and the dashed lines show the probabilities for the best-fit of neutrino decay (upper figures) and neutrino decoherence (lower figures). Four figures correspond to L/E resolution cuts of 60, 70, 80 and 90 %.

8.5.2 Determination of Resolution Cut

The selection criteria of the L/E resolution cut are determined to maximize the sensitivity to distinguish neutrino oscillation from the other models, neutrino decay and neutrino decoherence. Figure 8.19 shows the survival probability distributions as a function of reconstructed L/E for the atmospheric neutrino Monte Carlo events with various L/E resolution cuts, in which the points show the probabilities assuming neutrino oscillation with $(\sin^2 2\theta,\ \Delta m^2) = (1.00,\ 2.0 \times 10^{-3}\,\mathrm{eV}^2)$ and the error bars show the statistical errors normalized to the live-time of the SK-I data (1489.2 days), and the lines show that of the best-fit for neutrino decay (upper figures) and neutrino decoherence (lower figures). Absolute normalization factor is considered as free parameter in the fit. Figure 8.20 shows the differences of log likelihood between neutrino oscillation and the other models as a function of the resolution cut value. The resolution cut of $\Delta(L/E) < 70\,\%$ is adopted, since this cut value gives a most significant difference of log likelihood between neutrino oscillation and the other models.

The event summary for L/E analysis after 70 % of the L/E resolution cut are shown in Table 8.2 together with the Monte Carlo prediction and the fraction of $\nu_\mu + \overline{\nu}_\mu$ CC interactions.

8.6 L/E Distributions

In Figure 8.21 the left-hand figure shows the L/E distributions for FC + PC observed data and the atmospheric neutrino Monte Carlo events without neutrino oscillation, and the right-

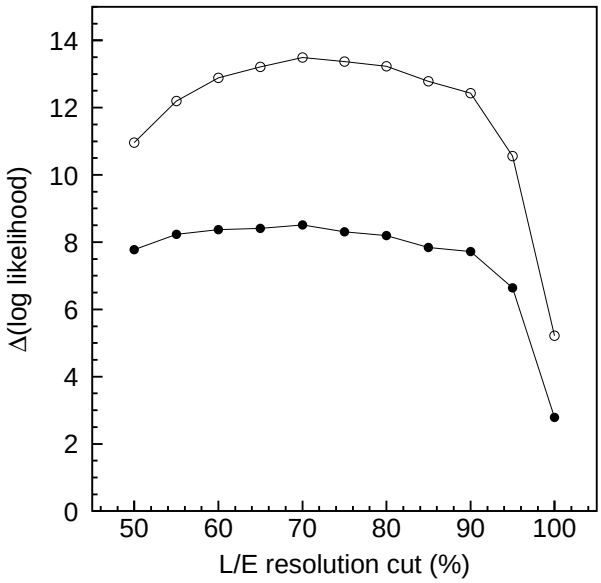

Figure 8.20: Differences of log likelihood between neutrino oscillation and neutrino decay (black points) and between neutrino oscillation and neutrino decoherence (white points) as a function of the resolution cut value. The cut is determined as $\Delta(L/E) < 70\,\%$ to give most significant differences between neutrino oscillation and the other models.

	Data	Monte Carlo	$\nu_\mu + \overline{\nu}_\mu$ CC
FC			
single-ring μ-like	1619	2105.6	(98.3 %)
multi-ring μ-like	502	813.0	(94.2 %)
PC			
OD stopping	114	137.0	(95.4 %)
OD through-going	491	670.1	(99.2 %)

Table 8.2: Summary of atmospheric neutrino events after 70 % of L/E resolution cut. Number of the Monte Carlo events are normalized by the live time of the data. Neutrino oscillation is not included in the Monte Carlo events. Numbers in the parentheses show the fraction of $\nu_\mu + \overline{\nu}_\mu$ CC interactions in each sample.

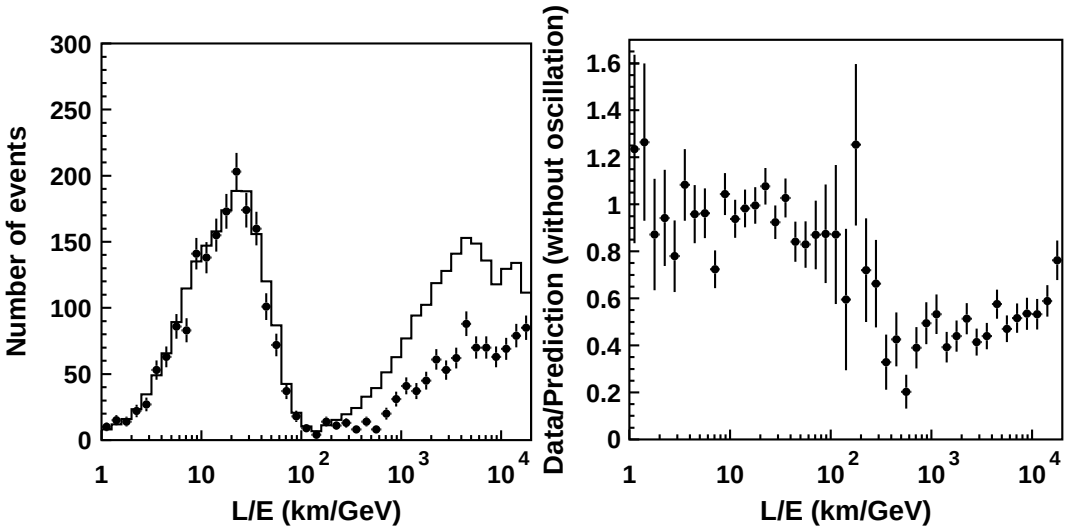

Figure 8.21: The left-hand figure shows L/E distributions for FC + PC data (points with error bars) and the atmospheric neutrino Monte Carlo events without neutrino oscillation (line), and the right-hand figure shows the ratio of the data to the Monte Carlo events. L/E resolution cut is set to be 70 % for those figures. The error bars of data indicate only statistical errors.

hand figure shows the ratio of the data to the Monte Carlo events without neutrino oscillation, in which live-time of the Monte Carlo events is normalized to that of the data. The clear first dip expected from neutrino oscillation is seen in the observed data.

Figure 8.22 shows the fraction of each sample as a function of the reconstructed neutrino energy (left) and L/E (right) for the data and the atmospheric neutrino Monte Carlo events, in which 2-flavor $\nu_\mu \leftrightarrow \nu_\tau$ oscillation is assumed with $(\sin^2 2\theta,\ \Delta m^2) = (1.00,\ 2.0 \times 10^{-3}\,\mathrm{eV}^2)$. The horizontally going events have been eliminated by L/E resolution cut and only high energy events, mainly PC events, remained around the dip at several hundred km/GeV.

8.7 Neutrino Oscillation Analysis Using L/E Distribution

An neutrino oscillation analysis is carried out using the L/E distribution. In the analysis, the L/E distribution is divided into 43 bins from $log(L/E) = 0.0$ to 4.3, and a test is carried out to evaluate the goodness of the fit between the data and the expectation by a likelihood method. The same systematic errors as that for the standard oscillation analysis (see Section 7.2.1) are considered in this analysis.

Since the statistic of the data are not enough, the analysis is performed based on Poisson statistics. The likelihood with systematic errors is defined as follows :

$$L(N_{\mathrm{exp}}, N_{\mathrm{obs}}) = \prod_i \frac{\exp(-N_i^{\mathrm{exp}})(N_i^{\mathrm{exp}})^{N_i^{\mathrm{obs}}}}{N_i^{\mathrm{obs}}!} \times \prod_j \exp\left(\frac{\epsilon^j}{\sigma_j^{sys}}\right) \tag{8.23}$$

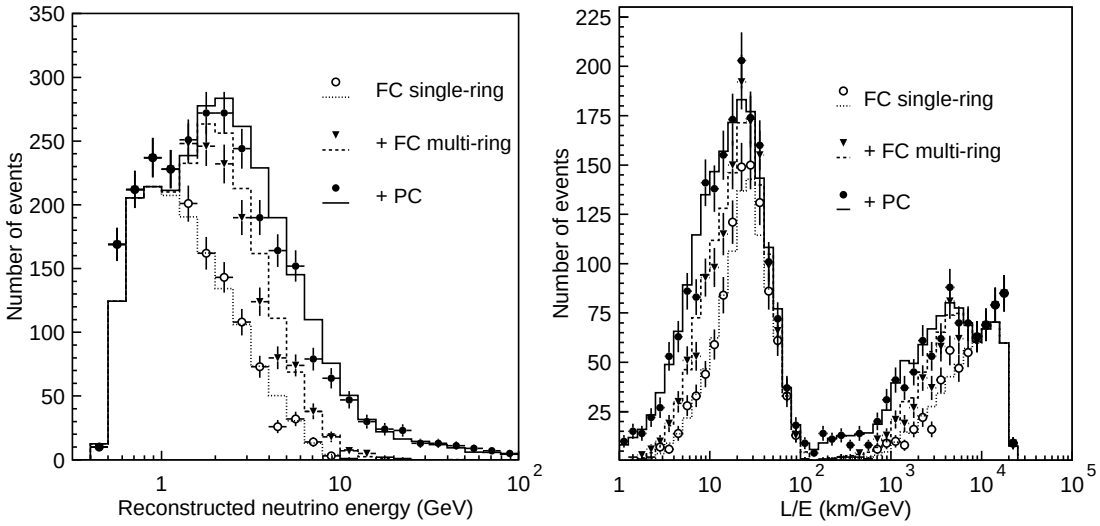

Figure 8.22: Fraction of each sample as a function of reconstructed neutrino energy (left) and L/E (right) for the data (points) and the atmospheric neutrino Monte Carlo events (lines), in which 2-flavor $\nu_\mu \leftrightarrow \nu_\tau$ oscillation is assumed with $(\sin^2 2\theta,\ \Delta m^2) = (1.00,\ 2.0 \times 10^{-3}\,\mathrm{eV}^2)$.

We define the log likelihood as $\tilde{\chi^2}$ as follows :

$$\begin{aligned}
\tilde{\chi^2} &\equiv -2\ln\left(\frac{L(N_{\rm obs}, N_{\rm exp})}{L(N_{\rm obs}, N_{\rm obs})}\right) \\
&= \sum_{i=1}^{43}\left[2\left(N_i^{\rm exp}(1+\sum_{j=1}^{37} f_j^i\cdot\epsilon^j) - N_i^{\rm obs}\right) + 2N_i^{\rm obs}\ln\left(\frac{N_i^{\rm obs}}{N_i^{\rm exp}(1+\sum_{j=1}^{37} f_j^i\cdot\epsilon^j)}\right)\right] \\
&\qquad + \sum_{j=1}^{22}\left(\frac{\epsilon^j}{\sigma_j^{sys}}\right)^2
\end{aligned} \tag{8.24}$$

where $N_i^{\rm obs}$ is the number of observed events in the i-th bin, $N_i^{\rm exp}$ is the expected number of events from the Monte Carlo simulation. $N_i^{\rm exp}$ are corrected for neutrino oscillation and the systematic uncertainties. ϵ_j represents the systematic uncertainty and the parameter f_j^i represents the fractional change in the predicted event rate in the i-th bin due to a variation of the parameter ϵ_j. The second sum in the definition collects the contributions from the systematic errors.

The systematic errors considered in this analysis are listed in Tables 8.3, 8.4, 8.5 and 8.6 with their estimated uncertainties and the resulting best-fit values. The explanations of the systematic error sources have already been described in section 7.2.1. During the fit, these parameters are optimized to give a minimum $\tilde{\chi^2}$ for each choice of oscillation parameters.

A global scan is carried out on a $(\sin^2 2\theta,\ \log\Delta m^2)$ grid, minimizing $\tilde{\chi^2}$ by optimizing 22 systematic error parameters. Using the similar way as shown in section 7.1 [103], the local minimum of $\tilde{\chi^2}$ can be mathematically derived at each grid point. The minimization of the $\tilde{\chi^2}$

			uncertainty (%)	best-fit (%)
(A) Systematic uncertainties in neutrino flux				
Absolute normalization			free	5.6
Anti-neutrino/neutrino ratio	$\overline{\nu}_\mu/\nu_\mu$		5.0	0.1
Up/down ratio	FC single-ring	< 400 MeV	0.8	0.0
		> 400 MeV	2.1	0.1
		Multi-GeV	0.7	0.0
	FC multi-ring	Sub-GeV	1.0	0.0
		Multi-GeV	0.2	0.0
	PC		0.1	0.0
Horizontal/vertical (3D)	FC single-ring	< 400 MeV	0.4	0.0
		> 400 MeV	2.5	0.2
		Multi-GeV	3.1	0.3
	FC multi-ring	Sub-GeV	2.0	0.2
		Multi-GeV	3.1	0.3
	PC		0.8	0.1
L_ν (production height)			10.0[a]	-0.4
Energy spectrum			0.05[b]	-0.007
Sample-by-sample normalization	FC Multi-GeV		5.0	-2.7

Table 8.3: Summary of systematic uncertainties in the prediction of the atmospheric neutrino flux. Estimated uncertainty and the best-fit value are listed for each error.

[a] 10 % uncertainty in atmospheric density structure
[b] 0.05 uncertainty in spectral index of neutrino energy

	uncertainty (%)	best-fit (%)
(B) Systematic uncertainties in neutrino interaction		
Quasi-elastic scattering (total cross section)	15.0	9.5
Single-meson production (total cross section)	15.0	-7.5
Multi-pion production (a few GeV region)	1.0[a]	1.04
Multi-pion production (total cross section)	5.0	-0.2
Coherent pion production (total cross section)	30.0	-0.1
NC/CC ratio	20.0	0.6

Table 8.4: Summary of systematic uncertainties in neutrino interactions. Estimated uncertainty and the best-fit value are listed for each error.

[a] Difference from the Bodek model is set to 1.0

		uncertainty (%)	best-fit (%)
(C) Systematic uncertainties in event selection			
Reduction for fully contained event		1.0	0.0
Reduction for partially contained event		3.2	0.2
Separation of FC and PC event		2.6	0.0
Up/down ratio (non-neutrino background)	Sub-GeV	0.2	0.0
	Multi-GeV	0.4	0.0

Table 8.5: Summary of systematic uncertainties in event selection. Estimated uncertainty and the best-fit value are listed for each error.

			uncertainty (%)	best-fit (%)
(D) Systematic uncertainties in event reconstruction				
Single-ring/multi-ring separation	FC single-ring	< 400 MeV	2.0	0.5
		> 400 MeV	1.2	0.3
		Multi-GeV	5.2	1.3
	FC multi-ring	Sub-GeV	3.4	-0.8
		Multi-GeV	6.1	-1.4
Particle identification	FC single-ring	Sub-GeV	0.5	-0.1
		Multi-GeV	0.4	-0.1
	FC multi-ring	Sub-GeV	5.4	-1.3
		Multi-GeV	3.2	-0.7
Energy calibration for FC event			2.0[a]	0.2
Up/down symmetry of energy calibration			0.6[b]	0.1

Table 8.6: Summary of systematic uncertainties in event reconstruction. Estimated uncertainty and the best-fit value are listed for each error.

[a] 2 % uncertainty in absolute energy scale

[b] 0.6 % uncertainty in up/down symmetry of energy calibration

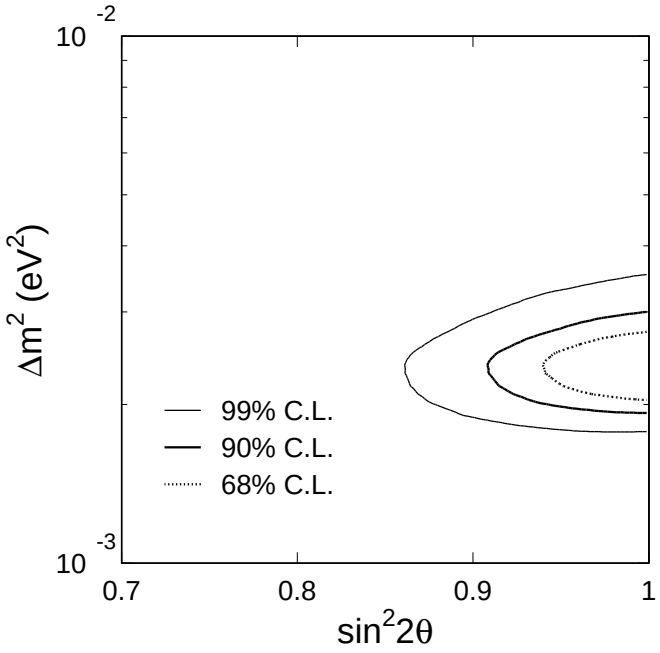

Figure 8.23: Allowed oscillation parameters from L/E analysis for $\nu_\mu \leftrightarrow \nu_\tau$ oscillations. Horizontal axis shows $\sin^2 2\theta$ and vertical axis shows Δm^2. Three contours correspond to the 68 % (dotted line), 90 % (solid line) and 99 % (thin line) C.L. allowed regions, respectively.

in Equation 8.24 is equivalent to solving the following $k = 1, 22$ linear equations:

$$\sum_{j=1}^{22}\left[\frac{1}{(\sigma_j^{sys})^2}\delta_{jk} + \sum_{i=1}^{43} N_i^{\rm exp}\cdot f_j^i \cdot f_k^i\right]\cdot\epsilon_k = \sum_{i=1}^{43}\left[\left(1+(f_j^i\cdot\epsilon^j)^2+...\right)N_i^{\rm obs} - N_i^{\rm exp}\right]\cdot f_k^i \quad (8.25)$$

where σ_j^{sys} is the estimated uncertainty in the parameter ϵ_j.

The minimum $\tilde{\chi^2}$ is 37.7/40 d.o.f. at $(\sin^2 2\theta,\ \Delta m^2) = (1.00,\ 2.4\times10^{-3}\,{\rm eV}^2)$, where θ is the mixing angle and $\Delta m^2 = m_3^2 - m_2^2$ is the difference of the squared mass of ν_3 and ν_2. Systematic errors at the best-fit point are shown in Tables 8.3, 8.4, 8.5 and 8.6. Including unphysical parameter region ($\sin^2 2\theta > 1$), the best-fit is obtained at $(\sin^2 2\theta,\ \Delta m^2) = (1.03,\ 2.4\times10^{-3}\,{\rm eV}^2)$, at which $\tilde{\chi^2}_{min}$ is lower than that in physical region by 0.26 . Figure 8.23 shows the contour plots of the allowed oscillation parameters regions. Three contours correspond to the 68%, 90% and 99% confidence levels (C.L.) allowed regions, which are defined to be $\tilde{\chi^2} = \tilde{\chi^2}_{min} + 2.59$, 4.96, and 9.58 based on the minimum in the physical region, respectively. These intervals are derived by using the 2-dimensional Gaussian approximation from the minimum in the unphysical region [105]. The 90 % allowed parameter region is obtained as follows :

$$1.9\times10^{-3}\,{\rm eV}^2 \ < \ \Delta m^2 < 3.1\times10^{-3}\,{\rm eV}^2 \quad (8.26)$$

$$0.90 \ < \ \sin^2 2\theta \quad (8.27)$$

The result is consistent with that of the standard oscillation analysis. Figure 8.24 shows the

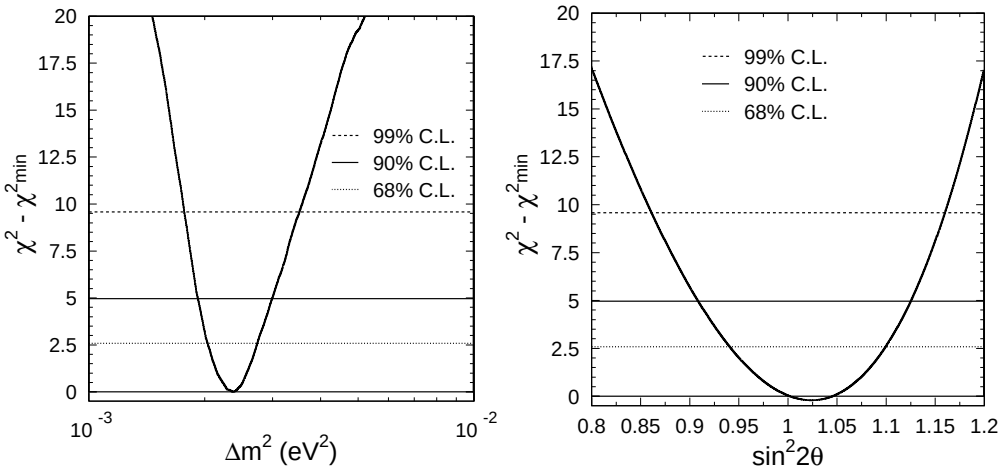

Figure 8.24: $\tilde{\chi^2} - \tilde{\chi^2}_{min}$ distributions as a function of Δm^2 (left) and $\sin^2 2\theta$ (right), in which $\tilde{\chi^2}_{min}$ is the minimum value of $\tilde{\chi^2}$ in physical parameter region. $\sin^2 2\theta$ is set to be 1.00 in the left-hand figure and Δ^2_m is set be 2.4×10^{-3}eV^2 in the right-hand figure. Three horizontal lines correspond to the 68 % (dotted line), 90 % (solid line) and 99 % (dashed line) C.L. intervals, respectively.

$\tilde{\chi^2} - \tilde{\chi^2}_{min}$ distributions as a function of $\sin^2 2\theta$ and Δm^2, which are sliced at $\Delta m^2 = 2.4 \times 10^{-3}\,\mathrm{eV}^2$ and $\sin^2 2\theta = 1.00$.

Figure 8.25 shows the ratio of data to the Monte Carlo events without neutrino oscillation together with the best-fit expectation for 2-flavor $\nu_\mu \leftrightarrow \nu_\tau$ oscillations as a function of the reconstructed L/E. The $\nu_\mu \leftrightarrow \nu_\tau$ oscillation hypothesis gives a good explanation to the observed data. If the Monte Carlo prediction reproduces the nature, we expect that the L/E distribution should be flat at small and large L/E values as shown in Figure 8.18 (right). However, due to various systematic errors, the distribution shows a slight inclination. This inclination is mainly due to the uncertainties in neutrino interactions listed in Table 8.4.

8.8 Test for Non-Standard Models

8.8.1 Neutrino Decay

Neutrino decay models can explain the zenith angle dependent deficit of muon neutrinos as predicted by neutrino oscillations [106]. In the Standard Model, neutrinos cannot decay because they are described as massless particles. However, several models predict the decay of massive neutrinos. The lower limits of the lifetime of neutrinos are obtained only for radiative decay channels as $\tau/m > 15.4\,\mathrm{sec/eV}$, where τ is the lifetime of neutrino and m is the neutrino mass [107].

Phenomenologically, neutrino decay and neutrino oscillation can coexist. Assuming ν_μ is a mixing of mass eigenstates ν_2 and ν_3, and ν_2 to be the only unstable state and has a decay

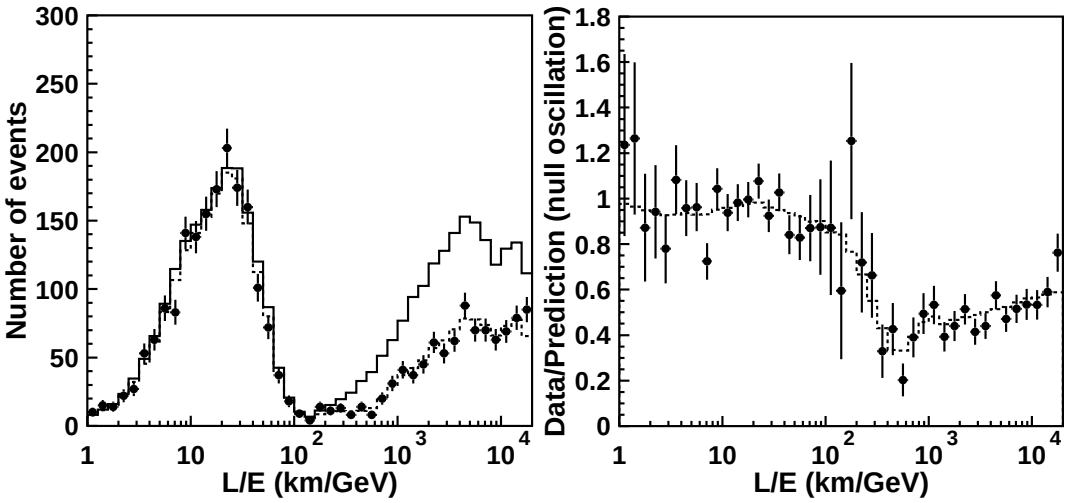

Figure 8.25: The left-hand figure shows the L/E distributions for the FC + PC data (points with error bars), the Monte Carlo events without neutrino oscillation (solid line) and the best-fit expectation for 2-flavor $\nu_\mu \leftrightarrow \nu_\tau$ oscillations (dashed line), and the right-hand figure shows the ratio of data to the Monte Carlo events without oscillation (points) together with the best-fit expectation for 2-flavor $\nu_\mu \leftrightarrow \nu_\tau$ oscillations (dashed line) as a function of the reconstructed L/E.

channel, the survival probability of ν_μ is expressed by :

$$P(\nu_\mu \to \nu_\mu) = \sin^4\theta + \cos^4\theta \exp\left(-\frac{m_2}{\tau_2}\frac{L_\nu}{E_\nu}\right) + 2\sin^2\theta\cos^2\theta \exp\left(-\frac{m_2}{2\tau_2}\frac{L_\nu}{E_\nu}\right)\cos\left(\frac{\Delta m^2 L_\nu}{2E_\nu}\right) \quad (8.28)$$

where m_2 and τ_2 are the mass and the lifetime of ν_2, θ and Δm^2 are the neutrino oscillation parameters, respectively. In case $\tau_2 \to \infty$, Equation (8.28) becomes Equation (8.1).

If $\Delta m^2 \to 0$, in which the oscillation length becomes much longer than the decay length and the effect of neutrino oscillation is negligibly small, the survival probability of ν_μ is written as :

$$P(\nu_\mu \to \nu_\mu) = \left[\sin^2\theta + \cos^2\theta \exp\left(-\frac{m_2}{2\tau_2}\frac{L_\nu}{E_\nu}\right)\right]^2 \quad (8.29)$$

The survival probability as a function of L_ν/E_ν is shown in Figure 8.1 with a dashed line.

A fit to the data is carried out assuming neutrino decay and neutrino oscillation coexist with 3 parameters ($\cos^2\theta$, m_2/τ_2, Δm^2) as expressed by Equation (8.28). The definition of the log likelihood ($\equiv \tilde{\chi}^2$) and the systematic errors used in the fit are identical to that for the neutrino oscillation analysis. Figure 8.26 shows the contour plots of the allowed parameters regions projected to the (m_2/τ_2, Δm^2) plane optimizing the mixing angle parameter $\cos^2\theta$. The minimum value of the $\tilde{\chi}^2$ is 37.7/40 d.o.f. obtained at (m_2/τ_2, Δm^2)=(1.0×10^{-7} GeV/km, 2.4×10^{-3} eV^2) on the plane, where $\cos^2\theta = 0.5$ at the minimum. Three contours correspond to the

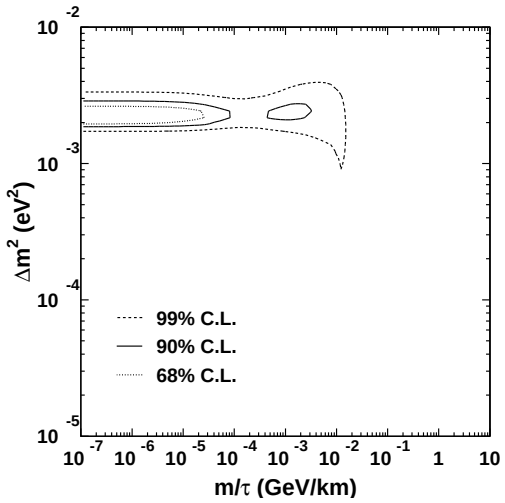

Figure 8.26: Contour plots of the allowed parameters regions projected to the (m/τ, Δm^2) plane optimizing the mixing angle parameter $\cos^2\theta$. The horizontal axis shows m/τ which characterizes neutrino decoherence and the vertical axis shows Δm^2 characterizes neutrino oscillation. The small Δm^2 region corresponds to the neutrino decay dominant case.

68%, 90% and 99% C.L. allowed regions, which are defined to be $\tilde{\chi^2} = \tilde{\chi^2}_{min}+$ 2.30, 4.61, and 9.21, respectively. The case that only neutrino decay is dominant ($\Delta m^2 \to 0$) is disfavored at more than 99 % C.L. .

In case of no oscillation ($\Delta m^2 = 0$) as expressed by Equation (8.28), the best-fit is obtained at ($\cos^2\theta$, m_2/τ_2) = (0.34, 1.41×10^{-2} GeV/km), and the minimum $\tilde{\chi^2}$ value is $\tilde{\chi^2}_{min} =$ 47.5/40 d.o.f., which is 9.8 larger than that for the case of neutrino oscillation. Figure 8.27 shows the ratio of data to the Monte Carlo events without neutrino oscillation together with the best-fit expectation for neutrino decay and best-fit for 2-flavor $\nu_\mu \leftrightarrow \nu_\tau$ oscillations as a function of the reconstructed L/E. Since neutrino decay model cannot predict the dip seen in the L/E distribution of the data, the $\tilde{\chi^2}$ difference from neutrino oscillation model becomes large.

8.8.2 Neutrino Decoherence

The deficit of ν_μ in atmospheric neutrino can be explained by a decoherence effect of neutrinos induced by new physics (e.g., by quantum gravity) [108]. The effect of decoherence is parameterized by $\gamma = \gamma_0(E_\nu/\mathrm{GeV})^n$, and the survival probability of ν_μ is written as :

$$P(\nu_\mu \to \nu_\mu) = 1 - \frac{1}{2}\sin^2 2\theta \left[1 - \exp(-\gamma L_\nu)\cos\left(\frac{\Delta m^2 L_\nu}{2E_\nu}\right)\right] \tag{8.30}$$

In the limit $\gamma \to 0$, Equation (8.30) reduces to Equation (8.1).

The case $n = -1$ gives a probable solution to explain zenith angle dependence of muon deficits in atmospheric neutrino data from Super-Kamiokande. If $\Delta m^2 \to 0$, pure decoherence case, the ν_μ survival probability is expressed by :

$$P(\nu_\mu \to \nu_\mu) = 1 - \frac{1}{2}\sin^2 2\theta \left[1 - \exp\left(-\gamma_0 \frac{L_\nu}{E_\nu}\right)\right] \tag{8.31}$$

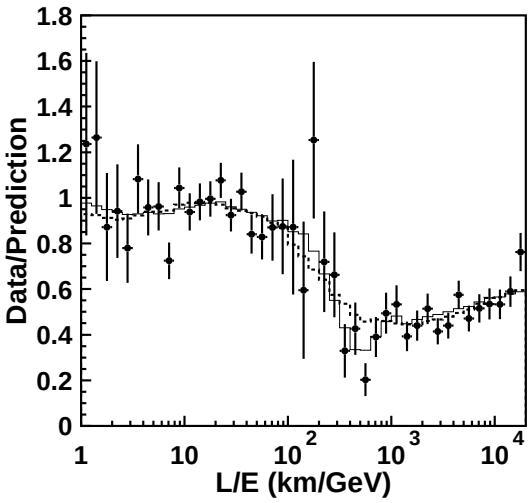

Figure 8.27: Ratio of data to the Monte Carlo events without neutrino oscillation (points) together with the best-fit expectation for neutrino decay (dashed line) and best-fit for 2-flavor $\nu_\mu \leftrightarrow \nu_\tau$ oscillations (thin solid line) as a function of the reconstructed L/E.

The survival probability as a function of L_ν/E_ν is shown in Figure 8.1 with a dotted line.

A fit to the data is carried out assuming neutrino decoherence and neutrino oscillation coexist with 3 parameters ($\sin^2 2\theta$, γ_0, Δm^2). The definition of the log likelihood ($\equiv \tilde{\chi}^2$) is identical to that for the neutrino oscillation analysis. Figure 8.28 shows the contour plots of the allowed parameters regions projected to the (γ_0, Δm^2) plane optimizing the mixing angle parameter $\sin^2 2\theta$. The minimum $\tilde{\chi}^2$ value is 37.7/40 d.o.f. obtained at (γ_0, Δm^2)=(1.0^{-24} GeV/km, 2.4×10^{-3} eV^2) on the plane, where $\sin^2 2\theta = 1.0$ at the minimum. Three contours correspond to the 68%, 90% and 99% C.L. allowed regions, which are defined to be $\tilde{\chi}^2 = \tilde{\chi}^2{}_{min} + 2.30$, 4.61, and 9.21, respectively. The case that only neutrino decoherence is dominant ($\Delta m^2 \to 0$) is disfavored at more than 99 % C.L..

In case of no oscillation ($\Delta m^2 = 0$) as expressed by Equation (8.31), the best-fit is obtained at ($\sin^2 2\theta$, γ_0) = (1.00, 1.32×10^{-21} GeV/km). The minimum $\tilde{\chi}^2$ value is $\tilde{\chi}^2{}_{min} = 52.5/40$ d.o.f., which is 14.8 larger than that for neutrino oscillation. Figure 8.29 shows the ratio of data to the Monte Carlo events without neutrino oscillation (points) together with the best-fit expectation for neutrino decoherence (dashed line) and best-fit for 2-flavor $\nu_\mu \leftrightarrow \nu_\tau$ oscillations (thin solid line) as a function of the reconstructed L/E. Neutrino decoherence model cannot predict the dip seen in the L/E distribution of the data.

8.9 Discussion

The present L/E analysis shows that the muon neutrino data sample has a dip in the L/E distribution as expected by neutrino oscillations. The data are inconsistent with the neutrino decay and neutrino decoherence models at more 99 % C.L., because these models cannot predict the dip seen in the L/E distribution of the data. This is the first statistically significant evidence

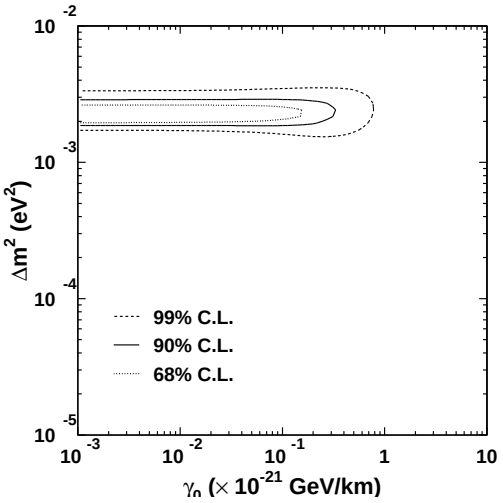

Figure 8.28: Contour plots of the allowed parameters regions projected to the (γ_0, Δm^2) plane optimizing the mixing angle parameter $\sin^2 2\theta$. The horizontal axis shows γ_0 which characterizes neutrino decoherence and the vertical axis shows Δm^2 characterizes neutrino oscillation. The small Δm^2 region corresponds to the neutrino decoherence dominant case.

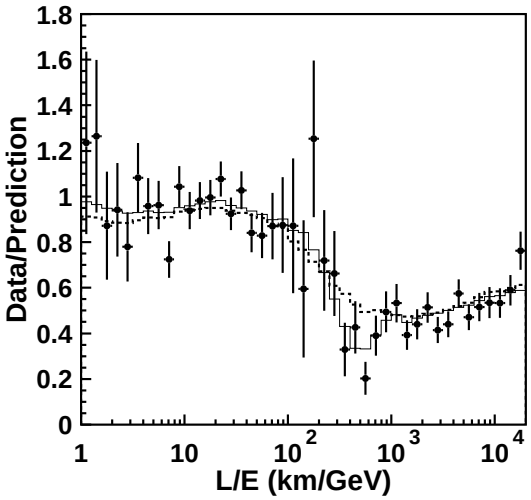

Figure 8.29: Ratio of data to the Monte Carlo events without neutrino oscillation (points) together with the best-fit expectation for neutrino decoherence (dashed line) and best-fit for 2-flavor $\nu_\mu \leftrightarrow \nu_\tau$ oscillations (thin solid line) as a function of the reconstructed L/E.

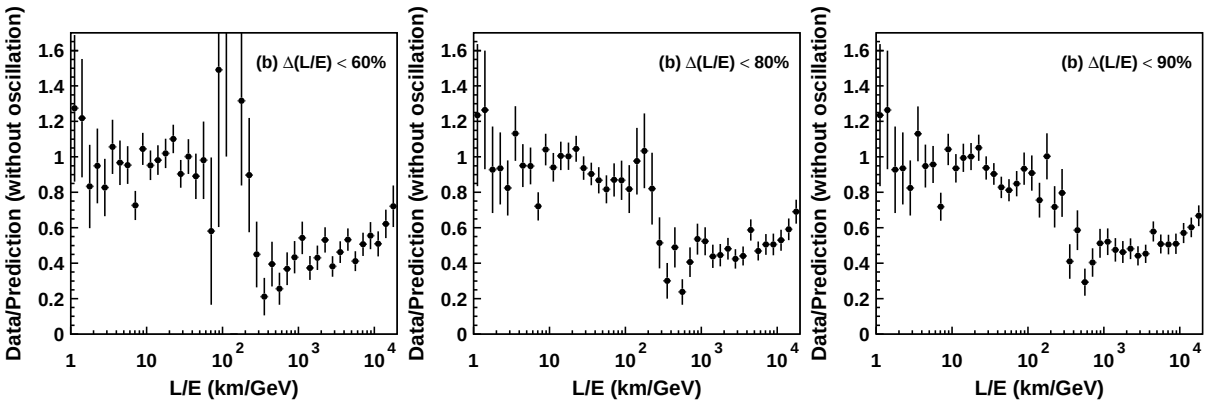

Figure 8.30: Ratio of the data to the Monte Carlo events without oscillation as a function of L/E with various L/E resolution cuts, $\Delta(L/E) < 60\,\%$ (a), $80\,\%$ (b) and $90\,\%$ (c).

that the neutrino flavor transition probability obeys the sinusoidal function as predicted in neutrino flavor oscillation formula. The reliability of the obtained L/E distribution is discussed in this section with some information for checking.

Figure 8.30 shows the ratio of the data to the Monte Carlo events without oscillation as a function of L/E with various L/E resolution cuts, $\Delta(L/E) < 60\,\%$ (a), $80\,\%$ (b) and $90\,\%$ (c). The cut is set to be $70\,\%$ in the determination of the neutrino oscillation parameters. The first dip expected from neutrino oscillation is seen in the observed data also for the other L/E resolution cuts. We can confirm that the first dip in L/E distribution of the data is not restricted to a specific L/E resolution cut. Figure 8.31 shows contour plot of the $90\,\%$ C.L. allowed oscillation parameters regions with various cuts. The best-fit parameters are obtained at $(\sin^2 2\theta,\, \Delta m^2) = (1.00,\, 2.4 \times 10^{-3}\,\mathrm{eV}^2)$ for $60\,\%$ cut, $(1.00,\, 2.4 \times 10^{-3}\,\mathrm{eV}^2)$ for $80\,\%$ cut, $(1.00,\, 2.2 \times 10^{-3}\,\mathrm{eV}^2)$ for $90\,\%$ cut and $(1.00,\, 2.4 \times 10^{-3}\,\mathrm{eV}^2)$ for $70\,\%$ cut. Although the statistics of the data are different for each L/E resolution cut, the allowed oscillation parameters regions are consistent.

Figure 8.32 shows the L/E distributions for the FC single-ring e-like sample, in which L/E resolution cut is set to be $70\,\%$. The L/E resolution cut is identical to that for FC single-ring μ-like sample. The observed data is consistent with the Monte Carlo prediction without oscillation, and the ratio is consistent with flat as expected.

In order to check the systematic discrepancy between the data and the Monte Carlo prediction without the influence of neutrino oscillation, the plus/minus sign of the cosine of zenith angle is reversed, then the L/E distribution is checked. This conversion corresponds to turning the direction of neutrinos upside down. Since the oscillation probabilities for the upward-going events are sufficiently small in the up/down reversed sample, the L/E distribution of the data around the first dip point, $300 < L/E < 700\,\mathrm{GeV/km}$, can be checked without the influence of neutrino oscillation. Using the up/down reversed sample, Figure 8.33 shows L/E distribution for the data together with the Monte Carlo events without oscillation and the best-fit expectation for 2-flavor $\nu_\mu \leftrightarrow \nu_\tau$ oscillations. No significant dip is seen in L/E distribution for the up/down reversed sample around the point where a dip is observed in the original sample.

These information give a confirmation that a dip in L/E distribution of muon data sample is not a systematic discrepancy but a direct evidence of neutrino oscillation.

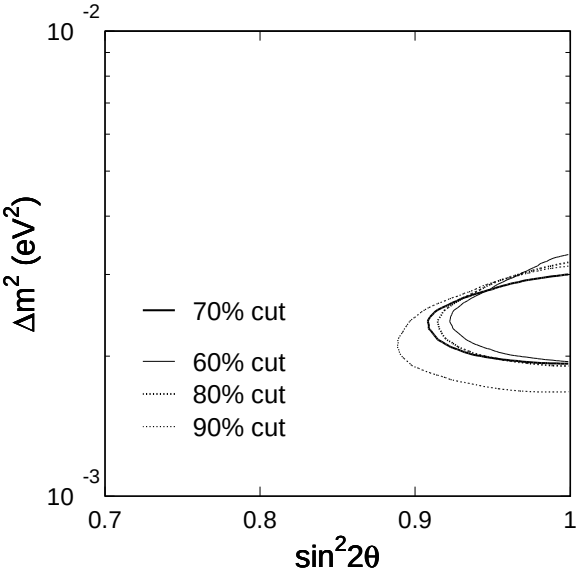

Figure 8.31: Ratio of the data to the Monte Carlo events without oscillation as a function of L/E with various L/E resolution cuts, $\Delta(L/E) < 60\,\%$ (a), $80\,\%$ (b) and $90\,\%$ (c).

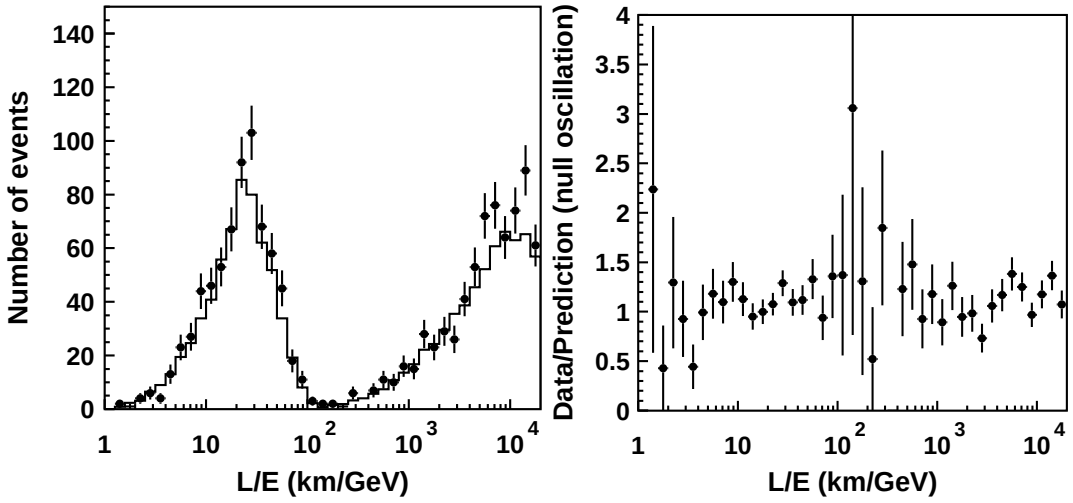

Figure 8.32: L/E distributions for the FC single-ring e-like sample (left-hand figure) for the data (points) and the Monte Carlo events without oscillation (solid line), and the ratio of the data to the Monte Carlo prediction (right-hand figure). L/E resolution cut is set to be $70\,\%$, which is identical to that for FC single-ring μ-like sample.

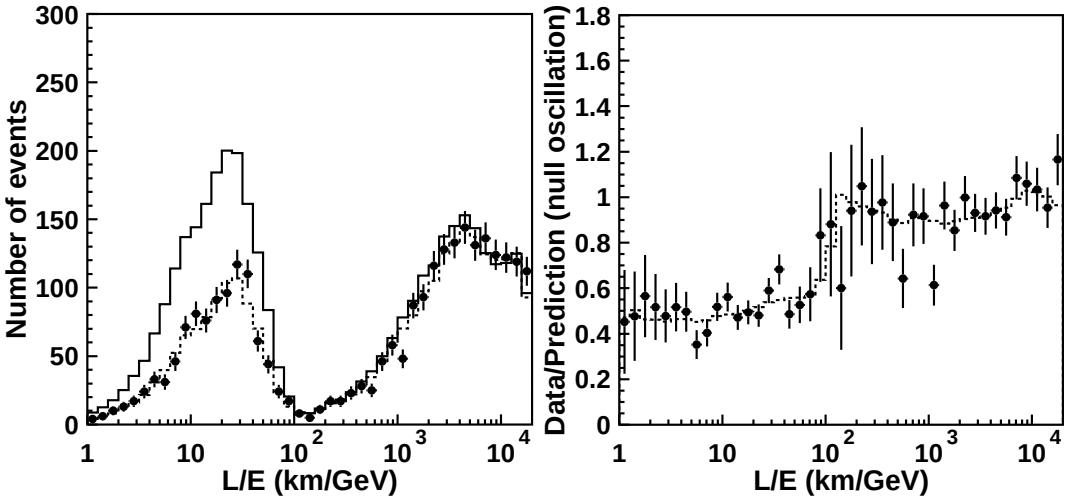

Figure 8.33: L/E distribution for the up/down reversed sample (left-hand figure) for the data (points), the Monte Carlo events without oscillation (solid line) and the best-fit expectation for 2-flavor $\nu_\mu \leftrightarrow \nu_\tau$ oscillations (dashed line), and the ratios of the data and the best-fit to the Monte Carlo prediction without oscillation (right-hand figure). L/E resolution cut is set to be 70 %..

Chapter 9

Conclusion

1489.2 days exposure data for fully-contained and partially-contained events, and 1645.9 days data for upward-going muons were accumulated during SK-I running period. The observed atmospheric neutrino data exhibit zenith angle dependent deficit of muon neutrinos. This deficit is inconsistent with the prediction from the Monte Carlo simulation and cannot be explained by any combination of the statistical and systematic errors, while the data are consistently explained by the prediction with neutrino oscillations.

A fit to the zenith angle distribution of the data was carried out assuming neutrino oscillations. The best fit parameters for 2-flavor $\nu_\mu \leftrightarrow \nu_\tau$ oscillation is $(\sin^2 2\theta,\ \Delta m^2) = (1.00,\ 2.1 \times 10^{-3}\,\mathrm{eV}^2)$. The 90 % confidence level allowed parameter region is :

$$1.5 \times 10^{-3}\,\mathrm{eV}^2 < \Delta m^2 < 3.4 \times 10^{-3}\,\mathrm{eV}^2 \quad (9.1)$$

$$0.92 < \sin^2 2\theta \quad (9.2)$$

The flavor transition probability of muon neutrinos was measured by comparing the observed L/E distribution with the Monte Carlo prediction without neutrino oscillation. The muon neutrino data show a dip in the L/E distribution as expected by neutrino oscillations. A fit to the observed L/E distribution assuming 2-flavor $\nu_\mu \leftrightarrow \nu_\tau$ oscillation gives the minimum χ^2 value of 37.7/40 d.o.f. .

The observed dip in the L/E distribution cannot be predicted by alternative models that could explain the zenith angle dependent deficit of muon neutrinos. These alternative models include neutrino decay and neutrino decoherence models. Tests to the neutrino decay and neutrino decoherence were carried out using the L/E distribution. The minimum χ^2 values are $\chi^2_{min} = 47.5/40$ d.o.f. for neutrino decay and $\chi^2_{min} = 52.5/40$ d.o.f. for neutrino decoherence. The difference of the χ^2 are 9.8 and 14.8, respectively. As a result of a fit to the data assuming neutrino decay and neutrino decoherence coexist with neutrino oscillation, the neutrino decay dominant case and neutrino decoherence dominant case ($\Delta m^2 \to 0$) are both disfavored at more than 99 % C.L. .

The observed L/E distribution, expecially the dip, is concluded to be the first statistically significant evidence that the neutrino flavor transition probability obeys the sinusoidal function as predicted in neutrino flavor oscillation formula.

As a result of the L/E analysis, the best fit parameters for 2-flavor $\nu_\mu \leftrightarrow \nu_\tau$ oscillation is obtained at $(\sin^2 2\theta,\ \Delta m^2) = (1.00,\ 2.4 \times 10^{-3}\,\mathrm{eV}^2)$, and the 90 % confidence level allowed parameter region is :

$$1.9 \times 10^{-3}\,\mathrm{eV}^2 \ < \ \Delta m^2 < 3.1 \times 10^{-3}\,\mathrm{eV}^2 \tag{9.3}$$

$$0.90 \ < \ \sin^2 2\theta \tag{9.4}$$

This parameter region is consistent with that from the oscillation analysis based on zenith angle distributions.

Bibliography

[1] M. Honda *et al.*, Phys. Rev. D **64**, 053011 (2001).

[2] M. Honda *et al.*, In *Proceedings of the 28th International Cosmic Ray Conferences, Tsukuba, Japan*, (2003).

[3] S.L. Glashow, Nucl. Phys. **22**, 579 (1961).

[4] S. Weinberg, Phys. Rev. Lett. **19**, 1264 (1967).

[5] A. Salam, In *Proceedings of the 8th Nobel Symposium on Elementary particle theory, relativistic groups and analyticity*, edited by N. Svartholm (1969).

[6] Z. Maki, M. Nakagawa, and S. Sakata, Prog. Theo. Phys. **28**, 870 (1962).

[7] Y. Fukuda *et al.*, Phys. Lett. **81**, 1562 (1998).

[8] K.S. Hirata *et al.*, Phys. Lett. B **205**, 416 (1988).

[9] K.S. Hirata *et al.*, Phys. Lett. B **280**, 146 (1992).

[10] The Soudan 2 Collaboration, *Observation of Atmospheric Neutrino Oscillations in Soudan 2* (hep-ex/0307069), submitted to Phys Rev D.

[11] The MACRO collaboration, Phys. Lett. B **566**, 35 (2003).

[12] S.H. Ahn *et al.*, Phys. Lett. B **511**, 178 (2001).

[13] I. Frank and I.Tamm, C. R. Acad. Sci. USSR **14**, 109 (1937).

[14] H. Kume *et al.*, Nucl. Inst. and Meth. **205**, 443 (1983).

[15] A. Suzuki *et al.*, Nucl. Inst. and Meth. A **329**, 299 (1993).

[16] R. Claus *et al.*, Nucl. Inst. and Meth. A **261**, 540 (1987).

[17] H. Ikeda *et al.*, Nucl. Inst. and Meth. A **320**, 310 (1992).

[18] T.Tanimori *et al.*, IEEE Trans. Nucl. Sci. **NS-36**, 497 (1989).

[19] J. George, Ph.D. Thesis, University of Washington (1998).

[20] T. Shiabata, Master Thesis, Niigata University (2002).

[21] P. Hanggi *et al.*, Phys. Lett. B **51**, 119 (1974).

[22] M. Yamada *et al.*, Phys. Rev. D **44** 617 (1991).

[23] M. Honda *et al.*, Phys. Rev. D **52**, 4985 (1995).

[24] G.Battistoni *et al.*, Astropart.Phys. **19** 269 (2003) [Erratum-ibid. **19** 291 (2003)]. (http://www.mi.infn.it/ battist/neutrino.html)

[25] G.Barr *et al.*, private communication.

[26] L.V. Volkova, Sov. J. Nucl. Phys. **31**, 784 (1980).

[27] W.R. Webber, R.L. Golden and S.A. Stephens, In *Proceedings of the 20th International Cosmic Ray Conference* (1987).

[28] E.S. Seo *et al.*, Astrophys. J. **378** 763 (1991).

[29] P. Pappini *et al.*, In *Proceedings of the 23rd International Cosmic Ray Conference* (1993).

[30] M. Boezio *et al.*, Astrophys. J. **518** 457 (1999).

[31] W. Menn *et al.*, Astrophys. J. **533** 281 (2000).

[32] T. Sanuki *et al.*, Astrophys. J. **545** 1135 (2000).

[33] J.Alcarez *et al.*, Phys. Lett. B **490** 27 (2000).

[34] M.J. Ryan, J.F. Ormes and V.K. Balasubrahmanyan, Phys. Rev. Lett. **28** 985 (1972).

[35] K. Asakamori *et al.*, Astrophys. J. **502** 985 (1998).

[36] I.P. Ivanenko *et al.*, In *Proceedings of the 23rd International Cosmic Ray Conference* (1993).

[37] Y. Kawamura *et al.*, Phys. Rev. D **40** 729 (1989).

[38] A.V. Apanasenko *et al.*, Astropart. Phys. **16** 13 (2001).

[39] M.Motoki *et al.*, Astropart.Phys. **19** 113 (2003).

[40] P. Hansen *et al.*, Phys.Rev. D **68** 103001518 (2003).

[41] M.Honda *et al.*, In *Proceedings of the 27th International Cosmic Ray Conferences, Hamburg, Germany*, (2001).

[42] R.A. Smith and E.J. Moniz, Nucl. Phys. B **43**, 605 (1972). [Erratum-ibid. B **101**, 547 (1975).]

[43] Y.Itow from K2K experiment, private communication.

[44] S.K.Singh and E.Oset, Phys. Rev. C **48**, 1246 (1993).

[45] C.H. Llewellyn Smith, Phys. Rep. **3**, 261 (1972).

[46] H. Grabosch *et al.*, Z. Phys. C **41**, 527 (1989).

[47] S. Barish *et al.*, Phys. Rev. D **16**, 3103 (1977).

[48] S. Bonetti *et al.*, Nouvo Cimento **38**, 260 (1977).

[49] M. Pohl *et al.*, Nuovo Cimento **26**, 332 (1979);
N. Arimenise *et al.*, Nucl. Phys. B **152**, 365 (1979).

[50] A.S. Vovenko *et al.*, Yad. Fiz. **30**, 1014 (1979).

[51] S. Belikov *et al.*, Z. Phys. **320**, 625 (1985).

[52] J.Brunner *et al.*, Z. Phys. C **45**, 551 (1990).

[53] C.H. Albright *et al.*, Phys. Rev. D **14**, 1780 (1976).

[54] K. Abe *et al.*, Phys. Rev. Lett. **56**, 1107 (1986).

[55] K. Nakamura *et al.*, Nucl. Phys. A **268**, 381 (1976).

[56] D. Rein and L.M. Sehgal, Ann. of Phys. **133**, 1780 (1981).

[57] R. Feynman *et al.*, Phys. Rev. D **3**, 2706 (1971).

[58] S.K. Singh, M.J. Vicente-Vacas and E.Oset, Phys. Lett. B **416**, 23 (1998).

[59] G. Radecky *et al.*, Phys. Rev. D **25**, 116 (1982).

[60] T. Kitagaki *et al.*, Phys. Rev. D **34**, 2554 (1986).

[61] P. Allen *et al.*, Nucl. Phys. B **264**, 221 (1986).

[62] P. Allen *et al.*, Nucl. Phys. B **176**, 269 (1980).

[63] W. Lerche *et al.*, Phys. Lett. **4**, 510 (1978).

[64] J. Bell *et al.*, Phys. Rev. Lett. **15**, 1008 (1978).

[65] D. Allisia *et al.*, Z. Phys. C **24**, 119 (1984).

[66] S.J. Barish *et al.*, Phys. Lett. B **91**, 161 (1980).

[67] M. Derrick *et al.*, Phys. Rev. D **23**, 569 (1981).

[68] C.H. Albright and C. Jarlskog, Nucl Phys. B **84**, 467 (1975).

[69] M. Glück, E. Reya and A. Vogt, Z. Phys. D **57**, 433 (1995).

[70] S.J. Barish *et al.*, Phys. Rev. D **17**, 1 (1978).

[71] S. Barlag *et al.*, Z. Phys. C **11**, 283 (1982).

[72] T. Sjöstrand *et al.*, CERN-TH-7112-93 (1994).

[73] A. Bodek and U. K. Yang Nucl.Phys.Proc.Suppl. **112**, 70 (2002)

[74] P. Musset and J.P. Vialle, Phys. Rep. C **39**, 1 (1978).

[75] J.E. Kim *et al.*, Rev. Mod. Phys. **53**, 211 (1981).

[76] P.S. Auchincloss *et al.*, Z. Phys. C **48**, 411 (1990).

[77] P. Berger *et al.*, Z. Phys. C **35**, 443 (1987).

[78] S. Campolillo *et al.*, Phys. Lett. **84B**, 281 (1979).

[79] O. Erriquez *et al.*, Phys. Lett. **89B**, 309 (1979).

[80] J.V. Allaby *et al.*, Z. Phys. C **38**, 403 (1988).

[81] N.J. Baker *et al.*, Phys. Rev. D **25**, 617 (1982).

[82] C. Baltay *et al.*, Phys. Rev. Lett. **44**, 916 (1980).

[83] D.C. Colley *et al.*, Z. Phys. C **2**, 187 (1979).

[84] V.B. Anikeev *et al.*, Z. Phys. C **70**, 39 (1996).

[85] A.S. Vovenko *et al.*, Yad. Fiz. **30**, 187 (1979).

[86] D.B. MacFarlane *et al.*, Z. Phys. C **26**, 1 (1984).

[87] D.S. Baranov *et al.*, Phys. Lett. **81B**, 255 (1979).

[88] D. Rein and L.M. Sehgal, Nucl. Phys. B **233**, 29 (1983).

[89] V. Ammosov for the SKAT Collaboration, NuInt01 Workshop at KEK, Tsukuba, Japan (2001).

[90] L. Salcedo *et al.*, Nucl. Phys. A **484**, 557 (1988).

[91] G. Rowe *et al.*, Phys. Rev. C **18**, 584 (1978).

[92] C. Ingram *et al.*, Phys. Rev. C **27**, 1578 (1983).

[93] GEANT, CERN Program Library Long Writeup W5013 (1994).

[94] C. Zeitnitz and T.A. Gabriel, Nucl. Inst. and Meth. A **349**, 106 (1994).

[95] M. Nakahata *et al.*, J. Phys. Soc. Jpn. **55**, 3786 (1986).

[96] E. Bracci *et al.*, CERN/HERA 72-1 (1972).

[97] A.S. Carrol *et al.*, Phys. Rev. C **14**, 635 (1976).

[98] ZEBRA, CERN Program Library Long Writeups Q100/Q101 (1995).

[99] J. Kameda, Ph.D. Thesis, University of Tokyo (2002).

[100] D. Shantanu, Ph.D. Thesis, Boston University, will be published.

[101] K. Nitta, Ph.D. Thesis, Osaka University (2003).

[102] E.R. Davies, *Machine Vision: Theory, Algorithms, Practicalities*, Academic Press, San Diego (1997).

[103] G.L.Fogli *et al.*, Phys.Rev. D **66** 053010 (2002)

[104] C.Saji *et al.*, In *Proceedings of the 28th International Cosmic Ray Conferences, Tsukuba, Japan*, (2003).

[105] Particle Data Groupe, Review of Particle Physics, Phys.Rev. D **54** 155 (1996)

[106] V. Barger *et al.*, Phys. Rev. Lett. **82**, 2640 (1999).

[107] D.A. Krakauer *et al.*, Phys. Rev. D **44**, R6 (1991).

[108] E. Lisi *et al.*, Phys. Rev. Lett. **85**, 1166 (2000).